Theoretical Studies of Electronic Structures and Conductive Properties of Functional Materials

Yuji Ikeda

Department of Micro Engineering

Kyoto University

2012

Contents

General Introduction **5**

I Theoretical Studies on Electronic Structures with Electric Currents and Local Electric Conductivities **11**

1 Calculation of the Electronic State in Electronic Current for Nanowire Models **12**

1.1 Introduction 12

1.2 Theory 14

1.3 Calculation Method 14

1.4 Model 17

1.5 Results 18

1.6 Summary and Discussion 22

2 Local Electric Conductive Property of Si Nanowire Models **26**

2.1 Introduction 26

2.2 Theory 28

2.2.1 Definition of the local properties 28

2.3 Calculation Methods 30

2.3.1 CPHF equations 30

2.3.2 Electronic structures with electric currents 31

2.3.3 Calculation method for local properties 33

2.3.4 Computational models 34

2.4 Results 36

2.4.1 Pristine model 36
2.4.2 Comparison with the Ge-substituted model 43
2.5 Conclusion 46

3 Local Transport Property of GaN Cluster as a Model of Nanowire 53
3.1 Introduction 53
3.2 Theory 54
3.3 Calculation Method 55
3.3.1 Quantum states of conductive electrons 55
3.3.2 Conductivity tensor 57
3.3.3 Computational model 57
3.4 Results 59
3.5 Summary and Discussion 63

4 Nanosize Electronics Material Analysis by Local Quantities Based on the Rigged QED Theory 68
4.1 Introduction 68
4.2 Theory 69
4.2.1 Spin torque and zeta force 69
4.2.2 Local conductivity 71
4.3 Results 72
4.3.1 Spin torque and zeta force 72
4.3.2 Local conductivity 75
4.4 Summary 77

II Theoretical Studies on Functional Materials in Terms of Their Bonding Nature 79

5 Theoretical Study of Gallium Nitride Crystal Growth Reaction Mechanism 80
5.1 Introduction 80
5.2 Computational Methods 81
5.2.1 Gas-phase reactions 81

5.2.2 Surface reactions . . . 82
5.2.3 Electronic quantum energy density . . . 84
5.3 Results and Discussion . . . 84
5.3.1 Reaction pathway in the gas phase . . . 84
5.3.2 GaN(0001) surface structure . . . 86
5.3.3 Chemical reactions on the GaN surface . . . 87
5.4 Conclusions . . . 93

6 Theoretical Study of Hydrogenated Tetrahedral Aluminum Clusters 97
6.1 Introduction . . . 97
6.2 Theory and Calculation Methods . . . 98
6.2.1 Ab initio electronic structure calculation . . . 98
6.2.2 RDFT analysis . . . 98
6.3 Results and Discussion . . . 100
6.3.1 Structures and stability . . . 100
6.3.2 Stress tensor analysis of chemical bond . . . 104
6.4 Summary . . . 107

7 Aluminum Hydride Clusters as Hydrogen Storage Materials and Their Electronic Stress Tensor Analysis 112
7.1 Introduction . . . 112
7.2 Theory and calculation method . . . 113
7.2.1 Electronic structure calculation . . . 113
7.2.2 Regional DFT calculation . . . 113
7.3 Results and discussion . . . 115
7.3.1 Energy density based bond order and spindle/pseudo-spindle structures 115
7.3.2 Electronic structure under the presence of electronic current and the electronic stress tensor . . . 117
7.4 Summary . . . 118

8 Theoretical Study of Adsorption of Lithium Atom on Carbon Nanotube 122
8.1 Introduction . . . 122
8.2 Computational Details . . . 123

8.3 Result and Discussion . . . 126
8.3.1 The electronic structure of one lithium adsorbed carbon nanotube models . . . 126
8.3.2 The electronic structure of multiple lithium atoms adsorption model . 130
8.4 Conclusions . . . 134

9 Local Dielectric Property of Cubic, Tetragonal, and Monoclinic Hafnium Oxides 140
9.1 Introduction . . . 140
9.2 Theory . . . 142
9.3 Computational Details . . . 143
9.3.1 Calculation models and conditions . . . 143
9.3.2 Local polarizability and dielectric constant densities . . . 146
9.4 Results and Discussion . . . 148
9.4.1 Appropriate termination conditions . . . 148
9.4.2 Local dielectric property of HfO_2 . . . 153
9.4.3 Comparison with the dielectric property of SiO_2 . . . 159
9.5 Conclusions . . . 163

General Conclusion 169

Acknowledgements 171

List of Publications 171

Conference Appearances 175

General Introduction

In recent years, researches and developments of nanoscale materials such as semiconductor nanowires and new functional materials have become popular. These new materials have excellent properties as compared to conventional ones, and hence they can construct new energy systems and further miniaturization of electronic devices. For such nanoscale materials, quantum effects are important and need to be considered. Therefore in this thesis, various materials are analyzed by using first-principles electronic structure calculations. The thesis is organized into two parts. PART I (consisting in Chapter 1-4) is devoted to reports of development of calculation methods for electronic structures with electric currents and calculations of local electric conductive properties by using these methods. In PART II (consisting in Chapter 5-9), analysis of bonding nature for understanding crystal growth, dielectric properties, and conductive properties are reported.

PART I is further devided to reports for developments of the calculation methods and ones for applications to semiconductor nanowire models. In these studies, local electric conductivities $\overleftrightarrow{\sigma}(\vec{r})$ are analyzed. $\overleftrightarrow{\sigma}(\vec{r})$ is defined in Rigged Quantum ElectroDynamics (QED) which is formalized and proposed by Tachibana. Ordinary global quantities for a whole device reveal effects of impurities, defects, and interfaces only indirectly, and hence $\overleftrightarrow{\sigma}(\vec{r})$ is important for the analysis of conductive properties for nanomaterials.

In Chapter 1, Calculation method for electronic structures with electric currents based on the method of self-consistent field (SCF) are shown. Application results for alminum nanowire models are also reported. Although there are many studies on the electric conductivity, most of them do not represent electric currents as flows of actual electrons, and interactions of the electrons are not safficiently described. For the method developed in this study, conduction electrons are represented as quantum states, and the Coulomb and exchange interactions between bound and condcution electrons are included. In addition,

effects of magnetic field caused by electrons are investigated by including vector potential in calculations of electronic structures. Since the electronic currents and vector potential depend on each other, electronic structures are calculated based on a SCF method. Calculations of electronic structures of two aluminum nanowire models which have different lengths are performed, and local electric current densities in these models are investigated.

Development of a calculation method of electronic structures with electric currents based on the perturbation theory is reported in Chapter 2. Calculation results for silicon nanowire models are also shown. In this study, a new calculation method for electronic structures with electric currents have been developed by using the coupled perturbed Hartree-Fock theory, the perturbation method at the Hartree-Fock level. Thus, analytical calculations of the local electrical conductivities have been available. In this study, calculations of local electric conductivities defined both for external and internal electric fields are performed. The one defined for internal electric field reveals the response of the current density to the electric field which is actually occurring at that point. It should be noted that this local quantity does not have corresponding macroscopic one. For calculation models, a silicon nanowire model without impurities and a model with a germanium atom which is substituted for one of the silicon atoms are considered. It is shown that regions where local electric conductivities have negative eigenvalues exist. These regions may be related to the origin of negative differential resistance. Regions with complex eigenvalues are also found. It can be shown that electric current densities responses "rotationally" to electric field in these regions. This can be proved by taking appropriate linear combinations of complex eigenvectors so that they are in real space. For the local electric conductivity defined for internal electric field, it shows a different position dependence from that of the external one. The impurity model shows changes for the value of the local conductivity in the vicinity of the germanium atom.

In Chapter 3, an analysis of conductive properties for a gallium nitride (GaN) nanowire model are reported. Since having a high mobilities due to ballistic conductions, semiconductor nanowires are candidate materials for next-generation field effect transistors. For such nanomaterials, analysis of local electric conductive properties is important. In this study, electric conductive properties are investigated in terms of local electrical conductivity tensor. This is calculated by using the method developed in Chapter 1. Analysis are performed for

a GaN nanowire which is one of the semiconductor nanowires. In this study, local electric conductivity tensors defined for external electric field is analyzed. It is confirmed that local electric conductivity tensor has large position dependence. In addition, it is found that regions which have complex eigenvalues are present in the model. As mentioned above, these regions show rotational response of electric currents to external electric field.

Chapter 4 is a research report for electronic spin dynamics and local electric conductive properties. Local electric conductivity tensors are calculated for a silicon nanowire model with [011] growth direction. In order to obtain electronic structures with electric currents, the method which is developed in the study reported in Chapter 1 are used. As a result, similar characteristics to the GaN nanowire model in Chapter 3 are found. In addition, electronic spin dynamics is investigated for dimers of alkali atoms. In this analysis, spin torque and zeta force which is defined in Rigged QED are used.

Analysis for crystal growth of GaN in terms of both gas phase reactions and ones on a surface is reported in Chapter 5. GaN has attracted much attention in the field of optoelectronic applications such as light emitting diodes and photodetectors because of its wide band gap. In recent years, a high-quality GaN crystal can be obtained by using a metal organic chemical vapor deposition technology. The stability of a GaN crystal depends on the state of its surface. Chemical reactions in the gas phase also play important roles in the crystal growth. In this study, gas-phase and surface reactions in the process of crystal growth are investigated by using first-principles calculations in order to obtain a high-quality GaN crystal. Trimethyl-gallium (TMG) and ammonia (NH_3) is considered as precursors in gas phase. First, the series of reactions where the methyl groups of TMG are replaced by an amino group derived from NH_3 is investigated in terms of stabilization and activation energies. Reactions where coordination bonds are made between NH_3 and the molecules produced in these reactions are also investigated. As a result, it is found that alkyl gallium molecules which have a coordination bond with NH_3 are relatively stable and supposed to be present in gas phase. Next, bonding between a gallium atom of the molecules in gas phase and the atom on the surface of GaN crystal is investigated. As a result, it is found that if a Ga-Ga bond between them are produced, it prevents the stable crystal growth. Furthermore, it is shown that if the alkyl gallium molecules with the coordination bond with NH_3 are produced in gas phase, they do not make the Ga-Ga bond and may help crystal

growth. Kinetic energy density defined in the Rigged QED is used for the determination of the presence or absence of bonds between atoms. This kinetic energy density may take both positive and negative values. In regions which have posivite values, electrons can move as if they follow classical mechanics, while regions with negative values means that electrons can move only by quantum effects. In addition, the surface where kinetic energy density is equal to zero can be interpreted as the boundary of the molecule, and this can determine the presence or absence of binding between the atoms. By using this property, the bond between the gallium atoms are examined.

In Chapter 6, Analysis for structures and stabilities for aluminum hydride clusters Al_4H_n (n = 0, 2, 4, 6, 8, 10, and 12) are reported. Chemical bonding in them are also investigated in terms of quantum energy density. There are several challenges to the spread of the fuel cell, and the development of high-performance hydrogen storage materials is one of them. Aluminum hydride clusters are candidates for the hydrogen storage materials. In this study, a tetrahedral cluster Al_4 and its hydrides are focused on, and their properties as a hydrogen storage material and characteristics of chemical bonds in the clusters are investigated. First, the structures of hydrides are determined, and their stability is analyzed in terms of total binding energies and average ones for a Al-H bond. As a result, the total binding energies increase with the increase in the number of hydrogen atoms adsorbed, while the average ones for a Al-H bond are decreased. Next, analysis of electronic stress tensor density and bond orders which are defined in the Rigged QED is performed for the obtained structures. As a result, it is found that the bond orders for Al-Al and Al-H bonds are well correlated with bond lengths, respectively. In addition, it is confirmed that the maximum eigenvalues of the electronic stress tensor density are negative around Al-Al bonds, while they are positive around Al-H bonds. This result indicates that our bond orders and electronic stress tensors can be used to characterize types of various chamical bonds.

In Chapter 7, almunum hydride clusters are analyzed as well as the report in Chapter 6. In this study, electronic stress tensor density is investigated for electronic states with electric currents by using the method which is reported in Chapter 1. As a result, difference from the results without conduction electrons and symmetry breaking are confirmed.

Chapter 8 is a research report on the adsorption of lithium atoms on a surface of a carbon nanotube (CNT) model. CNTs are considered as a candidate material for anodes of lithium-

ion batteries. A theoretical report has reported that CNTs have a capacity of lithium atom three times more than graphites. However, experiments do not show an increase in the capacity as many as expected. Instead, a large amount of irreversible lithium storage is reported. These features suggest that most lithium atoms are stored on interior surfaces of CNTs and cannot be available. In this study, a model for (12,0) zigzag single wall CNT is considered. The adsorption of a lithium atom to the inner surface of this model shows greater stabilization energy than the adsorption to the outer surface. In order to understand the cause of this feature, both charge transfer and local chemical potential density which is defined in Rigged QED are examined. For charge transfer, it is found that the lithium atom which adsorbed on the interior surface have slightly larger positive charge than that adsorbed on the exterior surface. Chemical potential denisity at a specific point reveals the energy per an electron on the corresponding point, and hence electrons are supposed to be transfered to the regions which have relatively small values of the chemical potential density in chemical reactions. It is found that the regions which have small values are distibuted around the inner surfaces more widely than those around the outer surfaces. In other words, electrons in lithium atom prefer the adsorption on the inner surface. In addition, adsorption of multiple lithium atoms on inner surface of nanotubes are investigated in terms of adsorption energy and charge transfer. As a result, it is shown that the repulsion between a lithium atoms destabilize the system.

Chapter 9 is a report on a local the dielectric properties of hafnium oxide (HfO_2). Field effect transistors require very thin gate insulating films, and the conventional ones made of silicon oxide (SiO_2) have reached their limits of thinning because of increasing leak currents. Hence, it is expected that HfO_2 which has a high dielectric constant is an alternative material. The thickness of gate insulating films are about few nanometers. For such nanomaterials, position dependences of local physical quantities are very important. In this study, local dielectric properties of HfO_2 are investigated by using a local polarizability and a local dielectric constant which is defined in Rigged QED. For the crystal structures of HfO_2, cubic, tetragonal, monoclinic ones are known, and the dielectric constants of them are different between them. In this study, the local dielectric properties for these structures are analyzed. In addition, SiO_2 also analyzed for comparison, and differences in the dielectric properties of ionic and covalent bondings are investigated. Although it is known that

lattice polarization contributes largely for dielectric constant of HfO_2, only the contribution of the electronic polarization is focused on. First of all, termination conditions of cluster models in this study are investigated in order to reproduce the properties of the crystals. As a result, it is found that the model with point charges is preferable for HfO_2, and the model with hydrogen termination is better for SiO_2, in order to reproduce the nature of the crystals. Next, the local polarizability and local dielectric constant for these models are calculated. As a result, it is found that regions around oxygen atoms paricularly has large eigenvalues of polarizability. Regions with complex eigenvalues are also found. As well as the local electrical conductivity described in Chapter 2, it can be said that the local polarization responses rotationally to external electric field for these regions. For the local dielectric constant, regions which have negative eigenvalues are found around oxygen atoms. This means that the magnitude of the local polarization induced by external electric field is greater than the magnitude of the field. The average values of the local polarizability and local dielectric constant in the vicinity of specific atoms and bonds are also investigated in this study. From the comparison with the results for SiO_2, it it found that the eigenvalues of local polarizability around silicon atoms in SiO_2 are significantly smaller than those around hafnium atoms in HfO_2. This is because electrons near the silicon atoms are bound covalently and hard to move.

Part I

Theoretical Studies on Electronic Structures with Electric Currents and Local Electric Conductivities

Chapter 1

Calculation of the Electronic State in Electronic Current for Nanowire Models

1.1 Introduction

Recently, semiconductor nanowire structure, in particular silicon nanowire, is paid much attention by many researchers [1–9]. Semiconductor nanowire is considered as a good candidate for materials of Field Effect Transistor (FET) devices. High electric conductance is expected due to the ballistic conduction. Among semiconductor nanowire, the most popular one is silicon nanowire, since this is the leading candidate for a material for post Moore devices [7–9]. For nanoscale materials, it is important that properties of them are predicted by the first principles calculations before the fabrication in laboratories.

Although the conductive properties are reported in many works, conductive electrons have not been included in calculations by a satisfactory manner. In other words, electronic current has not been represented by electrons in most calculations. Hence, there is little knowledge of the effect of the internal electronic current on small (semi)conductive materials, such as these nanowire. For example, when the electronic current exists in system, a magnetic field is induced by the current. The electronic state of the system is affected by the magnetic field induced by a large current. However, available calculation codes have not included this effect.

One of purposes of this work is to report the first step of our first principles calculations program representing electronic current. In our program, the conductive electrons are treated as quantum states which are calculated along with other electrons. In other words, the electronic current is represented by electrons. Since the wave functions of the conductive electrons can be calculated, the local electronic current density, which is defined by one of the authors [10, 11], can also be calculated. We can clarify the conductive properties of nanoscale materials by using this quantity. By doing so, the effects of the Coulomb and exchange interactions by conductive electrons on electrons in system are included. Another purpose of this work is to include the effect of the magnetic field. In addition to the representation of that induced by the internal electronic current, the magnetic field is used to realize a boundary condition that the calculating molecular system is embedded in a larger system, which includes electrodes. We develop the algorithm of first principles calculations considering electromagnetic field. Magnetic field is treated as the vector potential. In order to treat correctly large magnetic fields, which are even out of perturbative region, we take a self-consistent field (SCF) manner. This is because the vector potential and the electronic current are dependent on each other. In this work, we show our results for small aluminum nanowire models. Before semiconductor nanowires are studied, which is our goal for the present, we should check our results for conductor materials and clarify the required calculation condition for our purpose.

This paper is organized as follows. In the next section, we define the local electronic current density, and show how the vector potential is calculated by using the current density. In Sec. 1.3, the calculation method of our program code is summarized. We show how our code represents the conductive electrons and how the electronic current and the vector potential are determined in a SCF manner. The sample models used in this work are introduced in Sec. 1.4. In Sec. 1.5, we show our results for the small nanowire models. We compare our results of local electronic currents of the nanowire models. The effect of magnetic fields induced by the internal current is also discussed. Section 1.6 is devoted to the summary and discussion.

1.2 Theory

The covariant derivative for electromagnetic interaction for an electron is defined as $\hat{D}_\mu = \partial_\mu + iZ_e e/(\hbar c)\hat{A}_\mu(\boldsymbol{r})$, where $Z_e = -1$ for electrons, c is the speed of the light in the vacuum, and $\hat{A}_\mu$ is the four component vector potential. Hence, the four component momentum of the electron is $\hat{p}_\mu = i\hbar\partial_\mu - Z_e(e/c)\hat{A}_\mu(\boldsymbol{r})$ and the three dimensional one is given by

$$\hat{\boldsymbol{p}} = -i\hbar\boldsymbol{\nabla} - Z_e(e/c)\hat{\boldsymbol{A}}(\boldsymbol{r}). \tag{1.1}$$

The local electronic current density [10, 11] is given by using the local value of the probability current based on the Rigged QED theory [12–22]. In the nonrelativistic theory, this is given as

$$\begin{aligned} \hat{\boldsymbol{J}}(\boldsymbol{r}) &= \frac{Z_e e}{2m_e}\sum_i \left[\hat{\psi}_i^\dagger(\boldsymbol{r})\hat{\boldsymbol{p}}(\boldsymbol{r})\hat{\psi}_i(\boldsymbol{r}) + h.c.\right] \\ &= \frac{Z_e e}{2m_e}\sum_i \left[-i\hbar\hat{\psi}_i^\dagger(\boldsymbol{r})\boldsymbol{\nabla}\hat{\psi}_i(\boldsymbol{r}) - \frac{Z_e e}{c}\hat{\psi}_i^\dagger(\boldsymbol{r})\hat{\boldsymbol{A}}(\boldsymbol{r})\hat{\psi}_i(\boldsymbol{r}) + h.c.\right], \end{aligned} \tag{1.2}$$

where $\hat{\psi}_i$ is the i-th natural orbital and m_e is the mass of the electron.

The electronic current induces a magnetic field, i.e., vector potential. Hence, the vector potential is given as

$$\hat{\boldsymbol{A}}(\boldsymbol{r}) = \frac{1}{c}\int d^3\boldsymbol{s}\frac{\hat{\boldsymbol{J}}_T(cu, \boldsymbol{s})}{|\boldsymbol{r} - \boldsymbol{s}|}, \tag{1.3}$$

where $\hat{\boldsymbol{J}}_T(\boldsymbol{r})$ is the transverse component of $\hat{\boldsymbol{J}}(\boldsymbol{r})$ and $u \equiv t - |\boldsymbol{r} - \boldsymbol{s}|/c$. We show explicitly the time coordinate for this expression due to retardation effects. With the vector potential, the kinetic part of Hamiltonian is given as the following operator,

$$\hat{H}_k = \frac{1}{2m_e}\left[-i\hbar\boldsymbol{\nabla} - \frac{Z_e e}{c}\hat{\boldsymbol{A}}(\boldsymbol{r})\right]^2. \tag{1.4}$$

By using this Hamiltonian, the electronic states with considering the vector potential can be derived.

1.3 Calculation Method

In this work, conductive electrons are included in our electronic state calculation. Our calculation is performed based on the quantum mechanics. We use the linear combination

of atomic orbital (LCAO) method, since we pay attention to the relation between the local electronic current and the bonding state of molecules. For this purpose, the LCAO method is appropriate. In our calculation, wave functions are expanded by gaussian functions. Hence, the electronic states representing the electronic current is given by the linear combination of gaussian functions. The state of conductive electron is considered to be similar to a plain wave rather than gaussian functions. Therefore, we assume the following function as the initial electronic state representing electronic current,

$$f(\boldsymbol{r}) \equiv \exp(-a_x x^2)\exp(-a_y y^2)\exp(ik_z z), \tag{1.5}$$

where a_x, a_y, and k_z are parameters. These parameters are fixed during a calculation for simplicity. We expand this function by gaussian basis functions ϕ_i,

$$f_G(\boldsymbol{r}) = c_G \sum_i \langle \phi_i | f \rangle | \phi_i \rangle, \tag{1.6}$$

where c_G is the normalization factor. We adopt this function f_G as a conductive state in our calculation and replace the initial electronic state of the highest occupied molecular orbital (HOMO) by this function. The function f_G has complex number, and hence complex molecular orbital coefficients must be used in our calculation. We take $a_x = a_y = 1.0$ a.u. ($= 0.280$ Å^{-2}) as constants and k_z as an input parameter. In the following, the value of k_z is shown in the atomic unit. We checked that the results are not significantly dependent on $a_{x,y}$. Note that the effect of vector potential is not considered in this current.

In our calculations, the electronic state representing the electronic current is derived as follows. We inject the conductive state, i.e., $f_G(\boldsymbol{r})$ into as the initial condition of the HOMO for the SCF calculation. Of course, if the ordinary SCF calculation is completed, the derived electronic state is the ground state and has no net current. We want to derive conductive electronic states with including the Coulomb and exchange interactions by conductive electrons. Hence, we also replace the HOMO by the conductive state in every SCF cycle. This conductive state is generically not orthogonal to other orbitals. Hence, if so, the orthogonalization is performed in every cycle. Empirically, this orthogonalization is required in first several cycles, and after then, the conductive state is orthogonal to others within the accuracy. In other words, our procedure is to derive the most stable electronic states with the condition that the HOMO is the conductive state. In the sense, our procedure is interpreted as a boundary condition. This condition is a first step to derive conductive

electrons as quantum state by the boundary condition that the scalar and vector potentials appropriately represent the medium, in which the system is embedded.

Once electronic states with net electronic current are derived, the vector potential induced by the current can be calculated by the Maxwell equation. In our calculation, the vector potential is calculated as grid data, whose calculation region is wide enough. Data at each point require the integration over the whole region, which wastes very huge calculation resources. By the integration using the following Fourier expansion, this problem can be avoided,

$$\boldsymbol{A}(\boldsymbol{r}) = \frac{1}{c}\int d^3\boldsymbol{s}\sum_{\boldsymbol{k}} \boldsymbol{j}_{T_{\boldsymbol{k}}}\frac{e^{i\boldsymbol{k}\cdot\boldsymbol{s}}}{|\boldsymbol{r}-\boldsymbol{s}|} = \frac{1}{c}\left[\boldsymbol{j}_{T_0}\int d^3\boldsymbol{s}\frac{1}{|\boldsymbol{r}-\boldsymbol{s}|} + \sum_{\boldsymbol{k}\neq 0}\boldsymbol{j}_{T_{\boldsymbol{k}}}\frac{4\pi}{|\boldsymbol{k}|^2}e^{i\boldsymbol{k}\cdot\boldsymbol{r}}\right]. \tag{1.7}$$

However, another problem is seen to be arisen. The integration of the zero mode of Fourier expansion is divergent.

Our prescription for this divergence is the introduction of the cutoff parameter as,

$$\boldsymbol{A}(\boldsymbol{r}) = \frac{1}{c}\int d^3\boldsymbol{s}\frac{\boldsymbol{J}_T(\boldsymbol{s})}{|\boldsymbol{r}-\boldsymbol{s}|}e^{-\alpha|\boldsymbol{r}-\boldsymbol{s}|}, \tag{1.8}$$

where α is the cutoff parameter. This removes the source of the artificial divergence, which is the contributions from points at infinity. This cutoff parameter can also be interpreted as effective photon mass. In condensed matter, the photon cannot travel to an infinitely distant point. Therefore, we introduced this parameter to remove the divergence, and however, this is supported by the physical reason. After the inclusion of this parameter, Eq. (1.7) is reduced to

$$\boldsymbol{A}(\boldsymbol{r}) = \frac{1}{c}\left[\sum_{\boldsymbol{k}}\boldsymbol{j}_{T_{\boldsymbol{k}}}\frac{4\pi}{|\boldsymbol{k}|^2+\alpha^2}e^{i\boldsymbol{k}\cdot\boldsymbol{r}}\right]. \tag{1.9}$$

In this form of the vector potential, we can use the fast Fourier transformation routine. The parameter α can be determined by estimating the effective photon mass in materials. However, in this work, we take $\alpha = 1.0$ a.u. as an input parameter for simplicity.

After the vector potential is derived, the Hamiltonian with the vector potential (1.4) can be calculated. Then, the electronic states with the existence of the magnetic field can be derived. While the vector potential is determined by the electronic current, the electronic current is dependent on the vector potential. Hence, we should calculate these quantities by a SCF method. In our calculation, first the electronic current are calculated, and then the

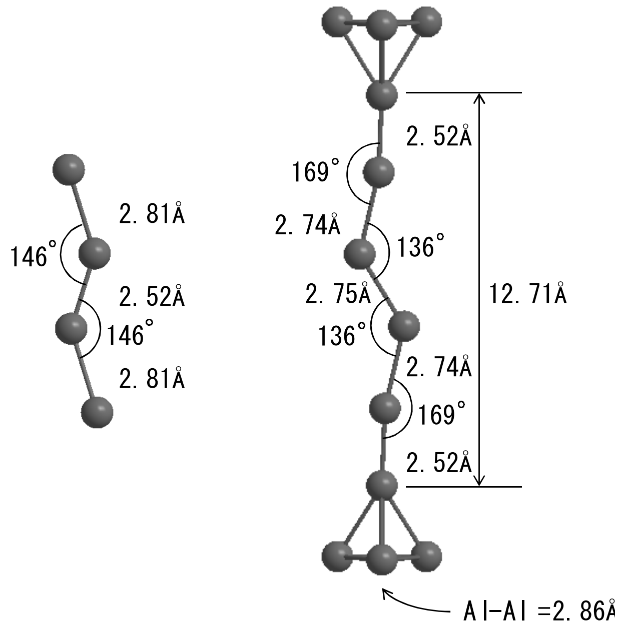

Figure 1.1: The structure of models are shown. The left figure shows the small zigzag Al_4 model, while the right figure shows the large Al_4-Al_4-Al_4 model.

vector potential induced by this current are estimated. Then, the electronic state calculation is performed again by using the Hamiltonian with the vector potential. A new electronic current is derived by this electronic state and a new vector potential is calculated by the new electronic current. This procedure is continued till the updated electronic state and vector potential remain unchanged within the accuracy.

We carry out a series of the calculation by the Molecular Regional DFT (MRDFT) program package [23], which is developed in our laboratory. In this work, we adopt the restricted Hartree-Fock (RHF) method as a first step. Of course, post SCF calculation is required to derive accurate enough results. This issue will be tried in near future works.

1.4 Model

We choose two simple models for demonstration. In Fig. 1.1, we show our models, the small model of zigzag Al_4 and the large model of Al_4-Al_4-Al_4. The structure of the both sides of the Al_4-Al_4-Al_4 model is the regular tetrahedron, whose directions are the same as each other. By using these extra aluminum atoms, we check the effects of the ends of

the model. The structure of the zigzag Al_4 models are optimized on the condition without the conductive state. For the Al_4-Al_4-Al_4 model, the structure of the middle Al_4 part is optimized.

For the aluminum atoms, the LANL2DZ basis set is taken for saving the calculation costs [24–27]. Larger basis sets are favored for our calculation method, since the input current state is expanded in basis sets. However, the purpose of this work is to check our method, and hence, the small basis set is used as a reference. We are now comparing with the results of different basis sets, which are shown elsewhere in near future. As the driving force to accelerate the electron, the electric field is imposed on z direction as $E_z = 0.001$ a.u.

1.5 Results

In Figs. 1.2 and 1.3, the z-component of the current density on the $y = 0$ plane is shown for the small and large models, respectively. The values of k_z are chosen as $k_z = -0.1, -0.5$, and 1.0 for (a), (b), and (c), respectively. The red (blue) color shows the positive value of electronic current density. The depth of the color shows the magnitude of the current density. The unit of the electronic current density is the atomic unit (1 a.u.$= 2.37 \times 10^{18}$ A/m^2). Since we use the basis set which has pseudopotential to represent the core electrons, the region close to the nuclei are not accurate. Hence, we put the filled circle indicating the nuclei on the regions. We confirmed that the current density is zero in the whole region for $k_z = 0$ and has the opposite sign and the same value for $k_z > 0$. We also confirmed that the strong correlation between the value of k_z and the electronic current density for $k_z = 0$ to (-1.0).

The results of the small and large models have some similarity. For larger k_z, the current density are widely distributed throughout nanowire. The net current is considered to pass straightly through nanowire. For smaller k_z, the current density is small between atoms. This is attributed to the smallness of the basis functions, which are the gaussian functions whose centers are the positions of nuclei. The straightness of the current is slightly worse in small model. On the other hand, there are some differences arisen from the difference of the structure. Around the aluminum atoms on both end of the small nanowire model, the negative current density can be seen. This feature cannot be seen in the center four

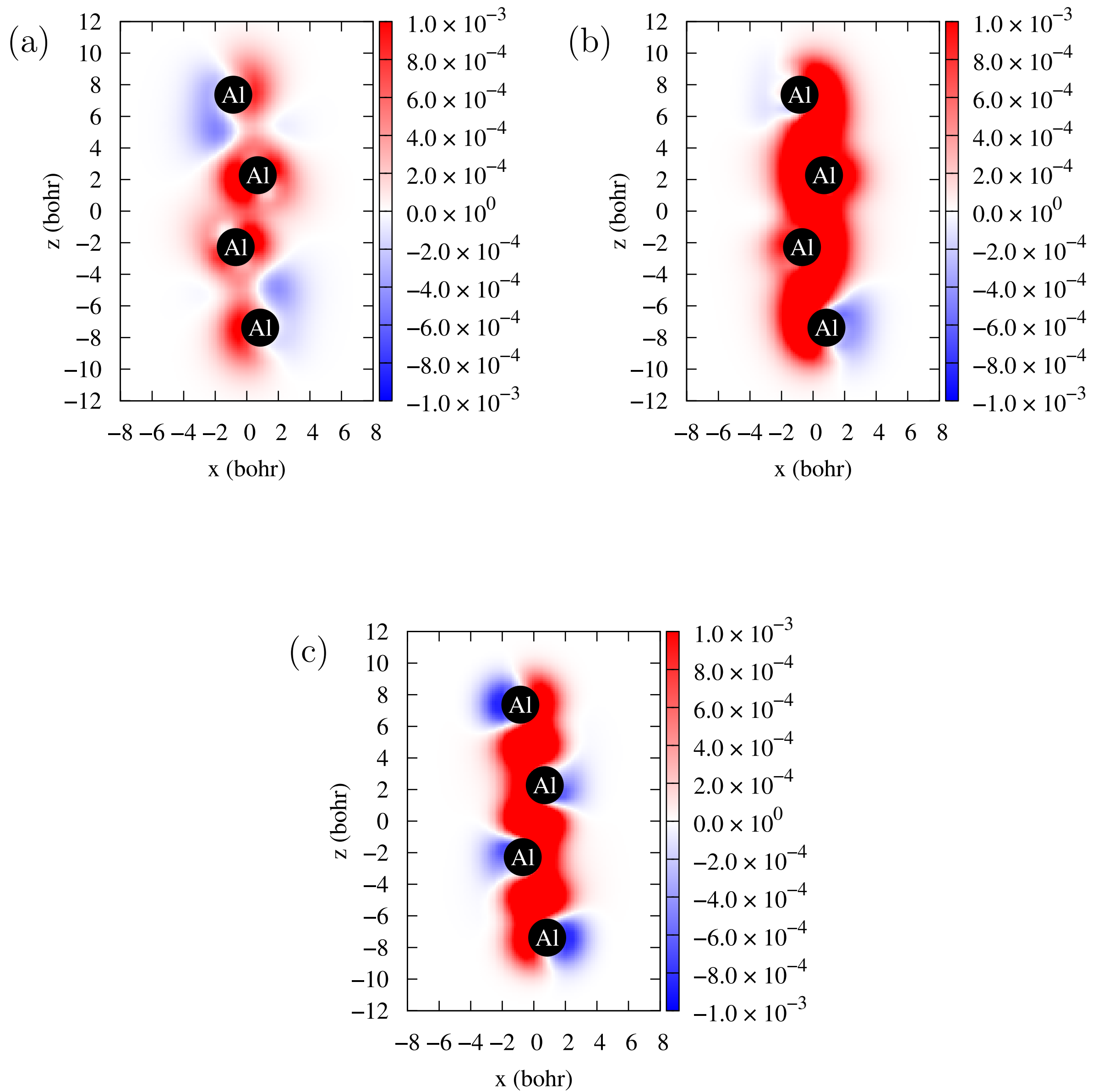

Figure 1.2: The z-component of the electronic current density of the small model is shown for the $y = 0$ plane. The values of k_z are chosen as $k_z = -0.1$ for (a), $k_z = -0.5$ for (b), and $k_z = -1.0$ for (c). The red (blue) color shows the positive value of electronic current density. The depth of the color shows the magnitude of the current density. The unit of the electronic current density is the atomic unit (1 a.u.$= 2.37 \times 10^{18}$ A/m^2).

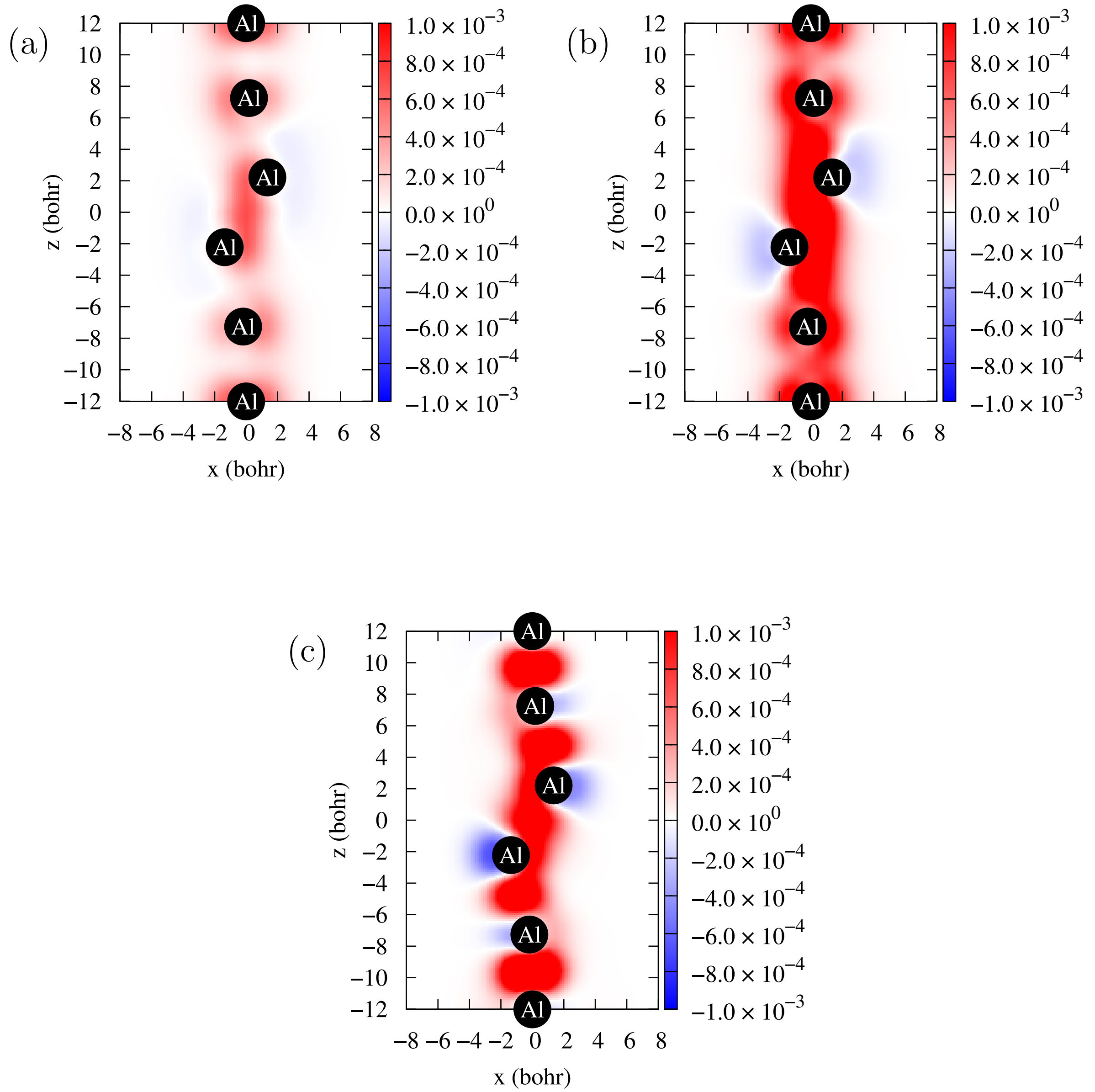

Figure 1.3: The z-component of the electronic current density of the large model is shown for the $y = 0$ plane. The values of k_z are chosen as $k_z = -0.1$ for (a), $k_z = -0.5$ for (b), and $k_z = -1.0$ for (c). The red (blue) color shows the positive value of electronic current density. The depth of the color shows the magnitude of the current density. The unit of the electronic current density is the atomic unit (1 a.u.$= 2.37 \times 10^{18}$ A/m^2).

aluminum atoms of the large model. The small Al_4 models have only four atoms. Hence, we speculate that the both ends cannot correctly represent the electronic state of the conductive electrons.

Here, we compare the electronic states with and without the conductive electron. For this purpose, we take the large model with $k_z = -1.0$ as a reference model. First, the energy of the system without the conductive state is calculated as -22.59 a.u., while that with the conductive state rises to -21.70 a.u. This energy difference is roughly close to the kinetic energy of the conductive state. (More strictly, the kinetic energy difference between the conductive state and the HOMO of the calculation without the conductive state.) However, the rise of the energy is not considered to be contributed only by the conductive state after the optimization of the electronic states. In the highest nine orbitals, the energy eigenvalues rise by 0.05-0.25 a.u., and the energy increases are larger for higher states. (Since the RHF is adopted, the number of orbitals are eighteen.) On the other hand, the lowest eight orbitals are stabilized by the conductive states by 0.02-0.10 a.u., and the energy decreases are larger for lower states. It is surprised that the conductive state stabilizes some orbitals, though the energy of the system rises. Since the energy eigenvalues for higher energy states rise, some electrons in the system can be moved by smaller external fields.

Unfortunately, the effect of the vector potential is very small in this calculation. In Fig. 1.4(a), the difference between the results with and without the vector potential is shown. The value of k_z is chosen as $k_z = -1.0$. The difference is very small, and hence, the effects of the vector potential are small within the present calculations. The effects on the electronic current is suppressed by the square of c as seen in Eqs. (1.2) and (1.3). Hence, the effects are negligible for small current density, which is the case in this calculation. In Fig. 1.4(b), the vector potential on this model is shown. The strong correlation of the vector potential to the current density can be seen. The wavy pattern of the vector potential is seen in Fig. 1.4(b). This is due to the restriction of the summation of $\boldsymbol{k}$ in Eq. (1.9). In our calculation, we chose the max value of $\boldsymbol{k}$ as (1/16, 1/16, 1/32) in units of a.u. Much larger model and larger electronic current are better for the discussion of the effects of vector potential in detail. This calculation is the first step to this goal.

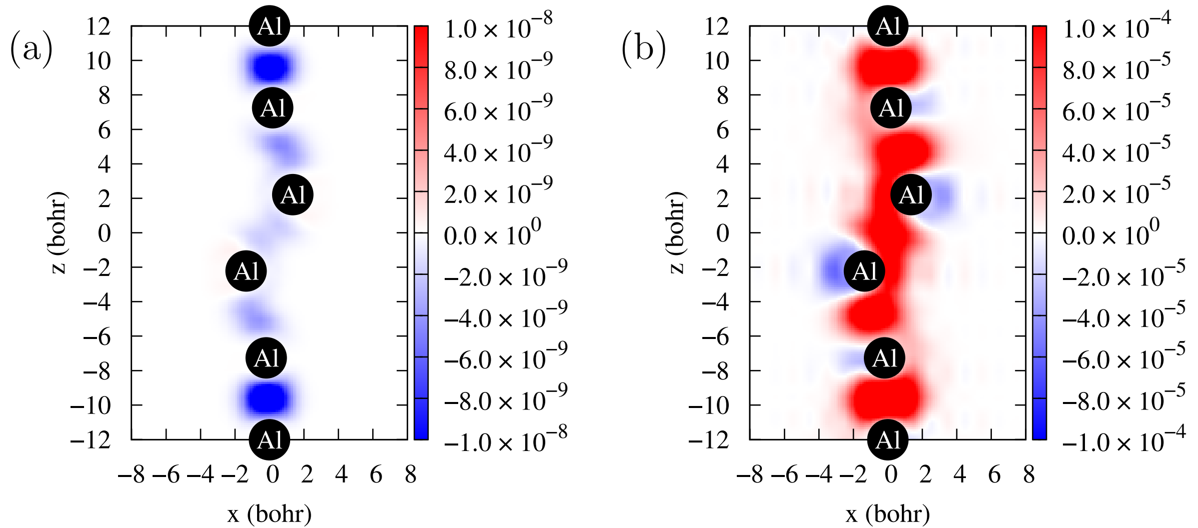

Figure 1.4: The difference between the results with and without the vector potential (left panel) and the vector potential (right panel). The results are shown on $y = 0$ plane. The value of k_z is chosen as $k_z = -1.0$.

1.6 Summary and Discussion

We have shown the first results of the calculations of our program code. In our code, the electronic current is treated as quantum states. Hence, the local electronic current density defined by one of the authors can be calculated and the Coulomb and exchange interactions by the conductive electrons are included. Moreover, the magnetic field induced by the electronic current is included in electronic state calculations. However, the vector potential has not been treated as the operator but classical fields in the present version of our code.

Two aluminum nanowire models are used for the study of the electronic states with the existence of the conductive electrons. We have confirmed the correlation between the value of k_z and electronic currents density. The basis set in this work is not large enough to represent conductive electrons, and hence, we compare these results and those of larger basis sets in future works. The effects of vector potential are negligibly small in the present calculations as expected. In order to discuss the effects of vector potential, we should study

much larger model with larger electronic current. The present version of our code is not suitable for large current, and moreover, requires huge calculation costs in spite of some technique to save it. We should bring some additional technique and/or innovate more sophisticated algorithm.

The effects on the electrons in the system by the conductive electrons have also been studied. The energy eigenvalues of higher orbitals rise, while the lower orbitals are stabilized by the conductive states. It may imply that materials are made more conductive by conductive electrons since electrons with higher energy in the materials are unstabilized by them.

In this work, the electronic current is injected by hand as the conductive state of plain wave. This is not the optimal current state for systems. Hence, we should improve the calculation code to realize the coductive electronic state by suitable boundary conditions. Moreover, the local conductivity defined in refs. 10, 11 should be investigated by codes to treat the conductive electrons as quantum states. The local conductivity can clarify the local conductive property of the system, qualitatively and quantitatively. The calculation code in this work is a first step to this goal.

Reference

[1] Y. Cui and C. M. Lieber, Science **291**, 851 (2001).

[2] D. Wang, J. G. Lu, C. J. Otten, and W. E. Buhro, Appl. Phys. Lett. **83**, 5280 (2003).

[3] D. Wang, C. J. Otten, W. E. Buhro, and J. G. Lul, IEEE Trans. Nanotechnol. **3**, 328 (2004).

[4] D. Kang, J.-H. Ko, E. Bae, J. Hyun, W. Park, B.-K. Kim, J.-J. Kim, and C. Lee, J. Appl. Phys. **96**, 7574 (2004).

[5] H. Y. Cha, H. Wu, S. Chae, and M. G. Spencer, J. Appl. Phys. **100**, 024307 (2006).

[6] W. M. Zhou, F. Fang, Z. Y. Hou, L. J. Yan, and Y. F. Zhang, IEEE Electron Devices Lett. **27**, 463 (2006).

[7] Y. Cui, L. J. Lauhon, M. S. Gudiksen, and J. Wang, Appl. Phys. Lett. **78**, 2214 (2001).

[8] Y. Wu, Y. Cui, L. Huynh, C. J. Barrelet, D. C. Bell, and C. M. Lieber, Nano Lett. **4**, 433 (2004).

[9] V. Schmidt, S. Senz, and U. Gösele, Nano Lett. **5**, 931 (2005).

[10] A. Tachibana, J. Mol. Model. **11**, 301 (2005).

[11] A. Tachibana, J. Mol. Struct.: THEOCHEM **943**, 138 (2010).

[12] A. Tachibana, Theor. Chem. Acc. **102**, 188 (1999).

[13] A. Tachibana, J. Chem. Phys. **115**, 3497 (2001).

[14] A. Tachibana, in *Stress Induced Phenomena in Metallization*, edited by S. P. Baker (American Institute of Physics, New York, 2002) p. 205.

[15] A. Tachibana, in *Reviews in Modern Quantum Chemistry: A Celebration of the Contributions of Robert Parr*, edited by K. D. Sen (World Scientific, Singapore, 2002) Vol. 2, p. 1327.

[16] A. Tachibana, in *Fundamental World of Quantum Chemistry: A Tribute to the Memory of Per-Olov Löwdin*, edited by E. J. Brändas and E. S. Kryachko (Kluwer, Dordrecht, 2003) Vol. 2, p. 211.

[17] A. Tachibana, Int. J. Quantum Chem. **100**, 981 (2004).

[18] A. Tachibana and R. G. Parr, Int. J. Quantum Chem. **41**, 527 (1992).

[19] A. Tachibana, Int. J. Quantum Chem., Quantum Chem. Symp. **21**, 181 (1987).

[20] P. Szarek, Y. Sueda, and A. Tachibana, J. Chem. Phys. **129**, 94102 (2008).

[21] A. Tachibana, Int. J. Quantum Chem. **57**, 423 (1996).

[22] A. Tachibana, K. Nakamura, K. Sakata, and T. Morisaki, Int. J. Quantum Chem. **74**, 669 (1999).

[23] M. Senami, K. Ichikawa, K. Doi, P. Szarek, K. Nakamura, and A. Tachibana, Molecular Regional DFT program package, ver. 3 (Tachibana Lab., Kyoto University, Kyoto, 2008).

[24] P. J. Hay and W. R. Wadt, J. Chem. Phys. **82**, 270 (1985).

[25] P. J. Hay and W. R. Wadt, J. Chem. Phys. **82**, 284 (1985).

[26] P. J. Hay and W. R. Wadt, J. Chem. Phys. **82**. 299 (1985).

[27] M. M. Francl, W. J. Petro, W. J. Hehre, J. S. Binkley, M. S. Gordon, D. J. DeFrees, and J. A. Pople, J. Chem. Phys. **77**, 3654 (1982).

Chapter 2

Local Electric Conductive Property of Si Nanowire Models

2.1 Introduction

Recently, semiconductor nanowires have gathered much attention since they have unique physical properties and can be applied in the fields of nano-electronics [1–6], nano-optoelectronics [7], and nano-photovoltics [8]. For instance, semiconductor nanowires are good candidates for next-generation materials of field effect transistor (FET) devices. Nanowire materials provide high electric conductance due to its ballistic conduction, and their structures are suitable for the suppression of the short channel effect by, for example, gate-all-around FET. Especially, Si nanowires are the leading candidate material for post-Moore devices [9–13] and have been studied intensively.

For electric conductive properties of nanosize materials, it is important to predict them by the first principles calculations before the fabrication in laboratories. In fact, many theoretical and computational studies have been performed for conductivity of nanomaterials. One of the most well-known approaches is non-equilibrium Green's function method [14]. By using this method, conductive properties of various nanodevices are analyzed [15–18]. These results show qualitatively sufficient consistency with experimental ones. However, we consider that this global and averaged conductivity for whole devices is not sufficient for understanding conductive properties of nanosize materials. For example, analysis by using global conductivity clarifies the effects of impurities only indirectly. Therefore, we have

proposed the analysis by local quantities such as local dielectric constant tensor [19–23], $\hat{\overleftrightarrow{\epsilon}}(\vec{r})$, and local electric conductivity tensors [24–27], $\hat{\overleftrightarrow{\sigma}}_{\rm ext}(\vec{r})$ and $\hat{\overleftrightarrow{\sigma}}_{\rm int}(\vec{r})$, which are defined in Rigged QED [24, 25]. The use of local conductivity tensors enables us to discuss the effects of impurities or interface, and the position dependence of conductivity efficiently. In addition, local conductivity tensors help us to investigate the origins of some unusual electric phenomena, such as negative differential resistance (NDR) effect which has been found for semiconductor nanowires [28–35] and molecular electronic devices [36–38].

In our previous work [27], we analyzed nanomaterials by only $\hat{\overleftrightarrow{\sigma}}_{\rm ext}(\vec{r})$ which represents the response to external electric field. In the present work, we show the validity of our analysis which uses both $\hat{\overleftrightarrow{\sigma}}_{\rm ext}(\vec{r})$ and $\hat{\overleftrightarrow{\sigma}}_{\rm int}(\vec{r})$, following our earlier works about the local quantity analyses [19–27, 39, 40]. It is especially noted that $\hat{\overleftrightarrow{\sigma}}_{\rm int}(\vec{r})$ is defined as the response of the electric current density to the internal electric field, and hence this does not have the corresponding macroscopic quantity. This quantity represents how the actual electric field at a specific position drives carriers such as electrons. This effect can never be analyzed by macroscopic conductivity. By using these two local electric conductivity tensors, we study electric conductive properties of Si nanowire models. In the present paper, we consider a pristine Si nanowire model and that which includes a Ge atom as an impurity.

In order to obtain the local electric conductivity tensors, the wave function of conductive electrons should be derived. However, most program codes for the calculations of electronic structures give us wave functions without net electric current. Hence, we must develop a calculation code to introduce electric current in a system. In our previous works, we developed a code which uses self-consistent field (SCF) procedure [26, 27]. Effects of the conductive electrons on other ones were also considered in this code. In this work, we improve the method, based on a perturbation theory. By using this, we can calculate linear response to external electric field strictly.

This paper is organized as follows. In the next section, we define local electric current density and two conductivity tensors. In Sec. 2.3, calculation method of our program code and computational models are summarized. In Sec. 2.4, we show results of our models in terms of our local electric conductivity tensors. Section 2.5 is devoted to the conclusion.

2.2 Theory

2.2.1 Definition of the local properties

In this section, we show the definition of the local quantities for the response to the electric field. These quantities are introduced by Rigged QED [24, 25]. We consider that a system (A) is embedded in an environmental background medium (M). The corresponding scalar potentials for A and M are given as the regional integrals of charge density,

$$\hat{A}_{0_{\mathrm{A,M}}}(\vec{r}) = \int_{\mathrm{A,M}} d^3\vec{s}\,\frac{\hat{\rho}(\vec{s})}{|\vec{r}-\vec{s}|}. \tag{2.1}$$

Here, $\hat{\rho}(\vec{r})$ is the electronic charge density defined as,

$$\hat{\rho}(\vec{r}) \equiv Z_e e \hat{\Psi}^\dagger(\vec{r})\hat{\Psi}(\vec{r}), \tag{2.2}$$

where e is the value of the elementary electric charge and $Z_e = -1$. The electric field $\hat{\vec{E}}(\vec{r})$ is given as the sum of the electric displacement $\hat{\vec{D}}(\vec{r})$ from M and the polarization $\hat{\vec{P}}(\vec{r})$ of A. These quantities are defined with the scalar potentials of these regions,

$$\hat{\vec{D}}(\vec{r}) = -\nabla \hat{A}_{0_{\mathrm{M}}}(\vec{r}), \tag{2.3}$$

$$\hat{\vec{P}}(\vec{r}) = \frac{1}{4\pi}\nabla \hat{A}_{0_{\mathrm{A}}}(\vec{r}), \tag{2.4}$$

where the time variation of the vector component of gauge fields is dropped, since only steady states are treated in this work. As a result, the electric field is given as the following equation,

$$\hat{\vec{E}}(\vec{r}) = \hat{\vec{D}}(\vec{r}) - 4\pi\hat{\vec{P}}(\vec{r}). \tag{2.5}$$

The electric displacement $\hat{\vec{D}}(\vec{r})$ from M acts as the external electric field for A. Hence, the polarization of A is considered to be linear response to $\hat{\vec{D}}(\vec{r})$,

$$\hat{\vec{P}}(\vec{r}) = \hat{\overleftrightarrow{\alpha}}(\vec{r})\hat{\vec{D}}(\vec{r}), \tag{2.6}$$

where $\hat{\overleftrightarrow{\alpha}}(\vec{r})$ is the polarizability tensor. The dielectric constant tensor $\hat{\overleftrightarrow{\epsilon}}(\vec{r})$ is given as,

$$\hat{\vec{D}}(\vec{r}) = \hat{\overleftrightarrow{\epsilon}}(\vec{r})\hat{\vec{E}}(\vec{r}) = \frac{1}{1-4\pi\hat{\overleftrightarrow{\alpha}}(\vec{r})}\hat{\vec{E}}(\vec{r}). \tag{2.7}$$

It is emphasized that $\hat{\overleftrightarrow{\alpha}}(\vec{r})$ and $\hat{\overleftrightarrow{\epsilon}}(\vec{r})$ are defined for every local point. There are several approaches which seems to be similar to our one. For example, Stone *et al.* have developed

distributed polarizabilities [41–43]. This theory is often used for the purpose of inducing efficient intermolecular potential functions [44, 45]. The advantage of our approach is its simple definitions of local quantities. They are quite similar to the definitions of corresponding macroscopic quantities.

From gauge covariant derivative, the local electric current density $\hat{\vec{j}}(\vec{r})$ can be given as,

$$\hat{\vec{j}}(\vec{r}) = \frac{Z_e e}{2m_e}[-i\hbar\hat{\Psi}^\dagger(\vec{r})\nabla\hat{\Psi}(\vec{r}) - \frac{Z_e e}{c}\hat{\Psi}^\dagger(\vec{r})\hat{\vec{A}}(\vec{r})\hat{\Psi}(\vec{r}) + h.c.]. \tag{2.8}$$

In our previous work [26], we have shown that the effects of vector potential are negligible for small current density. Therefore, we ignore the vector potential in this work. Local electric conductivity tensors $\hat{\overleftrightarrow{\sigma}}_{\text{ext}}(\vec{r})$ and $\hat{\overleftrightarrow{\sigma}}_{\text{int}}(\vec{r})$ are defined as [24, 25],

$$\begin{aligned}\hat{\vec{j}}(\vec{r}) &= \hat{\overleftrightarrow{\sigma}}_{\text{ext}}(\vec{r})\hat{\vec{D}}(\vec{r}) \\ &= \hat{\overleftrightarrow{\sigma}}_{\text{ext}}(\vec{r})\hat{\overleftrightarrow{\epsilon}}(\vec{r})\hat{\vec{E}}(\vec{r}) \\ &= \hat{\overleftrightarrow{\sigma}}_{\text{int}}(\vec{r})\hat{\vec{E}}(\vec{r}),\end{aligned} \tag{2.9}$$

where $\hat{\vec{D}}(\vec{r})$ and $\hat{\vec{E}}(\vec{r})$ are external and internal electric field, respectively. As mentioned above, $\hat{\overleftrightarrow{\sigma}}_{\text{int}}(\vec{r})$ represents how the actual electric field at each position drives electric carriers. This effect cannot be observed in macroscopic points of view. Some of computational works for the ballistic nanowire FET [46, 47] have reported that the I-V characteristics of ballistic nanowires have a linear region, where the drain current I_D is proportional to the drain voltage V_D, and a saturation region, where I_D is independent of V_D. For the method in the present study, we assume the linear region.

In this study, local electric conductivity tensors are mainly investigated by their eigenvalues and eigenvectors. We also use the average of the eigenvalues as,

$$\sigma_{\text{Ave.}} = \frac{1}{3}(\sigma_1 + \sigma_2 + \sigma_3) = \frac{1}{3}\text{Tr}(\overleftrightarrow{\sigma}). \tag{2.10}$$

where σ_1, σ_2, and σ_3 are the first, the second, and the third eigenvalue, respectively. Each element in these tensors is a Hermitian operator and its expected value is real. These tensors, however, are not symmetric. For example, $\hat{\sigma}_{xy}(\vec{r})$ and $\hat{\sigma}_{yx}(\vec{r})$ may have different expected values. Hence, these tensors possibly have a pair of conjugate complex eigenvalues as,

$$\begin{aligned}\sigma_2 &= \beta + i\gamma, \\ \sigma_3 &= \beta - i\gamma, \ (\beta, \gamma \in \mathbb{R}).\end{aligned} \tag{2.11}$$

In such cases, the complex eigenvalues do not have the corresponding eigenvectors in real space. Instead, we can make two vectors from the complex eigenvectors as,

$$\vec{v}_+ = \frac{1}{\sqrt{2}}(\vec{v}_2 + \vec{v}_3), \tag{2.12}$$

$$\vec{v}_- = \frac{1}{\sqrt{2}i}(\vec{v}_2 - \vec{v}_3). \tag{2.13}$$

$\vec{v}_+$ and $\vec{v}_-$ are real vectors and respond to $\overleftrightarrow{\sigma}(\vec{r})$ as,

$$\overleftrightarrow{\sigma}\vec{v}_+ = \beta\vec{v}_+ - \gamma\vec{v}_-, \tag{2.14}$$

$$\overleftrightarrow{\sigma}\vec{v}_- = \beta\vec{v}_+ + \gamma\vec{v}_-. \tag{2.15}$$

We call this response of the local quantities as "rotational response". Rotational responses are also seen in our previous works [21–23, 27]. The local property of rotational response is correctly described only in the analysis using matrix, since the complex eigenvalues originate in off-diagonal elements of the matrix.

2.3 Calculation Methods

2.3.1 CPHF equations

In this study, the response to electric field is calculated by using Coupled Perturbed Hartree-Fock (CPHF) method [48–50]. CPHF method enables us to calculate linear response to external electric field strictly. In this subsection, the CPHF method used in this study is summarized.

First, the power series expansions of Hamiltonian $\boldsymbol{h}$ and density matrix $\boldsymbol{R}$ are given for the strength parameter of the perturbation λ as

$$\boldsymbol{h}(\lambda) = \boldsymbol{h}^{(0)} + \lambda\boldsymbol{h}^{(1)}, \tag{2.16}$$

$$\boldsymbol{R}(\lambda) = \boldsymbol{R}^{(0)} + \lambda\boldsymbol{R}^{(1)} + \cdots. \tag{2.17}$$

The corresponding first order Fock matrix $\boldsymbol{h}^{F(1)}$ can be defined as

$$\boldsymbol{h}^{F(1)} = \boldsymbol{h}^{(1)} + \boldsymbol{G}(\boldsymbol{R}^{(1)}), \tag{2.18}$$

where matrix $\boldsymbol{G}$ is the two-electron interaction defined as

$$G_{pq}(\boldsymbol{R}) = \sum_{r,s} R_{rs}\big([\psi_p\psi_q|\psi_r\psi_s] - [\psi_p\psi_s|\psi_r\psi_q]\big), \tag{2.19}$$

where the subscripts p, q, r, s are used for all molecular orbitals (MOs). Then, the first order CPHF equation is written as

$$(\epsilon_a - \epsilon_i) R_{ai}^{(1)} = -h_{ai}^{F(1)}, \tag{2.20}$$

where ϵ is the zeroth order orbital energy, and the subscripts a and i are used for the virtual and the occupied MOs, respectively. From Eqs. (2.18) and (2.19), it is clear that $\boldsymbol{h}^{F(1)}$ includes only the linear terms of $\boldsymbol{R}^{(1)}$ with respect to $\boldsymbol{R}$. Therefore, $\boldsymbol{R}^{(1)}$ can be obtained by solving simultaneous linear equations. In a similar way, the second order CPHF equation is represented as

$$(\epsilon_a - \epsilon_i) R_{ai}^{(2)} = -h_{ai}^{F(2)} + \sum_p \left(R_{ap}^{(1)} h_{pi}^{F(1)} - h_{ap}^{F(1)} R_{pi}^{(1)} \right). \tag{2.21}$$

2.3.2 Electronic structures with electric currents

Calculations of the electronic structures with electric currents are generally difficult. There are several approaches to deal with these structures. For example, Stuchebrukhov has developed the formalism of tunneling currents [51–56]. This theory is helpful to understand charge transfer systems in terms of interatomic currents. In this study, we calculate them by imposing some restriction to general CPHF method. In this subsection, this treatment is explained.

First, it is assumed that electron conduction is ballistic. Then, plane wave is considered as one of the simplest approximations for the conduction state. Therefore, conduction orbitals are considered to have the form,

$$\begin{aligned} |f^{(x)}(\vec{r})\rangle &= \exp(ik_x x), \\ |f^{(y)}(\vec{r})\rangle &= \exp(ik_y y), \\ |f^{(z)}(\vec{r})\rangle &= \exp(ik_z z), \end{aligned} \tag{2.22}$$

where $k_{x,y,z}$ are the parameters which correspond to the wave number vector. The extension of the direction perpendicular to momentum is restricted by the extension of virtual MOs of a system. In other words, $|f^{(x,y,z)}(\vec{r})\rangle$ are projected onto them as,

$$\begin{aligned} |\psi_{\mathrm{PW}}^{(i)}\rangle &= C_{\mathrm{norm}} \sum_a |\psi_a\rangle\langle\psi_a|f^{(i)}(\vec{r})\rangle \\ &= C_{\mathrm{norm}} \sum_a |\psi_a\rangle \sum_\mu C_{\mu a}^* \langle\phi_\mu|f^{(i)}(\vec{r})\rangle \quad (i = x, y, z), \end{aligned} \tag{2.23}$$

where the subscript μ is used for basis functions ϕ_μ, $C_{\mu a}$ is the expansion coefficients of the virtual MOs, and C_{norm} is the normalization coefficient. The spreads of the plane waves are suppressed by this procedure. In this study, $|\psi_{\mathrm{PW}}^{(i)}\rangle$ is regarded as the perturbation of the Highest Occupied MO (HOMO) $|\psi_{\mathrm{HOMO}}^{(1i)}\rangle$. This is given as,

$$|\psi_{\mathrm{HOMO}}^{(i)}\rangle = |\psi_{\mathrm{HOMO}}^{(0)}\rangle + d|\psi_{\mathrm{HOMO}}^{(1i)}\rangle + \cdots \tag{2.24}$$

$$= |\psi_{\mathrm{HOMO}}^{(0)}\rangle + d|\psi_{\mathrm{PW}}^{(i)}\rangle + \cdots \quad (i = x, y, z), \tag{2.25}$$

where d is the perturbation mixing parameter related to the strength of the electric field, and $|\psi_{\mathrm{HOMO}}^{(0)}\rangle$ is an unperturbed HOMO. $|\psi_{\mathrm{HOMO}}^{(1i)}\rangle$ is fixed in corresponding CPHF equations, and the perturbation of the other occupied orbitals are determined as,

$$(\epsilon_a - \epsilon_j) R_{aj}^{(1)} = -h_{aj}^{F(1)}, \tag{2.26}$$

where the subscript j is used for occupied MOs except for the HOMO. The effect of the fixed wavefunction is included in $R_{ah}^{(1)}$ and $R_{ha}^{(1)}$, where the subscript h is used for the HOMO. In other words, the elements of $R_{ah}^{(1)}$ are not variables but constants in Eq. (2.26), which is different from Eq. (2.20).

The first order density matrix is dependent on the phase of $|f^{(x,y,z)}(\vec{r})\rangle$. Especially, if the phase changes by π, the sign of the first order density matrix $\boldsymbol{R}^{(1)}$ becomes opposite as,

$$\boldsymbol{R}^{(1)}(\theta + \pi) = -\boldsymbol{R}^{(1)}(\theta). \tag{2.27}$$

Therefore, the current caused by $\boldsymbol{R}^{(1)}$ also becomes opposite as,

$$\vec{j}^{(1)}(\vec{r}; \theta + \pi) = -\vec{j}^{(1)}(\vec{r}; \theta). \tag{2.28}$$

If the phase of $|f^{(x,y,z)}(\vec{r})\rangle$ can be taken arbitrarily and the average current caused by each phase is regarded as the real current, currents caused by the first order perturbation are equal to zero at all positions,

$$\vec{j}^{(1)}(\vec{r}; \mathrm{Ave.}(\theta)) = 0. \tag{2.29}$$

On the other hand, the second order density matrix $\boldsymbol{R}^{(2)}$ does not change for the opposite phase. Hence in this study, currents caused by $\boldsymbol{R}^{(2)}$ for $\theta = 0$ is treated as the lowest order density matrix. The lowest order perturbation current is assumed to be derived from it.

$\vec{j}(\vec{r})$ by our method is strongly dependent on $k_{x,y,z}$ and d. In the present study, we choose the values of $k_{x,y,z}$ so that the difference between the projection of the plane waves on the virtual MOs and the original plane waves is relatively small. The value of d can be chosen so that $\vec{j}(\vec{r})$ is consistent with the macroscopic value obtained by experiments or other theoretical calculations such as the global current of non-equilibrium Green's function method. Accordingly, this value changes as the change of external field. However, the value of d does not change the distribution pattern of $\vec{j}(\vec{r})$. Hence we assume $d = 1$ and discuss the dependence on sites only qualitatively by using this method.

2.3.3 Calculation method for local properties

In this subsection, our calculation method for the local quantity tensors is given. First, CPHF calculations are done by using the perturbation Hamiltonians corresponding to the electric current and external electric field,

$$\begin{aligned} \lambda_x \boldsymbol{h}^{(1x)} &= -\lambda_x D_0 Z_e e x, \\ \lambda_y \boldsymbol{h}^{(1y)} &= -\lambda_y D_0 Z_e e y, \\ \lambda_z \boldsymbol{h}^{(1z)} &= -\lambda_z D_0 Z_e e z, \end{aligned} \tag{2.30}$$

where x, y, z are the directions of the external electric field, D_0 is the unit electric field, and $\lambda_{x,y,z}$ are the strength parameters of the perturbation. The strength of the external electric field $D_{x,y,z}$ can be written as

$$D_j = \lambda_j D_0 \quad (j = x, y, z). \tag{2.31}$$

Then, density matrices $\boldsymbol{R}^{(2x,2y,2z)}$ are obtained. Local electric current density $\vec{j}(\vec{r})$ can be expanded as

$$\begin{aligned} j_i(\vec{r}, \lambda_x, \lambda_y, \lambda_z) = &\; j_i^{(0)}(\vec{r}) \\ &+ \lambda_x j_i^{(2x)}(\vec{r}) + \lambda_y j_i^{(2y)}(\vec{r}) + \lambda_z j_i^{(2z)}(\vec{r}) \\ &+ \cdots \\ &(i = x, y, z), \end{aligned} \tag{2.32}$$

where $j_i^{(2j)}(\vec{r})$ is caused by $\boldsymbol{R}^{(2)}$. By using this $\vec{j}(\vec{r})$, each element of $\overleftrightarrow{\sigma}(\vec{r})$ is calculated from Eq. (2.9). For instance, the value at $\vec{D}(\vec{r}) = 0$ is calculated as,

$$\begin{aligned}
\sigma_{ij}(\vec{r}) &= \left.\frac{\partial j_i(\vec{r})}{\partial D_j}\right|_{D_j=0} \\
&= \left.\frac{\partial j_i(\vec{r})}{\partial \lambda_j}\frac{\partial \lambda_j}{\partial D_j}\right|_{D_j=0} \\
&= \frac{j_i^{(2j)}(\vec{r})}{D_0}\ (i, j = x, y, z).
\end{aligned} \tag{2.33}$$

Local polarizability tensor, $\overleftrightarrow{\alpha}(\vec{r})$, can be calculated in a similar way, and then $\overleftrightarrow{\epsilon}(\vec{r})$ is obtained from Eq. (2.7).

In order to analyze the characteristics of the local quantities in specific regions, spatial averages of the local quantities are calculated with the equations,

$$\langle\overleftrightarrow{\alpha}\rangle_V = \frac{1}{V}\int_V \overleftrightarrow{\alpha}(\vec{r})d\vec{r}, \tag{2.34}$$

$$\langle\overleftrightarrow{\varepsilon}\rangle_V = \frac{1}{1 - 4\pi\langle\overleftrightarrow{\alpha}\rangle_V}, \tag{2.35}$$

$$\langle\overleftrightarrow{\sigma}_{\text{ext}}\rangle_V = \frac{1}{V}\int_V \overleftrightarrow{\sigma}_{\text{ext}}(\vec{r})d\vec{r}, \tag{2.36}$$

$$\langle\overleftrightarrow{\sigma}_{\text{int}}\rangle_V = \langle\overleftrightarrow{\sigma}_{\text{ext}}\rangle_V\langle\overleftrightarrow{\epsilon}\rangle_V, \tag{2.37}$$

where V indicates the integral region. In the present paper, V is taken as a sphere around a specific atom. The scheme of the spherical average is shown in Fig. 2.1. In order to focus on the valence region of the atom and remove the effects of core electrons, we do not include the core of the sphere in the integral region. The radius of the core sphere, r_0, is taken to be 1 (bohr) for reference. In the present paper, the spherical average is analyzed as the function of the radius, r.

2.3.4 Computational models

In this subsection, computational models used in this study are shown. It has been reported that Si nanowires which have $\langle 110\rangle$ growth direction have smaller electron and hole effective masses than those which have $\langle 100\rangle$ or $\langle 111\rangle$ growth direction [57]. Therefore in this work, we use Si nanowire models which have $\langle 110\rangle$ growth direction.

In Fig. 2.2 (a), our pristine Si nanowire model is shown. This model consists of eight layers. Each layer consists of three or four Si atoms. All dangling bonds are terminated

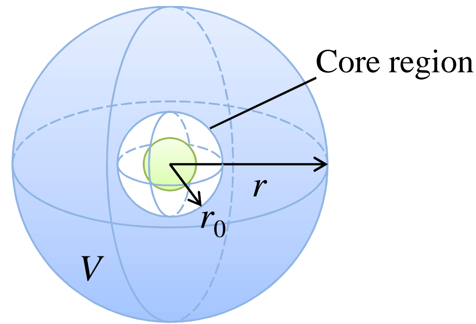

Figure 2.1: Scheme of the spherical average around a specific atom.

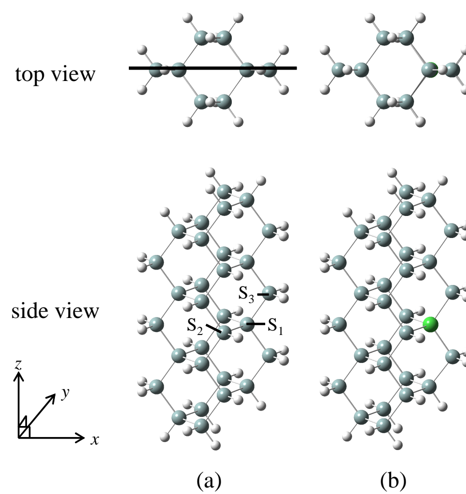

Figure 2.2: Si nanowire models. Light-gray, green, and white spheres correspond to Si, Ge, and H atoms, respectively. (a) Pristine model and (b) Ge-substituted model. Thick line in panel (a) corresponds to xz-plane, where some results are shown on this plane in the following.

with H atoms. Geometry is fully optimized. We also consider a model shown in Fig. 2.2 (b). From the analysis of this model, we investigate the effects on the local electric conductivities caused by the change of the electronic and geometrical structures. For the model (b), the Si atom on site S_1 in Fig. 2.2 (a), which makes bonds with four nearby Si atoms, is substituted by a Ge atom. All atoms are relaxed for the geometrical optimization calculation. The Model (b) is called the Ge-substituted model below in the present paper.

Electronic structures without perturbations (external electric field and electric current) are calculated by using the Hartree-Fock (HF) method, while those with perturbation Hamiltonians are calculated by CPHF method, as mentioned in this section. We choose the Dunning-Huzinaga double-zeta basis set with Effective Core Potential (ECP) by Hay and Wadt (LANL2DZ) [58–60] as basis set, and hence Si and Ge atoms in our models have ECP. Gaussian 09 [61] is used for HF calculations, and CPHF calculations are done by using our original code. All local physical quantities are calculated at the vicinity of $\vec{D}(\vec{r}) = 0$. For the parameters $k_{x,y,z}$ in Eq. (2.22), they are taken as $k_{x,y,z} = 1.0\,(\mathrm{bohr}^{-1})$ for reference, since the difference between the projection of the plane waves on virtual MOs and the original plane wave are relatively small for this value.

2.4 Results

2.4.1 Pristine model

In this subsection, we show the results for the pristine Si nanowire model. Local electric conductivity tensor for the external electric field, $\overleftrightarrow{\sigma}_{\mathrm{ext}}(\vec{r})$, on the xz-plane is shown in Fig. 2.3. We can find the regions which have negative eigenvalues, around Si atoms, the center axis of the nanowire, and the exterior of it. In these regions, $\vec{D}(\vec{r})$ and $\vec{j}(\vec{r})$ show opposite directions. An important factor inducing negative eigenvalues is the large off-diagonal elements of $\overleftrightarrow{\sigma}_{\mathrm{ext}}(\vec{r})$. For example, this is seen at $\vec{r} = (8, 0, 0)$, which is at the surface of the nanowire. The value of $\overleftrightarrow{\sigma}_{\mathrm{ext}}(\vec{r})$ is given as,

$$\overleftrightarrow{\sigma}_{\mathrm{ext}}(8,0,0) = \begin{pmatrix} 0.44 & 0.00 & 2.07 \\ 0.00 & 1.07 & 0.00 \\ 1.93 & 0.00 & 3.93 \end{pmatrix} (\times 10^{-4}\,\mathrm{a.u.}). \tag{2.38}$$

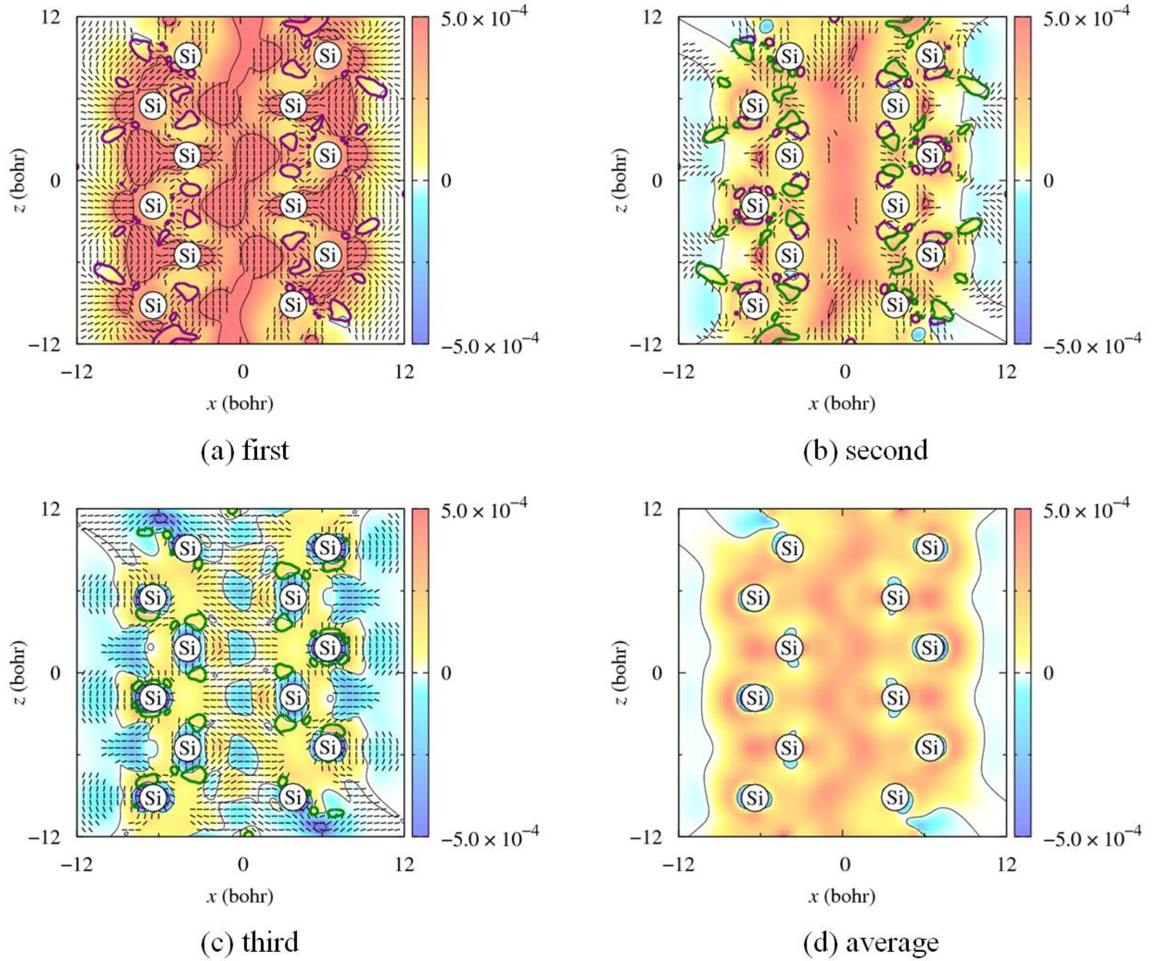

Figure 2.3: Eigenvalues of $\overleftrightarrow{\sigma}_{\mathrm{ext}}(\vec{r})$ (a.u.) for the pristine model. Results are shown on the xz-plane. Eigenvalues are sorted in descending order of their real part. Panels (a), (b), and (c) show the results of the first, second, and third eigenvalues. Panel (d) shows the average of those three eigenvalues. The solid line segments show the directions of the eigenvectors. The eigenvalues in the purple (green) contours have positive (negative) complex values.

It is found that the zx-element is larger than the xx-element. This means that when the external electric field is applied for the x-direction, the z-component of the current density is larger than the x-component. In addition, negative eigenvalues are seen in some unimportant regions, *e.g.*, around the center axis of the nanowire. In these regions, our basis set does not have enough degree of freedom for the accurate description, and hence we do not discuss those. Negative eigenvalues of $\overleftrightarrow{\sigma}_{\mathrm{ext}}(\vec{r})$ may be associated with NDR. It is considered that we can investigate the origin of NDR in more detail by using $\overleftrightarrow{\sigma}_{\mathrm{ext}}(\vec{r})$ than conventional global conductivity. In addition, if $\overleftrightarrow{\sigma}_{\mathrm{ext}}(\vec{r})$ is analyzed for various voltages, we can also study the dependence of NDR on voltage.

The regions which have complex eigenvalues are seen around Si atoms. As mentioned in Sec. 2.2, $\vec{j}(\vec{r})$ responds to $\vec{D}(\vec{r})$ rotationally in these regions. For example, $\overleftrightarrow{\sigma}_{\mathrm{ext}}(\vec{r})$ at $\vec{r} = (4, 0, 1)$ is given as,

$$\overleftrightarrow{\sigma}_{\mathrm{ext}}(4, 0, 1) = \begin{pmatrix} 2.57 & 0.00 & 1.16 \\ 0.00 & 0.56 & 0.00 \\ -0.17 & 0.00 & 2.04 \end{pmatrix} (\times 10^{-4}\,\mathrm{a.u.}). \tag{2.39}$$

We can find that the signs of xz- and zx-elements are opposite, and the difference of xx- and zz-element are small. The rotational response is caused by these response properties. In our previous works, these responses are also seen in the results of $\overleftrightarrow{\sigma}_{\mathrm{ext}}(\vec{r})$ or $\overleftrightarrow{\epsilon}(\vec{r})$ of HfO_2, SiO_2, and so on [21–23, 27]. Therefore, we consider that these characteristics are often seen in microscopic view.

Local electric conductivity tensor for the internal electric field, $\overleftrightarrow{\sigma}_{\mathrm{int}}(\vec{r})$, is shown in Fig. 2.4. Around Si-Si bonds, the third eigenvalues of $\overleftrightarrow{\sigma}_{\mathrm{int}}(\vec{r})$ has quite large negative eigenvalues, while those of $\overleftrightarrow{\sigma}_{\mathrm{ext}}(\vec{r})$ are positive there. It means that $\vec{j}(\vec{r})$ responds to $\vec{D}(\vec{r})$ in the same direction, while it responds to $\vec{E}(\vec{r})$ in the opposite direction. From the definition of $\overleftrightarrow{\sigma}_{\mathrm{int}}(\vec{r})$, which is shown in Eq. (2.9), it can be speculated that this difference is due to the effect of the local dielectric constant, $\overleftrightarrow{\epsilon}(\vec{r})$. Therefore it is helpful to analyze $\overleftrightarrow{\epsilon}(\vec{r})$ for the further understanding of the behavior of $\overleftrightarrow{\sigma}_{\mathrm{int}}(\vec{r})$ in these regions. The results of $\overleftrightarrow{\epsilon}(\vec{r})$ are shown in Fig. 2.5. As well as $\overleftrightarrow{\sigma}_{\mathrm{int}}(\vec{r})$, $\overleftrightarrow{\epsilon}(\vec{r})$ has negative eigenvalues around Si-Si bonds. In these regions, the polarization is significantly large and $\vec{E}(\vec{r})$ and $\vec{D}(\vec{r})$ show the opposite directions. If the eigenvalue of $\overleftrightarrow{\sigma}_{\mathrm{int}}(\vec{r})$ is negative, the change of $\vec{j}(\vec{r})$ at the position has the opposite direction to the change of $\vec{E}(\vec{r})$ for the direction of the corresponding eigenvector.

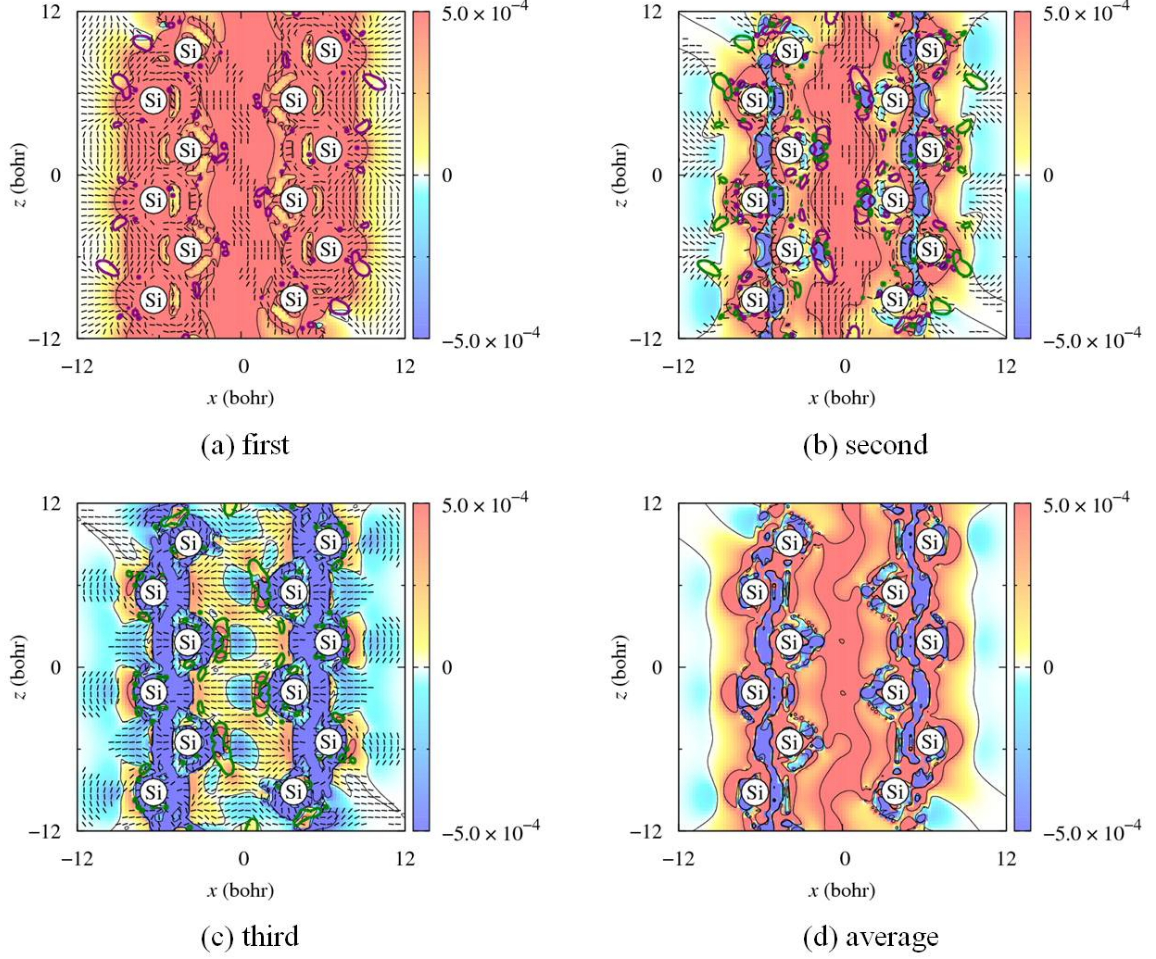

Figure 2.4: Eigenvalues of $\overleftrightarrow{\sigma}_{\rm int}(\vec{r})$ (a.u.) for the pristine model. Results are shown on the same plane as Fig. 2.3 in the same manner. See the caption of Fig. 2.3 for the details.

Regions with negative $\overleftrightarrow{\sigma}_{\rm int}(\vec{r})$ impede the current.

Next, in order to discuss the site dependence of $\overleftrightarrow{\sigma}_{\rm ext}(\vec{r})$ and $\overleftrightarrow{\sigma}_{\rm int}(\vec{r})$, we show the spherical average of the local electric conductivity tensors. In Fig. 2.6, the spherical average of $\overleftrightarrow{\sigma}_{\rm ext}(\vec{r})$ around the three Si atoms on the sites $S_{1,2,3}$ in Fig. 2.2 (a) are shown. We find that the third eigenvalues are negative or almost zero in the region of $1.0 < r < 2.0$ (bohr) for sites S_2 and S_3. This indicates that the electric current density $\vec{j}(\vec{r})$ may respond to the external electric field $\vec{D}(\vec{r})$ for the opposite direction or hardly respond to it for a specific direction. For the sites S_1 and S_3, we also find that all the eigenvalues are more scattered in the region of $1.0 < r < 2.0$ (bohr) than those in the region of $r > 2.0$ (bohr). This result means that the regions in the vicinities of the Si atoms on the sites S_1 and S_3 have relatively anisotropic

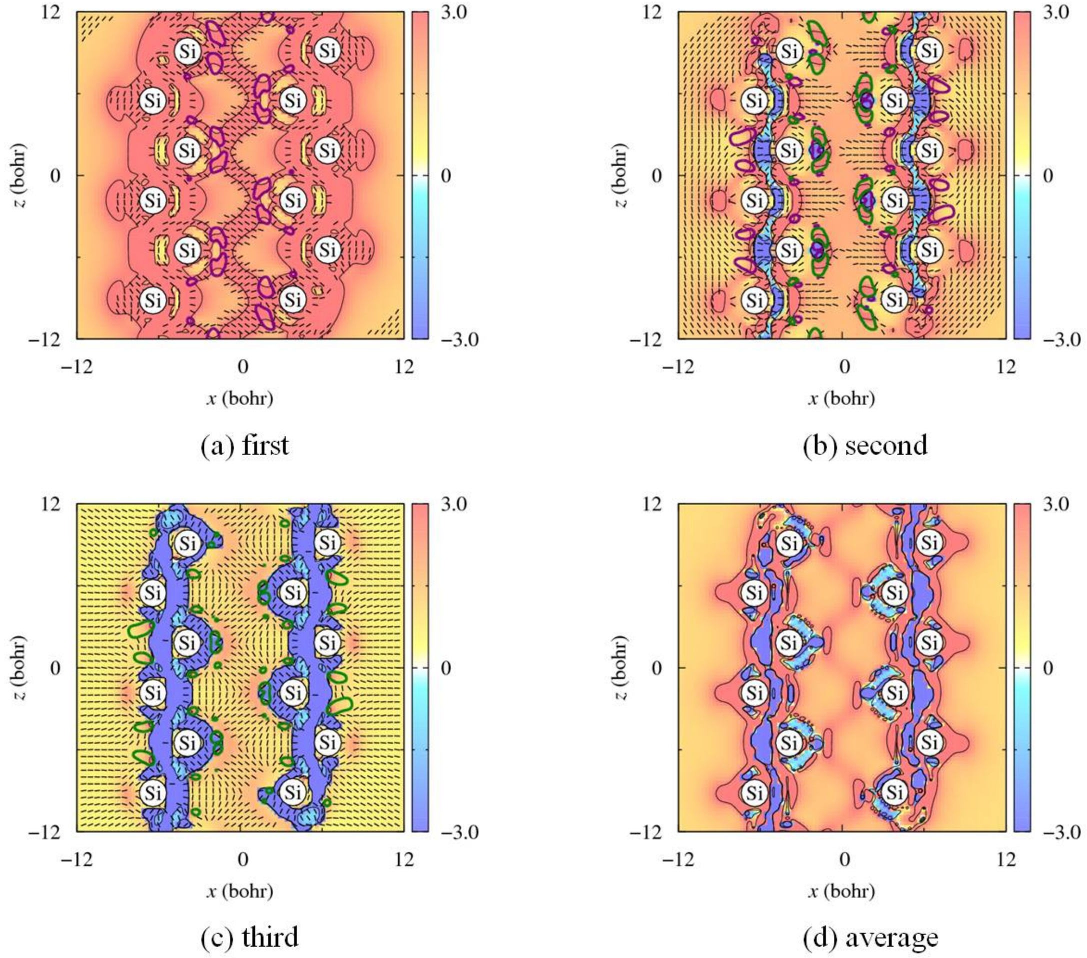

Figure 2.5: Eigenvalues of $\overleftrightarrow{\epsilon}(\vec{r})$ for the pristine model. Results are shown on the same plane as Fig. 2.3 in the same manner. See the caption of Fig. 2.3 for the details.

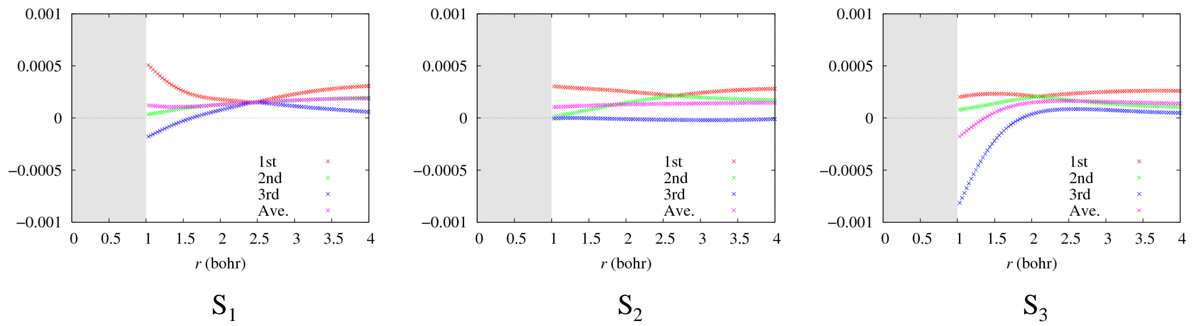

Figure 2.6: Spherical average of $\overleftrightarrow{\sigma}_{\text{ext}}(\vec{r})$ (a.u.) around three specific Si atoms on the sites $S_{1,2,3}$ shown in Fig. 2.2 (a). The gray regions represent the core regions of the atoms.

Table 2.1: Eigenvalues ($\times 10^{-4}$ a.u.) and eigenvectors $\vec{v} = (v_x, v_y, v_z)^T$ of $\langle \overleftrightarrow{\sigma}_{\text{ext}} \rangle_V$ at $r = 1.25$, 2.00, and 4.00 (bohr) for the Si atoms in the pristine model.

		S_1			S_2			S_3		
r		first	second	third	first	second	third	first	second	third
1.25	eigenvalue	3.672	0.614	−1.025	2.911	0.416	0.003	2.126	1.057	−4.978
	v_x	0.995	0.000	−0.038	−0.255	−0.151	0.961	0.000	0.013	1.000
	v_y	0.000	1.000	0.000	0.967	−0.066	0.244	1.000	0.000	0.000
	v_z	0.097	0.000	0.999	−0.018	0.986	0.131	0.000	1.000	0.009
2.00	eigenvalue	1.780	1.292	0.759	2.554	1.466	−0.109	2.112	1.975	0.369
	v_x	0.996	0.000	0.016	0.030	−0.012	1.000	0.000	0.023	1.000
	v_y	0.000	1.000	0.000	1.000	−0.009	−0.008	1.000	0.000	0.000
	v_z	0.085	0.000	1.000	0.008	1.000	0.008	0.000	1.000	0.002
4.00	eigenvalue	3.078	1.946	0.579	2.806	1.702	−0.111	2.599	1.066	0.487
	v_x	−0.001	0.000	0.999	0.001	0.012	1.000	0.005	0.000	1.000
	v_y	0.000	1.000	0.000	−0.004	1.000	0.021	0.000	1.000	0.000
	v_z	1.000	0.000	−0.045	1.000	0.006	−0.014	1.000	0.000	0.023

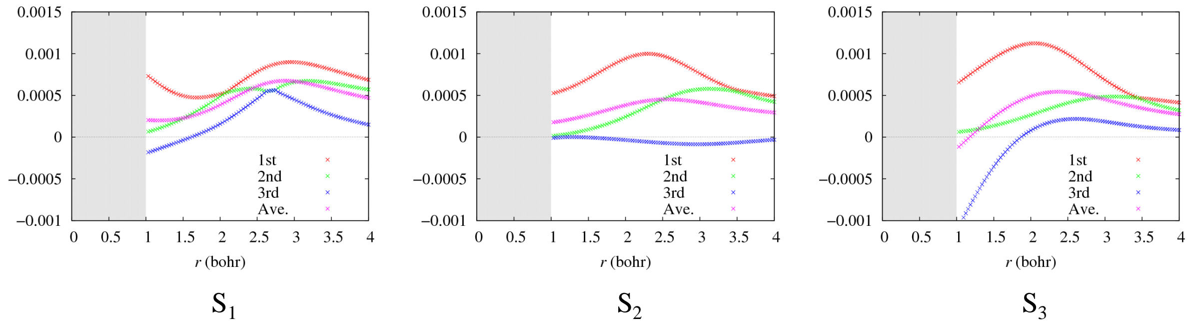

Figure 2.7: Spherical average of $\overleftrightarrow{\sigma}_{\rm int}(\vec{r})$ (a.u.) around the Si atoms. Results are shown in the same manner as Fig. 2.6.

Table 2.2: Eigenvalues, their averages, and the standard deviations (SDs) of $\langle\overleftrightarrow{\sigma}_{\rm int}\rangle_V$ ($\times 10^{-4}$ a.u.) at $r = 2.10$ (bohr).

	first	second	third	average	SD
S_1	5.49	5.37	2.10	4.32	1.57
S_2	9.71	2.82	−0.42	4.04	4.23
S_3	11.22	2.95	1.25	5.14	4.35

properties. In order to analyze $\langle\overleftrightarrow{\sigma}_{\rm ext}\rangle_V$ in more detail, its eigenvalues and eigenvectors at $r = 1.25$, 2.00, and 4.00 (bohr) are summarized in Table 2.1. We can find that the third eigenvectors for the sites S_2 and S_3 are almost correspond to the x-direction.

$\langle\overleftrightarrow{\sigma}_{\rm int}\rangle_V$ around the three Si atoms are shown in Fig. 2.7. It can easily be found that $\langle\overleftrightarrow{\sigma}_{\rm int}\rangle_V$ depends on r more heavily than $\langle\overleftrightarrow{\sigma}_{\rm ext}\rangle_V$. Due to this property, we can see the peak positions of the eigenvalues clearly. In order to discuss the difference between the sites in more detail, the results of $\langle\overleftrightarrow{\sigma}_{\rm int}\rangle_V$ at $r = 2.10$ (bohr) (covalent radius of a Si atom [62]) are summarized in Table 2.2. It is found that the average of the eigenvalues for $\langle\overleftrightarrow{\sigma}_{\rm int}\rangle_V$ around the Si atom on the site S_3 is the largest of the all sites, followed by the sites S_1 and S_2. It is also clear that the standard deviation of the eigenvalues is the smallest for the site S_1. This is obviously because the Si atoms on the site S_1 have four Si-Si bonds, and therefore have more isotropic characteristics.

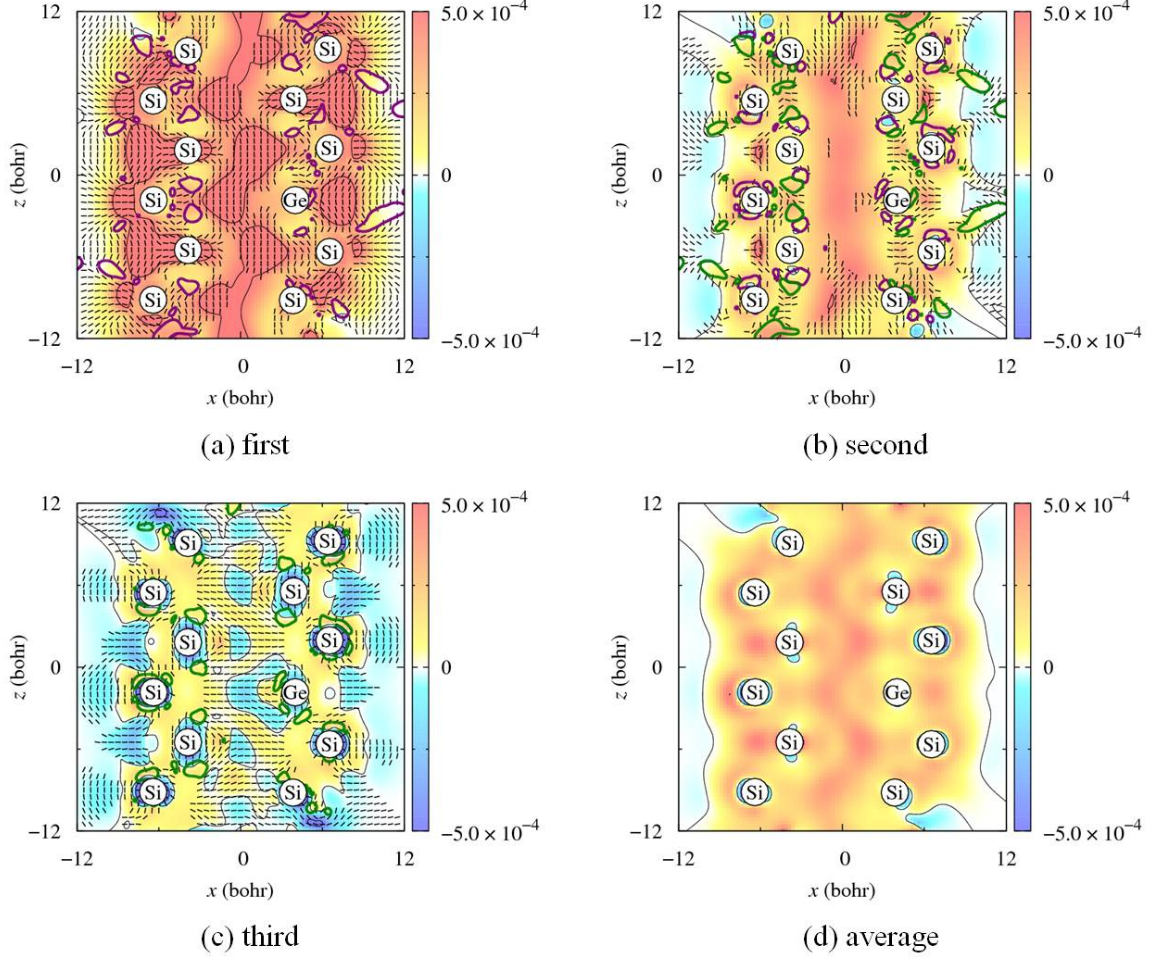

Figure 2.8: Eigenvalues of $\overleftrightarrow{\sigma}_{\rm ext}(\vec{r})$ (a.u.) for the Ge-substituted model. Results are shown on the same plane as Fig. 2.3 in the same manner. See the caption of Fig. 2.3 for the details.

2.4.2 Comparison with the Ge-substituted model

In this subsection, we show the results for the Ge-substituted model and compare them with those for the pristine Si nanowire model. $\overleftrightarrow{\sigma}_{\rm ext}(\vec{r})$ of the Ge-substituted model is shown in Fig. 2.8. The difference from the results of the pristine model is mainly seen around the substituted atom. The eigenvalues around the Ge atom are smaller than those around the Si atom on site S_1 in the pristine model. This feature is also seen in the results of $\overleftrightarrow{\sigma}_{\rm int}(\vec{r})$, which are shown in Figs. 2.9.

In Fig. 2.10, we show the spherical average of $\overleftrightarrow{\sigma}_{\rm ext}(\vec{r})$ around the Ge atom in the Ge-substituted model. The eigenvalues and eigenvectors for three specific r are summarized in

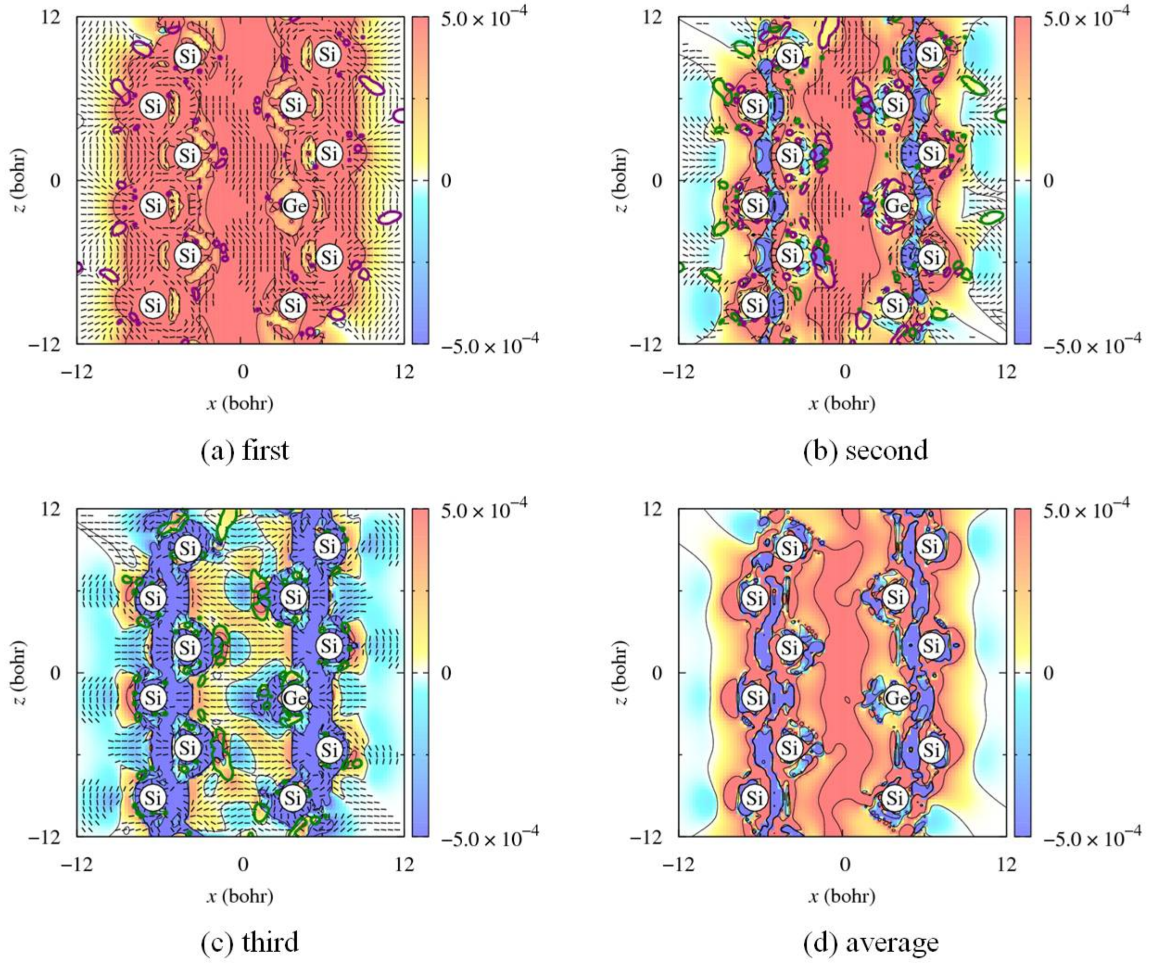

Figure 2.9: Eigenvalues of $\overleftrightarrow{\sigma}_{\rm int}(\vec{r})$ (a.u.) for the Ge-substituted model. Results are shown on the same plane as Fig. 2.3 in the same manner. See the caption of Fig. 2.3 for the details.

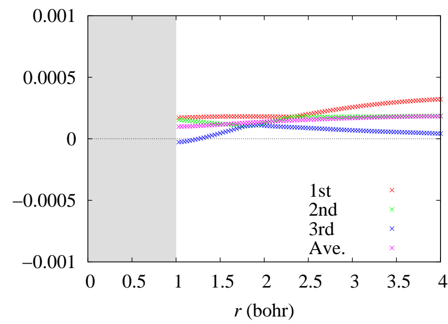

Figure 2.10: Spherical average of $\overleftrightarrow{\sigma}_{\rm ext}(\vec{r})$ (a.u.) around the Ge atom in the Ge-substituted model. Results are shown in the same manner as Fig. 2.6.

Table 2.3: Eigenvalues ($\times 10^{-4}$ a.u.) and eigenvectors $\vec{v} = (v_x, v_y, v_z)^T$ of $\langle \overleftrightarrow{\sigma}_{\text{ext}} \rangle_V$ at $r =$ 1.25, 2.00, and 4.00 (bohr) for the Ge atom in the Ge-substituted model.

r		Ge first	Ge second	Ge third
1.25	eigenvalue	1.769	1.389	−0.015
	v_x	0.000	0.991	−0.185
	v_y	1.000	0.000	0.000
	v_z	0.000	−0.136	0.983
2.00	eigenvalue	1.809	1.273	1.069
	v_x	0.000	0.164	0.868
	v_y	1.000	0.000	0.000
	v_z	0.000	0.987	0.497
4.00	eigenvalue	3.211	1.857	0.419
	v_x	0.001	0.000	1.000
	v_y	0.000	1.000	0.000
	v_z	1.000	0.000	−0.018

Table 2.3. We can find that the difference between the eigenvalues of $\langle \overleftrightarrow{\sigma}_{\text{ext}} \rangle_V$ is relatively moderate in the region of $r < 2.5$ (bohr), in comparison with the result of the Si atom on the site S_1 of the pristine model. In other words, $\langle \overleftrightarrow{\sigma}_{\text{ext}} \rangle_V$ around the Ge atom is more isotropic than that of the Si atom on the site S_1 in the pristine model. We speculate that this result corresponds to the fact that the valence electrons of a Ge atom are bound to the nucleus more weakly than those of a Si atom: They can move more freely. For $r = 4.00$ (bohr), the values become similar to those of the Si atoms. This is because the effects nearby Si atoms are included in this result.

Finally, we show the results of $\langle \overleftrightarrow{\sigma}_{\text{int}} \rangle_V$ for the Ge-substituted model in Fig. 2.11. The results at $r = 2.27$ (bohr) (covalent radius of a Ge atom [62]) are also summarized in Table 2.4. The second and the third eigenvalues of $\langle \overleftrightarrow{\sigma}_{\text{int}} \rangle_V$ around the covalent radius are close to each other for the Ge atom in the Ge-substituted model, while the first and second ones are close to each other for the Si atom at the site S_1 in the pristine model. This result represents a qualitative difference of the Si atom and the substituted Ge one. In addition, it

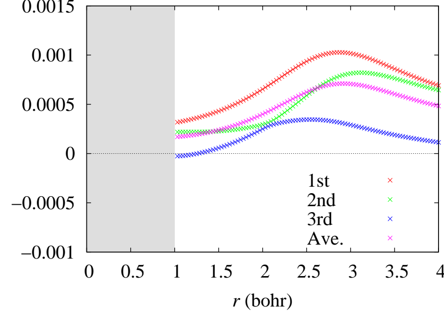

Figure 2.11: Spherical average of $\overleftrightarrow{\sigma}_{\rm int}(\vec{r})$ (a.u.) around the Ge atom in the Ge-substituted model. Results are shown in the same manner as Fig. 2.6.

Table 2.4: Eigenvalues, their average, and their SD of $\langle\overleftrightarrow{\sigma}_{\rm int}\rangle_V$ ($\times 10^{-4}$ a.u.) at $r = 2.27$ (bohr) for the Ge atom in the Ge-substituted model.

first	second	third	average	SD
8.12	4.30	3.24	5.22	2.09

can be found that both the first eigenvalue and the average of the eigenvalues at the covalent radius are larger than those the Si atom on the site S_1 for the pristine model. As mentioned above, this reflects the effect of the valence electrons of the Ge atom which can move more freely than those of the Si atom. It is also found that the standard deviation (SD) of the eigenvalues is larger than that of the Si atom on the site S_1 for the pristine model. Hence it can be said that $\langle\overleftrightarrow{\sigma}_{\rm int}\rangle_V$ around the Ge atom is more anisotropic than that of the Si atom on the site S_1 in the pristine model. This is the opposite result to that of $\langle\overleftrightarrow{\sigma}_{\rm ext}\rangle_V$ and clearly reflects the effect of anisotropic $\langle\overleftrightarrow{\epsilon}\rangle_V$.

2.5 Conclusion

In this work, we investigate the local response of Si nanowire models to the electric field. For this purpose, two local electric conductivity tensors, $\overleftrightarrow{\sigma}_{\rm ext}(\vec{r})$ and $\overleftrightarrow{\sigma}_{\rm int}(\vec{r})$, which are defined in Rigged QED, are used. We emphasize that $\overleftrightarrow{\sigma}_{\rm int}(\vec{r})$ can be defined as the electric current response to the internal electric field. $\overleftrightarrow{\sigma}_{\rm int}(\vec{r})$ does not have the corresponding

macroscopic quantity. $\overleftrightarrow{\sigma}_{\rm int}(\vec{r})$ can represent how the actual electric field at a specific position drives carriers such as electrons. In order to investigate the effects of impurities for the local response to electric field, we consider both a pristine Si nanowire model and Ge-substituted one which include a Ge atom.

For the results of $\overleftrightarrow{\sigma}_{\rm ext}(\vec{r})$ and $\overleftrightarrow{\sigma}_{\rm int}(\vec{r})$ of the pristine Si nanowire model, there are the regions which show complicated response to the electric field, such as rotational one. For $\overleftrightarrow{\sigma}_{\rm ext}(\vec{r})$, there are the regions which show negative eigenvalues around the center axis of the nanowire and the exterior of it. On the other hand, for $\overleftrightarrow{\sigma}_{\rm int}(\vec{r})$, the regions around the Si-Si bonds also show negative eigenvalues. Spherical average of $\overleftrightarrow{\sigma}_{\rm ext}(\vec{r})$ around three specific atoms is also shown. We can see the site dependence of $\overleftrightarrow{\sigma}_{\rm ext}(\vec{r})$ clearly. From the analysis of $\langle\overleftrightarrow{\sigma}_{\rm int}\rangle_V$, it is clarified that the difference among the eigenvalues is the smallest for the site S_1. This is because the Si atoms on the site S_1 have four Si-Si bonds, and therefore have more isotropic characteristics.

$\overleftrightarrow{\sigma}_{\rm ext}(\vec{r})$ and $\overleftrightarrow{\sigma}_{\rm int}(\vec{r})$ of the Ge-substituted model show different features from the pristine model. The difference from the pristine model is seen mainly around the Ge atom, but this is relatively small. The spherical average of $\overleftrightarrow{\sigma}_{\rm ext}(\vec{r})$ and $\overleftrightarrow{\sigma}_{\rm int}(\vec{r})$ for the Ge-substituted model is also shown. It is found that $\langle\overleftrightarrow{\sigma}_{\rm ext}\rangle_V$ of the substituted Ge atom is more isotropic than that of the corresponding Si atom in the pristine model, while $\langle\overleftrightarrow{\sigma}_{\rm int}\rangle_V$ shows the opposite result.

In this work, the conductive state is assumed to be represented as plane waves. To derive a more appropriate conductive state, we should improve the calculation code to realize conductive electronic states by more suitable boundary conditions, which is our future task.

Reference

[1] Y. Cui and C. M. Lieber, Science **291**, 851 (2001).

[2] D. Wang, J. G. Lu, C. J. Otten, and W. E. Buhro, Appl. Phys. Lett. **83**, 5280 (2003).

[3] D. Wang, C. J. Otten, W. E. Buhro, and J. G. Lul, IEEE Trans. Nanotechnol. **3**, 328 (2004).

[4] D. Kang, J.-H. Ko, E. Bae, J. Hyun, W. Park, B.-K. Kim, J.-J. Kim, and C. Lee, J. Appl. Phys. **96**, 7574 (2004).

[5] H. Y. Cha, H. Wu, S. Chae, and M. G. Spencer, J. Appl. Phys. **100**, 024307 (2006).

[6] W. M. Zhou, F. Fang, Z. Y. Hou, L. J. Yan, and Y. F. Zhang, IEEE Electron Device Lett. **27**, 463 (2006).

[7] X. Duan, Y. Huang, R. Argarawal, and C. M. Lieber, Nature **421**, 241 (2003).

[8] B. Tian, X. Zheng, T. J. Kempa, Y. Fang, N. Yu, G. Yu, J. Huang, and C. M. Lieber, Nature **449**, 885 (2007).

[9] Y. Cui, L. J. Lauhon, M. S. Gudiksen, and J. Wang, Appl. Phys. Lett. **78**, 2214 (2001).

[10] Y. Wu, Y. Cui, L. Huynh, C. J. Barrelet, D. C. Bell, and C. M. Lieber, Nano Lett. **4**, 433 (2004).

[11] V. Schmidt, S. Senz, and U. Gösele, Nano Lett. **5**, 931 (2005).

[12] S. D. Suk, S.-Y. Lee, S.-M. Kim, E.-J. Yoon, M.-S. Kim, M. Li, C. W. Oh, K. H. Yeo, S. H. Kim, D.-S. Shin, K.-H. Lee, H. S. Park, J. N. Han, C. J. Park, J.-B. Park, D.-W. Kim, D. Park, and B.-I. Ryu, IEDM Tech. Dig. 2005, p. 735.

[13] H. Lee, L.-E. Yu, S.-W. Ryu, J.-W. Han, K. Jeon, D.-Y. Jang, K.-H. Kim, J. Lee, J.-H. Kim, S. C. Jeon, G. S. Lee, J. S. Oh, Y. C. Park, W. H. Bae, H. M. Lee, J. M. Yang, J. J. Yoo, S. I. Kim, and Y.-K. Choi, Tech. Dig. VLSI Symp, 2006, p. 58.

[14] S. Datta, in *Electronic Transport in Mesoscopic Systems*, edited by H. Ahmed, M. Pepper, and A. Broers (Cambridge University Press, Cambridge, England, 1995).

[15] J. Taylor, H. Guo, and J. Wang, Phys. Rev. B **63**, 121104 (2001).

[16] J. Taylor, H. Guo, and J. Wang, Phys. Rev. B **63**, 245407 (2001).

[17] P. S. Damle, A. W. Ghosh, and S. Datta, Phys. Rev. B **64**, 201403 (2001).

[18] M. Brandbyge, J. -L. Mozos, P. Ordejón, J. Taylor, and K. Stokbro, Phys. Rev. B **65**, 165401 (2002).

[19] K. Doi, Y. Mikazuki, S. Sugino, T. Doi, P. Szarek, M. Senami, K. Shiraishi, H. Iwai, N. Umezawa, T. Chikyo, K.Yamada, and A. Tachibana, Jpn. J. Appl. Phys. **47**, 205 (2008).

[20] P. Szarek, Ph.D. dissertation, Kyoto University, 2008.

[21] A. Fukushima, Y. Tsuchida, M. Senami, and A. Tachibana, Jpn. J. Appl. Phys. **49**, 111504 (2010).

[22] A. Fukushima, S. Sugino, Y. Tsuchida, M. Senami, and A. Tachibana, Jpn. J. Appl. Phys. **49**, 121504 (2010).

[23] M. Senami, Y. Tsuchida, A. Fukushima, Y. Ikeda, and A. Tachibana, Jpn. J. Appl. Phys. **51**, 031101 (2012).

[24] A. Tachibana, J. Mol. Model. **11**, 301 (2005).

[25] A. Tachibana, J. Mol. Struct.: THEOCHEM **943**, 138 (2010).

[26] M. Senami, Y. Ikeda, A. Fukushima, A. Tachibana, Jpn. J. Appl. Phys. **49**, 115002 (2010).

[27] M. Senami, Y. Ikeda, A.Tachibana, Jpn. J. Appl. Phys. **50**, 010103 (2011).

[28] J. Chen, M. A. Reed, A. M. Rawlett, and J. M. Tour, Science **286**, 1550 (1999).

[29] J. Chen, W. Wang, M. A. Reed, A. M. Rawlett, D. W. Price, and J. M. Tour, Appl. Phys. Lett. **77**, 1224 (2000).

[30] I. Amlani, A. M. Rawlett, L. A. Nagahara, and R. K. Tsui, Appl. Phys. Lett. **80**, 2761 (2002).

[31] I. Kratochvilova, M. Kocirik, A. Zambova, J. Mbindyo, T. E. Mallouk, and T. S. Mayer, J. Mater. Chem. **12**, 2927 (2002).

[32] K. Walzer, E. Marx, N. C. Greenham, R. J. Less, P. R. Raithby, and K. Stokbro, J. Am. Chem. Soc. **126**, 1229 (2004).

[33] A. M. Rawlett, T. J. Hopson, L. A. Nagahara, R. K. Tsui, G. K. Ramachandran, and Stuart M. Lindsay, Appl. Phys. Lett. **81**, 3043 (2002).

[34] A. M. Rawlett, T. J. Hopson, I. Amlani, R. Zhang, J. Tresek, L. A. Nagahara, R. K. Tsui, and H. Goronkin, Nanotechnology **14**, 377 (2003).

[35] J. D. Le, Y. He, T. R. Hoye, C. C. Mead, and R. A. Kiehl, Appl. Phys. Lett. **83**, 5518 (2003).

[36] C. Thelander, M. T. Bj ork, M. W. Larsson, A. E. Hansen, L. R. Wallenberg, L. Samuelson, Solid State Commun. **131**, 573 (2004).

[37] D. Lin, H. Wu, and Wei Pan, Adv. Mater. **19**, 3968 (2007).

[38] W. -H. Chu, H. -W. Chiang, C. -P. Liu, Y. -F. Lai, K. -Y. Hsu, and H. -C. Chung, Appl. Phys. Lett. **94**, 182101 (2009).

[39] M. Senami, J. Nishikawa, T. Hara, and A. Tachibana, J. Phys. Soc. Jpn. **79**, 084302 (2010).

[40] T. Hara, M. Senami, and A. Tachibana, Phys. Lett. A **376**, 1434 (2012).

[41] A. J. Stone, Mol. Phys. **56**, 1065 (1985).

[42] C. R. L. Sueur and A. J. Stone, Mol. Phys. **78**, 1267 (1993).

[43] C. R. L. Sueur and A. J. Stone, Mol. Phys. **83**, 293 (1994).

[44] A. J. Stone and C. -S. Tong, Chem. Phys. **137** 121 (1989).

[45] G. J. Williams and A. J. Stone, J. Chem. Phys. **119**, 4620 (2003).

[46] K. Natori, J. Appl. Phys. **76**, 4879 (1994).

[47] K. Natori, IEEE Trans. Electron Devices **55**, 2877 (2008).

[48] R. M. Stevens, R. M. Pitzer, and W. N. Lipscomb, J. Chem. Phys. **38**, 550 (1960).

[49] J. Gerratt and I. M. Mills, J. Chem. Phys. **49**, 1719 (1968).

[50] D. B. Cook, *Handbook of Computational Quantum Chemistry* (Dover, New York, 2005), p. 653–668.

[51] A. A. Stuchebrukhov, J. Chem. Phys. **104**, 8424 (1996).

[52] A. A. Stuchebrukhov, J. Chem. Phys. **105**, 10819 (1996).

[53] A. A. Stuchebrukhov, J. Chem. Phys. **107**, 6495 (1997).

[54] A. A. Stuchebrukhov, J. Chem. Phys. **108**, 8499 (1998).

[55] A. A. Stuchebrukhov, J. Chem. Phys. **108**, 8510 (1998).

[56] A. A. Stuchebrukhov, J. Chem. Phys. **118**, 7898 (2003).

[57] Y. Lee, T. Nagata, K. Kakushima, K. Shiraishi, and H. Iwai, in *2008 International Workshop on Dielectric Thin Films for Future Electron Devices*, Tokyo, Japan, 2008, p. 83–84.

[58] P. J. Hay and W. R. Wadt, J. Chem. Phys. **82**, 270 (1985).

[59] W. R. Wadt and P. J. Hay, J. Chem. Phys. **82**, 284 (1985).

[60] P. J. Hay and W. R. Wadt, J. Chem. Phys. **82**, 299 (1985).

[61] M. J. Frisch, G. W. Trucks, H. B. Schlegel *et al.*, Gaussian 09, Revision B. 01. (Gaussian Inc., Wallingford CT, 2010).

[62] B. Cordero, V. Gómez, A. E. Platero-Prats, M. Revés, J. Echeverría, E. Cremades, F. Barragán, and S. Alvarez, Dalton Trans. **21**, 2832 (2008).

Chapter 3

Local Transport Property of GaN Cluster as a Model of Nanowire

3.1 Introduction

Recently, many researches for semiconductor nanowire have been reported [1–11]. The semiconductor nanowire is a good candidate for next generation materials of field effect transistor (FET) devices. Nanowire materials provide high electric conductance due to its ballistic conduction, and their structure is suitable for the suppression of the leak current by, for example, gate-all-around FET.

For nanosize materials, it is important to predict their properties by the first principles calculations before the fabrication in laboratories. In previous works, conductive properties are discussed in terms of global and averaged conductivity. However, local conductive properties are important for nanosize materials, as well as the dielectric properties of nano-materials are analyzed by local quantities [12–15]. By considering local conductive properties, we can discuss many features, the effects of impurities, interface, the position dependence of conductance, and so on. Hence, we have proposed the analysis by local conductivity density tensors [16–18].

In this work, we show the validity of our analysis using a local conductivity density tensor following our earlier works about the local quantity analyses [12–19] and nanowire models [20, 21]. By using this local conductivity density tensor, we study conductive properties of a GaN cluster model which attempts to mimic a GaN nanowire. Among the semiconductor

nanowires, the most popular one is the silicon nanowire, since this is the leading candidate material for post-Moore devices [7–11]. In addition to the silicon nanowire, we consider the GaN nanowire as an alternative candidate or a material next to the silicon nanowire. Hence, we investigate the conductivity of a GaN model in this work. For this purpose, the wave function of conductive electrons should be derived, since our local conductivity is calculated with local electronic current density. However, most program codes of electronic structure calculations give us a state without net electronic current. Hence, we have developed a calculation code to introduce electronic current in a system [18]. As a result, the effects of coulomb and exchange interactions by conductive electrons on electrons in a system are included.

This paper is organized as follows. In the next section, we define local electronic current density and a conductivity density tensor. In Sec. 3.3, the calculation method of our program code is summarized. Then, we show our cluster model used in this work. In Sec. 3.4, we show results of our model in terms of our local electronic current density and local conductivity. Section 3.5 is devoted to the summary and discussion.

3.2 Theory

The local electronic current density [16, 17] is given by using the local value of probability current based on the Rigged QED theory [20, 22–29, 31, 32]. It is explicitly given as,

$$\begin{aligned} \hat{\boldsymbol{J}}(\boldsymbol{r}) &= \frac{Z_e e}{2m_e} \sum_i \left[\hat{\psi}_i^\dagger(\boldsymbol{r}) \hat{\boldsymbol{p}}(\boldsymbol{r}) \hat{\psi}_i(\boldsymbol{r}) + h.c. \right] \\ &= \frac{Z_e e}{2m_e} \sum_i \left[-i\hbar \hat{\psi}_i^\dagger(\boldsymbol{r}) \boldsymbol{\nabla} \hat{\psi}_i(\boldsymbol{r}) - \frac{Z_e e}{c} \hat{\psi}_i^\dagger(\boldsymbol{r}) \hat{\boldsymbol{A}}(\boldsymbol{r}) \hat{\psi}_i(\boldsymbol{r}) + h.c. \right], \end{aligned} \tag{3.1}$$

where $\hat{\psi}_i$ is the i-th natural orbital, m_e is the electron mass, $Z_e = -1$ for electrons, and $\hat{\boldsymbol{A}}(\boldsymbol{r})$ is vector potential.

With this current density operator, we show the definition of electric conductivity operators. Here, the current is induced by three factors; (1) external electric field, (2) the time variation of magnetic field, and (3) radiation (photocurrent). Since we consider only the steady state, the latter two effects can be neglected. Hence, we consider only the external electric field, $\hat{\boldsymbol{D}}(\boldsymbol{r})$. The linear response of electrons in a system to an external field is

defined by using the external local electrical conductivity tensor $\hat{\boldsymbol{\sigma}}_{\text{ext}}$ as,

$$\hat{\boldsymbol{J}}(\boldsymbol{r}) = \hat{\boldsymbol{\sigma}}_{\text{ext}}(\boldsymbol{r})\hat{\boldsymbol{D}}(\boldsymbol{r}). \tag{3.2}$$

The ordinary electrical conductivity is defined as a global constant for a material. However, the averaged property, such as a global constant, is insufficient for the description of the conductive property of nanosize materials. Hence, we should treat the conductivity as a local quantity.

The external electric field $\hat{\boldsymbol{D}}(\boldsymbol{r})$ is related to the electric field including the effect of internal polarization,

$$\hat{\boldsymbol{D}}(\boldsymbol{r}) = \hat{\boldsymbol{\epsilon}}(\boldsymbol{r})\hat{\boldsymbol{E}}(\boldsymbol{r}), \tag{3.3}$$

where $\hat{\boldsymbol{\epsilon}}(\boldsymbol{r})$ is the local dielectric constant tensor operator. [12–15] Hence, we can consider the linear response to the internal electric field, $\hat{\boldsymbol{E}}(\boldsymbol{r})$. This internal electric conductivity $\hat{\boldsymbol{\sigma}}_{\text{int}}$ is defined as

$$\hat{\boldsymbol{J}}(\boldsymbol{r}) = \hat{\boldsymbol{\sigma}}_{\text{ext}}(\boldsymbol{r})\hat{\boldsymbol{\epsilon}}(\boldsymbol{r})\hat{\boldsymbol{E}}(\boldsymbol{r}) \tag{3.4}$$

$$= \hat{\boldsymbol{\sigma}}_{\text{int}}(\boldsymbol{r})\hat{\boldsymbol{E}}(\boldsymbol{r}). \tag{3.5}$$

The external conductivity, $\hat{\boldsymbol{\sigma}}_{\text{ext}}(\boldsymbol{r})$, is related to the internal conductivity, $\hat{\boldsymbol{\sigma}}_{\text{int}}(\boldsymbol{r})$, through the local dielectric tensor, $\hat{\boldsymbol{\epsilon}}(\boldsymbol{r})$.

These operators, $\hat{\boldsymbol{\sigma}}_{\text{ext}}(\boldsymbol{r})$, $\hat{\boldsymbol{\sigma}}_{\text{int}}(\boldsymbol{r})$, and $\hat{\boldsymbol{\epsilon}}(\boldsymbol{r})$, are Hermite, and hence all elements in these tensor are real. However, these tensors are not symmetric matrix. Therefore, three eigenvalues of these tensor are derived as three real numbers, or one real and two complex. Complex eigenvalues shows a remarkable feature, rotational response. This rotational response cannot correctly be described if the conductivity or dielectric constant is treated as a scalar quantity. Hence, $\hat{\boldsymbol{\sigma}}$ and $\hat{\boldsymbol{\epsilon}}$ should be treated as tensors for nanosize materials.

3.3 Calculation Method

3.3.1 Quantum states of conductive electrons

In this work, conductive electrons are included in our electronic structure calculations [18]. Our calculation is performed based on quantum mechanics. We use the linear combination of atomic orbital (LCAO) method, since one of the purposes of this work is to investigate

the relation between local electronic current and the bonding state between atoms. For this purpose, the LCAO method is appropriate. In our calculation, wave functions are expanded by Gaussian functions. Then, the electronic states representing the electronic current is given by the linear combination of Gaussian functions. However, since we focus on the steady state of the scattering of electrons, the states of conductive electrons are considered to be similar to plain waves rather than Gaussian functions. Therefore, we assume the following function as an electronic state representing electronic current,

$$f(\boldsymbol{r}) \equiv \exp(-a_x x^2)\exp(-a_y y^2)\exp(ik_z z), \tag{3.6}$$

where a_x, a_y, and k_z are parameters and the direction of current is taken to be the z direction. These parameters are fixed during a calculation. We expand this function in Gaussian basis functions ϕ_i as

$$f_G(\boldsymbol{r}) = c_G \sum_i \langle \phi_i | f \rangle | \phi_i \rangle, \tag{3.7}$$

where c_G is the normalization factor. We adopt this function f_G as a conductive state in our calculations and replace the initial electronic state of the highest occupied molecular orbital (HOMO) by this function. Since the function f_G is a complex one, complex molecular orbital coefficients must be used in our calculation. We take $a_{x,y,z} = 0.01$ a.u. (1 a.u.= 0.280 Å^{-2} for a_i) and the values of $k_{x,y,z}$ are chosen as $k_{x,y,z} = -0.5$ a.u. (1 a.u.= 1.890 Å^{-1} for k_i). We checked the dependence of the current on the values of a_i and k_i. The results are almost independent of the values of a_i for this model as long as $a_i \lesssim 0.01$ a.u. The correlation between the value of k_i and electronic current density has also been confirmed by the calculations of seven values of k_z for several models [18]. The current density is roughly proportional to the value of k_i in the range, $|k_i| = 0.01 - 1.0$. For too large $|k_i|$, conductive states cannot be expanded sufficiently in Gaussian basis functions. Note that the effect of vector potential is not considered in this current.

In our calculations, electronic states representing electronic current are derived as follows. We adopt the conductive state, $f_G(\boldsymbol{r})$, as the initial condition of the HOMO for our self-consistent field (SCF) calculations. Of course, if an ordinary SCF calculation is completed, the derived electronic state is the ground state and has no net current. We want to derive conductive electronic states including coulomb and exchange interactions by conductive electrons. Hence, we also inject the conductive state into the HOMO in every SCF

cycle. This conductive state is generically not orthogonal to other orbitals. Hence, the orthogonalization is performed in every cycle. Empirically, this orthogonalization is required only in first several cycles, and after that, the conductive state is orthogonal to others within the accuracy. In other words, our procedure gives the most stable electronic state under the condition that the HOMO is the conductive state. In the sense, this condition is interpreted as a boundary condition. Our procedure is a first step to derive conductive electrons as quantum state by the boundary condition that scalar and vector potentials represent embedding medium appropriately.

3.3.2 Conductivity tensor

The procedure of the calculation of $\boldsymbol{\sigma}_{\rm ext}(\boldsymbol{r})$ is summarized as follows. First, the calculations with external electric fields of the x direction, D_{1x} and D_{2x}, are carried out, and the current density $\boldsymbol{J}_1(\boldsymbol{r})$ and $\boldsymbol{J}_2(\boldsymbol{r})$ are derived. Uniform external fields are assumed in our calculations. Then three components of the external electrical conductivity tensor are given as

$$\Delta J^i(\boldsymbol{r}) = \sigma^{ix}_{\rm ext}(\boldsymbol{r})\Delta D_x \ (i = x, y, z), \tag{3.8}$$

where $\Delta D_x = D_{1x} - D_{2x}$ and $\Delta J^i(\boldsymbol{r}) = J^i_1(\boldsymbol{r}) - J^i_2(\boldsymbol{r})$. These calculations are repeated for other orthogonal directions, y and z, and all components of the external electrical conductivity tensor are derived as

$$\boldsymbol{\sigma}_{\rm ext}(\boldsymbol{r}) = \begin{pmatrix} \sigma^{xx}_{\rm ext}(\boldsymbol{r}) & \sigma^{xy}_{\rm ext}(\boldsymbol{r}) & \sigma^{xz}_{\rm ext}(\boldsymbol{r}) \\ \sigma^{yx}_{\rm ext}(\boldsymbol{r}) & \sigma^{yy}_{\rm ext}(\boldsymbol{r}) & \sigma^{yz}_{\rm ext}(\boldsymbol{r}) \\ \sigma^{zx}_{\rm ext}(\boldsymbol{r}) & \sigma^{zy}_{\rm ext}(\boldsymbol{r}) & \sigma^{zz}_{\rm ext}(\boldsymbol{r}) \end{pmatrix}. \tag{3.9}$$

In this work, we take $D_{1i} = 0.002\,\text{a.u.}$ and $D_{2i} = 0.001\,\text{a.u.}$ as a reference. Although the conductivity should be studied depending on values of D, we demonstrate the analysis using the local conductivity tensor only for these values of external fields. In this work, we study only the external conductivity tensor. The internal one will be discussed in our next article.

3.3.3 Computational model

Next, we show our cluster model in Fig. 3.1. This model is based on the [0001] wurtzite structure with lattice parameters, $a = 8.189\,\text{Å}$ and $c = 5.095\,\text{Å}$. This structure consists of

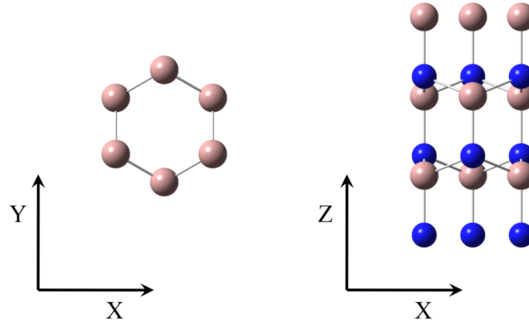

Figure 3.1: GaN cluster model for the analysis. The dark spheres are Ga atoms and the light spheres are N atoms.

six layers. Three Ga triangles and three N triangles are stacked mutually. This cluster model is motivated to extract some conductive properties of the GaN nanowire. Although our goal is the investigation of conductive properties for nanowires, we study this small model as demonstration because of limited computer resources. Of course, the cluster model is not connected to any other atoms at the ends of the model, and hence the electronic states near the ends are expected to be much different from those of nanowires. Hence, we should be careful, when we speculate a conductive property of the GaN nanowire from our cluster model. We will not discuss any conductive property near both ends in this work.

Basis sets are chosen as the Dunning-Huzinaga double-zeta basis set [33] with effective core potential by Hay and Wadt (LANL2DZ) [34–37]. Larger basis sets are favored for our calculation method, since an input current state is expanded in a basis set. We are now expanding our results to larger basis sets, which will be shown elsewhere in the near future. All electronic states calculations are based on the restricted Hartree-Fock (RHF) method. Of course, in order to include exchange correlation correctly, a post Hartree-Fock calculation is mandatory. However, in this work, we report our results within the RHF as a first step of our analysis method. We are now developing our code to complete active space (CAS) SCF method.

Once electronic states are determined by SCF calculations, local electronic current density can be determined by the equation of the operator, (3.1). We carry out the calculation of the local electronic current density and the conductivity density tensor by the molecular regional DFT (MRDFT) program package [38], which is developed in our laboratory. In this calculation, we ignore effects of magnetic fields, since calculations of vector potential waste

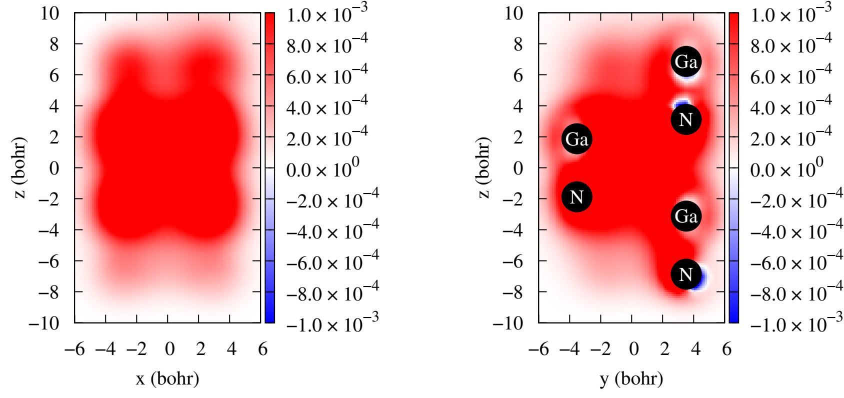

Figure 3.2: The z-component of the local current density for our model with $k_z = -0.5$ a.u. The left and right panels are results on $y = 0$ and $x = 0$ planes, respectively.

a tremendous machine resource. The effects of vector potential on current is suppressed by c. As a result, within the range of the current of this study, the effects are negligibly small. We have confirmed that the effects are not large in our previous works [18].

3.4 Results

The z-component of the local current density is shown in Fig. 3.2 for our model with $k_z = -0.5$ a.u. The left and right panels are results on $y = 0$ and $x = 0$ planes, respectively. The unit of current density is the atomic unit (1 a.u.$= 2.37 \times 10^{18}$ A/m^2). The net current is seen to pass straightly through the nanowire (z-direction). The current density is uniformly distributed within the nanowire. Our cluster model is very small for the representation of the GaN nanowire. Since the cluster model is not connected to any other medium atoms at the both ends of the z-direction, the electronic states near the ends are much different from those of the GaN nanowire. Hence, we should pay attention to the region apart from the ends. The region, $-4 < z < 4$ bohr, is taken into account for definiteness. We consider that this model may realize some properties of the nanowire, in this region. In Fig. 3.3, the electron density of our model is shown. The left and right panels are results on $y = 0$ and $x = 0$ planes, respectively. The electron density around Ga atoms are much smaller than that around N atoms. This is because we used the pseudopotential for the Ga atom and the Ga-N bond is ionic. In other words, this electron density shows the density of electrons which can move easily, since electrons in inner core are not expected to move easily. Comparing

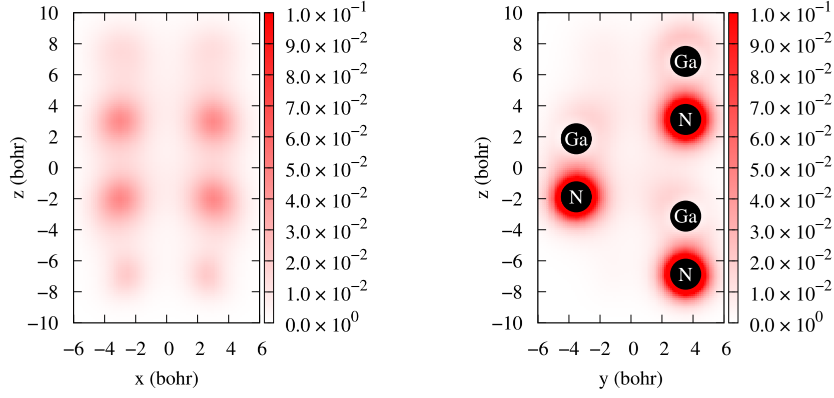

Figure 3.3: The electron density. The left and right panels are results on $y = 0$ and $x = 0$ planes, respectively.

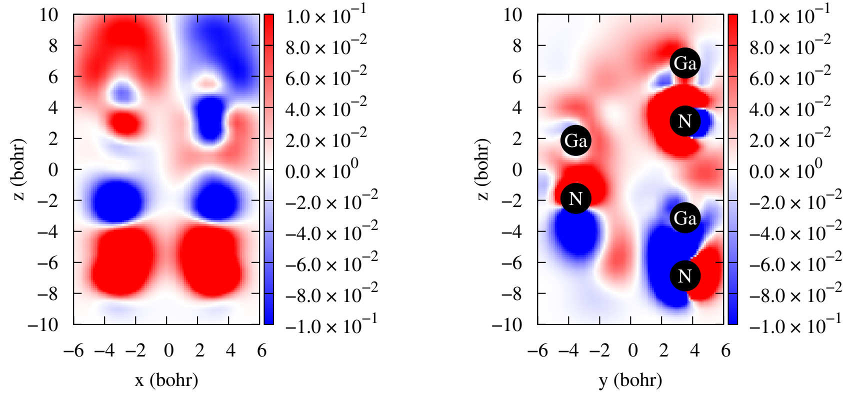

Figure 3.4: The zz component of the external conductivity density tensor. The left and right panels are results on $y = 0$ and $x = 0$ planes, respectively.

Figs. 3.2 and 3.3, the correlation between the electronic current and the electron density is weak for our calculations. Conductive electrons do not stay around atoms in this model.

The zz component of the external conductivity density tensor is shown in Fig. 3.4. The left and right panels are results on $y = 0$ and $x = 0$ planes, respectively. As seen in the right panel, the conductivity is large in the region between the left two atoms. The distance between the Ga and N atoms on the left side is much shorter than that between the middle Ga and N atoms on the right side, since these atoms on the left side are on the layers next to each other. The conductivity around the center of the nanowire is significantly smaller than around atoms. Since the electron density is small in the region, the response to an external electric field is speculated to be smaller than in other region. The region between upper Ga

and N atoms on the right side shows positive conductivity, while the region between bottom two atoms shows negative one. As mentioned above, the atoms at the both ends of our model are truncated from longer nanowire and have dangling bonds. Hence, the electronic states of these atoms should be different from that of the nanowire. As a result, we should not pay attention to these regions, and this difference is not discussed further. Note that since conductive states are included a la boundary condition in our code, the dependence of the conductive states on external fields cannot be described precisely in principle. However, some expected conductive properties are realized in our results. We will check our results by longer models and larger basis sets. The dependence of the conductivity on the value of internal fields is discussed in the next article.

In Fig. 3.5, the three eigenvalues of the external conductivity density tensor are shown for our model. The left and right panels are results on $y = 0$ and $x = 0$ planes. The top, middle, and bottom panels are the first, second, and third eigenvalues, respectively. The eigenvalues are arranged as the descending order for real eigenvalues. For complex eigenvalues, which exist in contours, the two complex eigenvalues are assigned as the second and third ones. The short line segments show the direction of eigenvectors. The depth of color means the eigenvalues for real eigenvalues, while for complex ones, the color means the sign of the real part, the depth means the absolute value, and the contour means the arguments of complex eigenvalues. In very wide area, complex eigenvalues of the conductivity are seen in Fig. 3.5. Hence, linear responses to external fields of this cluster model has rotational behavior. For nanosize materials, conductivity is dependent on positions, and conductivity tensor is not a diagonal matrix. Hence, we should analyze nanosize material by a local density and tensor quantity. Large conductivity between the left two atoms on the $x = 0$ plane appears again as the first eigenvalue. In this region, the direction of eigenvector is roughly the z one. The first eigenvalue of this region is dominated by the large zz component, as seen in Fig. 3.4. This implies that the path between the atoms is the conductive path in this model. On the other hand, the eigenvector for the first eigenvalue in the region around the Ga atom on the right side ($z \simeq -3$ bohr) does not indicate the z direction. The atoms nearest to this Ga atom and on the upper layer are located on different x and y positions, as seen in Fig. 3.1. (The Ga and N atoms on the left side have the same x and y positions.) Hence, we speculate that the conductive path of this region should have large x and y components. The property

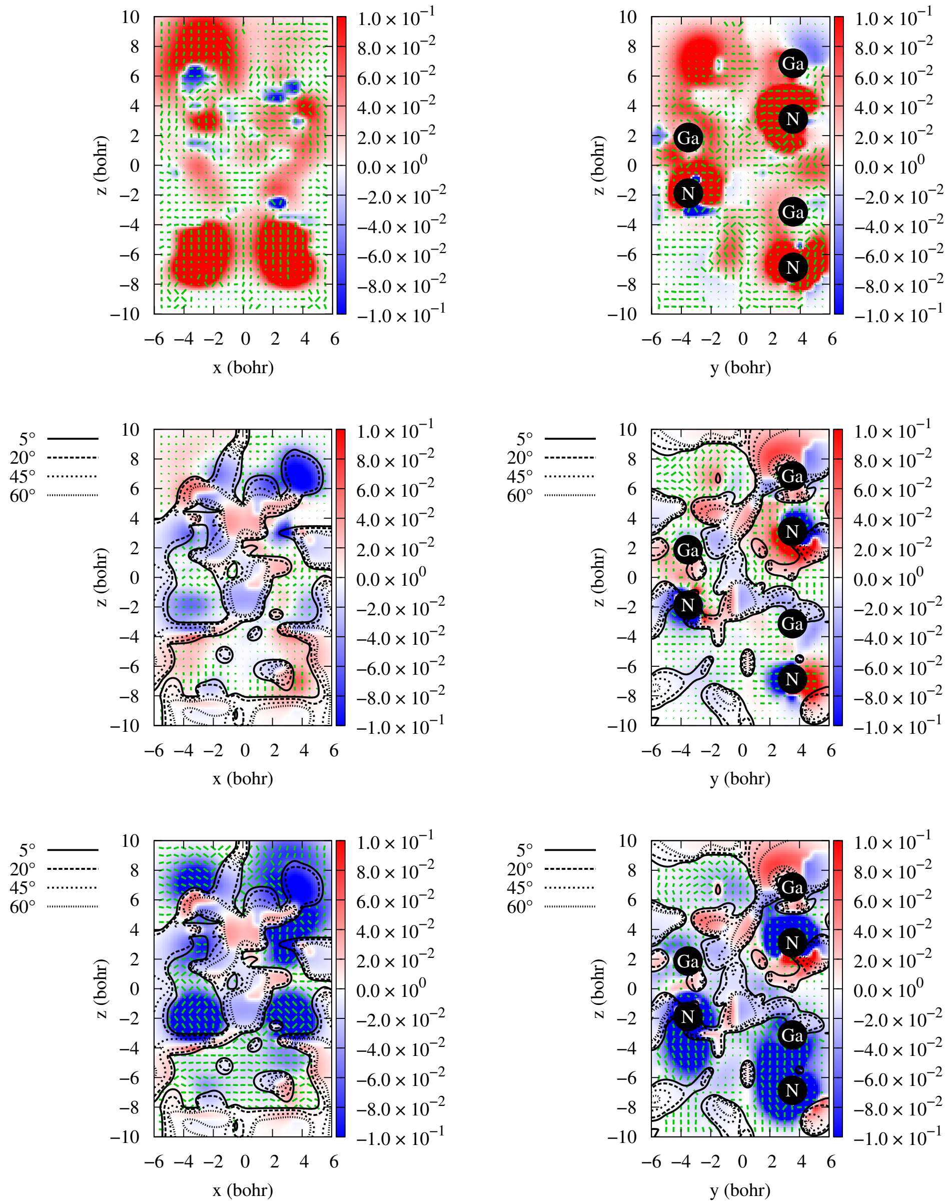

Figure 3.5: The three eigenvalues of the external conductivity density tensor. The left and right panels are results on $y = 0$ and $x = 0$ planes, respectively. The top, middle, and bottom panels are the first, second, and third eigenvalues, respectively. The eigenvalues are arranged as the descending order for real eigenvalues. For complex eigenvalues, which exist in contours, the two complex eigenvalues are assigned as the second and third ones. The short line segments show the direction of eigenvectors. The depth of color means the eigenvalues for real eigenvalues, while for complex ones, the color means the sign of the real part, the depth means the absolute value, and the contour means the arguments of complex eigenvalues.

of conductivity similar to that in this region is seen for the region where $z \gtrsim 2$ bohr around the Ga atom on the left side ($z \simeq 2$ bohr). As another feature, the regions around N atoms have large absolute values of eigenvalues. Compared with Fig. 3.3, this feature is seen to be related to the electron density. The strong response around these regions to an external electric field is attributed to larger electron density. In addition to the response by the large number of electrons, electrons in these regions have weak electric potential by N nuclei, due to the screen effect by the large number of electrons. Hence, the move of these electrons are easier than other regions.

We consider that some qualitative results are reasonable and appropriate in spite of small model and small basis sets, while many uncertainties remain for quantitative ones. Hence, it is desirable that these properties will be confirmed by the calculations with longer models and larger basis sets.

3.5 Summary and Discussion

We have shown the validity of our local conductivity density analysis method by using a GaN cluster model, which is motivated to imitate GaN nanowire. We have discussed conductive properties of GaN nanowire speculated from our cluster model by our new code, which can represent electronic current as quantum states. The properties are analyzed by one of our novel quantity, the external local conductivity density tensor. The local conductivity shows some reasonable conductive properties. For example, the conductive path between atoms next to each other is clarified. In addition, the rotational behavior of conductivity has been found as complex values of eigenvalues. This behavior can only be studied by the analysis using a tensor.

In this work, we have taken only two values of external electric fields. Since the conductivity can depend on external fields, we will investigate the relation between the local conductivity and values of external fields. In addition, the basis set is not large enough to represent conductive electrons precisely, and hence we should confirm our results by larger basis sets in future works. In this work, the electronic current is injected by hand as a conductive state of plain waves. To derive a more appropriate current state for systems, we should improve the calculation code to realize conductive electronic states by more suitable

boundary conditions.

Reference

[1] Y. Cui and C. M. Lieber, Science **291**, 851 (2001).

[2] D. Wang, J. G. Lu, C. J. Otten, and W. E. Buhro, Appl. Phys. Lett. **83**, 5280 (2003).

[3] D. Wang, C. J. Otten, W. E. Buhro, and J. G. Lul, IEEE Trans. Nanotechnol. **3**, 328 (2004).

[4] D. Kang, J.-H. Ko, E. Bae, J. Hyun, W. Park, B.-K. Kim, J.-J. Kim, and C. Lee, J. Appl. Phys. **96**, 7574 (2004).

[5] H. Y. Cha, H. Wu, S. Chae, and M. G. Spencer, J. Appl. Phys. **100**, 024307 (2006).

[6] W. M. Zhou, F. Fang, Z. Y. Hou, L. J. Yan, and Y. F. Zhang, IEEE Electron Device Lett. **27**, 463 (2006).

[7] Y. Cui, L. J. Lauhon, M. S. Gudiksen, and J. Wang, Appl. Phys. Lett. **78**, 2214 (2001).

[8] Y. Wu, Y. Cui, L. Huynh, C. J. Barrelet, D. C. Bell, and C. M. Lieber, Nano Lett. **4**, 433 (2004).

[9] V. Schmidt, S. Senz, and U. Gösele, Nano Lett. **5**, 931 (2005).

[10] S. D. Suk, S.-Y. Lee, S.-M. Kim, E.-J. Yoon, M.-S. Kim, M. Li, C. W. Oh, K. H. Yeo, S. H. Kim, D.-S. Shin, K.-H. Lee, H. S. Park, J. N. Han, C. J. Park, J.-B. Park, D.-W. Kim, D. Park, and B.-I. Ryu, IEDM Tech. Dig. 2005, p. 735.

[11] H. Lee, L.-E. Yu, S.-W. Ryu, J.-W. Han, K. Jeon, D.-Y. Jang, K.-H. Kim, J. Lee, J.-H. Kim, S. Jeon, G. Lee, J. Oh, Y. Park, W. Bae, H. Lee, J. Yang, J. Yoo, S. Kim, and Y.-K. Choi, Tech. Dig. VLSI Symp, 2006, p. 58.

[12] K. Doi, Y. Mikazuki, S. Sugino, T. Doi, P. Szarek, M. Senami, K. Shiraishi, H. Iwai, N. Umezawa, T. Chikyo, K. Yamada, and A. Tachibana, Jpn. J. Appl. Phys. **47**, 205 (2008).

[13] P. Szarek, Dr. thesis, Kyoto University, Kyoto (2008) [http://hdl.handle.net/2433/66212].

[14] A. Fukushima, M. Senami, Y. Tsuchida, and A. Tachibana, Jpn. J. Appl. Phys. **49**, 111504 (2010).

[15] A. Fukushima, S. Sugino, Y. Tsuchida, M. Senami, and A. Tachibana, Jpn. J. Appl. Phys. **49**, 121504 (2010).

[16] A. Tachibana, J. Mol. Modeling **11**, 301 (2005).

[17] A. Tachibana, J. Mol. Struct.: THEOCHEM **943**, 138 (2010).

[18] M. Senami, Y. Ikeda, A. Fukushima, and A. Tachibana, Jpn. J. Appl. Phys. **49**, 115002 (2010).

[19] M. Senami, J. Nishikawa, T. Hara, and A. Tachibana, J. Phys. Soc. Jpn. **79**, 084302 (2010).

[20] A. Fukushima, K. Doi, M. Senami, and A. Tachibana, J. Power Sources **184**, 60 (2008).

[21] A. Fukushima, K. Hirai, M. Senami, and A. Tachibana, Surf. Sci. **604**, 1718 (2010).

[22] A. Tachibana, Theor. Chem. Acc. **102**, 188 (1999).

[23] A. Tachibana, J. Chem. Phys. **115**, 3497 (2001).

[24] A. Tachibana, in *Stress Induced Phenomena in Metallization*, edited by S. P. Baker (American Institute of Physics, New York, 2002) p. 205.

[25] A. Tachibana, in *Reviews in Modern Quantum Chemistry: A Celebration of the Contributions of Robert Parr*, edited by K. D. Sen (World Scientific, Singapore, 2002) Vol. 2, p. 1327.

[26] A. Tachibana, in *Fundamental World of Quantum Chemistry: A Tribute to the Memory of Per-Olov Löwdin*, edited by E. J. Brändas and E. S. Kryachko (Kluwer, Dordrecht, 2003) Vol. 2, p. 211.

[27] A. Tachibana, Int. J. Quantum Chem. **100**, 981 (2004).

[28] A. Tachibana and R. G. Parr, Int. J. Quantum Chem. **41**, 527 (1992).

[29] A. Tachibana, Int. J. Quantum Chem., Quantum Chem. Symp. **21**, 181 (1987).

[30] P. Szarek, Y. Sueda, and A. Tachibana, J. Chem. Phys. **129**, 94102 (2008).

[31] A. Tachibana, Int. J. Quantum Chem. **57**, 423 (1996).

[32] A. Tachibana, K. Nakamura, K. Sakata, and T. Morisaki, Int. J. Quantum Chem. **74**, 669 (1999).

[33] T. H. Dunning Jr, P. J. Hay, in *Modern Theoretical Chemistry*, edited by H. F. Schafer III (Plenum, New York, 1976) Vol. 3, p. 1.

[34] P. J. Hay and W. R. Wadt, J. Chem. Phys. **82**, 270 (1985).

[35] P. J. Hay and W. R. Wadt, J. Chem. Phys. **82**, 284 (1985).

[36] P. J. Hay and W. R. Wadt, J. Chem. Phys. **82**, 299 (1985).

[37] M. M. Francl, W. J. Petro, W. J. Hehre, J. S. Binkley, M. S. Gordon, D. J. DeFrees, and J.A. Pople, J. Chem. Phys. **77**, 3654 (1982).

[38] M. Senami, K. Ichikawa, K. Doi, P. Szarek, K. Nakamura, and A. Tachibana, Molecular Regional DFT program package, ver. 3 (Tachibana Lab., Kyoto University, Kyoto, 2008).

Chapter 4

Nanosize Electronics Material Analysis by Local Quantities Based on the Rigged QED Theory

4.1 Introduction

We propose the novel analysis method, using the novel local quantity. In this article, we introduce two types of analysis method. One is the spin torque and the zeta force, which are related to the dynamics of the electron spin. Hence, these quantities are especially related to the spintronics. The other is the conductivity. The microscopic viewpoint is important for the analysis of nanosize material.

The control of electron spin becomes more and more important recently. The spin quantum number is widely used in many fields of research and technology, for example, spintronics. In order to control the spin of specific electron in atoms or molecules, the knowledge of the torque for the spin of these electrons is inevitably important. However, we have not established the way to estimate the torque for the spin, though some works tackle this issue [1]. In this article, we propose the novel theoretical approach to predict the torque for spin. One of the authors proposed previously the novel quantities of the spin torque and the zeta force [2]. These quantities are the torque for electronic spin and govern the motion of the spin of electrons. Therefore, the essential description of the dynamics of the spin can be clarified by our approach. Hence, these quantities are widely applicable to spin

phenomenology in various fields. For example, to analyze or design spin electronics devices, we may use these quantity and control electronic spin in the devices. In this article, the spin torque and zeta force are shown for the dimer of alkali atoms. To derive these quantities, we use Molecular Regional DFT (MRDFT) program package [3], which developed in our laboratory. In this work, we consider the stationary spin state as a first step. The stationary spin state is maintained by the balance between the spin torque and the zeta force. We clarify the relation of the torque for spin to the bonding states.

Recently, the semiconductor Integrated Circuits (ICs) have been downsized rapidly. To achieve further downsizing beyond the Moore's law, field effect transistors (FETs) with semiconductor nanowires are proposed [4]. Especially, silicon nanowires are the most hopeful materials. For nanoscale materials like silicon nanowires, the prediction of physical properties by electronic state calculations is important. In this article, we report the analysis method of electron transport properties by first-principles calculations. For this purpose, we investigate electron transport properties by the local electrical conductivity obtained by the first-principles calculations which treat conduction electrons as quantum states. The local electrical conductivity can clarify the currents of the electrons which move around the vicinity of atoms. This property is useful for the investigation of the effect of defects and dopants on carrier transport properties. In this article, we show our results for small silicon nanowire model favored by the calculations for the band structures. In particular, we mention the difference of the external and internal local electrical conductivity, which are defined for the external electric field and the local electric field including the effect of the polarization, respectively. We also stress the importance of the treatment of the conductivity as a tensor for nanosize materials.

4.2 Theory

4.2.1 Spin torque and zeta force

In this work, the spin of electrons is discussed in relativistic theory since the degree of freedom of the spin can essentially be described only in the relativistic theory. The spin

angular momentum density operator is given by,

$$\frac{1}{2}\hbar\hat{\sigma}_e^k(\vec{r}) = \frac{1}{2}\hbar\hat{\psi}^\dagger(\vec{r})\sigma^k\hat{\psi}(\vec{r}), \tag{4.1}$$

where $k = 1-3$. In the relativistic theory, $\hat{\psi}$ is the four component spinor. Hence, the Pauli matrix σ^k is extended to 4×4 matrix. The equation of motion of the spin angular momentum density is given by

$$\frac{\partial}{\partial t}\left[\frac{\hbar}{2}\hat{\sigma}_e^k(\vec{r})\right] = \hat{t}_e^k(\vec{r}) + \hat{\zeta}_e^k(\vec{r}), \tag{4.2}$$

where the first term is the spin torque and the second one is the zeta force [2]. The spin torque is defined by using the relativistic stress tensor density operator,

$$\hat{t}_e^k(\vec{r}) = -\epsilon_{lnk}\hat{\tau}_e^{\Pi ln}(\vec{r}). \tag{4.3}$$

The relativistic stress tensor density operator is given by

$$\hat{\tau}_e^{\Pi kl}(\vec{r}) = \frac{i\hbar c}{2}\left[\hat{\bar{\psi}}(\vec{r})\gamma^l\hat{D}_k(\vec{r})\hat{\psi}(\vec{r}) - \hat{D}_k^\dagger(\vec{r})\hat{\bar{\psi}}(\vec{r})\gamma^l\hat{\psi}(\vec{r}).\right]. \tag{4.4}$$

This stress tensor density is known to classify the properties of chemical bonding [5]. This relativistic stress tensor is not symmetric tensor for the exchange of indices k and l. On the other hand, the nonrelativistic stress tensor is symmetric, and hence, the spin torque is derived only in the relativistic theory. The other term is the zeta force,

$$\hat{\zeta}_e^k(\vec{r}) = -c\partial_k\left[\hat{\bar{\psi}}(\vec{r})\gamma^k\frac{1}{2}\hbar\sigma^l\hat{\psi}(\vec{r}).\right], \tag{4.5}$$

where the multiple appearance of the index k does not means the summation. After easy algebra, the zeta force and the spin torque are derived as the product of the large and small components of a four component wave function.

In this work, only the steady states of the spin are considered. In the steady states, the expectation value of the spin angular momentum density operator should be independent of the time. Accordingly, the spin torque should be in balance with the zeta force in the steady states. We can interpret the stability of the spin vector of an electron by this balance. This stability is similar to the balance between the Lorentz force and the tension force [5], which may explain the quantum condition, such as the stability of the electronic energy level in atoms. In an unsteady state of the spin, this balance is no longer maintained. The unsteady state is realized, for example, by the existence of an external magnetic field. Hence, the electronic structure calculation with an external magnetic field will clarify a torque to rotate the spin vector of an electron. This work is a first step to this goal.

4.2.2 Local conductivity

The electronic charge current density is given by using the local value of the probability current [1],

$$\hat{\vec{J}}(\vec{r}) = \frac{Z_e e}{2m_e}\left[\hat{\psi}^\dagger(\vec{r})\hat{\vec{p}}(\vec{r})\hat{\psi}(\vec{r}) + h.c.\right] \tag{4.6}$$

$$= \frac{Z_e e}{2m_e}\left[-i\hbar\hat{\psi}^\dagger(\vec{r})\vec{\nabla}(\vec{r})\hat{\psi}(\vec{r}) - \frac{Z_e e}{c}\hat{\psi}^\dagger(\vec{r})\vec{A}(\vec{r})\hat{\psi}(\vec{r}) + h.c.\right]. \tag{4.7}$$

The current induces a magnetic field, i.e., vector potential. This induced vector potential is given as,

$$\hat{\vec{A}}(ct,\vec{r}) = \frac{1}{c}\int d^3\vec{s}\,\frac{\hat{\vec{J}}_T(cu,\vec{s})}{|\vec{r}-\vec{s}|}, \tag{4.8}$$

where subscript T means the transverse component and u includes the retardation effects. Next, we explain the formulation of the electric conductivity operator. The linear response of electrons in a system is defined by using the local electrical conductivity tensor,

$$\hat{\vec{J}}(\vec{r}) = \hat{\overleftrightarrow{\sigma}}_{\mathrm{ext}}(\vec{r})\hat{\overleftrightarrow{\epsilon}}(\vec{r})\hat{\vec{E}}(\vec{r}) \tag{4.9}$$

$$= \hat{\overleftrightarrow{\sigma}}_{\mathrm{int}}(\vec{r})\hat{\vec{E}}(\vec{r}). \tag{4.10}$$

The ordinary electrical conductivity is defined as a global constant for a material. However, the averaged property, such as global constants, is insufficient for the description of the conductive property of the nanoscale material. Hence, we should treat the conductivity as the local quantity. The external electric field is related to the electric field included the effect of the internal polarization by the dielectric constant. Hence, the first and second equations mean the linear response to the external and internal electric fields. These conductivity operators are Hermite, and all elements in these tensors are real. However, these tensors are not symmetric matrices. Therefore, three eigenvalues of these tensors are derived as three real numbers or one real and two complex numbers. The case of the complex eigenvalues shows remarkable feature. Even if the direction of the eigenvector is chosen as that of the electric field, the response is rotated to other direction. This rotational response cannot correctly be described if the conductivity or dielectric constant is treated as scalar quantity.

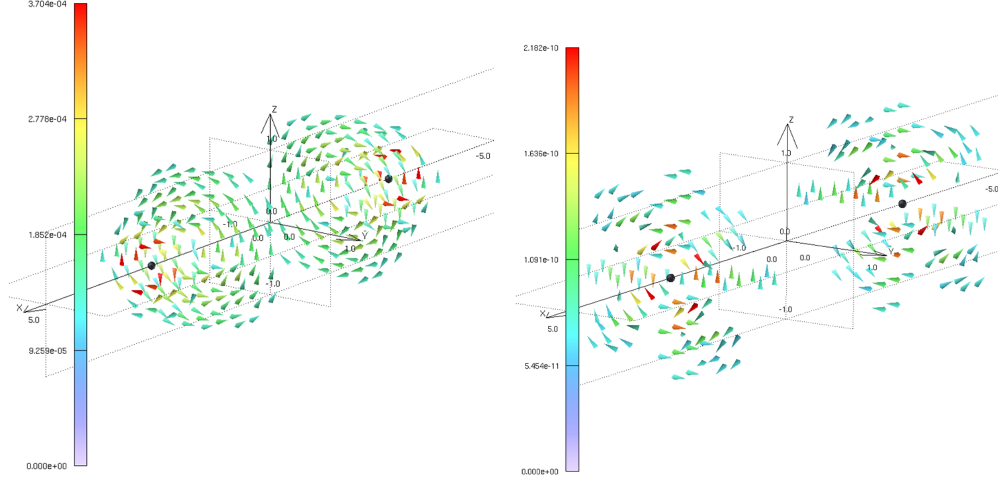

Figure 4.1: The spin torque (left) and the zeta force (right) of the lithium dimer. The unit of the axes are angstrom, and the unit of the spin torque and the zeta force are the atomic unit.

4.3 Results

4.3.1 Spin torque and zeta force

The spin torque and zeta force of D =2.8, 3.2, 4.2, and 4.8 Angstrom (D is the distance between atoms.) for the ground state of the dimmers of lithium, sodium, potassium and rubidium are shown with three dimensional representation in Figs. 4.1, 4.2, 4.3 and 4.4, respectively. The left panel is the results of the spin torque, while the right one is the results of the zeta force.

The spin torque and the zeta force are localized around the atoms and disappears on the x=0 plane, which is equidistant from the two atoms, for all models. The rotational pattern of the spin torque can be seen around the x axis for all atoms, and it is not seen for other directions. The rotational pattern around two nuclei has the opposite directions of the rotation. For all four models, the rotational and distribution patterns are almost the same. On the other hand, the zeta force of potassium dimer is significantly different from the others. The other three results are similar to each other. These results show rotational pattern around the nuclei. The pattern for that of the other atom has the opposite direction, which are the same feature for the spin torque. However, the pattern is significantly different from that of the spin torque in the region apart from the x axis. In the region, even the

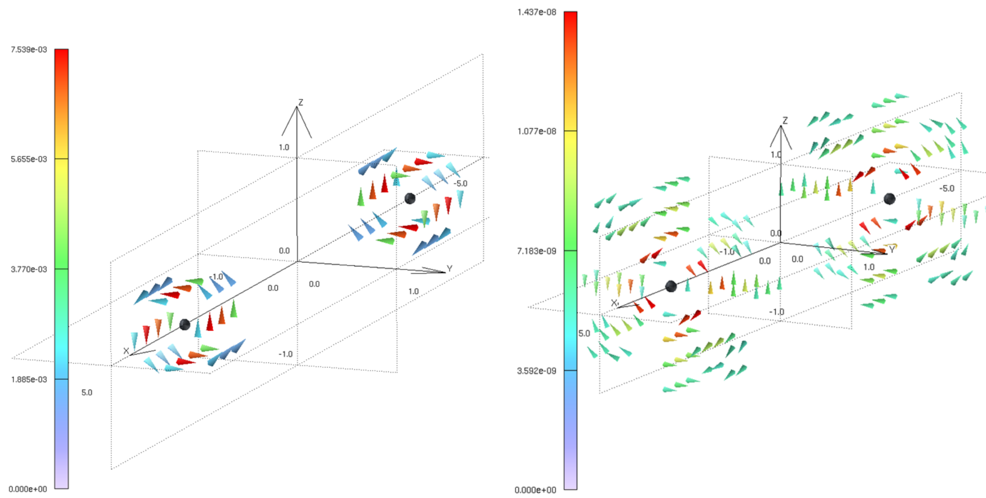

Figure 4.2: The spin torque (left) and the zeta force (right) of the sodium dimer. The unit of the axes are angstrom, and the unit of the spin torque and the zeta force are the atomic unit.

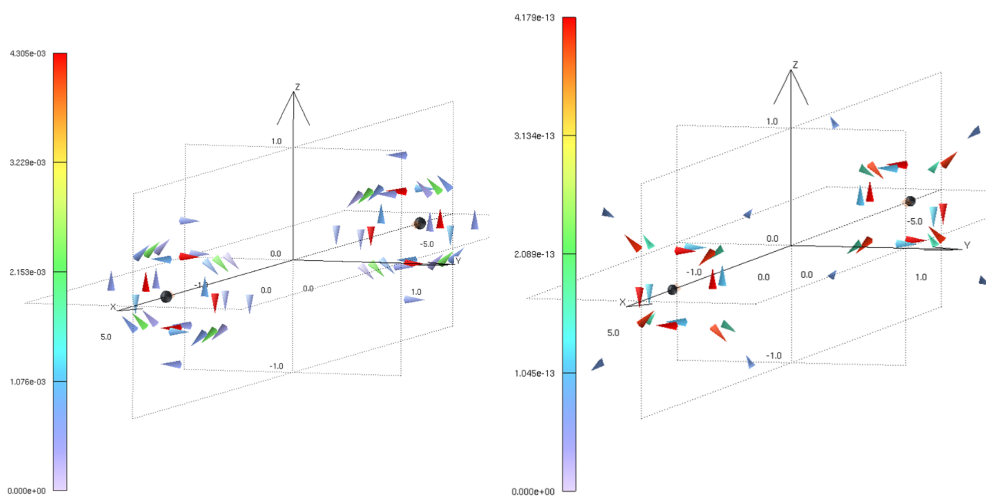

Figure 4.3: The spin torque (left) and the zeta force (right) of the potasium dimer. The unit of the axes are angstrom, and the unit of the spin torque and the zeta force are the atomic unit.

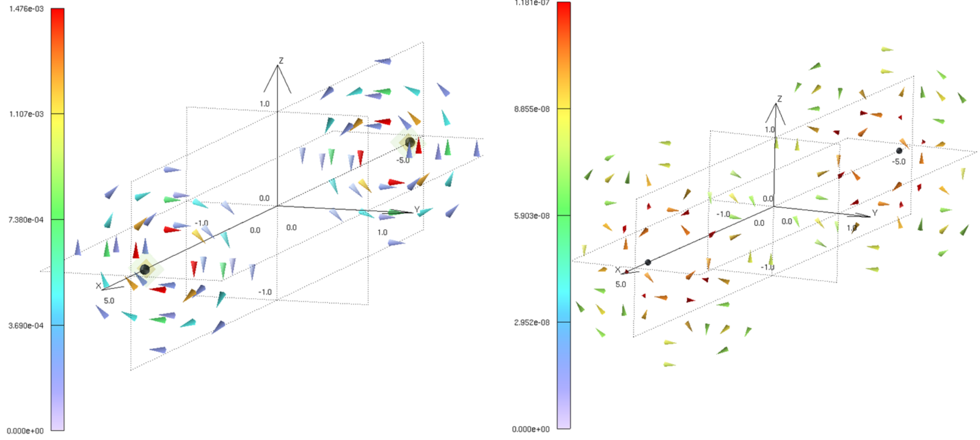

Figure 4.4: The spin torque (left) and the zeta force (right) of the rubidium dimer. The unit of the axes are angstrom, and the unit of the spin torque and the zeta force are the atomic unit.

rotational pattern cannot be seen, and the vectors of zeta force face each other in some place. Since the value of the zeta force for the region is small, the analysis of three dimensional pattern of the zeta force may require more accurate calculation, unfortunately. In other words, the rotational pattern of the zeta force is found by our results.

The values of the spin torque and the zeta force are different by several orders of magnitude. The reason why the spin torque and the zeta force are not in balance within this calculation is discussed in Ref. 6. The similarity of the rotational and distribution patterns between the dimers of alkali atoms except for potassium is attributed to the similarity of the electronic states of these atoms. However, the values of the spin torque and the zeta force are significantly different between them.

The electron spin rotates in the unsteady state by the existence of an external magnetic field. Then, the torque for the electron spin can be described by the spin torque, which is dependent on the vector potential, while the zeta force is not. Hence, the balance between the spin torque and the zeta force are not maintained. Hence, in the future work, the electronic structure calculation with an external magnetic field will be tackled for the clarification of the torque to rotate the electron spin.

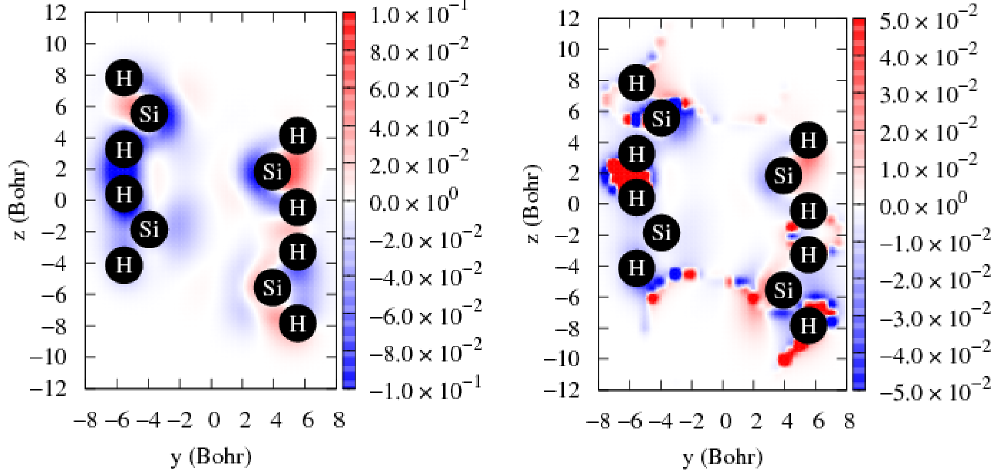

Figure 4.5: The external conductivity (left) and the internal conductivity (right) of the silicon nanowire model. Only the zz component of conductivity tensors is shown.

4.3.2 Local conductivity

We discuss the local electrical conductivity for small [011] silicon nanowire models. Figure 4.5 shows the zz component of the external and internal local conductivity of silicon nanowire model. This conductivity is defined as the difference between the results of the external electric field, 0.002 a.u. and 0.001 a.u. The difference between them can be clearly seen. This result shows that the internal electric field including the internal polarization should be considered for nanoscale materials.

Figure 4.6 shows the three eigenvalues of the external conductivity tensor of silicon nanowire model. For real parts, the first eigenvalue is much larger values than the others. We speculate that this is due to the quantum confinement effect of one dimensional structure. We can also see that the electrical conductivity show the complex values in many regions. In the regions, linear response for the complex conductivity gives the rotational response. Particularly, the complex values appear around atoms. We speculate that the electric fields by nuclei produce complicated conductivity in silicon nanowire model. As a result, we emphasize that this result can be seen only when the electrical conductivity is treated as tensor. Hence, we should treat conductivity as tensor, even for the material with the isotropic dielectric constant as macroscopic property.

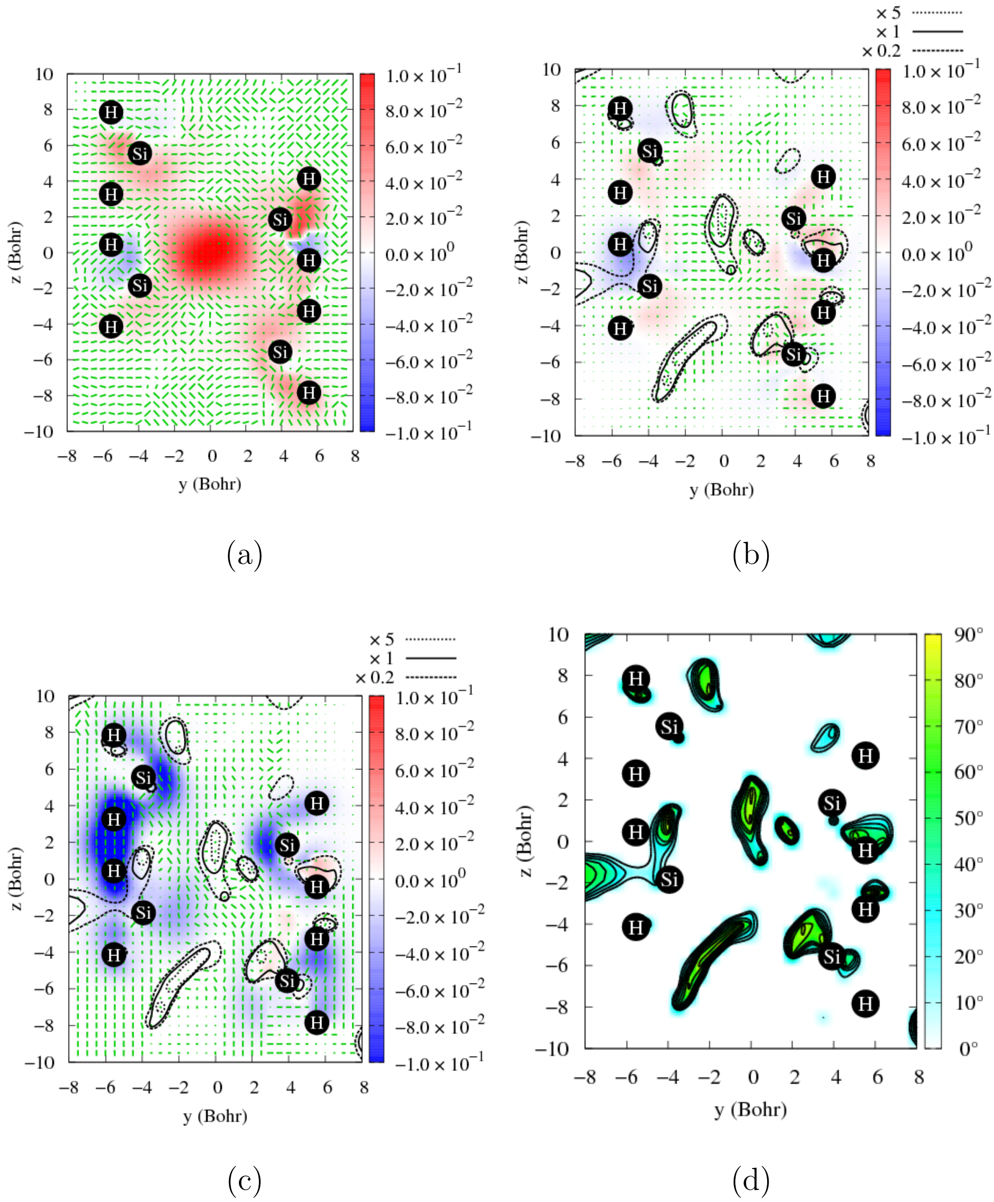

Figure 4.6: The first(a), second(b), and third(c) eigenvalues and rotational parameters(d) of the external local electrical conductivity tensor for the [011] silicon nanowire with H termination. The red (blue) color shows the positive (negative) value of the eigenvalues. The black lines show the ratio of the imaginary parts of the eigenvalues to the real parts of them. The green lines show the directions of eigenvectors. The rotational parameters (d) mean the absolute values of the arguments of the complex eigenvalues. The eigenvalues are sorted into the descending order. If there are complex eigenvalues, they are shown as the second and third eigenvalues.

4.4 Summary

In this article, we have introduced the two novel analysis methods by using the novel local quantities. One is the spin torque and the zeta force, which essentially clarify the dynamics of the electron spin. The other is the external and internal local conductivities. As a first step, we have shown the validity and usefulness of our methods. The zeta force clarifies how the local torque works on the electron spin in molecules. The external and internal local conductivities show how electrons pass through nanosize materials and how electrons are locally accelerated in the materials.

Reference

[1] For example see, D.C. Ralph and M.D. Stiles, J. Magn. and Magn. Mater. **320**, 1190 (2008).

[2] A. Tachibana, J. Mol. Model. **11**, 301 (2005); J. Mol. Struct.: THEOCHEM **943**, 138 (2010).

[3] M. Senami, K. Ichikawa, K. Doi, P. Szarek, K. Nakamura and A. Tachibana, Molecular Regional DFT program package, ver. 3 (Tachibana Lab., Kyoto University, Kyoto, 2008).

[4] S.D. Suk, S.-Y. Lee, S.-M. Kim, E.-J. Yoon, M.-S. Kim, M. Li, C.W. Oh, K.H. Yeo, S.H. Kim, D.-S. Shin, K.-H. Lee, H.S. Park, J.N. Han, C.J. Park, J.-B. Park, D.-W. Kim, D. Park and B.-I. Ryu, Tech. Dig. - Int. Electron Devices Meet. (2005), p. 735; H. Lee, L.-E. Yu, S.-W. Ryu, J.-W. Han, K. Jeon, D.-Y. Jang, K.-H. Kim, J. Lee, J.-H. Kim, S. Jeon, G. Lee, J. Oh, Y. Park, W. Bae, H. Lee, J. Yang, J. Yoo, S. Kim and Y.-K. Choi, Tech. Dig. VLSI Symp (2006), p. 58.

[5] A. Tachibana, Theor. Chem. Acc. **102**, 188 (1999); J. Chem. Phys. **115**, 3497 (2001); in *Stress Induced Phenomena in Metallization*, edited by S. P. Baker (AIP, New York, 2002), p. 205; in *Reviews in modern quantum chemistry: a celebration of the contributions of Robert Parr*, edited by K. D. Sen (World Scientific, Singapore, 2002), Vol. 2, p. 1327; Int. J. Quantum Chem. **57**, 423 (1996); ibid **100**, 981 (2004); ibid, Quantum Chem. Symp. **21**, 181 (1987); A. Tachibana, *et al.*, Int. J. Quantum Chem. **41**, 527 (1992); P. Szarek, *et al.*, J. Chem. Phys. **129**, 94102 (2008); A. Tachibana, *et al.*, Int. J. Quantum Chem. **74**, 669 (1999).

[6] M. Senami, J. Nishikawa, T. Hara and A. Tachibana, J. Phys. Soc. Jpn., **79**, 084302 (2010).

Part II

Theoretical Studies on Functional Materials in Terms of Their Bonding Nature

Chapter 5

Theoretical Study of Gallium Nitride Crystal Growth Reaction Mechanism

5.1 Introduction

Rapid progress in the metalorganic chemical vapor deposition (MOCVD) technology makes it possible to fabricate high quality gallium nitride (GaN) based devices under the condition of atmospheric pressure [1]. GaN, which has wide band gap energy, is currently paid great attention due to its potential ability in optoelectronics and microelctronics, such as light-emitting diodes, laser diodes, and photodetectors [2, 3]. For a commercial use of this material, the fabrication of high quality GaN single crystal is required. It is already known that high NH_3 partial pressure and high temperature (1300-1400 K) are desirable as a steady growth condition of GaN. In order to improve the quality of fabricated GaN crystal, we should study how the crystal of GaN grows.

The stability of GaN crystal is dependent on its surface aspect, and GaN surfaces show several types of growth mechanism [4]. Besides the surface dependence, chemical reactions which progress in the gas phase have important roles in the crystal growth. Hence, it is important for the growth of GaN crystal that both reactions on the surface and in the gas phase are under the control, though this control is very difficult. It is required to understand the mechanism of the surface and gas-phase reactions. Recently, many researchers study the mechanism by experimental analysis and computational simulation.

In our previous studies [5–10], we discussed parasitic reactions of trimethylgallium (TMG)

and trimethylaluminum in the gas phase, which disturbed the growth of AlGaN single crystals. In these works, it has been found that there is no energy barrier for the reaction,

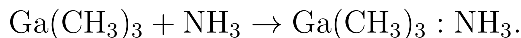

$$\mathrm{Ga(CH_3)_3 + NH_3 \rightarrow Ga(CH_3)_3 : NH_3}.$$

Therefore, parasitic reactions easily occur, so that they may affect the growth of GaN crystal as well as AlGaN. It has also been found that the activation energy required for the reaction,

$$\mathrm{Ga(CH_3)_3 + NH_3 \rightarrow Ga(CH_3)_2(NH_2) + CH_4},$$

is 14.8 kcal/mol (0.64 eV) [7]. This activation energy is not so large that substitution reactions also occur.

In this work, we analyze both gas-phase and surface reactions on the growth of GaN crystal by *ab initio* calculations. We consider the initial surface for the GaN crystal growth and adsorptions of various compounds of Ga and N atoms on the surface. The effect of a Ga-Ga bond formed on the GaN(0001) surface on the crystal growth is investigated in detail. Then, we suggest reaction processes avoiding the Ga-Ga bond.

5.2 Computational Methods

5.2.1 Gas-phase reactions

Before the analysis of chemical reactions occurred on the GaN(0001) surface, we need to know what molecules exist in the gas phase. Therefore, we first study gas-phase reactions in detail. We perform *ab initio* quantum chemical calculations of equilibrium structures of molecules in the gas phase. We also calculate transition states (TSs) to obtain the activation energies of the reactions. All the geometries are fully optimized using the density functional theory (DFT) based on the Lee-Yang-Parr gradient-corrected functional [11, 12] with Becke's three hybrid parameters [13] (B3LYP). In this calculation, the Dunning-Huzinaga double-zeta basis set [14] with effective core potential by Hay and Wadt [15–17] (LanL2DZ) are used for Ga atoms. On the other hand, D95** [14] basis set is employed for the other atoms. Vibrational frequency analysis is performed to calculate zero-point energy correction. These calculations are performed by Gaussian 09 program package [18].

5.2.2 Surface reactions

To simulate surface reactions, cluster models are used. However, we also use periodic model to decide the optimized structure of the initial surface for the GaN crystal growth (and which surface is more stable, Ga or N), and to check whether cluster models realize a feature of bulk crystal.

As the periodic model, a 2×2 periodic surface on the GaN(0001) wurtzite structure is considered. Lattice constants for initial atom positions of our GaN surface model are determined by our calculation of the optimized GaN bulk structure. The GaN surface model consists of six layers and vacuum thicker than 11 Å. The top layer of them is four Ga atoms, while the bottom one is N atoms, which are passivated with hydrogen atoms. For geometrical optimization calculations, the positions of atoms of two layers from the top are relaxed, and those of the others are fixed. First principles calculations of the periodic models are carried out by supercell approximation techniques, using CASTEP program package [19]. The electron-ion potential is described by Vanderbilt type ultra-soft pseudopotentials [20]. The generalized-gradient approximation (GGA) method by Perdew-Burke-Ernzerhof (PBE) [21] is employed for density functional exchange-correlation interactions. For the calculation of bulk crystal and those of surface, kinetic energy cutoff of plane-wave expansion (k-point) is taken as 800 eV (the 9×9×6 k-point set) and 280 eV (the 4×4×1 k-point set), respectively.

The density of state (DOS) of the GaN surface model is calculated for the model which consists of seven layers with periodic boundary conditions using ADF program package [22]. In this calculation, the GGA method by Perdew and Wang (PW91) [23] is employed for the density functional exchange-correlation interaction.

Electronic structure of GaN(0001) surface and its reactions are investigated in detail by using a cluster model. This cluster model is required to realize a large crystal surface. Hence, this cluster model needs to be sufficiently large in order to reproduce the electronic structure of models with periodic boundary condition. Calculations of this model are done by using the combined quantum mechanics and molecular mechanics (QM/MM) method [24–28], so called ONIOM method [29–32] of Gausssian 09 program package. In Fig. 5.1, we show this cluster model. The QM($Ga_{24}N_{24}$) and the MM($Ga_{141}N_{141}$) regions are shown in Figs. 5.1(a) and (b), respectively. This model consists of six layers. The MM region surrounds the QM region. In the geometrical optimization calculation, four Ga atoms in the top layer, four N

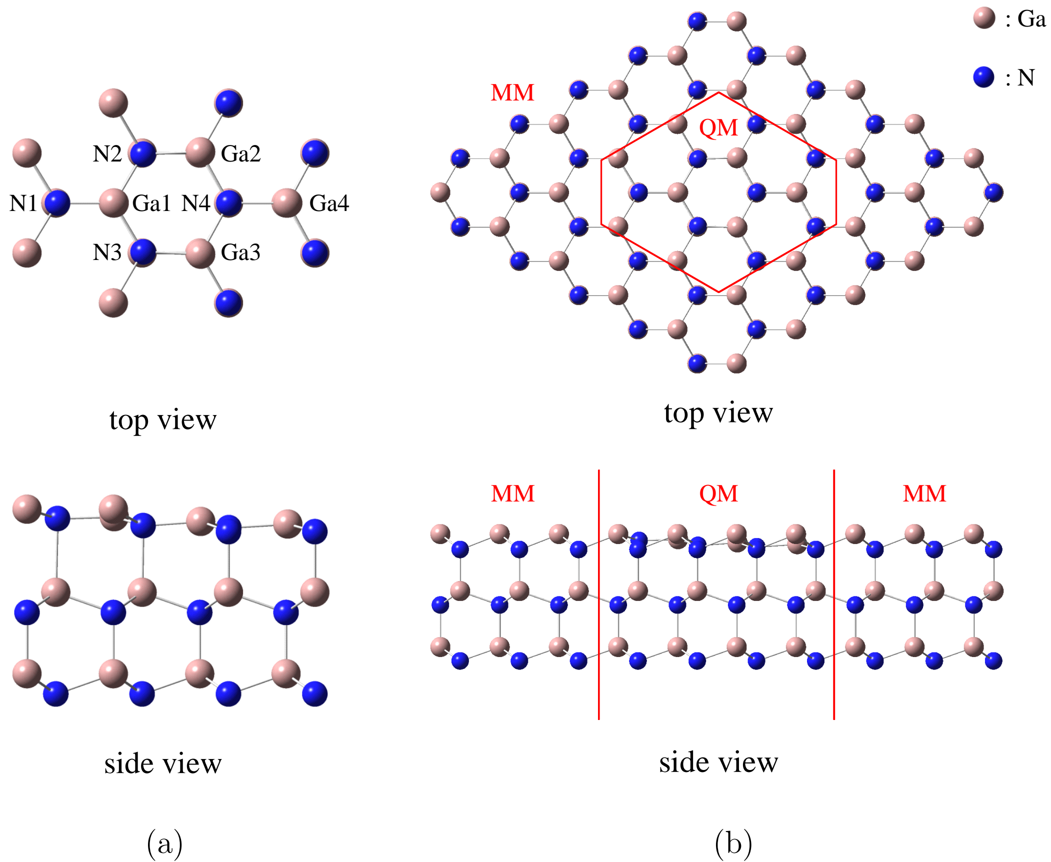

Figure 5.1: (a) QM and (b) MM regions of GaN(0001) cluster model.

atoms in the second layer [Ga1-4 and N1-4 in Fig. 1(a)], and admolecules are relaxed and the others are fixed. For the QM calculation, we use the DFT method based on B3LYP, and basis sets are chosen as LanL2DZ basis set for Ga atoms and D95** basis set for the others. The universal force field (UFF) method [33] is used for the calculation of the MM region.

Calculations for kinetic energy density as explained below are also carried out by extending QM region as including the atoms bonding to the atoms in the original QM region. In these calculations, other Ga and N atoms in the MM region are replaced by pointing charges. Ga (N) atoms are replaced by $+0.9e$ ($-0.9e$) point charges. These values of the point charge are determined in order to correspond to the average of the Mulliken charges [34] of the Ga atoms on the top surface layer.

5.2.3 Electronic quantum energy density

After electronic structure calculations, we analyze local electronic properties such as the electronic quantum energy density. According to the Rigged QED theory [35–41], the kinetic energy density $n_T(\mathbf{r})$ is given as follows:

$$n_T(\mathbf{r}) = \frac{1}{2}\sum_i \nu_i \left\{ \left[-\frac{\hbar^2}{2m}\Delta\psi_i^*(\mathbf{r}) \right] \psi_i(\mathbf{r}) + \psi_i^*(\mathbf{r}) \left[-\frac{\hbar^2}{2m}\Delta\psi_i(\mathbf{r}) \right] \right\}, \tag{5.1}$$

where m is the electron mass, $\psi_i(\mathbf{r})$ is ith natural orbital, and ν_i is the occupation number of $\psi_i(\mathbf{r})$. The integration of kinetic energy density over the whole space is the kinetic energy of a system. In classical mechanics, only positive kinetic energy is allowed, while negative kinetic energy appears in quantum mechanics. This means that electrons can also exist in regions with negative kinetic energy density by quantum effects. The surface of zero kinetic energy density can be interpreted as the boundary of the molecule. In this study, we show this value for the discussion whether atoms have a chemical bond or not. To calculate the kinetic energy density, we use Molecular Regional DFT program package [42].

5.3 Results and Discussion

5.3.1 Reaction pathway in the gas phase

For the comprehension of the growth of GaN crystal, it is important to understand gas-phase reactions. If we know the reactions well, we can know what molecules exist in the gas phase. Then, the knowledge let us speculate which molecules promote the growth of GaN by surface reactions.

Actually, it is known that many species of Ga compounds exist in the gas phase. Experimentally, gallium-nitrogen compounds made by alkylgallium and NH_3 molecules and molecules made by dissociation reactions of TMG were reported [43]. On the other hand, in computational simulation works by Kusakabe *et al.* [44], many reaction paths were studied and many compounds are reported such as GaN and TMG:NH_3. Unfortunately, experimental and theoretical results are not consistent sufficiently. Hence, we assume several promising reaction paths in the gas phase and investigate surface reactions for the paths.

In this work, it is assumed that TMG and NH_3 are used as Ga and N precursors, respectively. Many species of compounds of Ga and N atoms can be produced by reactions

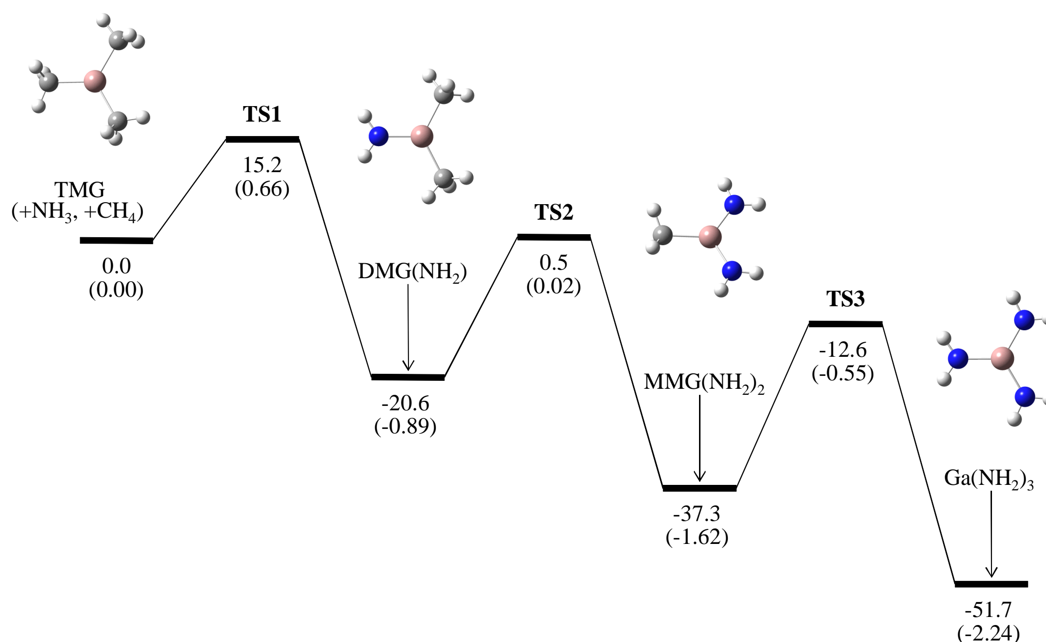

Figure 5.2: The relative potential energy diagram of gas-phase reactions. Values are written in kcal/mol (eV).

between TMG and NH_3 molecules. For example, they are produced by reactions that methyl groups of TMG are sequentially replaced by NH_2 groups [45]. In this work, we focus on these reactions. These reactions are summarized as follows:

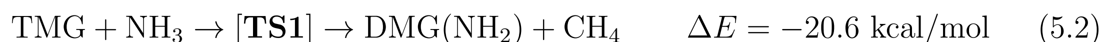

$$\mathrm{TMG} + \mathrm{NH_3} \rightarrow [\mathbf{TS1}] \rightarrow \mathrm{DMG(NH_2)} + \mathrm{CH_4} \qquad \Delta E = -20.6 \text{ kcal/mol} \tag{5.2}$$

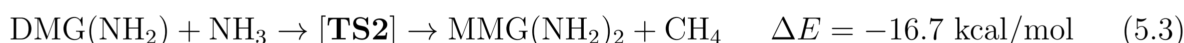

$$\mathrm{DMG(NH_2)} + \mathrm{NH_3} \rightarrow [\mathbf{TS2}] \rightarrow \mathrm{MMG(NH_2)_2} + \mathrm{CH_4} \qquad \Delta E = -16.7 \text{ kcal/mol} \tag{5.3}$$

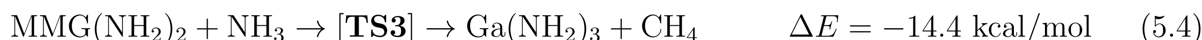

$$\mathrm{MMG(NH_2)_2} + \mathrm{NH_3} \rightarrow [\mathbf{TS3}] \rightarrow \mathrm{Ga(NH_2)_3} + \mathrm{CH_4} \qquad \Delta E = -14.4 \text{ kcal/mol} \tag{5.4}$$

Here, DMG (MMG) is a dimethyl (monomethyl) gallium. Figure 5.2 shows the relative potential energy diagram of these reactions. From this figure, we can see that all reactions are exothermic. As a result, we can find that $Ga(NH_2)_3$ is the most stable compound in this reaction chain. However, it is also found that activation energy of these reactions are 15.2 kcal/mol, 21.1 kcal/mol, and 24.7 kcal/mol, respectively. This result indicates that $Ga(NH_2)_3$ is the most difficult to be produced among $DMG(NH_2)$, $MMG(NH_2)_2$, and $Ga(NH_2)_3$. From another viewpoint, it can be said that if $Ga(NH_2)_3$ are sufficiently produced, $DMG(NH_2)$ and $MMG(NH_2)_2$ should be also produced in the gas phase.

Next, molecules which make the coordinate bond with NH_3 are considered. These gas-

phase reactions are given as follows:

$$\mathrm{TMG} + \mathrm{NH_3} \rightarrow \mathrm{TMG} : \mathrm{NH_3} \qquad \Delta E = -15.6 \text{ kcal/mol} \tag{5.5}$$

$$\mathrm{DMG(NH_2)} + \mathrm{NH_3} \rightarrow \mathrm{DMG(NH_2)} : \mathrm{NH_3} \qquad \Delta E = -12.6 \text{ kcal/mol} \tag{5.6}$$

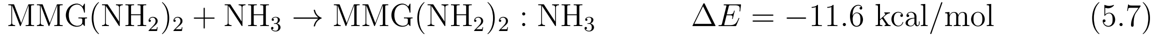

$$\mathrm{MMG(NH_2)_2} + \mathrm{NH_3} \rightarrow \mathrm{MMG(NH_2)_2} : \mathrm{NH_3} \qquad \Delta E = -11.6 \text{ kcal/mol} \tag{5.7}$$

The stabilization energies of TMG:NH_3, DMG(NH_2):NH_3, and MMG(NH_2):NH_3 are 15.6 kcal/mol (0.68 eV), 12.6 kcal/mol (0.55 eV), and 11.6 kcal/mol (0.51 eV), respectively. From this result, it can be found that these molecules are more stabilized than TMG, DMG(NH_2), and MMG(NH_2)$_2$. It can also be found that there is no activation energy for these reactions. Ga-N parts in cores of these molecules, which we call GaN core, are attached on the GaN surface and promote the GaN growth. In other words, it is supposed that two layers, namely Ga and N layers, are stacked simultaneously.

5.3.2 GaN(0001) surface structure

Before the analysis of the reactions on the GaN(0001) surface, we calculate optimized surface structures of Ga covered GaN(0001) surface to study surface reactions. As shown below, N covered surface is not suitable for a successful crystal growth.

First, we optimize the wurtzite GaN bulk structure, and their lattice constants are obtained as $a = 3.235$ Å, $c = 5.279$ Å. To investigate surface reactions, we make a surface model with these lattice constants. In Fig. 5.3(a), we show this model. This model is a 2×2 GaN(0001) surface model whose top layer consists of Ga atoms.

For this initial structure, we calculate the optimized structure of this surface model. As a result, the parameters of d_{12} and d_{23} are derived as 0.729 Å and 1.963 Å, respectively. In the following, we use this model as Ga-covered surface of the GaN crystal.

Next, we optimize the N-covered surface. In other words, we study the reaction between N atoms and Ga atoms on the surface. For this purpose, we consider a GaN(0001) surface model whose top Ga surface is terminated by N atoms. The structures before and after geometrical optimization are shown in Figs. 5.3(b) and (c), respectively. It can be seen that a N atom on the surface approaches another N atom. It is considered that N atoms of N adlayer make bonds with other N atoms of the adlayer. Thus, N atoms form dimers whose bond length is 1.27 Å. The optimized surface is more stabilized than the initial surface

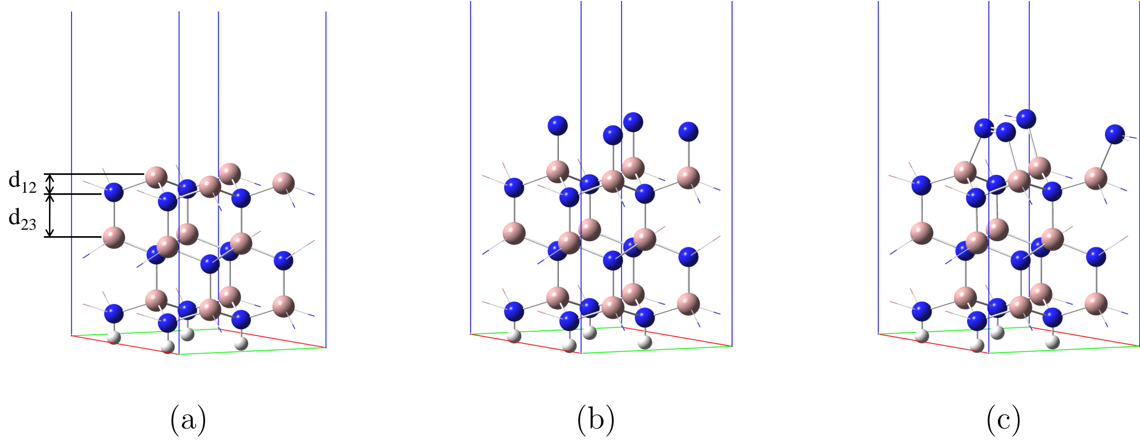

Figure 5.3: Structures of (a) Ga-covered GaN(0001) surface, (b) non-reconstructed N-covered surface, and (c) reconstructed N-covered surface.

shown in Fig. 5.3(b) by 302.7 kcal/mol (13.1 eV). Hence, we consider that this N-N bond is too strong for subsequent adsorption of Ga atoms, which inevitably requires to cut the bond. Therefore, N-covered surface interrupts the crystal growth. These results also suggest that adsorption of bare N atoms on the Ga-covered surface is not suitable for the growth of GaN.

Hence, in the next subsection, we consider the adsorption of compounds with Ga and N atoms on the Ga-covered surface as shown in Fig. 5.3(a), which we call GaN(0001) surface for abbreviation below.

5.3.3 Chemical reactions on the GaN surface

In § 5.3.1, we have chosen some reaction pathways to produce GaN cores in the gas phase. In this subsection, reactions between GaN(0001) surface and the GaN cores are investigated. To study the reactions in detail, we use a large surface cluster model which has electronic properties similar to a GaN(0001) surface periodic model.

Electronic state of GaN(0001) cluster model

We have made the GaN surface cluster model shown in Fig. 5.1. To check whether this cluster model has properties similar to the 2×2 periodic GaN(0001) surface model, we compare the electronic structure of the cluster model with that of the periodic model calculated

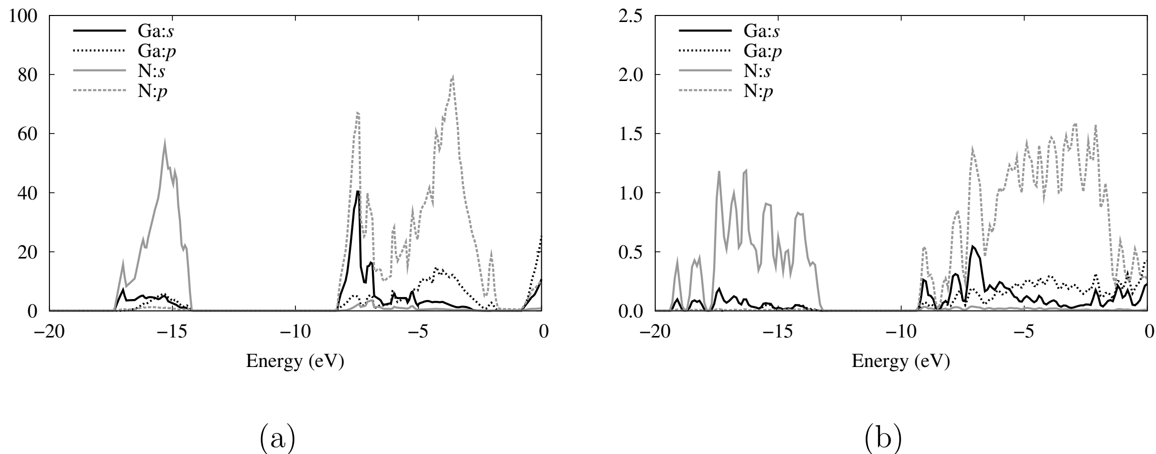

Figure 5.4: (a) PDOS of the periodic model. Fermi energy level is set as 0 eV. (b) GPDOS of the cluster model. The highest occupied energy level is set as 0 eV.

by ADF program package. Figures 5.4(a) and (b) show the partial DOS (PDOS) of the periodic model and the gross population DOS (GPDOS) of the cluster model, respectively. By comparing these results, it is found that both electronic structures have various common features. First, these electronic structures are divided into two regions dominated by N(s) or N(p). Second, N(p) region consists of two parts. In higher energy level of this region, the contribution from Ga is mainly occupied by Ga(p), while that is mainly from Ga(s) in lower one. Third, near the Fermi level (0 eV), namely in the highest orbital energy level, Ga orbitals have larger contribution to occupation than N orbitals. From these similarities, we consider that our GaN cluster model reproduces properties of the periodic model. Therefore, we can take this model as a reference model to study the GaN surface.

Adsorption reaction of $Ga(NH_2)_3$

First, we calculate the adsorption reaction of $Ga(NH_2)_3$. This reaction is represented as follows:

$$Ga(NH_2)_3 + GaN(0001) \rightarrow Ga(NH_2)_3/GaN(0001) \qquad \Delta E = -78.8 \text{ kcal/mol} \qquad (5.8)$$

Figure 5.5 shows the optimized structure of $Ga(NH_2)_3$/GaN(0001). The Ga-N bond length between the surface and the admolecule is 1.98 Å and the length of Ga-N bond in the admolecule is 2.22 Å. For comparison, we calculated the same reaction for the periodic

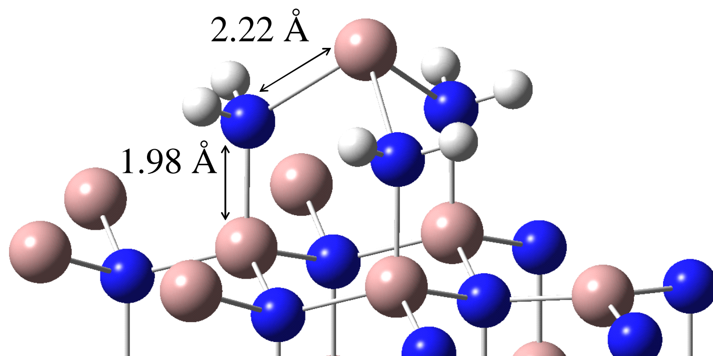

Figure 5.5: Optimized structure of $Ga(NH_2)_3/GaN(0001)$ in the cluster model.

model and two Ga-N bond lengths were 1.96 and 2.19 Å. The values of the cluster model are close to these values. This confirms again that our surface cluster model reproduces the features of the periodic model for adsorption reactions. The Ga atom at the top of this model is considered to be a new Ga-terminated GaN(0001) surface. Three amino groups of $Ga(NH_2)_3$ are appropriately used to make bonds with the Ga atom on the top layer.

However, in actual fabrication processes, it has been reported that $Ga(NH_2)_3$ is not produced from TMG by only gas-phase reactions [43]. As discussed in the previous section, $DMG(NH_2)$ and $MMG(NH_2)_2$ exist more abundantly in the gas phase. Therefore, other reactions should also be studied.

Surface reactions of $DMG(NH_2)$ and $MMG(NH_2)_2$

Next, we consider the optimized structures after the adsorption of $DMG(NH_2)$ and $MMG(NH_2)_2$. These reactions are given as follows:

$$\mathrm{GaN(0001)} + \mathrm{DMG(NH_2)} \rightarrow \mathrm{DMG(NH_2)/GaN(0001)} \qquad \Delta E = -39.6 \text{ kcal/mol} \qquad (5.9)$$

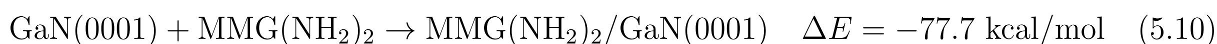

$$\mathrm{GaN(0001)} + \mathrm{MMG(NH_2)_2} \rightarrow \mathrm{MMG(NH_2)_2/GaN(0001)} \qquad \Delta E = -77.7 \text{ kcal/mol} \qquad (5.10)$$

Figures 5.6(a) and (b) show optimized structures of these reactions, respectively. In these figures, Ga-Ga bonds are seen in both $DMG(NH_2)/GaN(0001)$ and $MMG(NH_2)_2/GaN(0001)$, which have not been seen in the case of $Ga(NH_2)_3/GaN(0001)$ shown in Fig. 5.5. Obviously, Ga-Ga bonds formed on the GaN(0001) surface are one of serious problems which disturb steady GaN crystal growth. Therefore, the GaN crystal growth is not expected to proceed by the adsorption of these GaN cores and surface reactions. It is necessary to prevent Ga-Ga

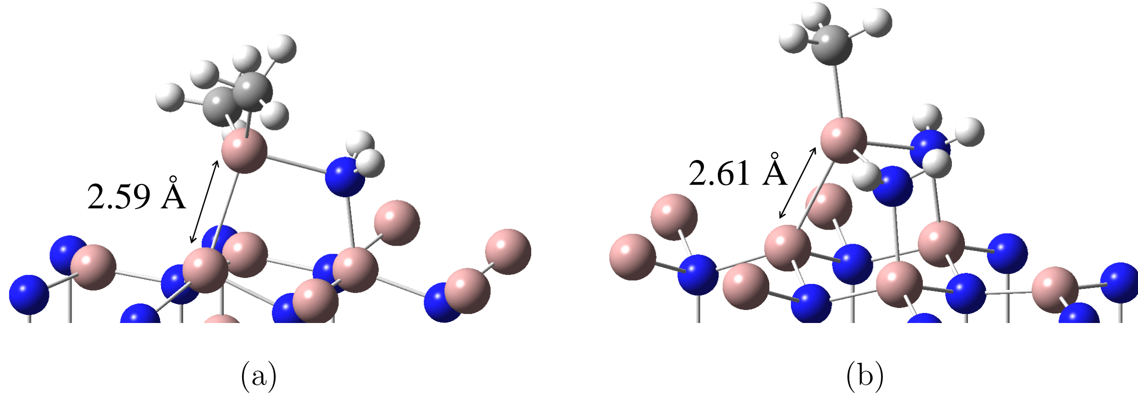

Figure 5.6: Optimized structures of (a) $DMG(NH_2)/GaN(0001)$ and (b) $MMG(NH_2)_2/GaN(0001)$ after surface reactions.

bonds for the crystal growth with the adsorption of GaN cores. As mentioned above, in the presence of $Ga(NH_2)_3$, $DMG(NH_2)$ and $MMG(NH_2)_2$ also exist. Hence, these molecules should prevent the steady GaN crystal growth.

To study these Ga-Ga bonds in detail, we calculate the electronic kinetic energy density of $MMG(NH_2)_2/GaN(0001)$. The values on a plane including the Ga-Ga bond are shown in Fig. 5.7(a). In red (blue) regions, the kinetic energy density is positive (negative). Circles on Ga atoms show pseudopotential. From this figure, it is confirmed that the values are positive between the Ga atoms. As mentioned above, only positive kinetic energy is allowed in classical mechanics, while negative kinetic energy appears in quantum mechanics. Therefore, it can be said that electrons are bound to the region between the Ga atoms of admolecule and surface, and that there is a strong bond there.

Surface reactions of the molecules with coordinate bond of NH_3

We have discussed that Ga-Ga bonds disturb the crystal growth via adsorption of GaN cores. Hence, GaN cores which do not make Ga-Ga bonds are suitable for a steady growth of the GaN crystal.

In the following, we study optimized structures and adsorption energies of GaN cores with a coordinate bond with NH_3. First, it cannot be expected that $TMG{:}NH_3$ is adsorped on the GaN(0001) surface, since it does not have lone electron pair. Reactions for other

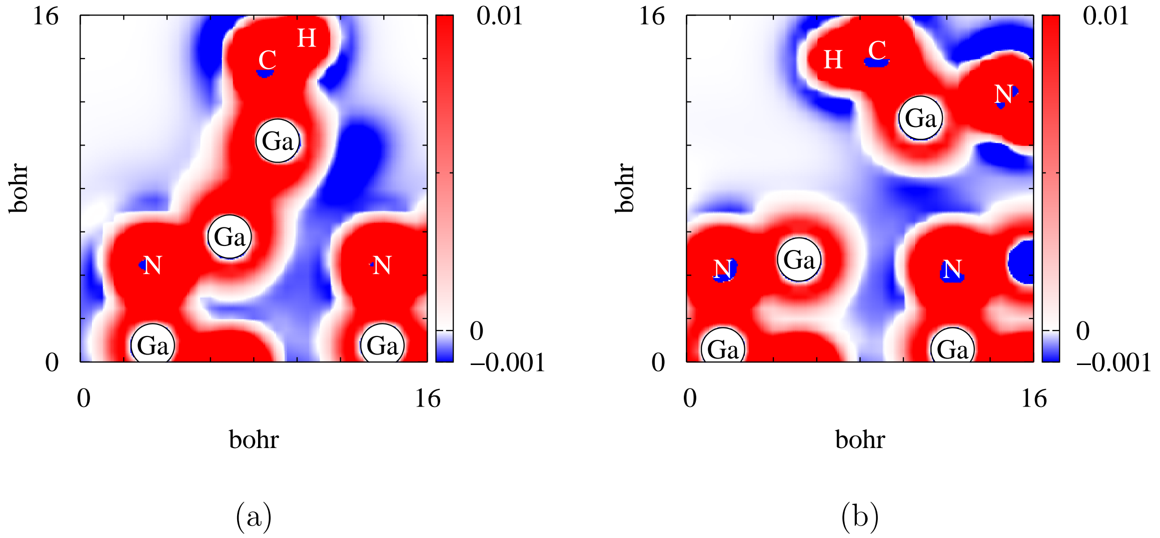

Figure 5.7: The values of the kinetic energy density on the planes including the Ga-Ga bond (a) in $MMG(NH_2)_2/GaN(0001)$ and (b) in $MMG(NH_2)_2{:}NH_3/GaN(0001)$. In red (blue) region, the kinetic energy density is positive (negative). Circles on Ga atoms show pseudopotential.

molecules are written as follows:

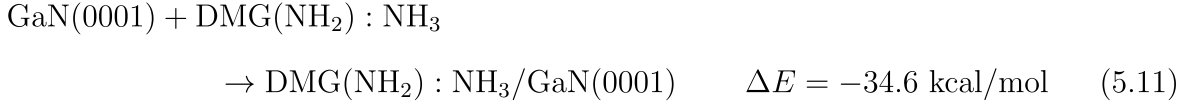

$$\begin{aligned} &\mathrm{GaN(0001) + DMG(NH_2) : NH_3} \\ &\qquad \rightarrow \mathrm{DMG(NH_2) : NH_3/GaN(0001)} \qquad \Delta E = -34.6 \ \mathrm{kcal/mol} \end{aligned} \tag{5.11}$$

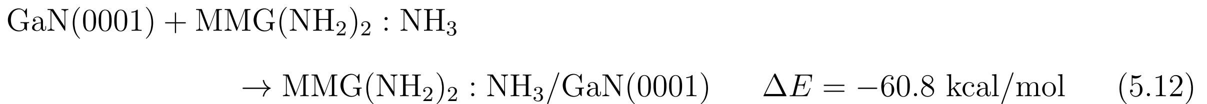

$$\begin{aligned} &\mathrm{GaN(0001) + MMG(NH_2)_2 : NH_3} \\ &\qquad \rightarrow \mathrm{MMG(NH_2)_2 : NH_3/GaN(0001)} \qquad \Delta E = -60.8 \ \mathrm{kcal/mol} \end{aligned} \tag{5.12}$$

In Figs. 5.8(a) and (b), the optimized structures of $DMG(NH_2){:}NH_3/GaN(0001)$ and $MMG(NH_2)_2{:}NH_3/GaN(0001)$ are shown, respectively. Lengths between the Ga atom in GaN cores and its closest Ga atom are about 4 Å in these structures. These lengths are much longer than those for $DMG(NH_2)/GaN(0001)$ and $MMG(NH_2)_2/GaN(0001)$ in Fig. 5.6. We show the values of the kinetic energy density on the plane including these Ga atoms in Fig. 5.7(b). The values of $MMG(NH_2)_2{:}NH_3/GaN(0001)$ are negative between the Ga atoms of admolecule and surface. This contrasts to the results of $MMG(NH_2)_2/GaN(0001)$ shown in Fig. 5.7(a). From this result, it is confirmed that strong Ga-Ga bonds do not appear between these Ga atoms for $MMG(NH_2)_2{:}NH_3/GaN(0001)$. We speculate that

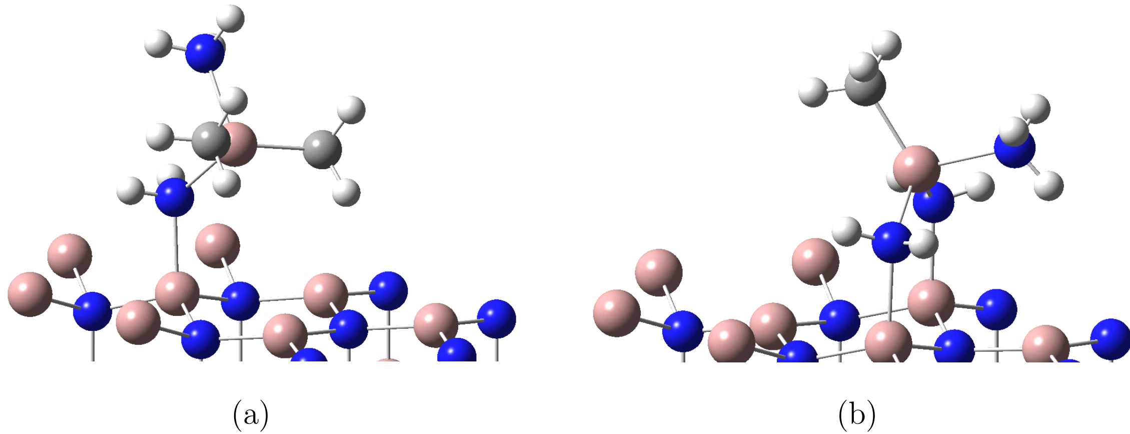

Figure 5.8: Optimized structures of (a) $DMG(NH_2){:}NH_3/GaN(0001)$ and (b) $MMG(NH_2)_2{:}NH_3/GaN(0001)$.

this difference consists in that of the highest occupied molecular orbital (HOMO) of these molecules. HOMO of $DMG(NH_2)$ and $MMG(NH_2)_2$ are mainly occupied with Ga(p) and N(p). For $DMG(NH_2){:}NH_3$ and $MMG(NH_2)_2{:}NH_3$, Ga(p) is stabilized to a lower energy level and only N(p) dominantly occupies their HOMO. As a result, when $DMG(NH_2){:}NH_3$ or $MMG(NH_2)_2{:}NH_3$ is adsorbed on the GaN(0001) surface, only amino groups make bonds with the surface. In conclusion, these results suggest the possibility of the crystal growth without Ga-Ga bonds by adsorption of $DMG(NH_2){:}NH_3$ and $MMG(NH_2)_2{:}NH_3$, which are more stabilized than $DMG(NH_2)$ and $MMG(NH_2)_2$ in the gas phase.

It is known that $DMG(NH_2){:}NH_3$ exists in the gas phase for low temperature (≤ 650 K) [43]. At high temperature of the MOCVD process (1300-1400 K), a density of these molecules may be insufficient. However, since reactions in gas phase are not known well, we consider that these molecules remain one of candidates promoting the GaN crystal growth. In addition, it may be considered that NH_3 or NH_2 attached on the GaN surface plays also the same role in a growth process. Under the MOCVD condition that high NH_3 partial pressure and high temperature, NH_3 or NH_2 molecules are stuck on the surface of GaN, without making N-N bonds due to the protection by hydrogen atoms. These molecules prevent an approaching Ga molecule from bonding a surface Ga atom as the NH_3 in $DMG(NH_2){:}NH_3$ or $MMG(NH_2)_2{:}NH_3$. Hence, Ga-Ga bonds are considered to be sufficiently suppressed for NH_3 or NH_2-covered surface.

5.4 Conclusions

In this work, we have investigated the GaN(0001) crystal growth focusing on both gas-phase and surface reactions. As initial surface of GaN(0001), Ga-covered one is suitable for the crystal growth, while N-covered one is not, due to N-N bonds. We have studied the adsorption of gallium-nitrogen compounds on the Ga-covered surface. For the adsorption of compounds of Ga and N atoms, we have pointed out that unwanted Ga-Ga bonds are one of serious problems for the steady growth, and DMG(NH_2):NH_3 and MMG(NH_2)$_2$:NH_3 can be a solution for this problem. This result contrasts the fact that parasitic reactions are not suitable for the steady growth in the case of the AlGaN crystal growth.

Reference

[1] H. Amano, N. Sawaki, I. Akasaki, Y. Toyoda, Appl. Phys. Lett. **48**, 353 (1986).

[2] S. Nakamura, Acta Phys. Pol. A **95**, 153 (1999).

[3] I. Akasaki, H. Amano, Jpn. J. Appl. Phys. **36**, 5393 (1997).

[4] A. Denis, G. Goglio, G. Demazeau, Mater. Sci. Eng. R **50**, 167 (2006).

[5] A. Tachibana, O. Makino, S. Tanimura, H. Tokunaga, N. Akutsu, K. Matsumoto, Phys. Status Solidi A **176**, 699 (1999).

[6] O. Makino, K. Nakamura, A. Tachibana, H. Tokunaga, N. Akutsu, K. Matsumoto, Appl. Surf. Sci. **374**, 159 (2000).

[7] K. Nakamura, O. Makino, A. Tachibana, K. Matsumoto, J. Organomet. Chem. **611**, 514 (2000).

[8] M. Ikenaga, K. Nakamura, A. Tachibana, K. Matsumoto, J. Cryst. Growth **237**, 936 (2002).

[9] K. Matsumoto, A. Tachibana, J. Crsyt. Growth **272**, 360 (2004).

[10] T. Okada, K. Doi, K. Nakamura, A. Tachibana, Phys. Status Solidi B **241**, 2744 (2004).

[11] C. Lee, W. Yang, R. G. Parr, Phys. Rev. B **37**, 785 (1998).

[12] B. Miehlich, A. Savin, H. Stoll, H. Preuss, Chem. Phys. Lett. **157**, 200 (1989).

[13] A. D. Becke, J. Chem. Phys. **98**, 5648 (1993).

[14] T. H. Dunning Jr, P. J. Hay, in *Modern Theoretical Chemistry*, edited by H. F. Schafer III (Plenum, New York, 1976) Vol. 3, p. 1.

[15] P. J. Hay, W. R. Wadt, J. Chem. Phys. **82**, 270 (1985).

[16] W. R. Wadt, P. J. Hay, J. Chem. Phys. **82**, 284 (1985).

[17] P. J. Hay, W. R. Wadt, J. Chem. Phys. **82**, 299 (1985).

[18] Gaussian 03, Revision B. 05 (Gaussian, Inc., Pittsburgh PA 2003).

[19] V. Milman, B. Winkler, J. A. White, C. J. Pickard, M. C. Payne, E. V. Akhmatskaya, R. H. Nobes, Int. J. Quantum Chem. **77**, 895 (2000).

[20] D. Vanderbilt, Phys. Rev. B **41**, 7892 (1990).

[21] J. P. Perdew, K. Burke, M. Ernzerhof, Phys. Rev. Lett. **77**, 3865 (1996).

[22] G. te Velde, F. M. Bickelhaupt, S. J. A. van Gisbergen, C. Fonseca Guerra, E. J. Baerends, J. G. Snijders, T. Ziegler, J. Comput. Chem. **22**, 931 (2001).

[23] J. P. Perdew, Y. Wang, Phys. Rev. B **45**, 13244 (1992).

[24] A. Warshel, M. Levitt, J. Mol. Biol. **103**, 227 (1976).

[25] U. C. Singh, P. A. Kollman, J. Comput. Chem. **7**, 718 (1986).

[26] M. J. Field, P. A. Bash, M. Karplus, J. Comput. Chem. **11**, 700 (1990).

[27] J. Gao, in *Reviews in Computational Chemistry*, edited by K. B. Lipkowitz, D. B. Boyd, (VCH, New York, 1996) Vol. 7, p. 119.

[28] T. Z. Mordasini, W. Thiel, Chimia **58**, 288 (1998).

[29] F. Maseras, K. Morokuma, J. Comput. Chem. **16**, 1170 (1995).

[30] M. Svensson, S. Humbel, R. D. J. Froese, T. Matsubara, S. Sieber, K. Morokuma, J. Phys. Chem. **100**, 19357 (1996).

[31] S. Dapprich, I. Komáromi, K. S. Byun, K. Morokuma, M. J. Frisch, J. Mol. Struct.: THEOCHEM **1**, 461 (1999).

[32] T. Vreven, K. Morokuma, J. Comput. Chem. **16**, 1419 (2000).

[33] A. K. Rappé, C. J. Casewit, K. S. Colwell, W. A. Goddard III, W. M. Skiff, J. Am. Chem. Soc. **114**, 10024 (1992).

[34] R. S. Mulliken, J. Chem. Phys. **23**, 1833 (1955).

[35] A. Tachibana, Theor. Chem. Acc. **102**, 188 (1999).

[36] A. Tachibana, J. Chem. Phys. **115**, 3497 (2001).

[37] A. Tachibana, in *Stress Induced Phenomena in Metallization* edited by S. P. Baker (American Institute of Physics, New York, 2002) p. 105.

[38] A. Tachibana, in *Reviews in Modern Quantum Chemistry*, edited by K. D. Sen (World Scientific, Singapore, 2002) Chap. 45, p. 1327.

[39] A. Tachibana, in *Fundamental World of Quantum Chemistry*, edited by E. J. Brändas and E. S. Kryachko (Kluwer Academic, Dordrecht, 2003) Vol. 2, p. 211.

[40] A. Tachibana, Int. J. Quantum Chem. **100**, 981 (2004).

[41] A. Tachibana, J. Mol. Modeling **11**, 301 (2005).

[42] M. Senami, K. Ichikawa, K. Doi, P. Szarek, K. Nakamura, and A. Tachibana, Molecular Regional DFT program package, ver.3 (Tachibana Lab., Kyoto University, Kyoto, 2008).

[43] J. Schäfer, A. Simons, J. Wolfrum, R. A. Fischer, Chem. Phys. Lett. **319**, 477 (2000).

[44] A. Hirako, K. Kusakabe, K. Ohkawa, Jpn. J. Appl. Phys. **44**, 874 (2005).

[45] K. Doi, N. Maida, K. Kimura, A. Tachibana, Phys. Status Solidi C **4**, 2293 (2007).

Chapter 6

Theoretical Study of Hydrogenated Tetrahedral Aluminum Clusters

6.1 Introduction

Recently, hydrogen is paid much attention as new primary energy source because of the depletion of fossil fuels and environmental issues such as global warming. There are three basic research challenges – production, storage, application – for a "hydrogen economy". Our study in this paper is related to hydrogen storage. As is emphasized in the recent reports on basic research challenges for hydrogen storage, its high efficiency is a key factor in enabling the success of the hydrogen economy [1, 2]. Hydrogen storage systems must exhibit following properties: appropriate thermodynamics, fast kinetics, high storage capacity (more than 10 wt %), effective heat transfers, high volumetric densities, long cycle lifetime, safety under normal use [3]. To implement these properties, solid-state storage is useful. Metal hydrides, chemical storage materials, nanostructured materials are well known for effective solid-state storage systems.

Among them, we investigate aluminum hydrides in the form of aluminum clusters. More specifically, we deal with an aluminum tetrahedral cage (Al_4) and its hydrides which were recently observed in experiment and confirmed to have enhanced stability [4, 5]. Although the clusters found in Refs. [4, 5] are produced by vaporizing aluminum metal in hydrogen gas and do not lead to immediate application for hydrogen storage material at this stage, it would be useful to study their properties theoretically to further explore possible connection with

more realistic materials for hydrogen storage. It is also interesting to study the tetrahedral cage in the aspect that it is the fundamental structure of an aluminum icosahedral cage (Al_{12}) [6]. In this paper, we report on the structures of aluminum hydrides which can be constructed by adding H_2 molecules to an Al_4 tetrahedral cluster.

We also evaluate and discuss the chemical properties of aluminum clusters and hydrogen adsorption by using a novel method of the electronic stress tensor based on the Regional Density Functional Theory (RDFT) and Rigged Quantum Electrodynamics (RQED) [7–19].

This paper is organized as follows. In the next section, we briefly explain our quantum chemical computation method. We also describe our analysis method based on the RDFT and the RQED, and in particular we define our bond orders and regional chemical potential. In Sec. 6.3, we discuss our results. Sec. 6.3.1 shows structures of hydrogenated Al_4 tetrahedral clusters and discuss their binding energies. In Sec. 6.3.2, we analyze the structures using the electronic stress tensor and our bond orders. We summarize our paper in Sec. 6.4.

6.2 Theory and Calculation Methods

6.2.1 Ab initio electronic structure calculation

We perform ab initio quantum chemical calculation for several clusters of aluminum hydrides derived from an Al_4 tetrahedral cage. In this work, calculations are performed by Gaussian03 program package [20] using density functional theory (DFT) with Perdew-Wang 1991 exchange and correlation function (PW91) [21, 22]. The split-valence triple-zeta 6-311G** basis set [23–25] with polarization functions has been used. Optimization was performed without imposing symmetry. The visualization is done using Visual Molecular Dynamics (VMD) [26] and PyMOL Molecular Viewer programs [27].

6.2.2 RDFT analysis

In the following section, we use quantities derived from the electronic stress tensor to analyze electronic structures of hydrogenated Al_4 clusters. This method based on RDFT and RQED [7–13, 19] include useful quantities to investigate chemical bonding and reactivity such as new definition of bond order and regional chemical potential [14–16]. We briefly

describe them below. (For other studies of quantum systems with the stress tensor in a slightly different context, see Refs. 28–39.)

The basic quantity in this analysis is the electronic stress tensor density $\overleftrightarrow{\tau}^{S}(\vec{r})$ whose components are given by

$$\begin{aligned}\tau^{Skl}(\vec{r}) &= \frac{\hbar^2}{4m}\sum_i \nu_i \left[\psi_i^*(\vec{r})\frac{\partial^2\psi_i(\vec{r})}{\partial x^k \partial x^l} - \frac{\partial\psi_i^*(\vec{r})}{\partial x^k}\frac{\partial\psi_i(\vec{r})}{\partial x^l}\right. \\ &\quad \left. + \frac{\partial^2\psi_i^*(\vec{r})}{\partial x^k \partial x^l}\psi_i(\vec{r}) - \frac{\partial\psi_i^*(\vec{r})}{\partial x^l}\frac{\partial\psi_i(\vec{r})}{\partial x^k}\right], \end{aligned} \tag{6.1}$$

where $\{k, l\} = \{1, 2, 3\}$, m is the electron mass, $\psi_i(\vec{r})$ is the ith natural orbital and ν_i is its occupation number.

Taking a trace of $\overleftrightarrow{\tau}^{S}(\vec{r})$ can define energy density of the quantum system at each point in space. The energy density $\varepsilon_\tau^S(\vec{r})$ is given by

$$\varepsilon_\tau^S(\vec{r}) = \frac{1}{2}\sum_{k=1}^{3}\tau^{Skk}(\vec{r}). \tag{6.2}$$

We note that, by using the virial theorem, integration of $\varepsilon_\tau^S(\vec{r})$ over whole space gives usual total energy E of the system: $\int \varepsilon_\tau^S(\vec{r})d\vec{r} = E$.

Regional chemical potential μ_R [7] is calculated approximately using $\varepsilon_\tau^S(\vec{r})$ [14].

$$\mu_R = \frac{\partial E_R}{\partial N_R} \approx \frac{\varepsilon_\tau^S(\vec{r})}{n(\vec{r})}, \tag{6.3}$$

where $n(\vec{r})$ is the ordinary electron density at $\vec{r}$. Since electrons tend to move from high μ_R region to low μ_R region, the distribution of μ_R maps the chemical reactivity.

Now, we define bond orders as $\varepsilon_\tau^S(\vec{r})$ or μ_R at "Lagrange point" [14]. The Lagrange point $\vec{r}_L$ is the point where the tension density $\vec{\tau}^S(\vec{r})$ given by the divergence of the stress tensor

$$\begin{aligned}\tau^{Sk}(\vec{r}) &= \sum_l \partial_l \tau^{Skl}(\vec{r}) \\ &= \frac{\hbar^2}{4m}\sum_i \nu_i \left[\psi_i^*(\vec{r})\frac{\partial\Delta\psi_i(\vec{r})}{\partial x^k} - \frac{\partial\psi_i^*(\vec{r})}{\partial x^k}\Delta\psi_i(\vec{r})\right. \\ &\quad \left. + \frac{\partial\Delta\psi_i^*(\vec{r})}{\partial x^k}\psi_i(\vec{r}) - \Delta\psi_i^*(\vec{r})\frac{\partial\psi_i(\vec{r})}{\partial x^k}\right], \end{aligned} \tag{6.4}$$

vanishes. Namely, $\tau^{Sk}(\vec{r}_L) = 0$. $\vec{\tau}^S(\vec{r})$ is the expectation value of the tension density operator $\hat{\vec{\tau}}^S(\vec{r})$, which cancels the Lorentz force density operator $\hat{\vec{L}}(\vec{r})$ in the equation of

motion for stationary state [11]. Therefore, we see that $\vec{\tau}^S(\vec{r})$ expresses purely quantum mechanical effect and it has been proposed that this stationary point might characterize chemical bonding [14]. Then, our newly defined bond orders are

$$b_\varepsilon = \frac{\varepsilon^S_{\tau \mathrm{AB}}(\vec{r}_L)}{\varepsilon^S_{\tau \mathrm{HH}}(\vec{r}_L)}, \tag{6.5}$$

and

$$b_\mu = \frac{\varepsilon^S_{\tau \mathrm{AB}}(\vec{r}_L)/n_{\mathrm{AB}}(\vec{r}_L)}{\varepsilon^S_{\tau \mathrm{HH}}(\vec{r}_L)/n_{\mathrm{HH}}(\vec{r}_L)}. \tag{6.6}$$

One should note normalization by the respective values of a H_2 molecule calculated at the same level of theory (including method and basis set).

We use Molecular Regional DFT (MRDFT) package [40] to compute these quantities introduced in this section.

6.3 Results and Discussion

6.3.1 Structures and stability

The bare tetrahedral optimized structure of Al_4 is shown in Fig. 6.1 (a). We found that all the six Al—Al bonds have an equal length of 2.74 Å to a great accuracy. Al_4 is considered to have a structure very close to a regular tetrahedron. We note that this regular tetrahedral structure is stable only for high spin state (multiplicity = 5). Also it should be noted that the global minimum of Al_4 cluster is planar rhombus with multiplicity 3 [41, 42], which has lower energy by 0.5 eV. Below, we investigate the structures when hydrogens adsorbs to this tetrahedral structure.

We first considered the adsorption of two hydrogen atoms. We examined many combinations of adsorption sites and multiplicities 1, 3 and 5. We found that Al_4H_2 with two hydrogen atoms at terminal sites as shown in Fig. 6.1 (b) and with multiplicity 3, has the lowest energy.

We further added hydrogen atoms to this structure. Fig. 6.1 (c)-(g) show structures of most stable isomer of Al_4H_n ($n = 4, 6, 8, 10$ and 12) we have obtained. We have tried to adsorb more hydrogen, without success. We could not find a stable structure for Al_4H_{14}. Thus, we believe Al_4H_{12} is the saturated structure of the Al_4 cluster.

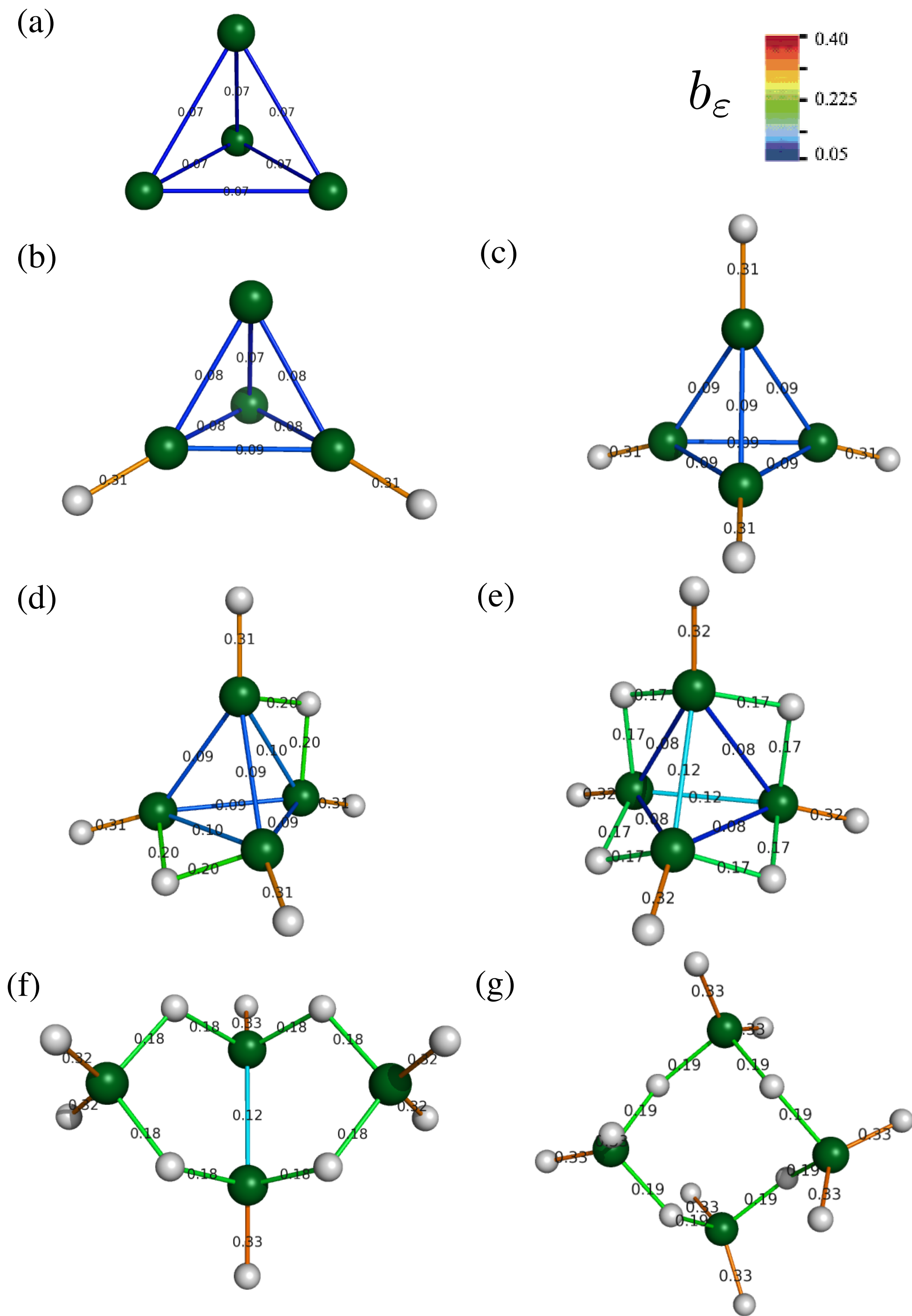

Figure 6.1: Optimized structures for Al_4 tetrahedral cage and its hydrides Al_4H_n ($n = 2, 4, 6, 8, 10, 12$). The bonds are drawn at which Lagrange points are found and our energy density based bond order b_ε is shown.

Here, we comment on the comparison with the structures which were reported in literatures. The structure of Al_4H_4, Fig. 6.1 (c), is consistent with Ref. 5, 43 and Al_4H_6, Fig. 6.1 (d), is consistent with Ref. 5. As for Al_4H_{12}, there are several literatures which investigated stable structures for this as a tetramer of alane $Al\,H_3$ [43–46]. This structure also attracts interest because of its high hydrogen storage capacity of 10.0 wt%, which exceeds the target value of a hydrogen storage system specified by some technical report [3]. Ref. 43 has pointed out that structures in Refs. 44 and 45 are not stable in light of recent quantum chemical computation and reported a structure with S_4 symmetry as the global minimum. Our results, Fig. 6.1 (g), agrees with the structure found in Ref. 43. Ref. 43 also reported stable structures of Al_4H_{10}, including the structure we have found as Fig. 6.1 (f). They have shown that there is a structure with lower energy but since that structure is chain-like, we adopt the structure of Fig. 6.1 (f) as the one which is derived by adding hydrogen atoms to Fig. 6.1 (e).

In order to investigate the stability of these structures, we here define two types of binding energies (B.E.). The total B.E. of Al_4H_m is

$$\Delta E_{\text{total}} = E(\text{Al}_4\text{H}_m) - [4E(\text{Al}) + mE(\text{H})], \tag{6.7}$$

where $E(\text{X})$ is the energy of X. ΔE_{total} represents the sum of the strength of all the bonds existing in the molecule. The average B.E. of H atoms is defined as

$$\Delta E_{\text{H}} = \frac{1}{m}\left\{E(\text{Al}_4\text{H}_m) - [E(\text{Al}_4) + mE(\text{H})]\right\}, \tag{6.8}$$

which represents the strength of Al—H bond per one hydrogen atom. We use the structure of Fig. 6.1 (a) to calculate $E(\text{Al}_4)$.

The results for these two types of binding energy are summarized in Table 6.1 and Fig. 6.2. As is shown in Fig. 6.2 (a), ΔE_{total} decreases as more hydrogens are adsorbed. This indicates that adsorption of hydrogen stabilizes the cluster. On the other hand, as we plot in Fig. 6.2 (b), ΔE_{H} is almost same for Al_4H_2 and Al_4H_4 but increases as more hydrogens are adsorbed. This is considered to be due to the increased hydrogens at bridge sites for larger clusters than Al_4H_6. It should be stressed that lower total B.E. and higher average B.E. of H atoms are favorable for hydrogen storage systems. This means that hydrogen atoms turn into state such that they are easily desorbed, while clusters become more stable as hydrogen are adsorbed.

Table 6.1: Total B.E. ΔE_{total}, average B.E. of H atoms ΔE_{H} and mean nearest-neighbor bond lengths $d_{\text{x-x}}$ of Al_4H_n ($n = 2, 4, 6, 8, 10$ and 12). H(t) and H(b) denote a hydrogen at the terminal site and the bridge site respectively.

	ΔE_{total} (eV)	ΔE_{H} (eV)	$d_{\text{Al-Al}}$ (Å)	$d_{\text{Al-H(t)}}$ (Å)	$d_{\text{Al-H(b)}}$ (Å)
Al_4	−5.59	—	2.74	—	—
Al_4H_2	−11.5	−2.94	2.66	1.61	—
Al_4H_4	−17.3	−2.94	2.60	1.61	—
Al_4H_6	−22.7	−2.84	2.63	1.60	1.74
Al_4H_8	−27.6	−2.75	2.69	1.59	1.77
Al_4H_{10}	−32.2	−2.66	3.11	1.59	1.74
Al_4H_{12}	−36.6	−2.59	3.47	1.59	1.72

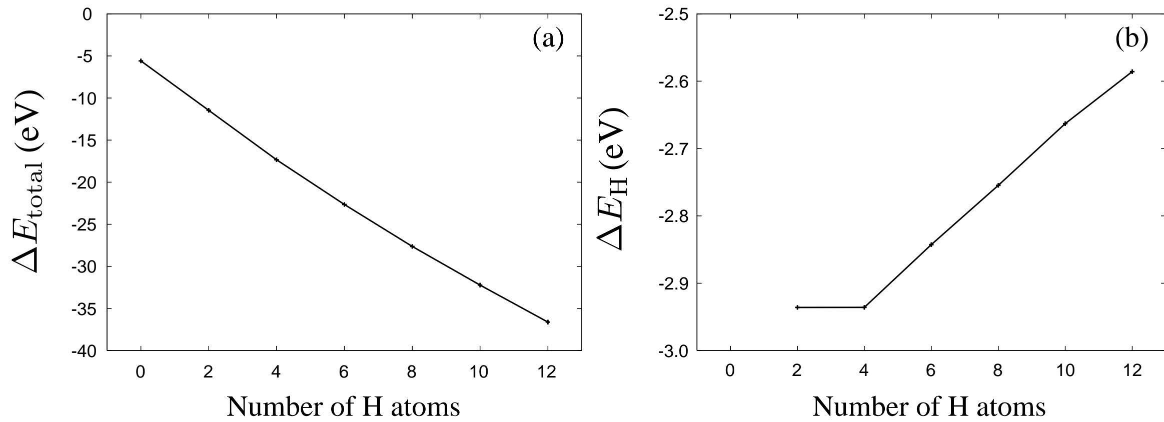

Figure 6.2: Total B.E. ΔE_{total} (panel(a)) and average B.E. of H atoms ΔE_{H} (panel (b)) of Al_4H_n ($n = 0, 2, 4, 6, 8, 10$ and 12).

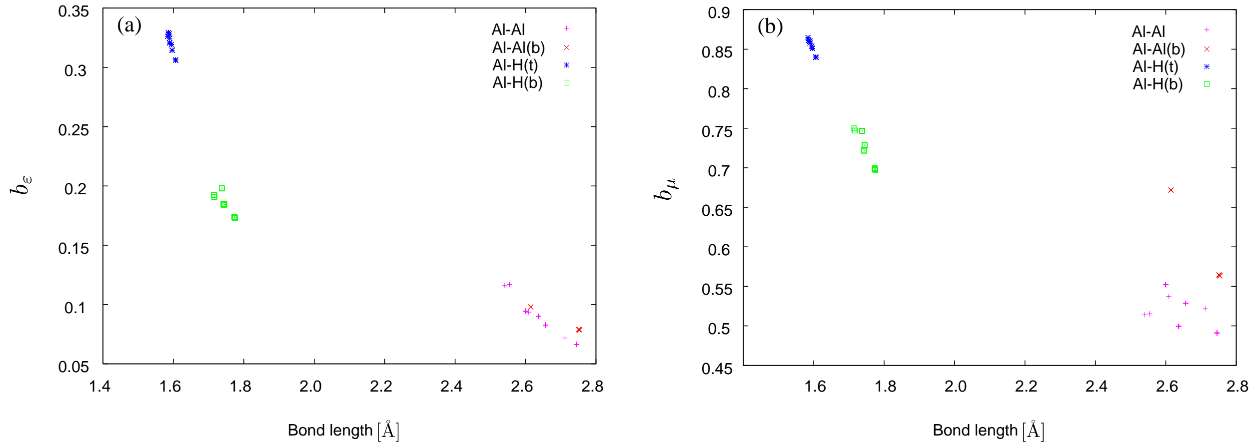

Figure 6.3: Energy density bond order b_ε (panel (a)) and chemical potential bond order b_μ (panel (b)) as functions of bond length. Data are taken from the structures of Al_4H_n ($n = 0, 2, 4, 6, 8, 10$ and 12) as shown in Fig. 6.1. Al–Al bonds with bridging hydrogen are plotted with red crosses and those without are plotted with magenta plus marks. Al–H bonds at terminal sites are plotted with blue asterisks and those at bridge sites are plotted with green squares.

6.3.2 Stress tensor analysis of chemical bond

In the previous subsection, we have shown structures of aluminum hydrides derived from the Al_4 tetrahedral cage and discussed the stability of these clusters by the usual binding energy. In this section, we discuss their chemical bonds using RDFT analysis introduced in Sec. 6.2.2.

Actually, we have already used the RDFT concept to draw Fig. 6.1. There, we draw bond lines when the Lagrange point is found between two atoms. The Lagrange point is the point at which tension density vanishes (Sec. 6.2.2) and considered to be suitable to define chemical bond [14–16]. Two types of bond orders, b_ε (Eq. (6.5)) and b_μ (Eq. (6.6)), are computed and summarized as functions of bond distance in Fig. 6.3. The b_ε describes bond strength in relation to bond in H_2 molecule and how particular bond contributes to lowering of total energy of a structure, whereas b_μ shows bond electrophilicity in relation to H_2 molecule as reference bond.

In the figure, we distinguish different types of bonds. Al–Al bonds with and without bridging hydrogen are denoted by "Al–Al(b)" and "Al–Al". Al–H bonds at terminal sites

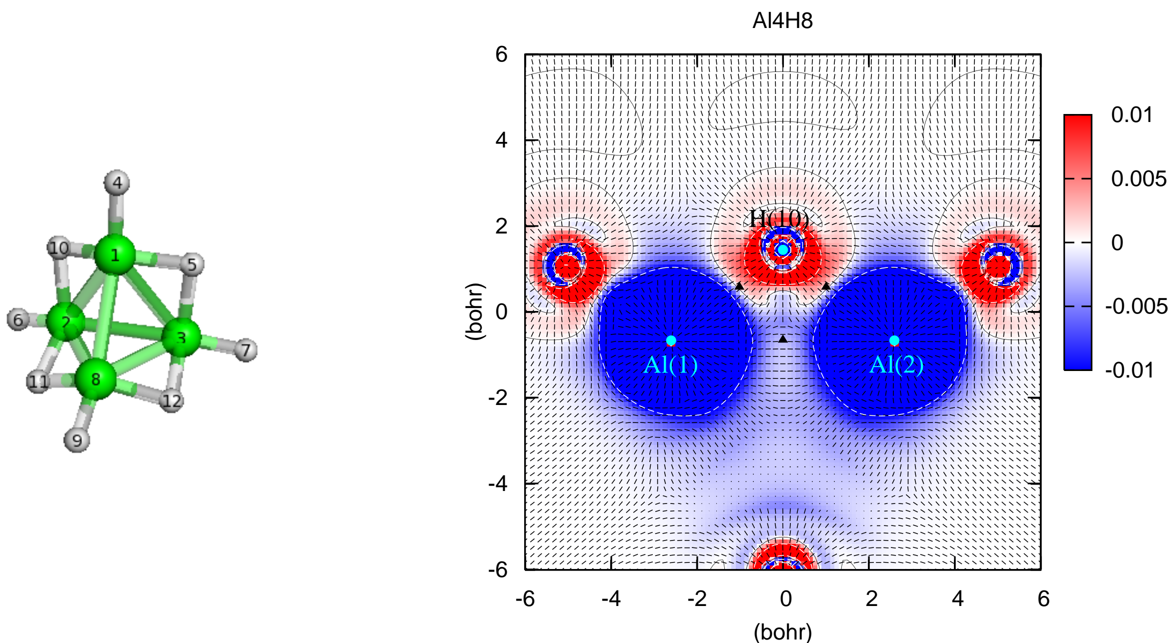

Figure 6.4: The largest eigenvalue of the stress tensor and corresponding eigenvector of Al_4H_8 on the right panel. They are shown on a plane which includes three labeled atoms. As for the eigenvectors, the projection on this plane is plotted. The positions of these atoms are shown by the circle dots. Parenthesized numbers in the labels correspond to the numbers on atoms on the left panel. As for the eigenvalue, we only show for the range $[-0.01, 0.01]$ with color scale shown on the right and the contours for 0.01 and -0.01 are shown by white dashed lines. The triangle dots shows the locations of the Lagrange points.

are denoted as "Al–H(t)" and those at bridge sites are denoted as "Al–H(b)". We find good correlation between bond distance and our bond orders as has been found in other molecules [14–16]. b_ε and b_μ basically exhibit similar features regarding the correlation between bond length in the sense that the slope for Al–Al bonds are larger than Al-H bonds. There is a subtle difference in Al–H bonds between b_ε and b_μ. For b_ε, Al-H(t) and Al-H(b) together make a single slope but there seems to appear three families of slopes for b_μ. Since b_μ concerns the regional chemical potential, the difference may reflect the chemical reactivity of these bonds.

We can further examine features in chemical bonds by analyzing the electronic stress tensor (Eq. (6.1)). For example, hydrogen bridged Al–Al bonds are investigated for Al_4H_8, Al_4H_{10} and Al_4H_{12}. Figs. 6.4, 6.5 and 6.6 plot the largest eigenvalue of the stress tensor

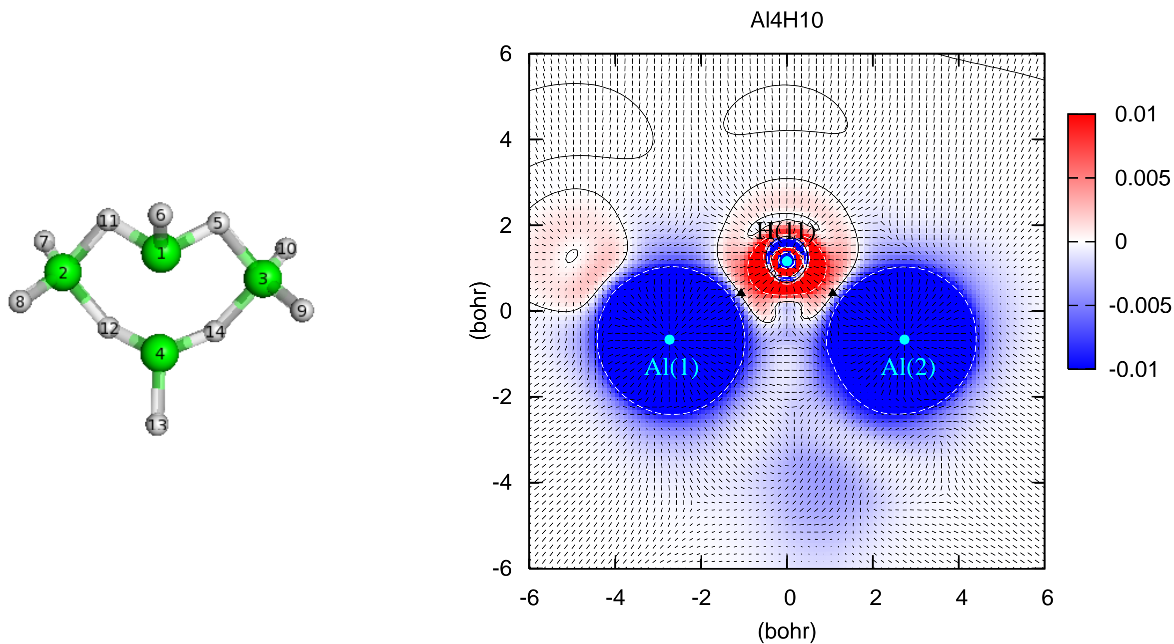

Figure 6.5: The largest eigenvalue of the stress tensor and corresponding eigenvector of Al_4H_{10}, plotted in the same manner as Fig. 6.4.

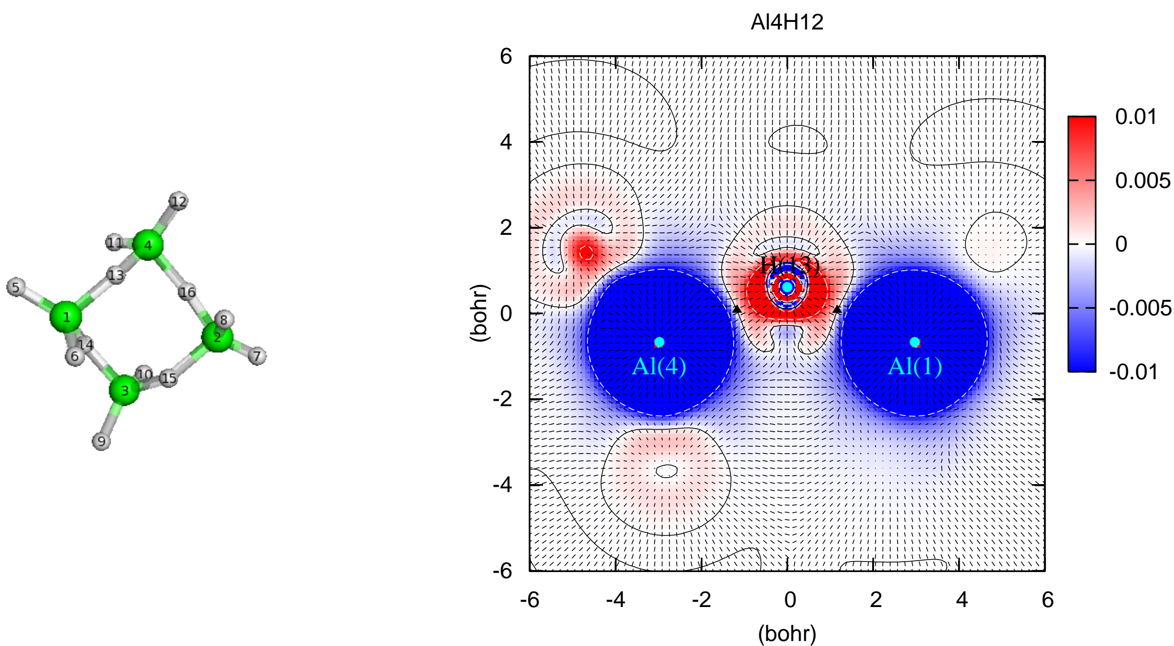

Figure 6.6: The largest eigenvalue of the stress tensor and corresponding eigenvector of Al_4H_{12}, plotted in the same manner as Fig. 6.4.

and corresponding eigenvector on a plane with includes three atoms which participate in the bridging bonds, respectively for Al_4H_8, Al_4H_{10} and Al_4H_{12}. Since the eigenvectors have three spatial components, namely they are 3D objects, we express them by projecting on the plane. In all these clusters, there are Lagrange points between Al and H. There is a region with positive eigenvalue of the stress tensor (tensile stress) between them, which is typical for covalent bond involving H atom [12, 18]. Also, there is a flow of corresponding eigenvectors connecting Al and H which indicates a formation of strong bonding.

For Al_4H_8, which has a Lagrange point between Al atoms, also has a flow of eigenvectors between them. In contrast to the case of Al-H bond, the eigenvalue of the stress tensor turns out to be negative (compressive stress) indicating a different nature of bonding. In the case of Al_4H_{10}, we did not find a Lagrange point between Al atoms. In Fig. 6.5, there is a similar flow of eigenvectors as in Fig. 6.4 between Al atoms, but this structure is shifted off the region between Al atoms likely to be because the H atom came close to Al atoms. Therefore we may conclude there is not so much direct interaction between Al atoms as to call bonding. We can reach similar conclusion for the case of Al_4H_{12}. Fig. 6.6 shows similar structure but it is further away from the region between Al atoms and in fact (when we see the flow in 3D) the flow is connected to H(11) atom which locates at slightly off this plane. This indicates that Al–Al bonding is completely disrupted by the existence of H atoms.

Another example of the electronic stress tensor analysis is provided for Al_4H_{10} in Fig. 6.7. This concerns the somewhat radical structural change between $n = 0, 2, 4, 6, 8$ and $n = 10, 12$ of Al_4H_n. As shown in Fig. 6.1, in terms of Lagrange points, four Al atoms form a tetrahedral cage for $n \leq 8$ and but the cage seems to be broken for $n \geq 10$. This is also seen in a jump in the average Al-Al distance (Table 6.1). We can confirm this by analyzing the stress tensor density. As is shown in Fig. 6.7, there is a region between Al(2) and Al(3) in which eigenvectors go perpendicular to the plane (so that expressed by dots), showing total disconnection of these atoms.

6.4 Summary

In this paper, we investigated the structures of aluminum hydrides derived from a tetrahedral aluminum (Al_4) cluster using *ab initio* quantum chemical calculation. We reported

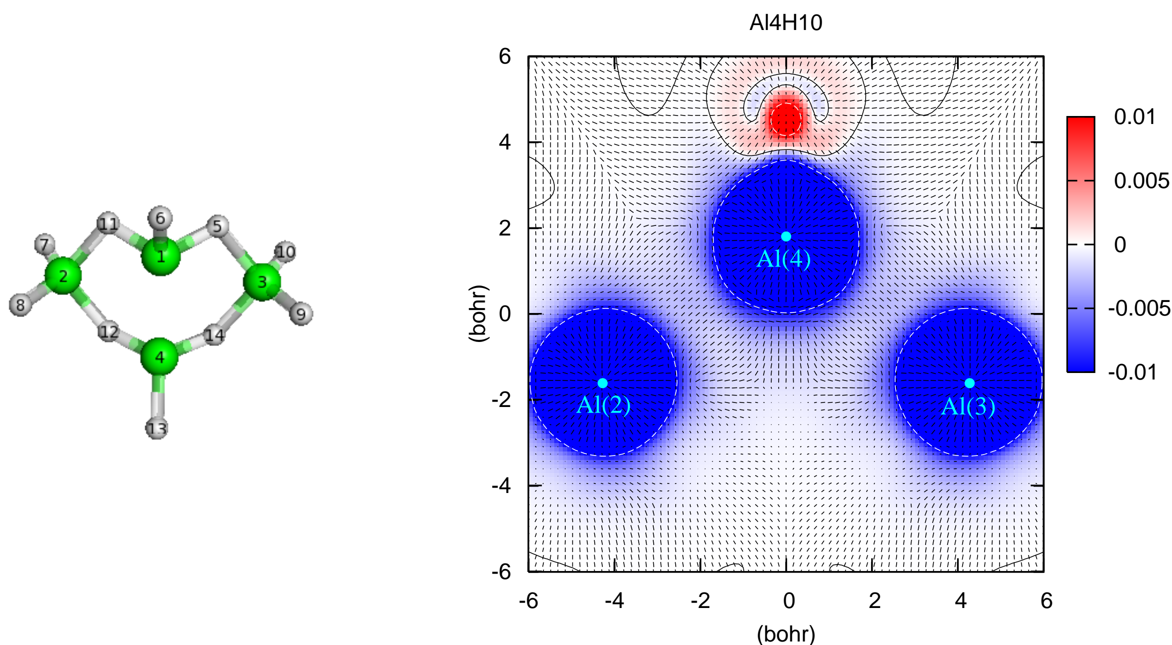

Figure 6.7: The largest eigenvalue of the stress tensor and corresponding eigenvector of Al_4H_{10} (but on the different plane from Fig. 6.5), plotted in the same manner as Fig. 6.4.

stable structures of Al_4H_n ($n = 0, 2, 4, 6, 8, 10$ and 12), which include structures already found in the literature who had investigated the hydrogenated aluminum clusters from other aspects. We calculated binding energies of the aluminum hydrides and found interesting properties as hydrogen storage material: stability of the clusters increases as more hydrogen atoms are adsorbed, while stability of Al–H bonds decreases.

We also analyzed and discussed the chemical bonds of those clusters by using the electronic stress tensor. The bond orders defined from energy density and regional chemical potential (which are in turn calculated from the stress tensor) are shown to have a good correlation with respect to the bond distance and to be able to distinguish types of bonding to some extent. As far as metallic elements are concerned, our bond order analysis had been only applied to Pt clusters [16] so the present analysis can be useful basis for further research using our stress tensor based analysis. This is also true for the eigenvalue and eigenvector analysis of the stress tensor. We have found that Al–H bonds have a positive eigenvalue (tensile stress) at the region between the atoms where as Al–Al bonds have a negative value. This indicates that the stress tensor can be a powerful tool to classify chemical bonding and may provide a deeper insight into the nature of chemical bonds.

Reference

[1] C. Read, J. Petrovic, G. Ordaz, and S. Satyapal, Mater. Res. Soc. Symp. Proc. 885A, warrendale, PA (2006).

[2] Report by ACIL Tasman and Parsons Brinckerhoff for Australian Government: "National Hydrogen Study," (2003).

[3] Argonne National Laboratory. Report on Basic Energy Sciences Workshop on Hydrogen Production, Storage, and Use "Basic Research Needs for the Hydrogen Economy," May 13-15, 2003.

[4] X. Li *et al.*, Science **315**, 356 (2007).

[5] A. Grubisic, J. Am. Chem. Soc., 129 (18), 5969 (2007)

[6] A. Goldberg and I. Yarovsky, Phys. Rev. B **75**, 195403 (2007).

[7] A. Tachibana, Theor. Chem. Acc. **102**, 188 (1999).

[8] A. Tachibana, J. Chem. Phys. **115**, 3497 (2001).

[9] A. Tachibana, in *Stress Induced Phenomena in Metallization*, edited by S. P. Baker, (American Institute of Physics, New York, 2002), p. 105.

[10] A. Tachibana, in *Reviews in Modern Quantum Chemistry, A Celebration in the Contributions of Robert Parr*, edited by K. D. Sen, (World Scientific, Singapore, 2002), Chap. 45, p. 1327.

[11] A. Tachibana, in *Fundamental World of Quantum Chemistry, A Tribute to the Memory of Per-Olov Löwdin*, edited by E. J. Brändas and E. S. Kryachko, (Kluwer Academic, Dordrecht, 2003), Vol. 2, p. 211.

[12] A. Tachibana, Int. J. Quant. Chem. **100**, 981 (2004).

[13] A. Tachibnana, J. Mol. Model. **11** 301 (2005).

[14] P. Szarek and A. Tachibana, J. Mol. Model. **13**, 651 (2007).

[15] P. Szarek, Y. Sueda, and A. Tachibana, J. Chem. Phys. **129**, 094102 (2008).

[16] P. Szarek, K. Urakami, C. Zhou, H. Cheng, and A. Tachibana, J. Chem. Phys. **130**, 084111 (2009).

[17] K. Ichikawa, T. Myoraku, A. Fukushima, Y. Ishihara, R. Isaki, T. Takeguchi and A. Tachibana, J. Mol. Struct. (THEOCHEM) **915**, 1 (2009).

[18] K. Ichikawa and A. Tachibana, Phys. Rev. A **80**, 062507 (2009).

[19] A. Tachibana, J. Mol. Struct. (THEOCHEM), **943**, 138 (2010).

[20] M. J. Frisch *et al.*, Gaussian 03, Revision B.05, Gaussian, Inc., Pittsburgh PA (2003).

[21] D. R. Hamann, Phys. Rev. B **40**, 2980 (1989).

[22] J. P. Perdew and Y. Wang, Phys. Rev. B **45**, 13244 (1992).

[23] R. C. Binning Jr. and L. A. Curtiss, J. Comp. Chem. **11**, 1206 (1990).

[24] M. P. McGrath and L. Radom, J. Chem. Phys. **94**, 511 (1991).

[25] L. A. Curtiss, M. P. McGrath, J.-P. Blaudeau, N. E. Davis, R. C. Binning Jr., and L. Radom, J. Chem. Phys. **103**, 6104 (1995).

[26] W. Humphrey, A. Dalke, and K. Schulten, J. Molec. Graphics, **14**, 33 (1996).

[27] W. L. DeLano, The PyMOL Molecular Graphics System. (2008) DeLano Scientific LLC, Palo Alto, CA, USA. `http://www.pymol.org`

[28] R. F. W. Bader, J. Chem. Phys. **73**, 2871 (1980).

[29] O. H. Nielsen and R. M. Martin, Phys. Rev. Lett. **50**, 697 (1983).

[30] O. H. Nielsen and R. M. Martin, Phys. Rev. B **32**, 3780 (1985).

[31] N. O. Folland, Phys. Rev. B **34**, 8296 (1986).

[32] N. O. Folland, Phys. Rev. B **34**, 8305 (1986).

[33] M. J. Godfrey, Phys. Rev. B **37**, 10176 (1988).

[34] A. Filippetti and V. Fiorentini, Phys. Rev. B **61**, 8433 (2000).

[35] A. M. Pendás, J. Chem. Phys. **117**, 965 (2002).

[36] C. L. Rogers and A. M. Rappe, Phys. Rev. B **65** 224117 (2002).

[37] S. Morante, G. C. Rossi, and M. Testa, J. Chem. Phys. **125**, 034101 (2006).

[38] J. Tao, G. Vignale, and I. V. Tokatly, Phys. Rev. Lett. **100**, 206405 (2008).

[39] P. W. Ayers and S. Jenkins, J. Chem. Phys. **130**, 154104 (2009).

[40] M. Senami, K. Ichikawa, K. Doi, P. Szarek, K. Nakamura, and A. Tachibana, Molecular Regional DFT program package, ver. 3. Tachibana Lab, Kyoto University, Kyoto (2008).

[41] R. O. Jones, Phys. Rev. Lett. **67**, 224 (1991).

[42] H. Kawamura, V. Kumar, Q. Sun and Y. Kawazoe, Phys. Rev. B**65** 045406 (2001).

[43] J. Moc, K. Bober, and K. Mierzwicki, Chem. Phys. **327**, 247 (2006).

[44] M. Shen, C. Liang, and H. F. Schaefer III, Chem. Phys. **171** 325 (1993).

[45] B. G. Willis and K. F. Jensen, J. Phys. Chem. A **104** 7881 (2000).

[46] H. Kawamura, V. Kumar, Q. Sun and Y. Kawazoe, Phys. Rev. A**67** 063205 (2003).

Chapter 7

Aluminum Hydride Clusters as Hydrogen Storage Materials and Their Electronic Stress Tensor Analysis

7.1 Introduction

Aluminum hydride is one of promising materials for hydrogen storage. For example, AlH_3 has very high volumetric hydrogen density (~ 150 kgH_2/m^3) and gravimetric hydrogen density (~ 10 wt%). Also, it is known that the hydrogen desorption reaction proceeds with relatively low temperature (~ 400 K) compared with other metal hydrides. These attractive properties lead to a lot of experimental and theoretical studies of aluminum hydride. Among them, nano-size aluminum hydride clusters attract much attention due to their different properties from bulk materials, which sometimes turn out to be more advantageous as hydrogen storage material.

To achieve a goal to find a useful hydrogen storage material, it would be important for theoretical side to predict the stability of the clusters and details of hydrogen desorption reactions. We report results of such computational studies for aluminum hydride clusters with relatively small numbers of aluminum atoms. We introduce our novel approach to analyse electronic structures of molecules using "electronic stress tensor" and apply this

method to the aluminum hydride clusters. We, in particular, discuss chemical bonds between aluminum and hydrogen. We also introduce our recently-developed way to study electronic structures of molecules under the existence of electronic current. We apply this to the aluminum hydride clusters and investigate its effect on the aluminum-hydrogen bonds. This may lead to provide us a hint to control hydrogen desorption from materials.

7.2 Theory and calculation method

7.2.1 Electronic structure calculation

We perform ab initio quantum chemical calculation for hydrogenated aluminum clusters. The optimizations of the geometries of the clusters and electronic structures are calculated by GAUSSIAN03 program package [1] using density functional theory (DFT) with B3LYP functional [2,3]. 6-311++G** basis set [4-6] is used for the diffuse and polarization functions. As for the calculation of the electronic state in electronic current, we follow our recently developed procedure, which is described in Ref. 7.

7.2.2 Regional DFT calculation

The theoretical method utilized in this study (Regional Density Functional Theory: RDFT) allows one to assign energy density to any point in space according to associated electronic density. The obtained energy density might be decomposed into following energy densities: the kinetic energy density, the external potential energy density, and the interelectron potential energy density [8]. The details of the theory can be found elsewhere [8-15] and here we would like to only briefly review a part of it, directly related to this study. The non-positively defined kinetic energy density $n_T(\vec{r})$ [9] plays a particular role in the theoretical method used in this study. The unique concept of electronic drop ($R_{\rm D}$) and electronic atmosphere ($R_{\rm A}$) regions, separated with interface surface (S) is used to define shape of atoms and molecules [9]. In the $R_{\rm D}$ region, where kinetic energy density, the classical movement of electrons is granted, while in $R_{\rm A}$ ($n_T(\vec{r}) < 0$) only quantum effects for electrons are possible and the S defines a turning point for an electron. Below, m denotes

the electron mass and ν_i denotes the occupation number of the natural orbital $\psi_i(\vec{r})$. Here,

$$n_T(\vec{r}) = -\frac{\hbar^2}{4m}\sum_i \nu_i[\psi_i^*(\vec{r})\Delta\psi_i(\vec{r}) + \Delta\psi_i^*(\vec{r})\psi_i(\vec{r})], \tag{7.1}$$

and

$$\begin{aligned} R_{\rm D}: &\quad n_T(\vec{r}) > 0, \\ R_{\rm A}: &\quad n_T(\vec{r}) < 0, \\ \mathrm{S}: &\quad n_T(\vec{r}) = 0. \end{aligned} \tag{7.2}$$

The electronic structure of system under study is characterized using electronic stress tensor $\tau^{Skl}(\vec{r})$ [9-15]

$$\tau^{Skl}(\vec{r}) = \frac{\hbar^2}{4m}\sum_i \nu_i\Big[\psi_i^*(\vec{r})\frac{\partial^2\psi_i(\vec{r})}{\partial x^k x^l} - \frac{\partial\psi_i^*(\vec{r})}{\partial x^k}\frac{\partial\psi_i(\vec{r})}{\partial x^l} + \frac{\partial^2\psi_i^*(\vec{r})}{\partial x^k x^l}\psi_i(\vec{r}) - \frac{\partial\psi_i^*(\vec{r})}{\partial x^l}\frac{\partial\psi_i(\vec{r})}{\partial x^k}\Big], \tag{7.3}$$

which describes the internal distortion of electronic density. The three eigenvalues of stress tensor and their eigenvectors determining principal axis can be used for geometrical visualization of bonding as well as quantitative evaluation of its properties and reactive regions in molecules [16-18]. The trace over the eigenvalues of stress produces energy density $\varepsilon_\tau^S(\vec{r})$ in non-relativistic limit of the Rigged QED [12],

$$\varepsilon_\tau^S(\vec{r}) = \frac{1}{2}\sum_k \tau^{Skk}(\vec{r}), E = \int d^3\vec{r}\varepsilon_\tau^S(\vec{r}). \tag{7.4}$$

The total force acting on electrons in the system is composed of Lorentz force $\hat{\vec{L}}^S(\vec{r})$ and tension force $\hat{\vec{\tau}}^S(\vec{r})$. For system in stationary state the total force at every point in space equals zero, thus Lorentz force exactly cancels the tension force.

$$\hat{\vec{F}}^S(\vec{r}) = \hat{\vec{\tau}}^S(\vec{r}) + \hat{\vec{L}}^S(\vec{r}), \tag{7.5}$$

$$\langle\hat{\vec{\tau}}^S(\vec{r})\rangle + \langle\hat{\vec{L}}^S(\vec{r})\rangle = 0, \tag{7.6}$$

$$\begin{aligned} \tau^{Sk}(\vec{r}) &= \partial_l\tau^{Skl}(\vec{r}) \\ &= \frac{\hbar^2}{4m}\sum_i \nu_i\Big[\psi_i^*(\vec{r})\frac{\partial\Delta\psi_i(\vec{r})}{\partial x^k} - \frac{\partial\psi_i^*(\vec{r})}{\partial x^k}\Delta\psi_i(\vec{r}) + \frac{\partial\Delta\psi_i^*(\vec{r})}{\partial x^k}\psi_i(\vec{r}) - \Delta\psi_i^*(\vec{r})\frac{\partial\psi_i(\vec{r})}{\partial x^k}\Big]. \end{aligned} \tag{7.7}$$

If one investigates the tension force in the bonding regions of molecule in stationary state, one might find a point where (along with condition $\vec{F}^S(\vec{r}) = 0$) the tension (as well as Lorentz force) itself will vanish and any force acting on electron density at that point will be zero [9-15]. The point is called a Lagrange point ($\vec{r}_{Lagrange}$) and it is a stationary point for electron density distribution in a molecule [16,17]. The properties calculated at $\vec{r}_{Lagrange}$ can be used to characterize respective interaction between atoms. The energy density based bond order indices were proposed [16,17]:

$$b_\varepsilon = \frac{\varepsilon^S_{\tau AB}(\vec{r}_{Lagrange})}{\varepsilon^S_{\tau HH}(\vec{r}_{Lagrange})}, \tag{7.8}$$

$$b_\mu = \frac{\varepsilon^S_{\tau AB}(\vec{r}_{Lagrange})}{n^S_{AB}(\vec{r}_{Lagrange})}\left(\frac{\varepsilon^S_{\tau HH}(\vec{r}_{Lagrange})}{n^S_{HH}(\vec{r}_{Lagrange})}\right)^{-1}, \tag{7.9}$$

$$\tag{7.10}$$

where $\varepsilon^S_{\tau AB}(\vec{r}_{Lagrange})$ is the energy density at the Lagrange point of bond of interest and $\varepsilon^S_{\tau HH}(\vec{r}_{Lagrange})$ is the energy density at Lagrange point of the H-H bond in a H_2. In b_μ index, $n_{AB}(\vec{r}_{Lagrange})$ and $n_{HH}(\vec{r}_{Lagrange})$ denote corresponding electronic density respectively. The ratio of energy density to electronic density gives a linear approximation of the regional electronic chemical potential μ_R [16-18]

$$\mu_R = \frac{\partial E_R}{\partial N_R} \approx \frac{\varepsilon^S_\tau(\vec{r})}{n_R(\vec{r})}, \tag{7.11}$$

thus b_μ index is called chemical potential bond order.

These quantities are calculated by Molecular Regional DFT program (MRDFT) package developed by our group [19].

7.3 Results and discussion

7.3.1 Energy density based bond order and spindle/pseudo-spindle structures

We begin by showing the results of the Lagrange point search and bond order calculation for Al clusters (Al_n, $n = 2-8$) and hydrogenated Al clusters (Al_nH_m , $n = 1-8$ and $m = 1,2$). The optimized structures are obtained based on those reported in Ref. 20. After we obtain the structures, we search for the Lagrange point, where tension vector vanishes,

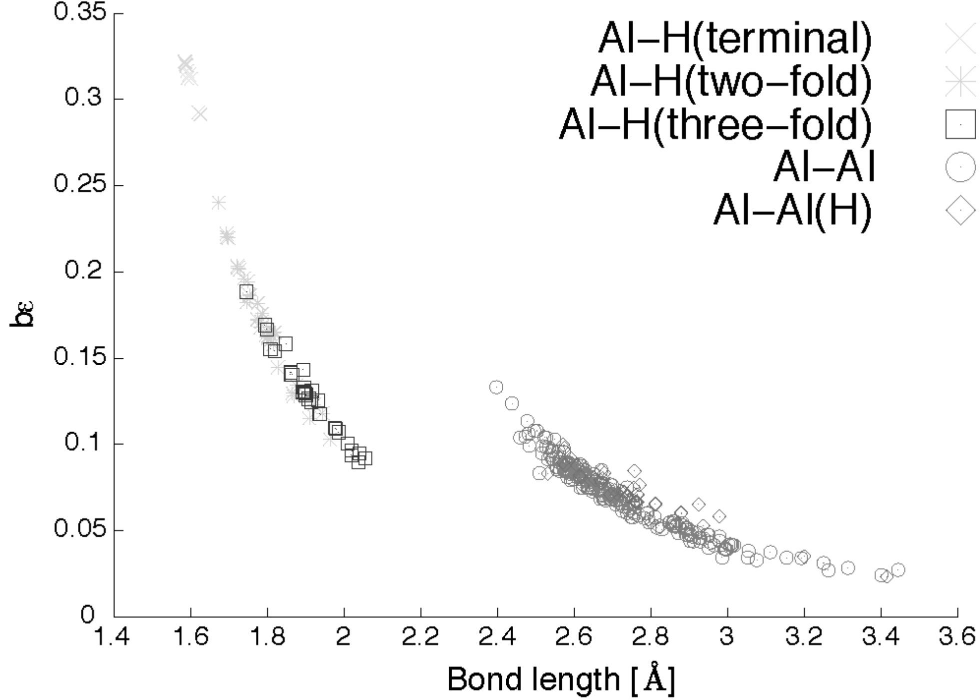

Figure 7.1: The relation between bond length and energy density bond order b_ε for Al clusters (Al_n, $n = 2 - 8$) and hydrogenated Al clusters (Al_nH_m , $n = 1 - 8$ and $m = 1, 2$).

between atom pairs and if found, we compute the energy density and bond order as Eq. (8). For similar calculation for hydrogenated tetrahedral Al_4 clusters, we refer to Ref. 21. We summarize the result in Fig. 7.1. We plot bond order against the bond length for all the bonds in the clusters mentioned above.

In the figure, we distinguish between different types of bonding. The types we consider are Al-Al, terminal Al-H, two-fold Al-H and three-fold Al-H. Here, two-fold Al-H bond is associated with the H atom bridging two Al atoms like Al-H-Al and, similarly for three-fold Al-H bond with the H atom bonded to three Al atoms. As for Al-H bonds, although two-fold and three-fold bonds have lower bond order than terminal ones, they seem to be on the same family of curve in the plot. Hence we expect there is not much difference among Al-H bonds with different number of coordination. As for Al-Al bonds, bare Al clusters and hydrogenated Al clusters are on the same curve in the plot. Therefore it can be said that the bonding nature do not change much upon hydrogenation.

We next examine Al-H-Al bridging bond more closely via electronic stress tensor. We plot the largest eigenvalue of the electronic stress tensor and corresponding eigenvector, which is

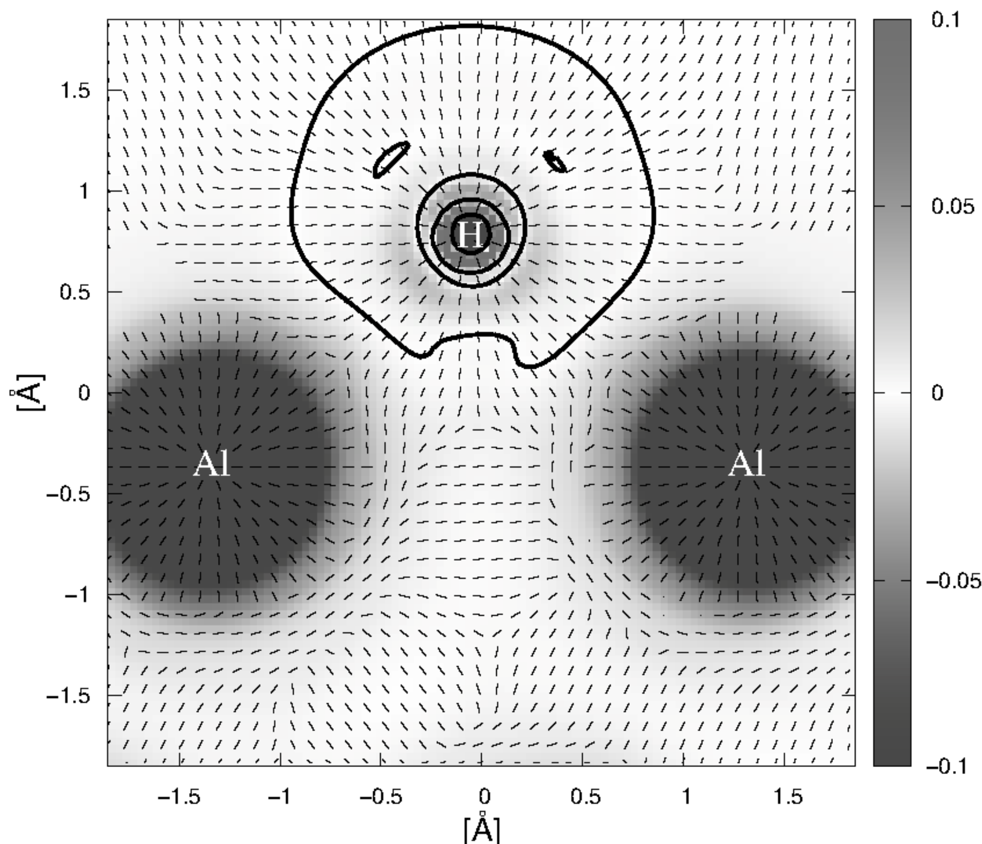

Figure 7.2: The largest eigenvalue of the electronic stress tensor and corresponding eigenvector for Al-H-Al bridging bond. The solid lines show zero contour of the eigenvalue and regions including Al atoms has negative values.

considered to give the directionality of the chemical bond. We see a bundle of flow lines that connects Al and H. We see similar structure between two Al's. The difference is that the former has a positive eigenvalue region ("spindle structure") and the latter has a negative eigenvalue region ("pseudo-spindle structure"). The spindle structure defines covalency of the bonding. The pseudo-spindle structure is known to represent some different types of bonding. One of them is a bond between metallic atoms as in this case.

7.3.2 Electronic structure under the presence of electronic current and the electronic stress tensor

We analyze the electronic structure of AlH_3 by the electronic stress tensor when there is electronic current. We we use our recently developed procedure, which is described in

Ref. 7 for the calculation of the electronic structure under the existence of the electronic current. In Ref. 7, the electronic current is realized by the boundary condition on HOMO, which is constrained to have a form as $\exp(-a_x x^2)\exp(-a_y y^2)\exp(ik_z z)$. Here, a_x and a_y are constants which are taken to be 0.01 a.u. and k_z is a parameter for the electronic current. We take k_z to be -0.1 and -0.5 below.

The results of stress tensor calculation are shown in Fig. 7.3. The panel (a) shows the result when there is no electronic current. There is a spindle structure between three Al-H pairs but the flow lines do not connect between two H atoms. For k_z = -0.1, shown in the panel (b), we see the spindle structure is formed between one of the H-H pairs (center bottom part of the figure). Other H-H pairs seem to exhibit pseudo-spindle structure. For k_z = -0.5, as shown in the panel (c), the spindle structure between the H-H pair is changed to the pseudo-spindle structure. The turning point is about k_z = -0.3.

7.4 Summary

In this paper, we have studide the chemical bonds of small Al clusters (Al_n, n=2-8) and hydrogenated Al clusters (Al_nH_m , n=1-8 and m=1,2) using electronic stress tensor. We calculated the energy density based bond order for these clusters and found that we can classify bond type on the bond length v.s. bond order plot. We have also studied the electronic structure under the presence of electronic current by the electronic stress tensor for AlH_3 molecule. When we turned on the electronic current, a spindle structure first formed between one of the H-H pairs and as we increase the electronic current, the spindle structure changed to a pseudo-spindle structure.

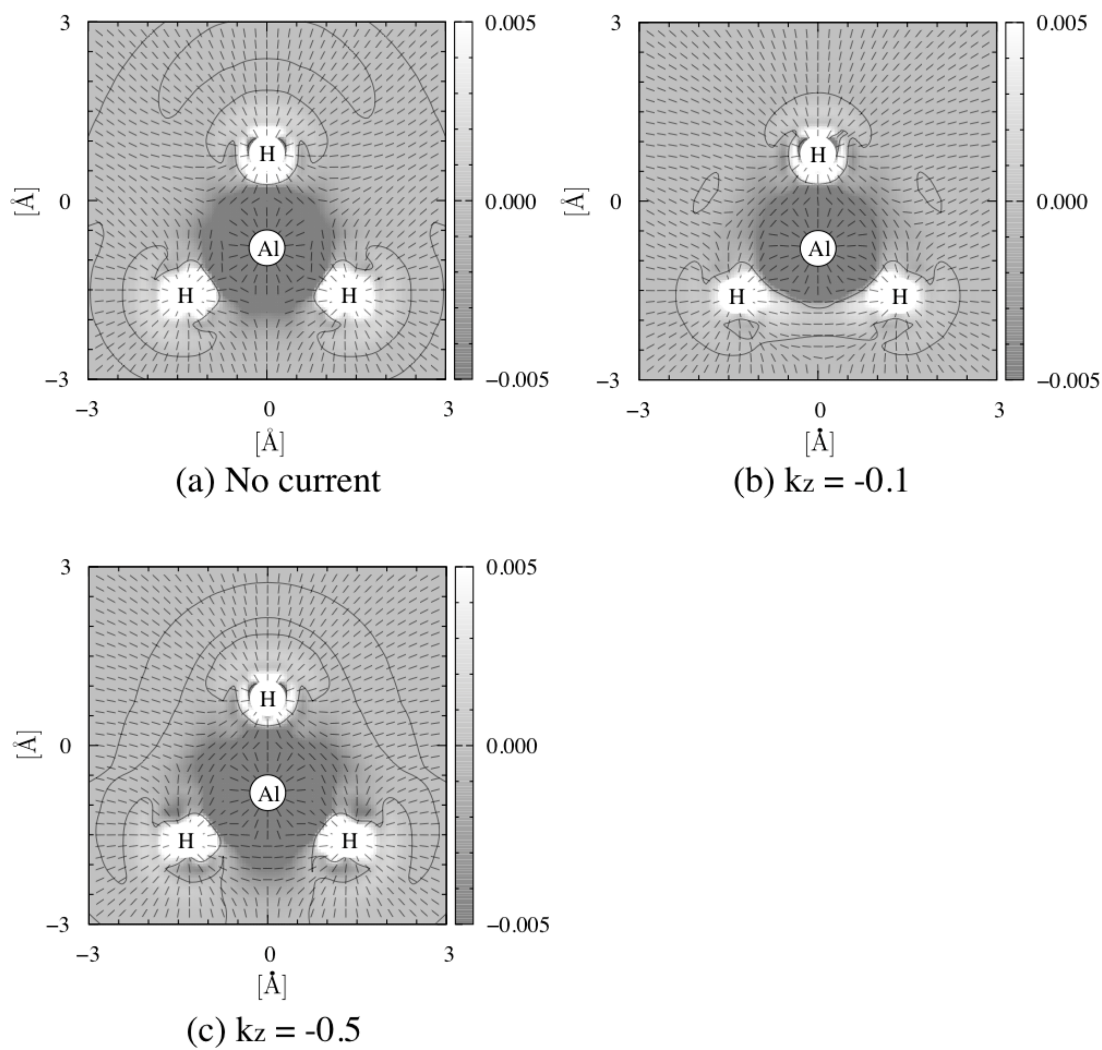

Figure 7.3: Comparison of the largest eigenvalue of the electronic stress tensor and corresponding eigenvector for AlH_3 : (a) no electronic current, (b) electronic current k_z = -0.1, and (c) k_z = -0.5. The solid lines show zero contour of the eigenvalue.

Reference

[1] Gaussian 03, Revision C.02, M. J. Frisch et al, Gaussian, Inc., Wallingford CT, (2004).

[2] A. D. Becke, J. Chem. Phys. **98**, 5648 (1993).

[3] C. Lee, W. Yang and R. G. Parr, Phys. Rev. B **37**, 785 (1988).

[4] R. C. Binning Jr. and L. A. Curtiss, J. Comp. Chem. **11**, 1206 (1990).

[5] L. A. Curtiss, M. P. McGrath, J.-P. Blaudeau, N. E. Davis, R. C. Binning Jr., and L. Radom, J. Chem. Phys. **103**, 6104 (1995)

[6] M. P. McGrath and L. Radom, J. Chem. Phys. **94**, 511 (1991).

[7] M. Senami, Y. Ikeda, A. Fukushima, and A. Tachibana, Jpn. J. Appl. Phys. **49**, 115002 (2010).

[8] A. Tachibana, Theor. Chem. Acc. **102**, 188 (1999).

[9] A. Tachibana, J. Chem. Phys. **115**, 3497 (2001).

[10] A. Tachibana, in *Stress Induced Phenomena in Metallization*, edited by S. P. Baker, (American Institute of Physics, New York, 2002), p. 105.

[11] A. Tachibana, in *Reviews in Modern Quantum Chemistry, A Celebration in the Contributions of Robert Parr*, edited by K. D. Sen, (World Scientific, Singapore, 2002), Chap. 45, p. 1327.

[12] A. Tachibana, in *Fundamental World of Quantum Chemistry, A Tribute to the Memory of Per-Olov Löwdin*, edited by E. J. Brändas and E. S. Kryachko, (Kluwer Academic, Dordrecht, 2003), Vol. 2, p. 211.

[13] A. Tachibana, Int. J. Quant. Chem. **100**, 981 (2004).

[14] A. Tachibnana, J. Mol. Model. **11**, 301 (2005).

[15] A. Tachibana, J. Mol. Struct.: THEOCHEM **943**, 138 (2010).

[16] P. Szarek and A. Tachibana, J. Mol. Model. **13**, 651 (2007).

[17] P. Szarek, Y. Sueda, and A. Tachibana, J. Chem. Phys. **129**, 94102 (2008).

[18] P. Szarek, K. Urakami, C. Zhou, H. Cheng, and A. Tachibana, J. Chem. Phys. **130**, 084111 (2009).

[19] M. Senami, K. Ichikawa, K. Doi, P. Szarek, K. Nakamura, and A. Tachibana, Molecular Regional DFT program package, ver.3 (Tachibana Lab., Kyoto University, Kyoto, 2008).

[20] H. Kawamura, V. Kumar, Q. Sun, and Y. Kawazoe, Phys. Rev. B **65**, 045406 (2001).

[21] K. Ichikawa, Y. Ikeda, A. Wagatsuma, K. Watanabe, P. Szarek, and A. Tachibana, Int. J. Quant. Chem. **111**, 3548 (2011).

Chapter 8

Theoretical Study of Adsorption of Lithium Atom on Carbon Nanotube

8.1 Introduction

Carbon nanotubes (CNTs) have been paid much attention since its discovery in 1991 [1], due to their outstanding mechanical and electric properties [2–5]. Very high Young's modulus of CNTs has been predicted by theoretical studies [3] and confirmed in experiments [4]. Electric properties such as conductance are dependent on the radius and chirality of a CNT through the change of band gap [5, 6].

CNTs have been considered as a candidate of anode materials for lithium ion battery. A theoretical study reported that the density of lithium insertion attains LiC_2, since both the interior and exterior of CNTs are suitable for storage [7]. This lithium storage capability is three times higher than that of normal graphite, LiC_6 [8]. However, primary experiments reported only a poor increase of the reversible capacity of lithium compared to that of graphite [9]. In addition, a very large amount of irreversible lithium storage was reported. These features suggests that lithium are stored in the inside of CNTs as unavailable form.

It was reported that the reversible capacity is independent of whether the ends of single wall CNTs (SWCNTs) are open, though the amount of lithium storage is increased due to the diffusion into the inside of CNTs [10]. This imply two facts. One is that the direct diffusion through the sidewalls of pristine CNTs is difficult for lithium ions. Second, lithium (not necessarily ions) stored in the interior of CNTs through open ends of CNTs is not

suitable for lithium ion battery as reversible resources. In other words, electrolyte molecules and lithium ions solvated with the electrolyte molecules can freely enter into the interior of CNTs, and this inner surface of the CNTs does not provide available site for lithium ion storage, since the inner surface is similar to the basal plane of the graphite in the electrolyte. Recently, some ideas using steric effects are proposed to improve the reversible capacity of lithium ions [11, 12]. It was proposed that the electrolyte molecules and the solvated lithium ions are eliminated by screen materials or defects on the end of CNTs and only bare lithium ions are stored in interior of the CNTs after the desolvation of the solvated lithium ions [12]. They argued that the inner surface of CNTs can provide available site for the bare lithium ions. In their results, the density of lithium storage only in the interior of the (12,0) zigzag SWCNT was shown as LiC_6 by *ab intio* quantum chemical calculations.

In this study, we investigate the adsorption of lithium atoms on the surface of the (12,0) SWCNT and the limit of the storage by using *ab initio* quantum chemical calculations. We clarify the difference between the adsorptions on the inside and outside of the SWCNT in viewpoints of charge transfer and regional chemical potential density, which is defined by one of the authors [13, 14]. As a result, the advantage of the adsorption on the inside of this SWCNT is shown. We also study the storage density on the interior of the SWCNT in terms of adsorption energy and charge transfer. As a result, we find that the interaction between lithium atoms is a key ingredient for this thin tube. We show that this interaction changes as lithium density increases, in viewpoints of the local charge density

8.2 Computational Details

We use the (12,0) zigzag type CNT model. The model is shown in Fig. 8.1. This model consists of 144 carbon atoms and 24 hydrogen atoms, which are used for the termination of dangling bonds. The structure of this model is determined by the geometrical optimization calculation. The positions of all atoms are relaxed. As a result, the averages of bond lengths are calculated as 1.43 Å for C-C bonds and 1.09 Å for C-H bonds.

In this paper, we study this SWCNT by using *ab initio* quantum chemical calculations. Electronic structure calculations are performed by density functional theory (DFT). In DFT calculations, the Lee-Yang-Parr gradient-corrected functions [15] is selected for

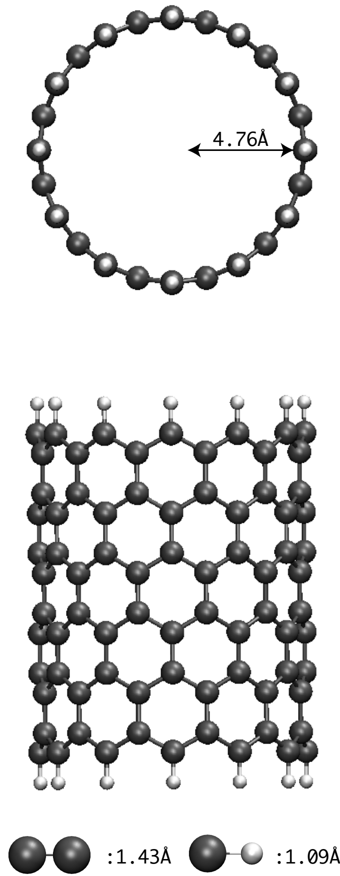

Figure 8.1: The (12,0) SWCNT model. Dark (black) circles are carbon atoms, and light (blue) ones are hydrogen atoms.

the correlation interaction, and it is employed with Becke's hybrid three parameters [16] for generalized-gradient-approximation exchange-correlation functions. These calculations are carried out by GAUSSIAN03 program package [17]. The basis sets are chosen as the 6−31G* basis set for carbon and lithium atoms [18, 19] and the 3−21G** basis set for hydrogen atoms [19, 20]. Zigzag SWCNTs with hydrogen termination are known to have spin polarized ground states [21]. Hence, we choose the lowest energy state among all spin multiplicity states in our calculations. Septet state gives the lowest one for the (12,0) CNT without lithium atoms.

We analyze electronic states and properties using quantum energy density, which is proposed by one of the authors [13, 22, 23]. One of the quantities of the quantum energy

density, the electronic kinetic energy density $n_T(\vec{r})$, is defined as,

$$n_T(\vec{r}) = \frac{1}{2}\sum_i \nu_i \left\{ \left[-\frac{\hbar^2}{2m}\Delta\psi_i^*(\vec{r}) \right] \psi_i(\vec{r}) + \psi_i^*(\vec{r}) \left[-\frac{\hbar^2}{2m}\Delta\psi_i(\vec{r}) \right] \right\}, \tag{8.1}$$

where m is the electron mass, $\psi_i(\vec{r})$ is the ith natural orbital, and ν_i is the occupation number of $\psi_i(\vec{r})$. The integration of kinetic energy density over the whole space is the kinetic energy of a system. In classical mechanics, only positive kinetic energy is allowed, while negative kinetic energy appears in quantum mechanics. This means that electrons can also exist in regions with negative kinetic energy density by quantum effects. The surface of zero kinetic energy density can be interpreted as the boundary of a covalent molecule.

The electronic structure of a system is characterized using electronic stress tensor $\tau^{Skl}(\vec{r})$,

$$\begin{aligned} \tau^{Skl}(\vec{r}) &= \frac{\hbar^2}{4m}\sum_i \nu_i \left[\psi_i^*(\vec{r})\frac{\partial^2\psi_i(\vec{r})}{\partial x^k \partial x^l} - \frac{\partial\psi_i^*(\vec{r})}{\partial x^k}\frac{\partial\psi_i(\vec{r})}{\partial x^l} \right. \\ &\quad \left. + \frac{\partial^2\psi_i^*(\vec{r})}{\partial x^k \partial x^l}\psi_i(\vec{r}) - \frac{\partial\psi_i^*(\vec{r})}{\partial x^l}\frac{\partial\psi_i(\vec{r})}{\partial x^k} \right], \end{aligned} \tag{8.2}$$

which describes the internal distortion of electronic density. The three eigenvalues of stress tensor and their eigenvectors determining principal axis can be used for quantitative evaluation of properties of bonding and reactive regions in molecules. The trace over the eigenvalues of stress tensor produces energy density $\epsilon_\tau^S(\vec{r})$ in the non-relativistic limit of the Rigged QED,

$$\epsilon_\tau^S(\vec{r}) = \frac{1}{2}\sum_k \tau^{Skk}(\vec{r}), \tag{8.3}$$

$$E = \int d^3\vec{r}\epsilon_\tau^S(\vec{r}). \tag{8.4}$$

The ratio of energy density to electronic density gives a linear approximation of the regional electronic chemical potential μ_R,

$$\mu_R = \frac{\delta E_R}{\delta n_R} \approx \frac{\epsilon_\tau^S(\vec{r})}{n_R(\vec{r})}. \tag{8.5}$$

In this work, the calculations of these quantities of quantum energy density are carried out by using Molecular Regional DFT program package (MRDFT) [24].

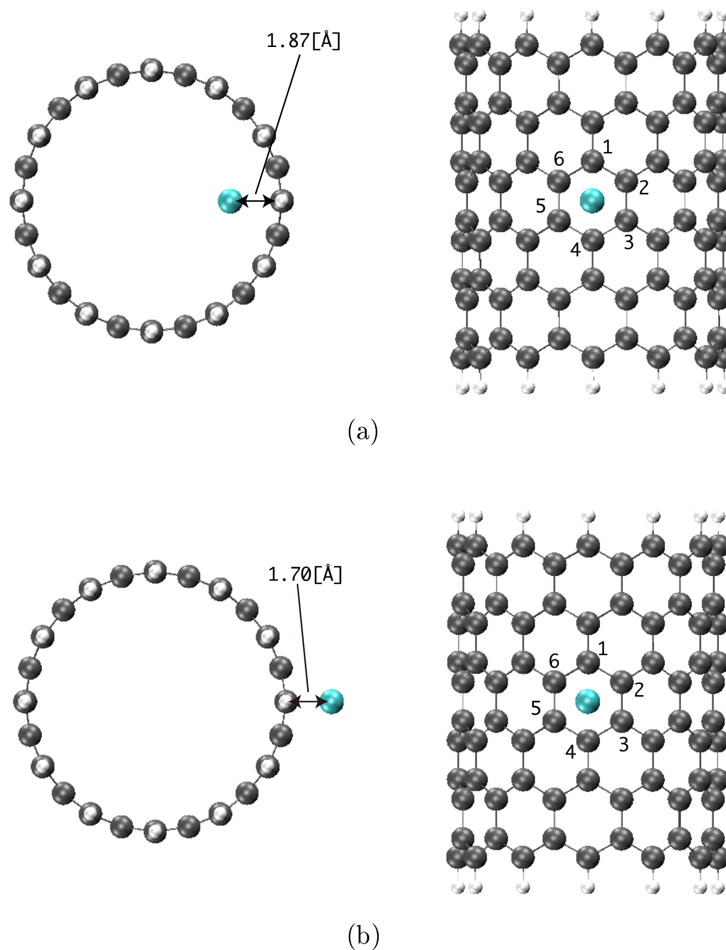

Figure 8.2: Optimized structures of the models of (12,0) SWCNTs with one lithium atom. Panels (a) and (b) show the structures of the CNT with one inside and outside lithium atom, respectively.

8.3 Result and Discussion

8.3.1 The electronic structure of one lithium adsorbed carbon nanotube models

First, we consider the difference between the adsorption of lithium atom on the inside and outside of the (12,0) SWCNT. Optimized structures of the models of (12,0) SWCNTs with one lithium atom are shown in Fig. 8.2. Panels (a) and (b) show the structures of the CNT with one inside and outside lithium atom, respectively. In geometrical optimization calculations, the positions of all atoms are relaxed. The deformation of the CNT by the

attachment of a Li atom is negligibly small. The optimized distances between the Li atom and CNT are 1.87 Å and 1.70 Å for the inside and outside adsorption, respectively.

The lithium adsorption energy in this work is defined as,

$$\Delta E \;=\; E_{\mathrm{CNT}+N_{\mathrm{Li}}\times\mathrm{Li}} - E_{\mathrm{CNT}} - N_{\mathrm{Li}} \times E_{\mathrm{Li}}, \tag{8.6}$$

where E_{Li} is the energy of one lithium atom and N_{Li} is the number of lithium atoms. The adsorption energy of one lithium atom on the inside is -0.98 eV, while that on the outside is -0.86 eV. As a result, the inside of the CNT is more favored for the adsorption of one lithium atom. This is in contrast to some results for the attachment on C_{60}[25], in which exohedral fullerenes are more favored. In the following, we study the reason of the difference of the adsorption energy.

To clarify the interaction between the CNT and the lithium atom, the charge transfer is known to be important [26, 27]. Hence, we analyze the NBO charge of the lithium atom. The NBO charge of the lithium atom of the inside of the CNT is calculated as 0.92, while that of the outside is 0.89. This small difference of the charge transfer is attributed to a curvature of the CNT. For the lithium atom on the outside, the nearest carbon atoms are C(1) and C(4), where the position of each carbon atom is shown in Fig. 8.2 by the number in a parenthesis. On the other hand, the nearest ones are C(2), C(3), C(5), and C(6) for the inside. In addition, the distances from the inside Li atom to carbon atoms in next hexagonal rings are shorter than those from the outside one. Hence, for the inside adsorption, the transfered charge from the Li atom can be distributed for the larger number of carbon atoms.

The distribution of the difference of electron density, i.e., charge transfer, is shown in Fig. 8.3. The charge transfer is given by the difference of the electron density,

$$\Delta\rho(\vec{r}) = \rho(\vec{r})_{\mathrm{CNT}+N_{\mathrm{Li}}\times\mathrm{Li}} - \rho(\vec{r})_{\mathrm{CNT}} - \rho(\vec{r})_{N_{\mathrm{Li}}\times\mathrm{Li}}, \tag{8.7}$$

where $\rho(\vec{r})_{\mathrm{X}}$ is the electron density of a system, X. Panels (a) and (b) are the results of the lithium adsorption on the inside of the CNT, while panels (c) and (d) are those for the outside adsorption. Panels (a) and (c) show the plane perpendicular to the axis. Panel (b) (panel (d)) shows the plane including the Li, C(2), and C(3) atoms (Li, C(1), and C(4)), where these carbon atoms are the nearest from the Li atom. The circles in panels (a) and (c) mean the cross section of our CNT model. As seen in Fig. 8.3, electrons around

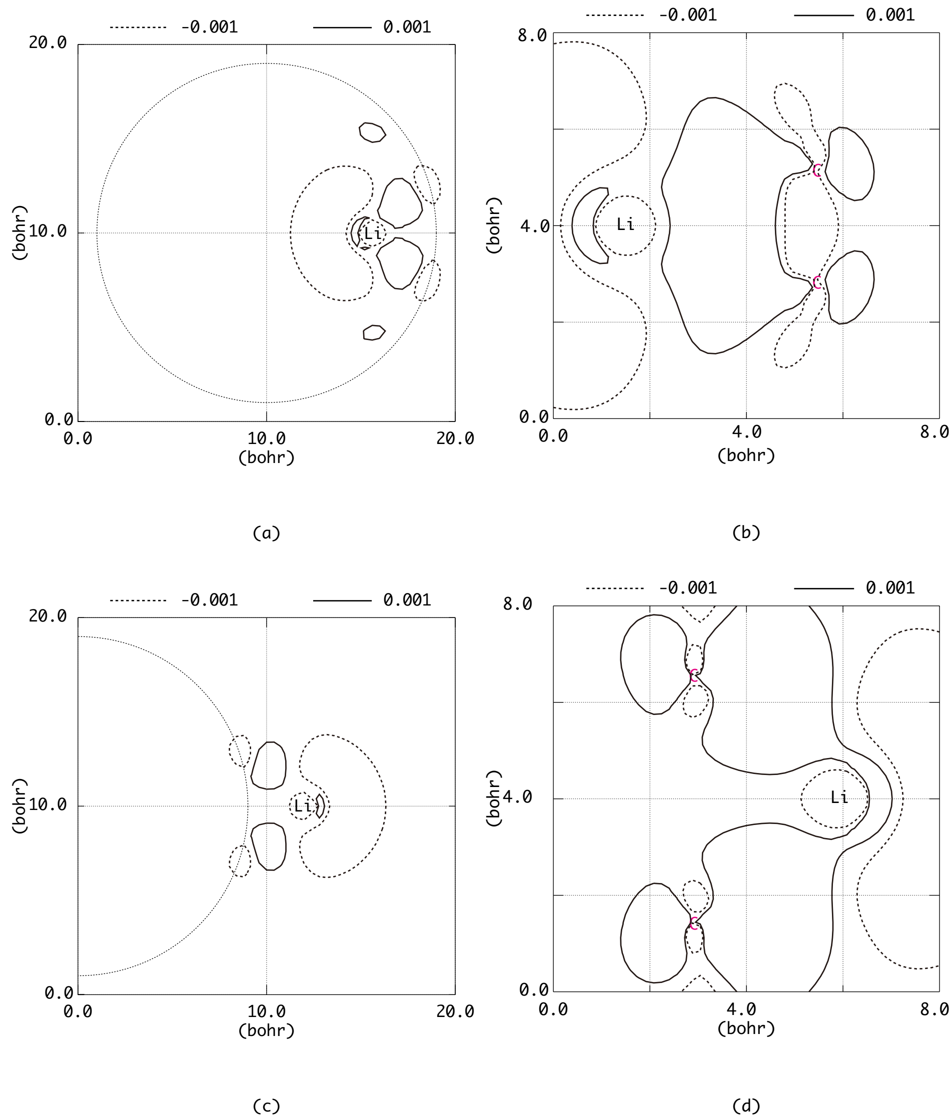

Figure 8.3: Distribution of the difference of electron density. Panels (a) and (b) are the results of the lithium adsorption on the inside of the CNT, while panels (c) and (d) are those on the outside. Panels (a) and (c) show the plane perpendicular to the axis. Panel (b) (panel (d)) shows the plane including the Li, C(2), and C(3) atoms (Li, C(1), and C(4)), where a carbon atom specified in a parenthesis corresponds to that shown in Fig. 8.2. The circles in panels (a) and (c) mean the cross section of our CNT model.

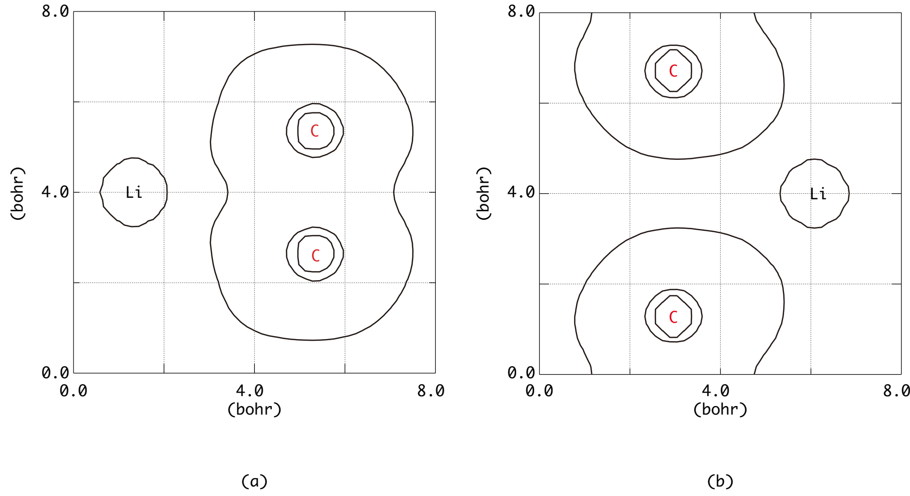

Figure 8.4: The zero kinetic energy density surface. Panels (a) and (b) are the results of the lithium adsorption on the inside and outside of the CNT, respectively. Panel (b) (panel (d)) shows the plane including the Li, C(2), and C(3) atoms (Li, C(1), and C(4)), where a carbon atom specified in a parenthesis corresponds to that shown in Fig. 8.2.

lithium atoms move to the regions around carbons for both cases. We can see some common properties for both distribution patterns. For example, the electron density decreases behind the lithium atom, and the density increases between Li and C atoms and around C atoms. However, one outstanding feature of the inside adsorption is the larger density increase around carbon atoms in next hexagonal rings as seen in panel (a). This is due to the difference of the distance from the lithium atom as explained above.

In Fig. 8.4, we show the zero kinetic energy density surface. The definition of the kinetic energy density is given in Eq. (8.1). Panels (a) and (b) show the results for the same planes in Fig. 8.3(b) and (d), respectively. It has been shown that this quantity classifies whether a bond has covalent property [13, 22, 23]. The positive kinetic energy region extends between atoms if the bond between the atoms has covalent property. This feature can be seen between carbon atoms in panel (b). For a bond with ionic property, we see two separate positive kinetic energy regions associated with two atoms. As seen in Fig. 8.4, since the positive kinetic energy regions associated with Li and C atoms are separate for both inside and outside adsorptions, we have confirmed that covalent property is weak and an ionic property is seen for the Li-C bond by our kinetic energy density. Hence, the inside adsorption is favored due to the difference of the charge transfer, which originates in the

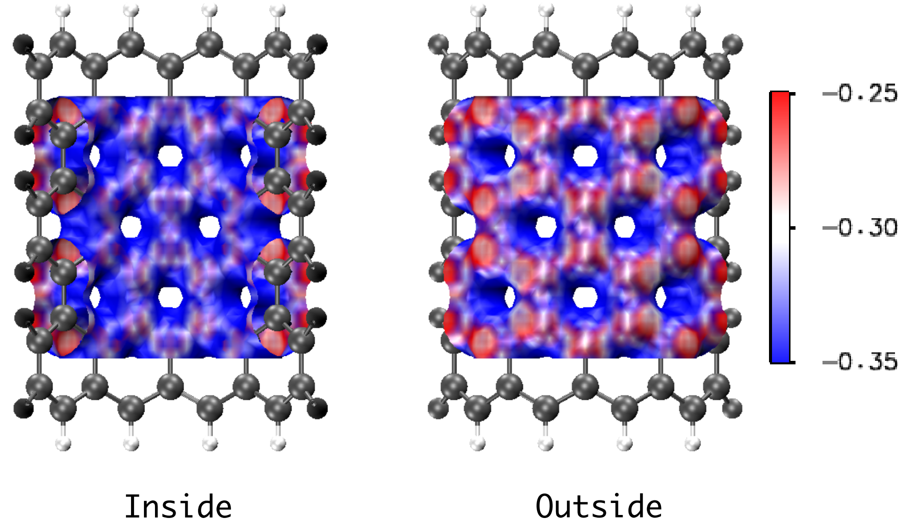

Figure 8.5: Regional chemical potential density of our CNT model without the lithium atom on the zero kinetic energy surface.

curved structure of the CNT wall.

Our novel analysis tool, the linear approximation of the regional chemical potential density [13, 14], supports the above conjecture. We show the regional chemical potential density on the zero kinetic energy density surface in Fig. 8.5. As seen in this figure, the value of the regional chemical potential density of the hexagon on the outer surface is larger than that on the inner surface. As seen in the definition, the regional chemical potential density means the energy per one electron. Our result shows that electrons on the inner surface have lower energy. The region where electrons have lower energy is more favored for the increase of electron density. For the attachment of lithium atoms, the charge is transfered from lithium atoms to the CNT as shown above. Therefore, the interior of isolated SWCNTs is more favorable for the attachment of lithium atoms compared to the exterior of them.

8.3.2 The electronic structure of multiple lithium atoms adsorption model

In previous subsection, we have confirmed that the interior of the (12,0) SWCNT is favored for the adsorption of a lithium atom compared to the exterior and shown a reason of this feature. In this subsection, we consider multiple attachment of lithium atoms on the

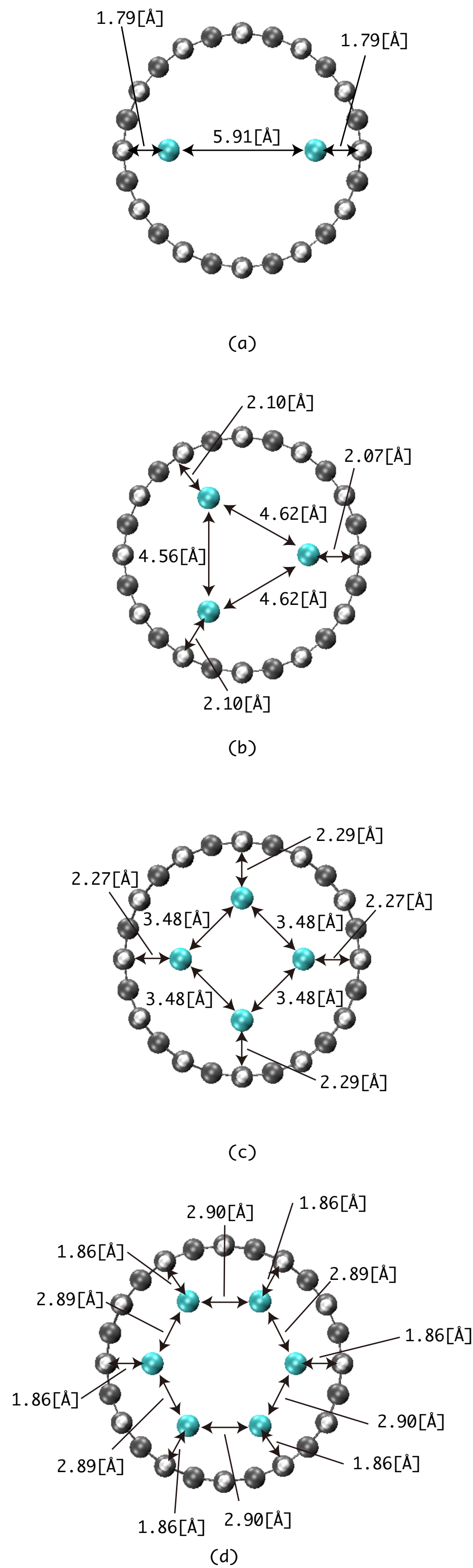

Figure 8.6: The optimized structures of the models of (12,0) SWCNTs with lithium atoms. In panels (a)-(d), two, three, four, and six lithium atoms are attached on the inside of the CNT.

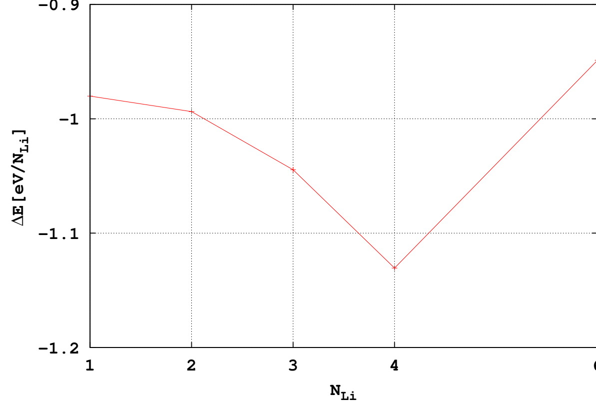

Figure 8.7: Adsorption energy as the function of the number of lithium atoms.

inside of our CNT model.

The structures of the models of (12,0) SWCNTs with lithium atoms are shown in Fig. 8.6. In panels (a)-(d), two, three, four, and six lithium atoms are attached on the inside of the CNT, respectively. The structure of these models are fully optimized by geometrical optimization calculations. We show also Li-Li and Li-CNT distances in Fig. 8.6. The deformation of our CNT models are very small. On the other hand, in a result of first principles calculations by other group [7], the deformation of CNTs by the intercalation of lithium was reported as about 10% in the aspect ratio. In their result, the density of lithium atom are much larger than ours. We consider that their deformation is attributed to the difference of the density. In Fig. 8.6(b), the Li-Li distance is shorter than that for $Li_2@C_{60}$ whose Li-Li distance is about 3 Å[28]. We consider that this difference of the length is due to a difference of reactivity between our CNT model and C_{60}.

In Fig. 8.7, the adsorption energy of lithium atoms is shown as a function of the number of lithium atoms, which is defined in Eq. (8.6). The adsorption energy of four lithium atoms is the largest (-1.13 eV) in this result, and the six lithium structure is strongly destabilized from the four lithium structure. This feature is explained from the viewpoint of the Li-Li distance. As seen from Fig. 8.6, the Li-Li distance becomes short as the number of lithium atoms increases. Particularly, for the insertion of six lithium atoms, Li-Li distances are about 2.9 Å, which is shorter than that of the bulk lithium structure (3.48 Å). Hence, a repulsive force between lithium atoms is expected for this short distance. In contrast, for four lithium model, Li-Li distances are very close to the value of the bulk structure and

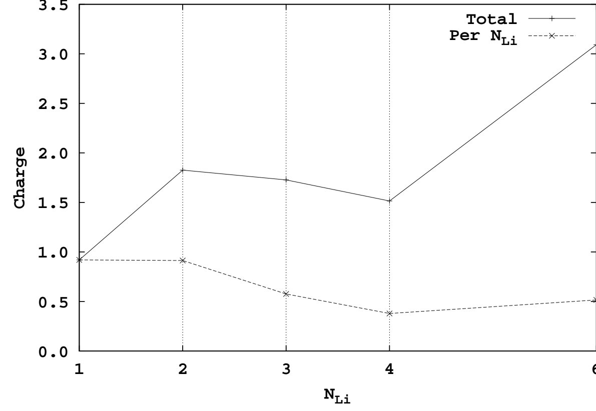

Figure 8.8: NBO charge of lithium atoms as the function of the number of lithium atoms. The solid line is the total charge, and the dashed line is the average for the charge at the number of lithium atoms.

the Li-Li interaction is expected to stabilize these lithium atoms. Therefore, we consider that Li-Li interaction is important for $N_{\mathrm{Li}} \geq 4$ for the (12,0) SWCNT. On the other hand, the Li-CNT distance is the longest for four lithium atoms. Hence, the stabilization of the four lithium model originates more significantly in the Li-Li interaction compared to other models. The decrease of the distance for six lithium atoms is due to the smallness of the cross section of the CNT. For six lithium atoms, lithium atoms does not occupy enough space, and hence they stay near the surface of the CNT. As a result, the six lithium structure is less stabilized than the four lithium one, due to the repulsion between lithium atoms arisen from this narrow space of the inside of the CNT.

Next, we discuss the difference of the stabilization in terms of the NBO charge of lithium atoms. In Fig. 8.8, the NBO charge is shown as the function of the number of lithium atoms. The solid line is the total charge, and the dashed line is the average for the charge per the number of lithium atoms. The average is small for $N_{\mathrm{Li}} \geq 3$, while the total charge is not small. The charge transfer is one of important factors for the stabilization of a system as attractive force between C-Li atoms and repulsive force between Li-Li atoms. For $N_{\mathrm{Li}} \leq 2$, the attractive force is dominantly important, since the average charge is the same for $N_{\mathrm{Li}} = 1$ and 2. On the other hand, the importance of the repulsive force is significant for $N_{\mathrm{Li}} \geq 3$, since the average value of charge is smaller than those for $N_{\mathrm{Li}} = 1$ and 2. Hence, the stabilization mechanism is not so simple and we study the charge transfer in detail below.

The distribution of the difference of electron density is shown in Fig. 8.9. Panels (a), (c), (e), and (g) show the plane perpendicular to the axis. Panels (b), (d), and (h) show the plane including the Li, C(2), and C(6) atoms, and panel (f) is for the Li, C(2), and C(5) atoms, where these carbon atoms are the nearest two C atoms. The circles in panels (a), (c), (e), and (g) mean the cross section of our CNT model. As seen in Fig. 8.9, electron density increase in the regions around carbons and between the nearest C atoms and the lithium atom as one lithium attachment. As seen in panels (a) and (b), the charge distribution difference for $N_{\mathrm{Li}} = 2$ is very similar to that for $N_{\mathrm{Li}} = 1$, and hence the stabilization mechanism is also considered to be the same. For three, four, and six lithium atoms, the electron density around the center of the CNT increases. This is caused by repulsive force by negative charge stored in the CNT wall. It can also be said that this charge increase is induced by the repulsion between lithium atoms, since this feature is only seen for $N_{\mathrm{Li}} \geq 3$ due to the high density of lithium atoms. This charge increase arises from the narrow space in the CNT. As a result, the stabilization is not simply explained by the amount of charge transfer. Although the largest total charge transfer occured for $N_{\mathrm{Li}} = 6$, this large charge also induces large repulsive force between lithium atoms.

8.4 Conclusions

In this study, we have investigated the adsorption of lithium atoms on the surface of the (12,0) zigzag CNT to clarify the interaction between lithium atoms and between a lithium atom and the CNT. For one lithium atom attachment on this CNT, it has been shown that the inside of this (12,0) zigzag CNT is more favorable than the outside. We have shown that after the lithium attachment, charge is transfered from the Li atom to the CNT and the bond between the Li atom and the CNT has ionic property. The amount of charge transfer is larger for the inside attachment than the outside. This feature is studied for the lithium atom adsorption on the (12,0) zigzag CNT in this work. The amount of charge transfer should be dependent on the curvature of the radius of a CNT, and hence it is important for us to investigate this feature for a CNT with different radius.

We have also shown that four lithium insertion for one layer of the carbon hexagon is the most stable. Our model have shown that the electron density around the center of the

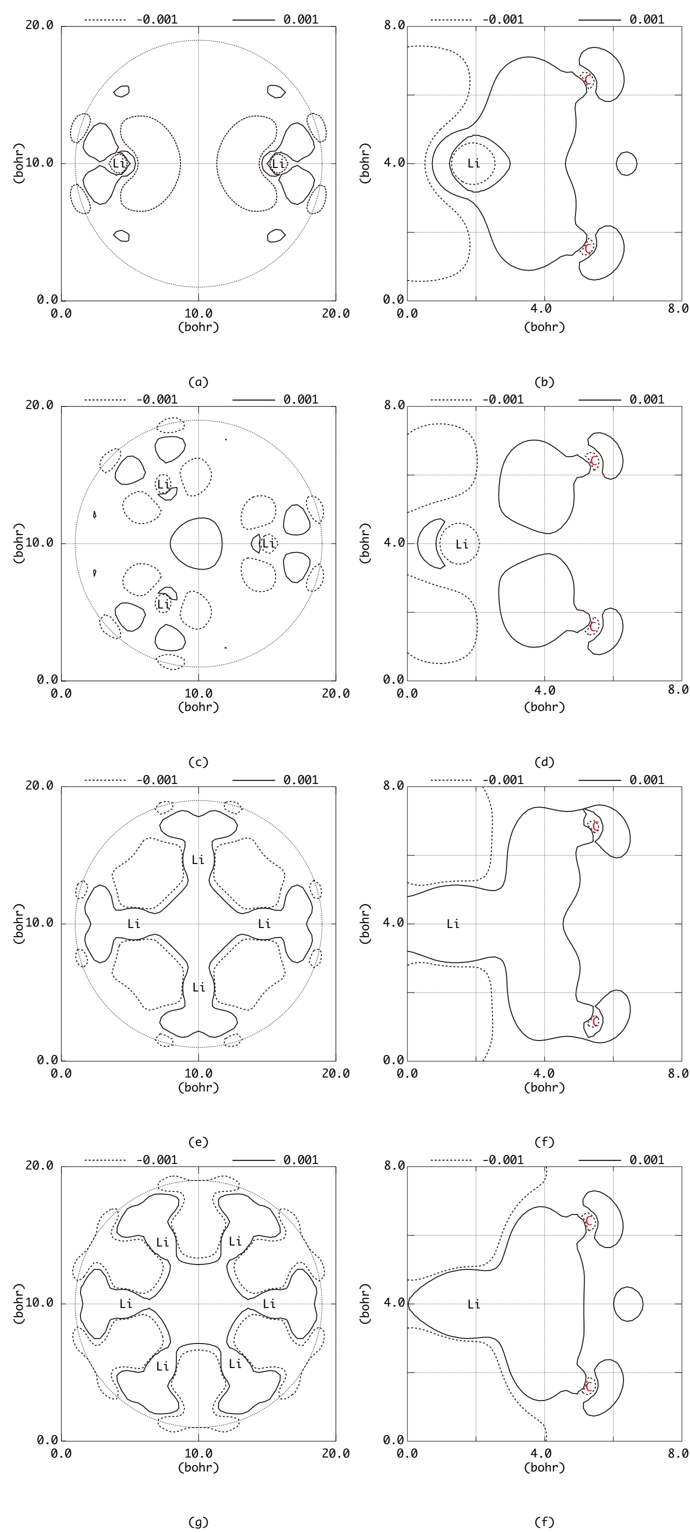

Figure 8.9: Distribution of the difference of electron density. Panels (a), (c), (e), and (g) show the plane perpendicular to the axis. Panels (a), (c), (e), and (g) show the plane perpendicular to the axis. Panels (b), (d), and (h) show the plane including the Li, C(2), and C(6) atoms, and panel (f) is for the Li, C(2), and C(5) atoms, where these carbon atoms are the nearest two C atoms. The circle in panels (a), (c), (e), and (g) means the cross section of our CNT model.

CNT increases significantly for $N_{\mathrm{Li}} \geq 3$. This increase originates in the repulsion between lithium atoms. For the six lithium atom structure, the distance between lithium atoms is shorter than that of the lithium bulk. Hence, the repulsive force between lithium atoms strongly destabilize the system. The structure of four lithium on one layer is much favorable compared to that of six.

Reference

[1] S. Iijima, Nature (London) **354**, 56 (1991).

[2] C.T. White and T.N. Todorov, Nature **393**, 240 (1998); J. Kong, E. Yenilmez, T.W. Tombler, W. Kim, H. Dai, R.B. Laughlin, L. Liu, C.S. Jayanthi, and S.Y. Wu, Phys. Rev. Lett. **87**, 106801 (2001); A. Javey, J. Guo, Q. Wang, M. Lundstrom, and H. Dai, Nature (London) **424**, 654 (2003).

[3] B.I. Yakobson, C.J. Brabeck, and J. Bernholc, Phys. Rev. Lett. **76**, 2511 (1996); J.P. Lu, Phys. Rev. Lett. **79**, 1297 (1997).

[4] M.M. Treacy, T.W. Ebbesen, and J.M. Gibson, Nature (London) **381**, 678 (1996); E.W. Wong, P.E. Sheehan, and C.M. Lieber, Science **277**, 1971 (1997); A. Krishnan, E. Dujardin, T.W. Ebbesen, P.N. Yianilos, and M.M. Treacy, Phys. Rev. B **58**, 14013 (1998); S. Akita, H. Nishijima, T. Kishida, and Y. Nakayama, Jpn. J. Appl. Phys. **39**, 3724 (2000).

[5] N. Hamada, S. Sawada, and A. Oshiyama, Phys. Rev. Lett. **68**, 1579 (1991); R. Saito, M. Fujita, G. Dresselhaus, and M.S. Dresselhaus, Phys. Rev. B **46**, 1804 (1992); R. Saito, M. Fujita, G. Dresselhaus, and M.S. Dresselhaus, Appl. Phys. Lett. **60**, 2204 (1992).

[6] J.W. Ding, X.H. Yan, and J.X. Cao, Phys. Rev. B **66**, 073401 (2002); J.W.G. Wildöer, L.C. Venema, A.G. Rinzler, R.E. Smalley, and C. Dekker, Nature (London) **391**, 59 (1998); T.W. Odom, J.-L. Huang, P. Kim, and C.M. Lieber, J. Phys. Chem. **104**, 2794 (2000); S. Reich, C. Thomsen, and P. Ordejón, Phys. Rev. B **65**, 155411 (2002).

[7] J. Zhao, A. Buldum, J. Han, and J. P. Lu, Phys. Rev. Lett. **85**, 1706 (2000).

[8] For a review, M. Inagaki, in *New Carbons Control of Structure and Functions*, (Elsevier, Amsterdam, 2000), Chap. 6.

[9] B. Gao, A. Kleinhammes, X.P. Tang, C. Bower, L. Fleming, Y. Wu, and O. Zhou, Chem. Phys. Lett. **307**, 153 (1999); G. Maurin, Ch. Bousquet, F. Henn, P. Bernier, R. Almairac, and B. Simon, Chem. Phys. Lett. **312**, 14 (1999).

[10] Z. Yang, H. Wu, Solid State Ionics 143 (2001) 173; S. Komiyama, M. Miyawasi, F. Okino, H. Kataura, H. Touhara, TANSO 216 (2005) 25 (in Japanese).

[11] S. Kawasaki, Y. Iwai, I. Watanabe, Mater. Res. Bull. 44 (2009) 415.

[12] S. Sano, M. Kusunoki, and A. Tachibana, The 50th Battery Symposium in Japan, Abstract No. 3A21 (2009).

[13] A. Tachibana, Theor. Chem. Acc. **102**, 188 (1999); P. Szarek, Y. Sueda, and A. Tachibana, J. Chem. Phys. **129**, 094102 (2008).

[14] P. Szarek and A. Tachibana, J. Mol. Model. **13**, 651 (2007); P. Szarek, K. Urakami, C. Zhou, H. Cheng, and A. Tachibana, J. Chem. Phys. **130**, 084111 (2009).

[15] C. Lee, W. Yann, and R.G. Parr, Phys. Rev. B **37**, 785 (1988).

[16] A.D. Becke, J. Chem. Phys, **98**, 5648 (1993).

[17] M.J. Frisch *et al.*, Gaussian 03, Revision B.05, Gaussian, Inc., Pittsburgh PA (2003).

[18] W.J. Hehre, R. Ditchfield, and J.A. Pople, J. Chem. Phys. **56**, 2257 (1972); J.D. Dill and J.A. Pople, J. Chem. Phys. **62**, 2921 (1975).

[19] P.C. Hariharan and J.A. Pople, Theo. Chim. Acta **28**, 213 (1973).

[20] J.S. Binkley, J.A. Pople, and W.J. Hehre, J. Am. Chem. Soc. **102**, 939 (1980).

[21] T. Pankewitz and W. Klopper, J. Phys. Chem. C **111**, 18917 (2007).

[22] A. Tachibana and R.G. Parr, Int. J. Quantum Chem. **41**, 527 (1992); A. Tachibana, Int. J. Quantum Chem. **32**, 181 (1987); Int. J. Quantum Chem. **57**, 423 (1996); Int. J. Quantum Chem. **100**, 981 (2004); A. Tachibana, K. Nakamura, K. Sakata, and

T. Morisaki, Int. J. Quantum Chem. **74**, 669 (1999); A. Tachibana, J. Chem. Phys. **115**, 3497 (2001); A. Tachibana, in *Stress Induced Phenomena in Metallization*, edited by S. P. Baker (American Institute of Physics, New York, 2002), p. 201-211; A. Tachibana, in *Reviews in modern quantum chemistry:A celebration of the contribution of Robert Parr*, edited by K. D. Sen (World scientific, Singapore, 2002) Vol. 2, p. 1327-1366; A. Tachibana, in *Fundamental Perspectives in Quantum Chemistry: A Tribute to the Memory of Per-Olov Löwdin*, edited by E.J. Brändas and E.S. Kryacho (Kluwer Academic, Dordrecht, 2003) vol. II, p. 211.

[23] A. Tachibana, J. Mol. Model. **11**, 301 (2005); A. Tachibana, J. Mol. Struct.: THEOCHEM **943**, 138 (2010).

[24] M. Senami, K. Ichikawa, K. Doi, P. Szarek, K. Nakamura, and A. Tachibana, Molecular Regional DFT program package, ver. 3 (Tachibana Lab., Kyoto University, Kyoto, 2008).

[25] W. Andreoni and A. Curioni, Appl. Phys. A **66**, 299 (1998); T. Aree, T. Kerdcharoen, and S. Hannongbua, Chem. Phys. Lett. **285**, 221 (1998).

[26] P. Dubot and P. Cenedese, Phys. Rev. B **63**, 241402(R) (2001).

[27] V. Meunier, J. Kephart, C. Roland, and J. Bernholc, Phys. Rev. Lett. **88**, 075506 (2002).

[28] A.A. Kuzubov, P.V. Avramov, S.G. Ovchinnikov, S.A. Varganov, and F.N. Tomilin, Phys. Sol. State **43**, 1721 (2001).

Chapter 9

Local Dielectric Property of Cubic, Tetragonal, and Monoclinic Hafnium Oxides

9.1 Introduction

Recently, semiconductor integrated circuits have been downsized rapidly. Although silicon dioxide (SiO_2) is well known as desirable gate insulator, it will reach its limit for maintaining reliability, since the thickness of the gate insulator becomes a few nanometers. Leak current in complementary metal-oxide-semiconductor (CMOS) is significantly large for very thin films of silicon dioxide. This leak current is a serious problem in viewpoints of the reliability of advanced electronic devices and the loss of electric power. To achieve further downsizing beyond the limit of the Moore's law, many researchers have argued that high-k materials such as hafnium dioxide (HfO_2) are superior to silicon dioxide as hopeful materials for gate dielectric thin film due to their high dielectric constant [1, 2].

Hafnia has several crystal structures, and their dielectric constants are dependent on them. The dielectric constant of the most stable monoclinic structure is reported to be about 22 [3], while metastable structures, cubic and tetragonal are reported to have higher dielectric constants. From the ab initio calculation, the dielectric constants of the cubic and tetragonal hafnia are predicted to be about 20-30 and 40-70, respectively [4, 5]. Experimentally, the cubic or tetragonal structures of hafnia derived by yttrium-doped hafnia

or a mixture film of HfO_2 and ZrO_2, show high dielectric constants of about 30 [6, 7]. In recent works, it has also been reported to fabricate the cubic hafnia without doping other elements owing to new metastable phase control technology [8]. The dielectric constant of their samples is about 40. While it is metastable in room temperature, many experimental attempts to fabricate the cubic and tetragonal hafnia are made with these technique. Hence, the cubic and tetragonal hafnia may be available as device material in the near future.

High-k gate insulator films such as hafnia films will be important for very small CMOS chips, which have a thickness of few nanometers. For such small materials, the position dependence of physical quantity is significantly important. For example, it is recently reported that the leak current is dependent on a position in materials [9]. Hence, to study the dielectric properties of nanosize materials, the macroscopic dielectric constant is not appropriate. It is important to investigate the local dielectric property.

In our laboratory, we study nano-materials in terms of local density quantities defined by Tachibana [10–19]. In particular, in our previous works [12, 13], we have clarified the relation between local dielectric property and electron population on a lanthanum atom in a lanthanum oxide (La_2O_3) cluster using local dielectric constant density. The existence of oxygen vacancies is an important topic for high-k gate thin films [20–24]. Regarding oxygen vacancies, we have also clarified the relation between the formation energy of oxygen vacancies in La_2O_3 and HfO_2 and their bonding states [14].

In this work, we investigate the dielectric properties of the cubic, tetragonal, and monoclinic hafnia in terms of the electronic contribution to the static dielectric constant density tensor following our previous work [15], in which we study the local dielectric property of cubic hafnia. First, we check termination conditions to realize the property of crystals in cluster models. Then, we study the local dielectric property of the cubic, tetragonal, and monoclinic hafnia crystals using the cluster models. Their dielectric properties are compared with each other. We also consider dielectric property of SiO_2 for a comparison. We pay special attention to the covalent property of Si-O bond. The difference between dielectric properties arising from ionic bond and those from covalent bond is discussed.

We note that in this work we consider only the electronic contribution to the dielectric response. It is well known that the lattice oscillation contribution dominates over the electronic one and is more sensitive to the structure of the material [4, 5, 25, 26]. One

of the purposes of this work is to clarify the electronic contribution to the local dielectric response before we include the lattice contribution, and to establish the local dielectric response analysis, since the electronic contribution is easy to handle and its calculations have less ambiguity than the lattice contribution.

This article is organized as follows. In the next section, we show the formalism of the local polarizability density tensor and dielectric constant density tensor operators. In §9.3, the calculation models and conditions are explained. The calculation procedure of the local polarizability and dielectric constant densities are also explained. Our results are shown in §9.4. In §9.4.1, we discuss appropriate termination conditions of cluster models for the evaluation of the local polarizability and dielectric constant densities. In §9.4.2, we study the local dielectric properties of cubic, tetragonal, and monoclinic hafnia. In §9.4.3, the dielectric properties of SiO_2 for comparison with HfO_2 are studied. The last section is devoted to the summary.

9.2 Theory

In this section, we show our formalism of the dielectric constant density operator, defined in the Rigged QED theory [10, 11]. We consider that a system (A) is embedded in an environmental background medium (M). The corresponding scalar potentials for the system and background are given as the regional integrals of the electric charge,

$$\hat{A}_{0_{A,M}}(\boldsymbol{r}) = \int_{A,M} d^3\boldsymbol{s} \frac{\hat{\rho}(\boldsymbol{s})}{|\boldsymbol{r}-\boldsymbol{s}|}. \tag{9.1}$$

Here, $\hat{\rho}(\boldsymbol{r})$ is the charge density defined as,

$$\hat{\rho}(\boldsymbol{r}) \equiv Z_e e \sum_a \hat{\psi}_a^\dagger(\boldsymbol{r})\hat{\psi}_a(\boldsymbol{r}), \tag{9.2}$$

where $Z_e = -1$ for the electron. The electric field $\hat{\boldsymbol{E}}(\boldsymbol{r})$ is given as the sum of the electric displacement $\hat{\boldsymbol{D}}(\boldsymbol{r})$ of the medium M and the polarization $\hat{\boldsymbol{P}}(\boldsymbol{r})$ of the system A. These are defined as follows,

$$\hat{\boldsymbol{D}}(\boldsymbol{r}) = -\mathrm{grad}\hat{A}_{0_M}(\boldsymbol{r}), \tag{9.3}$$

$$\hat{\boldsymbol{P}}(\boldsymbol{r}) = \frac{1}{4\pi}\mathrm{grad}\hat{A}_{0_A}(\boldsymbol{r}), \tag{9.4}$$

where the time variation of the vector potential is neglected, since only steady states are considered in this work. As a result, the electric field is given as

$$\hat{\boldsymbol{E}}(\boldsymbol{r}) = \hat{\boldsymbol{D}}(\boldsymbol{r}) - 4\pi\hat{\boldsymbol{P}}(\boldsymbol{r}). \tag{9.5}$$

The electric displacement $\hat{\boldsymbol{D}}(\boldsymbol{r})$ of the medium M works as the external electric field for the system A. The polarization of the system A is hence considered to be linear response to $\hat{\boldsymbol{D}}(\boldsymbol{r})$,

$$\hat{\boldsymbol{P}}(\boldsymbol{r}) = \hat{\boldsymbol{\alpha}}(\boldsymbol{r})\hat{\boldsymbol{D}}(\boldsymbol{r}), \tag{9.6}$$

where $\hat{\boldsymbol{\alpha}}(\boldsymbol{r})$ is the polarizability density tensor. The dielectric constant density tensor $\hat{\boldsymbol{\epsilon}}(\boldsymbol{r})$ is therefore defined as

$$\hat{\boldsymbol{D}}(\boldsymbol{r}) = \hat{\boldsymbol{\epsilon}}(\boldsymbol{r})\hat{\boldsymbol{E}}(\boldsymbol{r}) = \frac{1}{1 - 4\pi\hat{\boldsymbol{\alpha}}(\boldsymbol{r})}\hat{\boldsymbol{E}}(\boldsymbol{r}). \tag{9.7}$$

These operators of the polarizability density tensor and the dielectric constant density tensor are Hermite, and all elements of these tensors are real. However, these tensors are not symmetric, and hence its eigenvalues have three real values, or one real and two complex values. The case with the complex eigenvalues is interesting, since the dielectric response shows rotational behavior [15]. Note that the complex eigenvalues can be correctly described only in the analysis using tensor, since it is due to off-diagonal elements. The off-diagonal elements of the ordinary global dielectric constant tensor are negligible for large enough amorphous materials and crystals with high symmetry, such as cubic hafnia. However, the off-diagonal elements cannot be neglected for nano-materials and in a local region even for such materials. Hence, the local and tensor analyses are important for very thin dielectric films.

9.3 Computational Details

9.3.1 Calculation models and conditions

In this section, we explain our calculation models and conditions. In Fig. 9.1, we show the structures of cluster models of cubic, tetragonal, and monoclinic hafnia and SiO_2 (α-quartz). The cubic and tetragonal hafnia models have 13 Hf and 56 O atoms and the

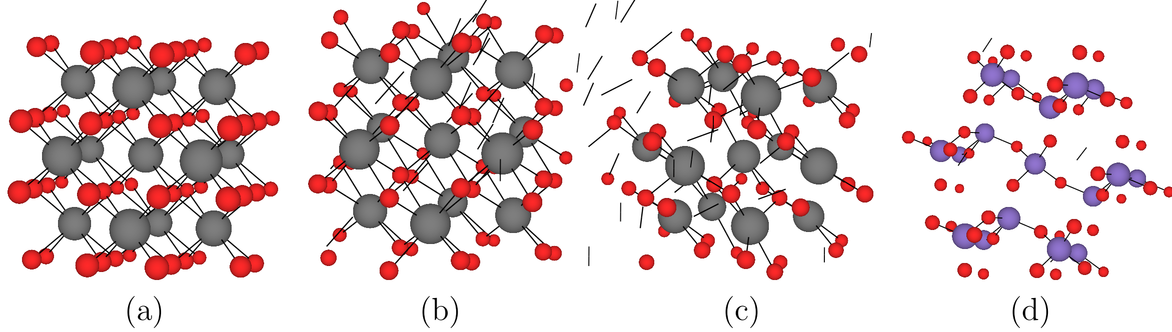

Figure 9.1: The cluster models of (a) cubic, (b) tetragonal, and (c) monoclinic hafnia and (d) SiO_2 (α-quartz) are shown. These models show the structures of point charge models. The gray (large), red (small), and violet (middle) spheres denote hafnium, oxygen, and silicon atoms, respectively. Point charges surrounding these clusters are not shown in these figures.

monoclinic hafnia model has 13 Hf and 53 O atoms. We consider SiO_2 for a comparison of dielectric property arising from ionic bond with that from covalent bond. In this SiO_2 model, there are 17 Si and 52 O atoms. These models are surrounded by point charges (point charge models), which are put on surrounding Hf, O, and Si sites. Point charges are used as the termination condition for the realization of the environment that an analyzed system in a large crystal is surrounded by other atoms in the crystal. The number of point charges are 606 for the cubic and tetragonal hafnia models, 600 for the monoclinic hafnia model, and 594 for the SiO_2 model. The charge of Hf(O) site is 1.0 (-0.5) for the cubic and tetragonal HfO_2 and 1.4 (-0.6 and -0.8 for three and four fold O sites) for the monoclinic one. The charges of Si and O sites of the SiO_2 model are 0.4 and -0.2, respectively. These values of the point charge are determined as follows. The point charges on the Hf sites have a positive charge, while those on the O sites have a negative charge, whose sum is the same as that on the Hf sites. The values of these charges are determined so that the Mulliken charges of the atoms in analyzed system are uniformly distributed, for the realization of a feature of crystals.

The parameters of structures of our models are summarized in Table 9.1. The distance between Hf and O atoms in the cubic hafnia is determined to be 2.200 Å by our geometric optimization calculations. In the calculations, only the Hf-O length is varied with the structure being preserved. This Hf-O length is consistent with the values of experimental

Table 9.1: Parameters of structures of three HfO_2 crystal phases and SiO_2 (α-quartz).

	Cubic (Expt.[a])	Tetragonal	Monoclinic	SiO_2
a (Å)	5.081 (5.08)	5.056	5.032	4.910
b (Å)	-	-	5.125	-
c (Å)	-	5.127	5.192	5.401
δz	-	0.042	-	-
β (deg)	-	-	99.580	-

[a]Ref. 29

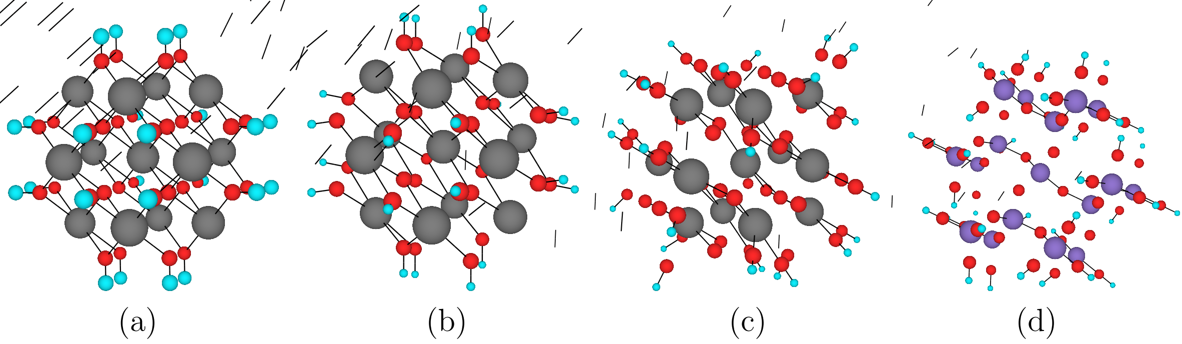

(a) (b) (c) (d)

Figure 9.2: The cluster models of (a) cubic, (b) tetragonal, and (c) monoclinic hafnia and (d) SiO_2 (α-quartz) are shown. These models show the structure of hydrogen termination models. The gray (large), red (dark small), and violet (middle) spheres denote hafnium, oxygen, and silicon atoms, respectively. The light blue (light small) spheres are hydrogen atoms.

results and other computational works [4, 27–29]. For other two models, tetragonal and monoclinic hafnia, geometric optimization calculations are not so easy task. Hence, instead of the optimization, we use the reported values of the geometrical parameters of theses structures [4, 30]. The differences of polarizability density and dielectric constant density are negligibly small for small difference of bond lengths. The geometrical parameters of SiO_2 model are also taken from the reported value [31].

In this work, we study dielectric property of hafnia using these point charge models, since the hafnia is known to be ionic crystal. On the other hand, in the field of ab initio quantum calculations, hydrogen termination is often used to make dangling bond harmless, which may be suitable for SiO_2. To compare two termination methods, we consider the models

with hydrogen termination shown in Fig. 9.2. The cubic and tetragonal hafnia models have 13 Hf and 32 O atoms, and the 24 outer oxygen atoms are terminated by hydrogen atoms. The monoclinic hafnia model has 13 Hf and 53 O atoms, and the 27 outer oxygen atoms are terminated. In the SiO_2 model, 17 Si and 52 O atoms exist, and the 36 outer oxygen atoms are terminated. The number of oxygen atoms of the cubic and tetragonal hafnia models is different from the point charge models, since condensed features are realized better for these choices of models. The distance between the hydrogen and oxygen atoms is taken as 0.958 Å for all hafnia models and 0.953 Å for the SiO_2 model.

In our previous works, we used silicon termination models [12, 13]. The silicon termination (more precisely SiH_3 termination) is superior to the hydrogen termination in viewpoints of representing condensed systems. However, the geometric optimization is required for silicon termination models. Crystal structures of hafnia never remain after the optimization, and hence we cannot use the silicon termination for our purposes. However, in other viewpoint, both of our termination models are interpreted as hafnium termination ones for the inner one Hf and oxygen atoms coupling to the Hf atom, which is superior to the silicon termination.

The electronic structure calculations are performed by using the Gaussian 03 program package [32]. The Hartree-Fock method is chosen to derive the electronic structure for the dielectric constant density tensor calculation, since the density functional theory (DFT) is known to overestimate the dielectric constant [33–37]. The basis sets are chosen as the LanL2DZ basis set for Hf atoms [38–40] and the 6-31G** basis sets for Si, O, and H atoms [41, 42]. We have checked that this choice of basis sets is accurate enough to evaluate the local value of dielectric constant. Then, we calculate the polarizability density tensor and the dielectric constant density tensor using these derived electronic states. These calculations are performed by the Molecular Regional DFT program package [43], which is developed in our laboratory.

9.3.2 Local polarizability and dielectric constant densities

In this section, we show in detail how to derive the dielectric constant density. In this work, the external electric field $\boldsymbol{D}(\boldsymbol{r})$ is assumed to be universal vector $\boldsymbol{D}$. The calculation procedure of the dielectric constant density tensor is summarized as follows. First, we

calculate electronic structures with two different external electric fields $D^i_{1,2}$ ($i = x,\ y,\ z$), which are taken as $D^i_{1,2} = \pm 0.001$ a.u. This calculation is carried out in three directions. The scalar potential and polarization are calculated by Eqs. (1) and (4) for these electronic states. The difference of the polarization $\Delta P^i(\boldsymbol{r})$ between these two results is divided by the difference of the external fields ($\Delta D^i \equiv D^i_1 - D^i_2$), and thus the polarizability density tensor can be derived as

$$\Delta P^i(\boldsymbol{r}) = \alpha^{ij}(\boldsymbol{r})\Delta D^j. \tag{9.8}$$

Only the response to external fields can be extracted by this procedure. For the dielectric constant density tensor, we show only the eigenvalues and their eigenvectors. These are easily derived by eq. (7) after the eigenvalues of the polarizability density tensor are calculated. Note that the lattice polarization effects are not included in this calculation, though the quantum states of nuclei are well defined in the Rigged QED [10, 11].

To display eigenvalues of the polarizability and dielectric constant density tensor, we defined the ordering of them as follows. When all eigenvalues are real, the order of the eigenvalues is the descending order of their values. On the other hand, when the eigenvalues include complex values, the real eigenvalue is defined as the first one, and two complex values are the second and third ones. The magnitude of the imaginary part is represented by the argument θ defined as follows:

$$\theta = \sin^{-1}\left(\frac{|\mathrm{Im}[\lambda_i]|}{|\lambda_i|}\right), \tag{9.9}$$

where λ_i is the corresponding eigenvalue.

We can also calculate the local averages of the polarizability density and the dielectric constant density, which mean contributions from the corresponding region. We can compare contributions from some particular regions. To calculate the averages, we consider a region with the volume, V, and integrate the local polarizability density as follows:

$$\langle \boldsymbol{\alpha} \rangle = \frac{1}{V}\int_V \hat{\boldsymbol{\alpha}}(\boldsymbol{r}) d\boldsymbol{r}. \tag{9.10}$$

Then, the average of the dielectric constant is given by

$$\langle \boldsymbol{\epsilon} \rangle = \frac{1}{1 - 4\pi\langle \boldsymbol{\alpha} \rangle}. \tag{9.11}$$

In order to know the macroscopic dielectric constant of a material, we calculate the average of the polarizability density and the dielectric constant density over the unit cell of crystal

structures. We also investigate the contributions from two particular regions. One is a region around atoms and the other is a region around bond axis, i.e., the region between hafnium (silicon) and oxygen atoms. Integration around an atom region is carried out for a sphere whose center is the position of the atom. We take the radius as free parameter and study the dependence on the volume of the region. For hafnium atoms, the region of the pseudopotential is removed, where the radius of the potential is taken as 0.9 bohr. On the other hand, integration around a bond axis region is carried out for a cylinder, whose length is that of a bond axis. The radius of the cylinder is also taken as free parameter. For the calculation around Hf-O bonds, we also remove the pseudopotential region.

9.4 Results and Discussion

9.4.1 Appropriate termination conditions

In this section, we show that point charge models are suitable for HfO_2 whose Hf-O bond has strong ionic property and a hydrogen termination model is suitable for SiO_2 whose Si-O bond has covalent property. We consider that point charge models use coulomb force by point charges to stabilizes electrons in the system, which is the same situation as ionic bond, while hydrogen termination models make dangling bonds of oxygen atoms harmless by the covalent bond between oxygen and hydrogen atoms. In this work, we use cluster models, and hence our calculation is restricted for finite system. The reason of this choice is that cluster model calculations based on molecular orbitals has advantages over calculations with periodic boundary conditions to realize local dielectric property, particularly, around impurities. On the other hand, periodic system is suitable for reproducing the properties of crystal.

We choose cluster models for our purpose, and check whether our models reproduce sufficiently the properties of crystal. For these purposes, we study the following three properties for two termination conditions; the first one is the density of states (DOS), the second one is the distribution of Mulliken charges, and the last one is the macroscopic value of dielectric constant.

First, we discuss DOS of cluster models and compare them with those of crystals. In particular, we check whether the pattern of DOS is similar to that of results of crystal

Table 9.2: HOMO-LUMO gap (eV) for three HfO_2 crystal phases and SiO_2.

Model	Cubic	Tetragonal	Monoclinic	SiO_2
Point charge	6.146	5.175	3.768	1.500
Hydrogen termination	6.994	6.990	8.942	15.886

and experimental values of band gap are reproduced. The band gap is important quantity to realize the property as insulator. Experimentally, the gap is reported to be 5.7 eV for poly-monoclinic HfO_2 [44]. As the quantity for a comparison with the band gap, we show the energy difference between the the highest occupied molecular orbital (HOMO) and the lowest unoccupied molecular orbital (LUMO), i.e. HOMO-LUMO gap, in Table 9.2. In the case of point charge models, the values of the gap of cubic and tetragonal HfO_2 are similar to the experimental value in spite of the structural difference. For monoclinic HfO_2, our value of the gap is slightly smaller than the experimental one. On the other hand, the HOMO-LUMO gaps of hydrogen termination models are relatively large compared to the experimental value. In particular, the value of monoclinic structure is larger than that of the point charge model by about 5.0 eV, though both models of point charges and hydrogen termination can reproduce the property of insulator. Then, we compare two termination conditions in viewpoints of the pattern of DOS.

In Fig. 9.3, the total DOS of our HfO_2 models are shown. The energy of HOMO is taken as 0 eV. All results of point charge models are reasonably consistent with results calculated with periodic boundary conditions [45, 46]. Hence, we consider that our point charge models sufficiently represent the electronic states of hafnia crystals. On the other hand, the results for cubic and tetragonal HfO_2 of the hydrogen termination models are significantly different from the calculation results of periodic systems. The hydrogen termination model of monoclinic HfO_2 has roughly correct pattern of DOS and large band gap. Therefore, in viewpoints of DOS, the point charge models are much better for cubic and tetragonal HfO_2, while for monoclinic model, it will be concluded after the comparison of the point charge and hydrogen termination models in terms of the distribution of Mulliken charges and the macroscopic dielectric constant.

The total DOS and the HOMO-LUMO gap in the point charge and hydrogen termination

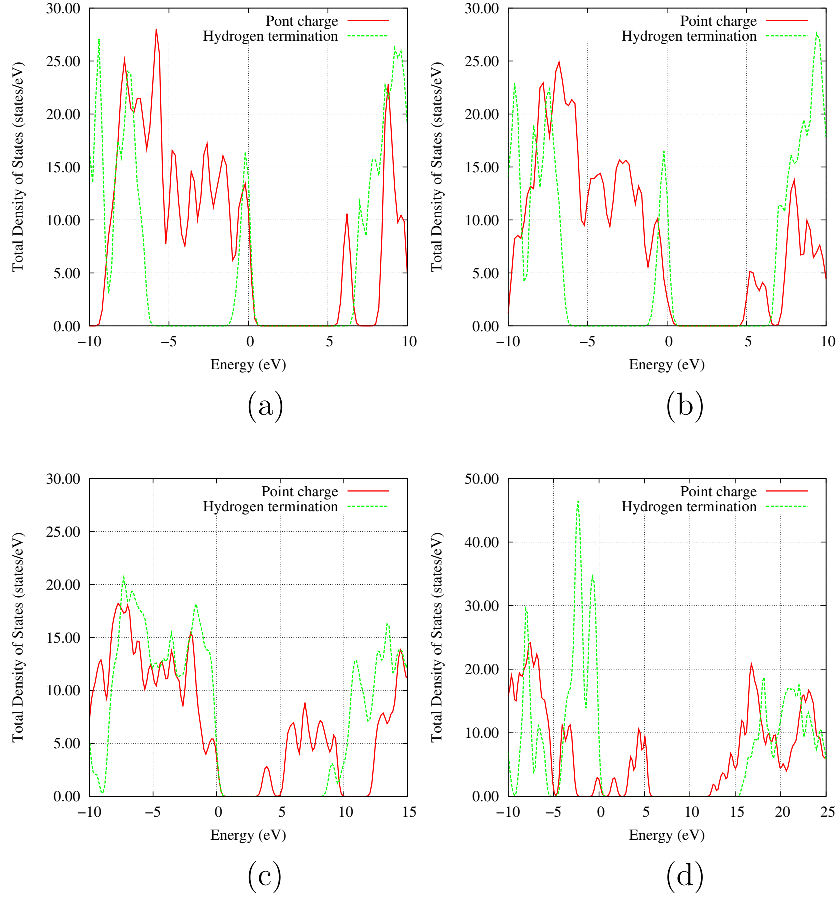

Figure 9.3: The total DOS of (a) cubic, (b) tetragonal, and (c) monoclinic HfO_2 and (d) SiO_2 are shown. The energy of the HOMO is taken as 0 eV. Red (solid) and green (dashed) lines show the DOS of point charge and hydrogen termination models, respectively.

models of SiO_2 are also shown in Fig. 9.3 and Table 9.2, respectively. The gap of the point charge model is much smaller than the experimental value, 9.2 eV [47]. The point charge model is disfavored in viewpoints of the realization of the property of SiO_2 as insulator. The gap of the hydrogen termination model is considerably larger than the experimental value [47]. Nevertheless, the pattern of DOS has similarity with computational result of periodic system [48]. On the other hand, the pattern of DOS of the point charge model is significantly different from the computational one. Therefore, for SiO_2, the hydrogen termination model is at least better in terms of DOS.

Next, we discuss the distribution of Mulliken charges. The dielectric property is studied by using only the inner parts of our models. Therefore, we consider the distribution of Mulliken charges in inner regions, where the Mulliken charges should uniformly be distributed.

Table 9.3: The distribution of Mulliken charges of the atoms for point charge (PC) and hydrogen termination (HT) models. The distance (bohr) from the center atom in cluster models is also shown.

Cubic				**Tetragonal**				**Monoclinic**				**SiO_2**			
	Distance	PC	HT		Distance	PC	HT		Distance	PC	HT		Distance	PC	HT
Hf	0.00	2.48	3.26	Hf	0.00	2.44	3.04	Hf	0.00	2.58	3.09	Si	0.00	1.72	1.70
	6.79	2.45	1.85		6.76	2.41	1.85		6.15	2.56	2.67		5.77	1.70	1.70
	6.79	2.42	1.85		6.76	2.41	1.85		6.37	2.48	2.66		5.77	1.67	1.69
	6.79	2.45	1.85		6.76	2.49	1.85		6.37	2.27	2.45		5.77	1.68	1.69
	6.79	2.42	1.85		6.76	2.49	1.85		6.41	2.34	2.54		5.77	1.70	1.70
	6.79	2.43	1.85		6.80	2.37	1.87		6.41	2.51	2.62	O	3.03	−0.85	−0.87
	6.79	2.45	1.85		6.80	2.43	1.87		6.44	2.42	2.65		3.03	−0.85	−0.87
	6.79	2.42	1.85		6.80	2.40	1.87		6.58	2.48	2.57		3.04	−0.86	−0.86
	6.79	2.41	1.85		6.80	2.44	1.87		7.28	2.39	2.56		3.04	−0.86	−0.86
	6.79	2.42	1.85		6.80	2.37	1.87		7.28	2.33	2.59		6.65	−0.84	−0.84
	6.79	2.41	1.85		6.80	2.44	1.87		7.46	2.39	2.61		6.65	−0.84	−0.84
	6.79	2.43	1.85		6.80	2.40	1.87		7.46	2.54	2.55		6.66	−0.84	−0.83
	6.79	2.45	1.85		6.80	2.43	1.87		8.41	2.46	2.55		6.66	−0.83	−0.83
O	4.16	−1.36	−1.36	O	3.93	−1.36	−1.36	O	3.76	−1.38	−1.39		7.36	−0.82	−0.85
	4.16	−1.36	−1.36		3.93	−1.38	−1.36		3.88	−1.36	−1.40		7.36	−0.81	−0.85
	4.16	−1.36	−1.36		3.93	−1.34	−1.36		3.95	−1.35	−1.37		7.53	−0.82	−0.82
	4.16	−1.36	−1.36		3.93	−1.37	−1.36		3.98	−1.41	−1.41		7.53	−0.81	−0.82
	4.16	−1.36	−1.36		4.41	−1.38	−1.36		4.02	−1.39	−1.43		7.76	−0.81	−0.82
	4.16	−1.36	−1.36		4.41	−1.36	−1.36		4.16	−1.40	−1.42		7.76	−0.81	−0.82
	4.16	−1.36	−1.36		4.41	−1.37	−1.36		4.18	−1.38	−1.41		7.90	−0.81	−0.82
	4.16	−1.36	−1.36		4.41	−1.34	−1.36						7.90	−0.81	−0.82

Table 9.4: The average of the dielectric constant density for a unit cell.

	Model	ϵ_1	ϵ_2	ϵ_3	Average of ϵ_i
Cubic	Point charge	3.45	$2.85 + 0.60i$	$2.85 - 0.60i$	3.05
	Hydrogen termination	1.31	1.31	1.31	1.31
Tetragonal	Point charge	2.32	$2.60 + 0.35i$	$2.60 - 0.35i$	2.51
	Hydrogen termination	1.33	1.32	1.31	1.32
Monoclinic	Point charge	4.88	3.72	3.07	3.89
	Hydrogen termination	1.55	$1.67 + 0.03i$	$1.67 - 0.03i$	1.63
SiO_2	Point charge	1.54	-4.29	-21.82	-8.19
	Hydrogen termination	1.39	1.22	1.19	1.27

The Mulliken charges of atoms in inner regions are shown in Table 9.3. For the point charge models of HfO_2, the Mulliken charges are distributed uniformly, while for the hydrogen termination models of HfO_2, the Mulliken charge of the center Hf atom is considerably different from other Hf atoms. On the other hand, for SiO_2, the distribution of the Mulliken charges of the hydrogen termination model is not so different from that of the point charge model, though the distribution of the charges of Si atoms is slightly better for the hydrogen termination model. Therefore, the point charge models are suitable for HfO_2, and for SiO_2, both models show the correct distribution of the Mulliken charges.

Finally, we discuss macroscopic value of dielectric constant. In Table 9.4, we show the average of the dielectric constant density for a unit cell. The average values of the dielectric constant of the hydrogen termination models for HfO_2 are much smaller than those of the point charge models. The electronic contribution to macroscopic dielectric constant of HfO_2 are reported to be about 5, almost independent of the structure of crystal [5, 25, 26]. Hence, the values of the hydrogen termination models are worse compared to those of the point charge models. This smallness of the dielectric constant confirms that the termination with hydrogen atoms is not suitable for HfO_2. On the other hand, the average of the dielectric constant of the point charge model for SiO_2 is never acceptable for the value for SiO_2. The electronic contribution to dielectric constant is reported to be about 2.5 [48]. Although the macroscopic dielectric constant of the hydrogen termination model of SiO_2 is smaller

than this value, the hydrogen termination is more suitable for our calculations than the point charge model. Our values for the point charge models of HfO_2 and the hydrogen termination model of SiO_2 are slightly smaller than other works [48, 49]. One of the reasons is that the accuracy of our results is somewhat worse for a unit cell calculation, since the outermost shell of the cluster models are included and electronic structures are worse than those around the center of the models. In fact, our HfO_2 models have slightly larger values of the band gap than those of other computational works. The larger band gap leads to smaller macroscopic dielectric constant.

Considering the above three properties comprehensively, appropriate termination conditions for our analysis are clarified. The point charge models are suitable for HfO_2, and the hydrogen termination model is better for SiO_2.

9.4.2 Local dielectric property of HfO_2

We investigate the dielectric property using cluster models of the cubic, tetragonal, and monoclinic structures of HfO_2 in terms of the local polarizability density and dielectric constant density. It will be found that the electronic contribution to the local dielectric properties is almost independent of the structure of HfO_2.

We show the eigenvalues and their eigenvectors of the polarizability density tensor of HfO_2 in Fig. 9.4. For cubic HfO_2, it can be seen that large polarizability density is distributed uniformly in the almost whole region for the first eigenvalue. The slightly larger values can be seen around atoms, particularly oxygen atoms. The polarizability nearby oxygen atoms (accepter) is larger than that nearby Hf atoms (donor). The electrons around Hf atoms weakly respond to external electric fields, since electrons are tightly bounded by the Hf atom due to the reduced number of screening electrons and the electric field between the Hf and oxygen atoms by the charge transfer. On the other hand, the response of electrons around oxygen atoms to the external electric fields is strong due to the weak binding in the oxygen atom by the increased number of screening electrons. The complex eigenvalues are widely seen in panels (a-2) and (a-3). Hence, the polarization response to external electric fields should have rotational behavior. These properties cannot be seen in the global and averaged scalar polarization analysis. It can only be described correctly in the local and tensor analysis, as stressed above. For tetragonal and monoclinic HfO_2, the almost

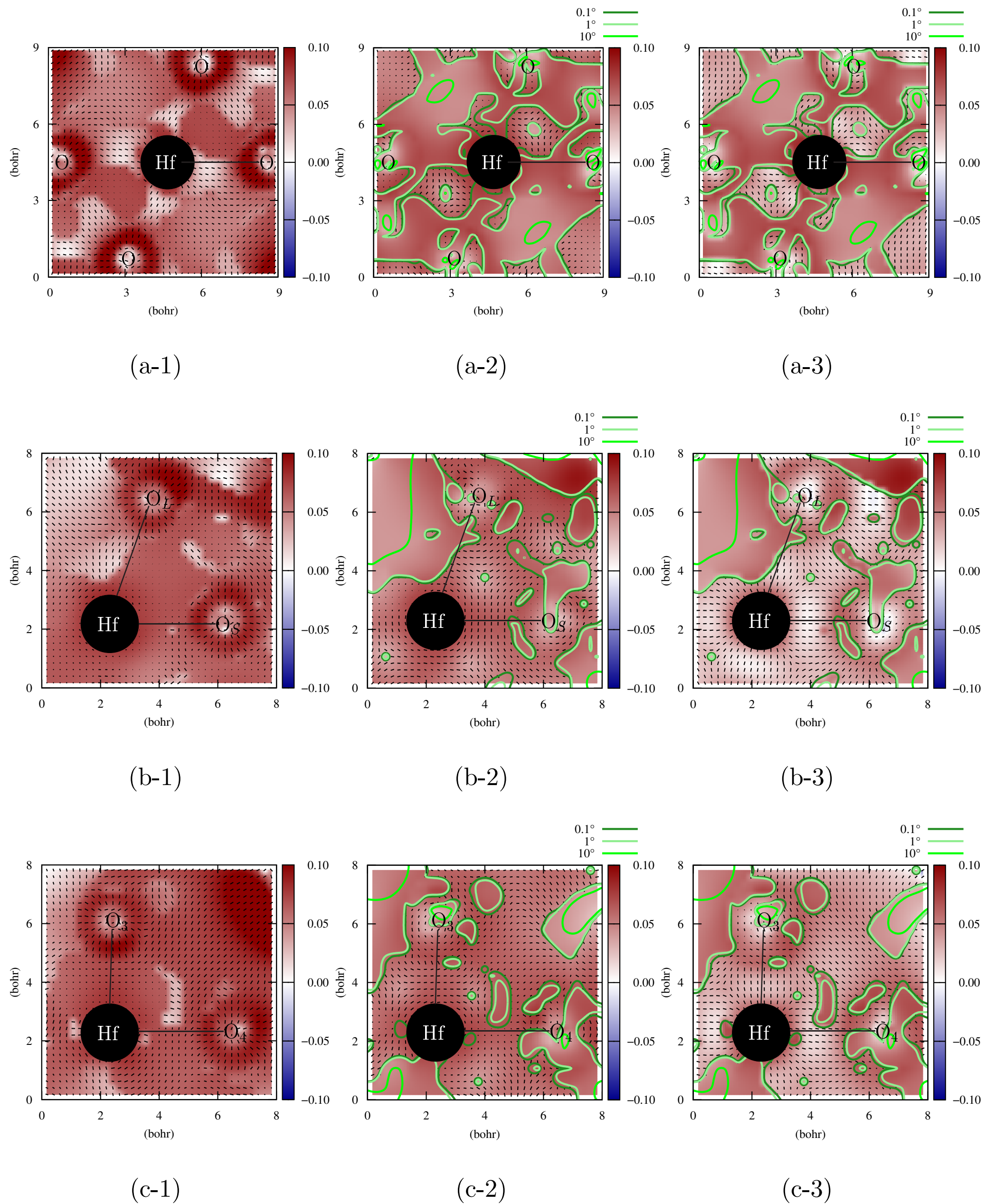

Figure 9.4: The eigenvalues and their eigenvectors of the polarizability density tensor of cubic, tetragonal, and monoclinic HfO_2. Panels (a), (b), and (c) show results of the cubic, tetragonal, and monoclinic HfO_2, respectively. The results are shown on the plane with one hafnium atom at the center of the model and two oxygen atoms next to the hafnium atom. Panels (1), (2), and (3) correspond to the first, second, and third eigenvalues ($\alpha_{1,2,3}$) of the polarizability density tensor. Two oxygen sites in monoclinic structure are labeled as O_3 for the three fold oxygen atom and O_4 for the four fold oxygen atom. There are also two Hf-O distances, long (O_L) and short (O_S) in tetragonal structure. The solid line segments show the directions of the eigenvectors. The eigenvalues in the green contours have complex values. The black blob shows the pseudopotential of the Hf atom.

same features can be seen. Although the regions of complex eigenvalues have different distribution patterns, the large rotational angle is commonly seen around oxygen atoms. Around oxygen atoms, after electrons respond to external fields, the electric field in the region is reconstructed and the direction of this electric field is not necessarily the same as the external electric field. The complicated response can be seen around oxygen atoms, since the reconstructed electric field is large due to the large electron density.

In Fig. 9.5, we show the dielectric constant density on the same planes and models as Fig. 9.4. Figure 9.5 shows the inverse of the eigenvalues ($\epsilon_{1,2,3}^{-1}$) of the dielectric constant density tensor. The eigenvalues are sorted for not ϵ_i^{-1} but ϵ_i. The pattern of the distribution of the dielectric constant density is not simple compared to the polarizability density. Small variations around $\alpha_i = 1/4\pi$ result in significant changes of the dielectric constant density, since $1/(1-4\pi\alpha_i)$ is divergent and changing the sign at $\alpha_i = 1/4\pi$ as seen in eq. (7). We can see the negative values of the dielectric constant density, particularly around oxygen atoms in all HfO_2 structures. In the region, the induced polarization overcomes external electric fields. The global response shows positive dielectric constant as is well known, while the local response can have negative dielectric constant density. The pattern of the region with complex eigenvalues is of course same as Fig. 9.4, while the rotational angle is much larger than that of the polarizability density. The small rotational response in the polarizability density may induce the large rotational one for the dielectric constant density. As a result, the analysis of the dielectric constant and polarizability as local quantity clarifies the complicated response dependent on positions in a system.

In Figs. 9.6, 9.7, and 9.8, we also show the eigenvalues and their average along Hf-O bond axes, which are shown in Figs. 9.4 and 9.5 as the solid lines, for the study of the local dielectric response in detail. The region nearby the Hf atom is within the pseudopotential (0-0.9 bohr). For all results, the local polarizability density has similar distribution pattern to each other. Around the oxygen atom (within about 0.5 bohr from the oxygen atom), the polarizability density is small, since electrons are strongly bounded by the electric field of the oxygen nucleus. Then, in outer region of the oxygen atom, the large polarizability can be seen. Since electrons in this region are valence electrons of the oxygen atom, these electrons are easy to be affected by external electric fields. The radius of the large polarizability region is roughly equal to the ionic radius of oxygen. The value of local polarizability around the

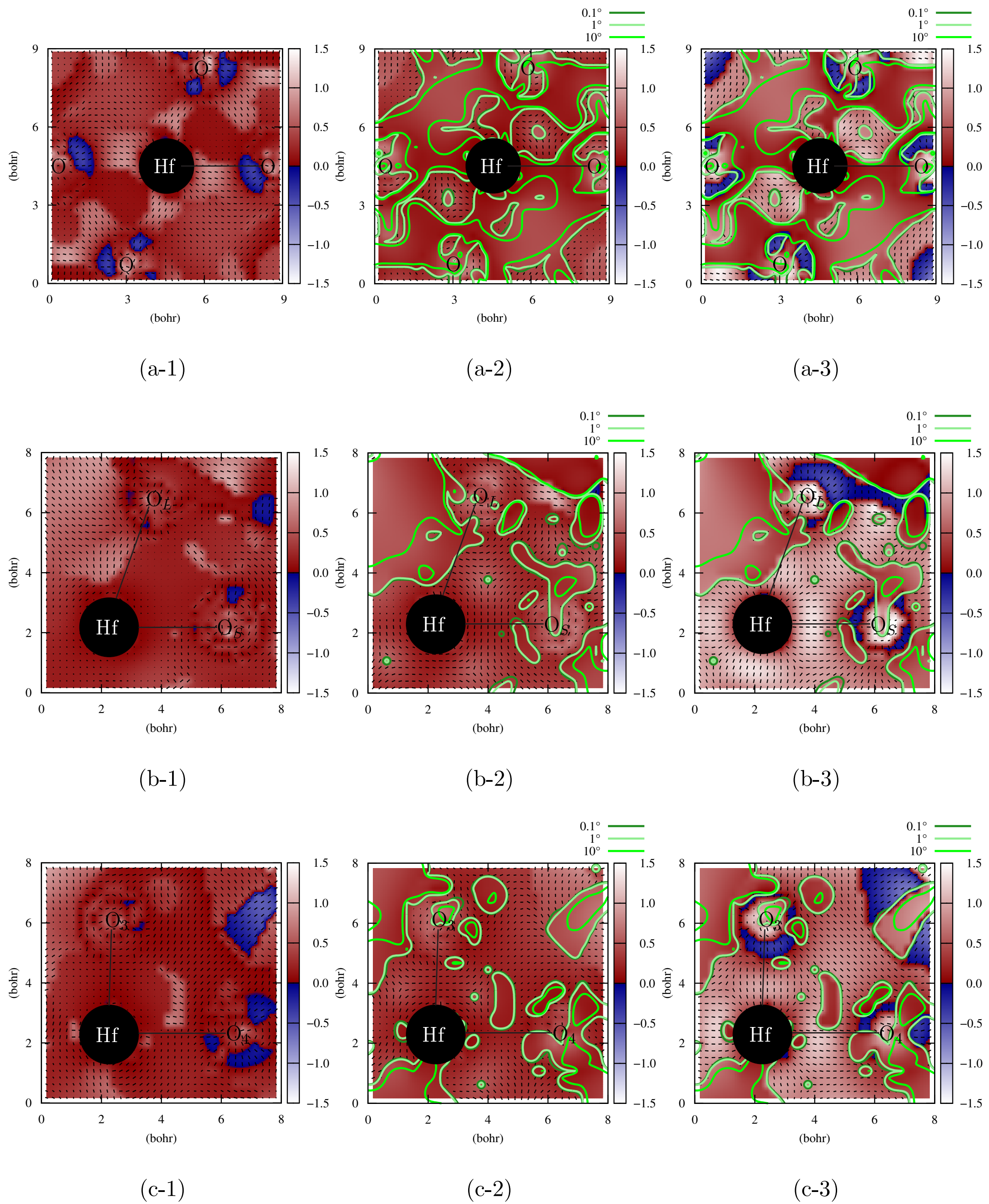

Figure 9.5: The inverse of eigenvalues and their eigenvectors of the dielectric constant density tensor of (a) cubic, (b) tetragonal, and (c) monoclinic HfO_2. Results are shown on the same plane as Fig. 9.4 in the same manner. See the caption of Fig. 9.4 for the details.

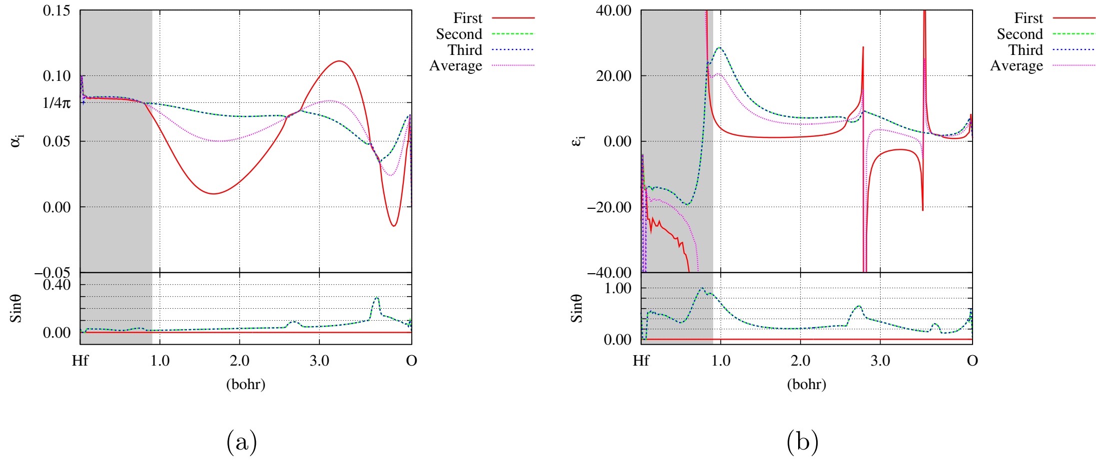

Figure 9.6: The eigenvalues and their average of (a) the polarizability density tensor and (b) the dielectric constant density tensor on the Hf-O line of cubic HfO_2, which is shown in Figs. 9.4 and 9.5. The upper part of these panels is the real part of three eigenvalues and their average, while the lower one is the argument. The shaded region around the Hf atom shows the pseudopotential.

Hf atom is significantly smaller than that around the O atom as explained above. The dielectric constant density has also similar distribution pattern to each other. For example, the positions of peaks are almost same for all models. However, the similarity is seen to be weaker than the polarizability density, since the value of dielectric constant is divergent for $\alpha_i = 1/4\pi$, as discussed above. Even small difference of polarizability density may result in large difference of dielectric constant density.

It is reported that the electronic contribution to macroscopic dielectric constant is almost independent of the structure of crystal [5, 25, 26]. The difference of dielectric constant between different structure of hafnia crystal is considered to originate in the contribution from nucleus. Here, we find that the electronic contribution to local polarizability and dielectric constant densities are also independent of the structure. This can be confirmed only by our local analysis.

Next, we calculate the averages in various regions of the dielectric constant density in order to investigate local effects on the macroscopic dielectric constant. The average of dielectric constant density over (a) the sphere around a Hf atom, (b) the sphere around an O atom, and (c) the cylinder around a Hf-O bond axis are shown in Fig. 9.9 as a function of the integration radius of sphere or cylinder. As seen in this figure, the average values

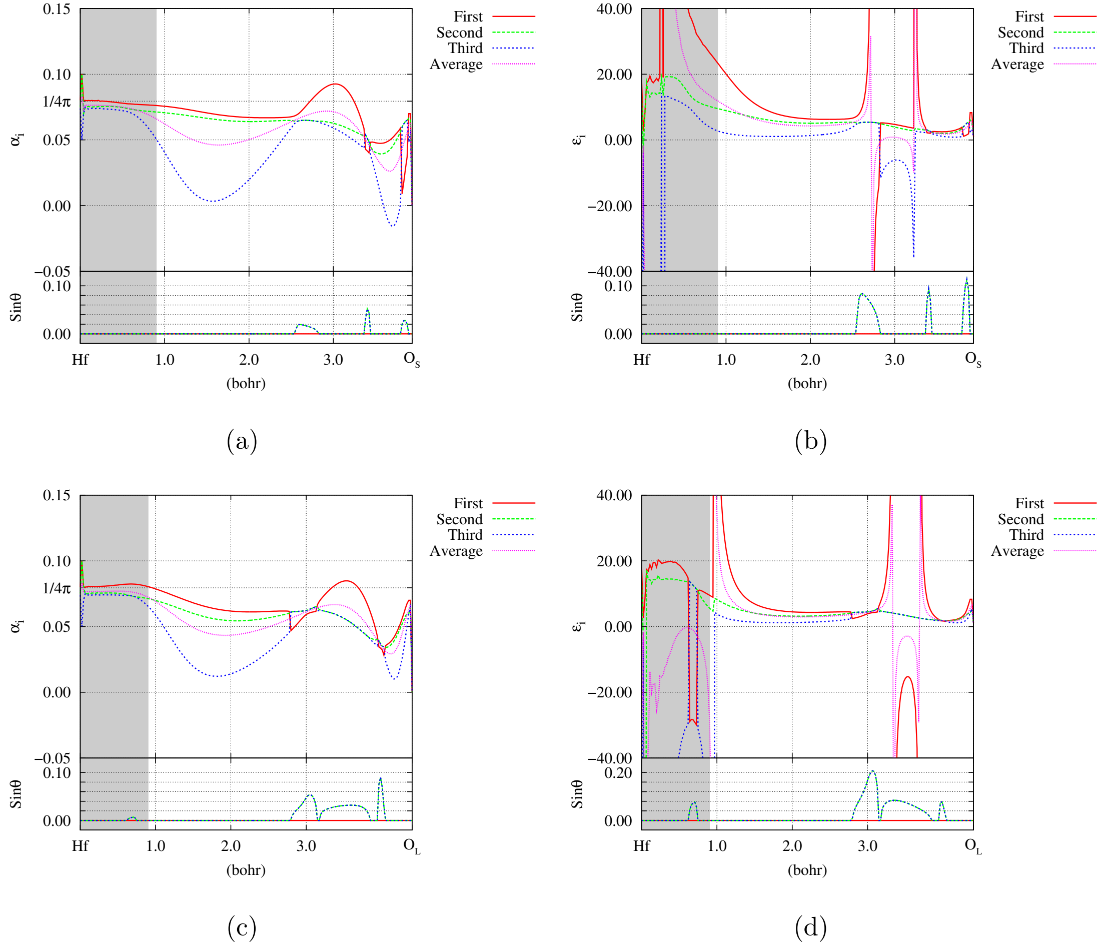

Figure 9.7: The eigenvalues and their average of (a) and (c) the polarizability density tensor and (b) and (d) the dielectric constant density tensor on Hf-O lines of tetragonal HfO_2, which are shown in Figs. 9.4 and 9.5. The results of Hf-O_S (Hf-O_L) are shown in panels (a) and (b) ((c) and (d)). Depicted in the same manner as Figs. 9.6.

around atoms are significantly dependent on the integration radius, while the dependence around the bond region is negligibly small. Apparently, the maximum values around oxygen atoms are significantly larger than those of bond regions. Comparing the results around the Hf and O atoms, the result of the Hf atom is significantly smaller than that of the O atom, particularly for a large radius. The bond region also shows larger value than that around the Hf atom. The contribution from Hf atoms to the macroscopic dielectric constant is smaller than that from O atoms in two points. The first one is that the averaged dielectric constant of Hf atoms is much smaller than that of O atoms. The other one is the smaller ionic radius of the Hf atom than the O atom. Larger volume of atom (ion) causes a larger

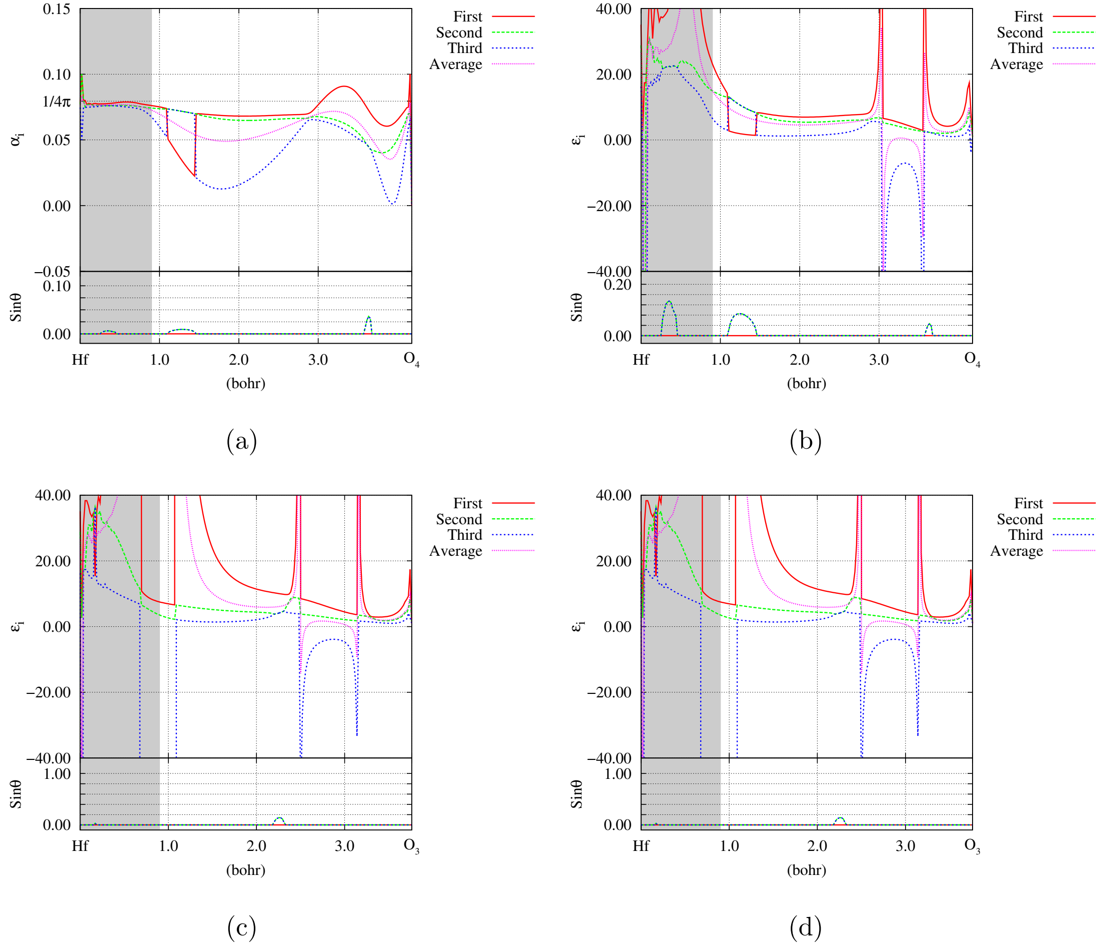

Figure 9.8: The eigenvalues and their average of (a) and (c) the polarizability density tensor and (b) and (d) the dielectric constant density tensor on Hf-O lines of monoclinic HfO_2, which are shown in Figs. 9.4 and 9.5. The results of Hf-O_4 (Hf-O_3) are shown in panels (a) and (b) ((c) and (d)). Depicted in the same manner as Figs. 9.6.

influence to macroscopic dielectric constant. As a result, the contribution of the O atom has larger value than the Hf atom for larger r in Fig. 9.9. In panel (a), the contribution of the Hf atom becomes a constant value in the region $r > 2.0$ bohr, while that of the O atom extends to $r \sim 3.0$ bohr as seen in panel (b).

9.4.3 Comparison with the dielectric property of SiO_2

In this section, we consider the dielectric property of SiO_2 for a comparison. One of the purposes is the investigation of the difference of the dielectric property of ionic Hf-O bond and covalent Si-O bond.

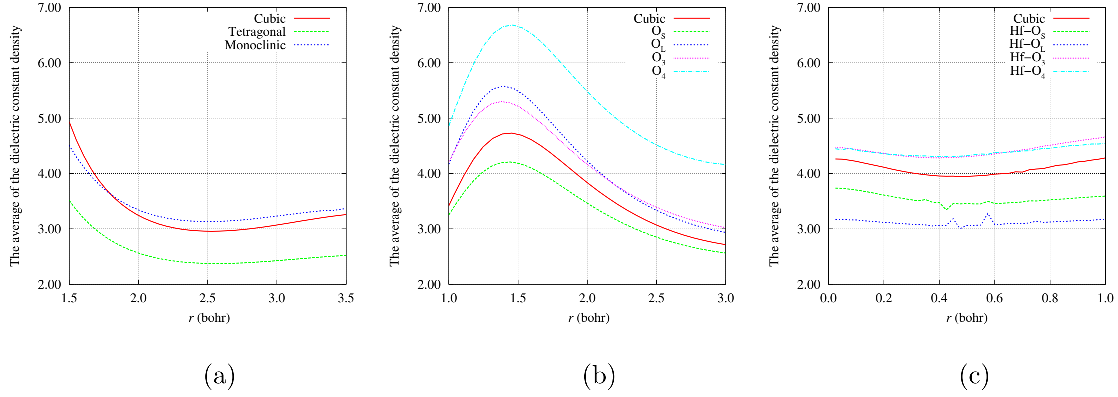

Figure 9.9: The average of dielectric constant density of (a) the sphere around a Hf atom, (b) the sphere around an O atom, and (c) the cylinder around a Hf-O bond axis as a function of the integration radius of sphere or cylinder.

In Fig. 9.10, we show the local polarizability density and local dielectric constant density on the plane defined by the center silicon atom and nearby two oxygen atoms. Similarity to those of HfO_2 can be seen around oxygen atoms in this figure; the large polarizability density, the negative dielectric constant, and the direction of the eigenvector for the first eigenvalue. On the other hand, the region around the Si atom is not similar to those around Hf atoms in HfO_2. The values of polarizability density are much smaller than those of HfO_2. The complex eigenvalues are seen in restricted regions. This is because the change of electric field by the moves of electrons is small. In SiO_2, the displacement of electrons is small, since the polarizability density shows low value. The displacement of electrons is considered to be restricted due to the strong covalent bond, particularly around Si atoms. This feature around Si atoms may originate from large band gap, as is the case of the macroscopic dielectric constant.

In Fig. 9.11, we show the eigenvalues and their average on the Si-O line, which is shown in Fig. 9.10 as the solid line, for the study of the local dielectric response in more detail. Local polarizaility density around the O atom is much larger than those around O atoms in HfO_2. It is also seen that local polarizability density around the Si atom is significantly smaller than those around O and Hf atoms in HfO_2. The polarizability density increases for a distant point from the Si atom. The reason of the tendency in this figure may be speculated that the Si-O bond has strong covalent property, the electrons in the Si atom somewhat move to oxygen atoms, and its valence electrons are distributed to significantly

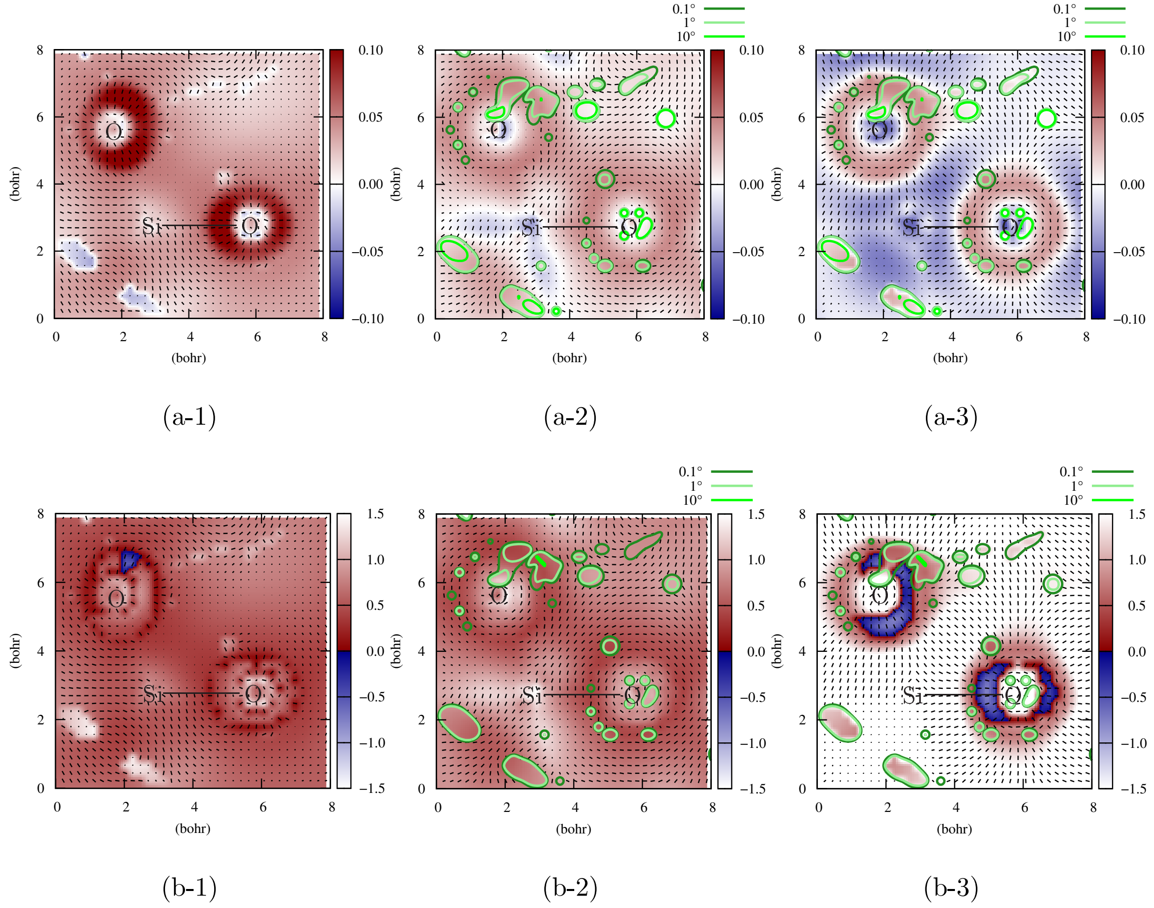

Figure 9.10: The eigenvalues and their eigenvectors of the polarizability density tensor and the inverse of eigenvalues and their eigenvectors of the dielectric constant density of SiO_2. Panels (a) and (b) show the polarizability density and the dielectric constant density, respectively. Depicted in the same manner as Figs. 9.4 and 9.5.

outer regions.

Next, we calculate the averages in various regions of the dielectric constant density in order to investigate local effects on the macroscopic dielectric constant. As discussed in §9.4.2, we show the average of dielectric constant density around (a) a Si atom, (b) an O atom, and (c) a Si-O bond as a function of the integration radius of sphere or cylinder. The results are shown in Fig. 9.12. The average value of dielectric constant around the O atom is much larger than those around the Si atom and bond axis, and it is significantly dependent on the radius. The average around the O atom in SiO_2 is significantly lower than that in HfO_2. This can be explained by the smallness of the average value of the polarizability density, as seen in Figs. 9.6-9.8 and 9.11. The value around the bond axis is larger than

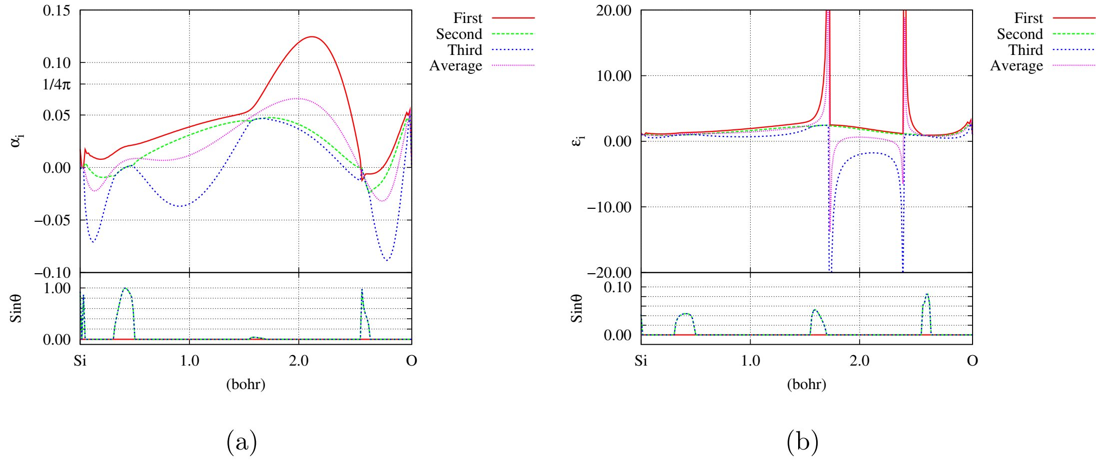

Figure 9.11: The eigenvalues and their average of (a) the polarizability density tensor and (b) the dielectric constant density tensor on the Si-O line of SiO_2 shown in Fig. 9.10. The upper part of these panels is the real part of three eigenvalues and their average, while the lower one is the argument.

that around the Si atom. This is attributed to the contribution from the O atom. The dependence on the radius around the bond region is negligibly small as in the case of HfO_2. In contrast with that of Hf atoms in HfO_2, the average values around the Si atom is almost independent of the radius. The value increases at around 2.0 Å, and this increase is due to the contribution from O atoms. Therefore, it is confirmed by this figure the electronic contribution of Si atoms to the macroscopic dielectric constant is very small, which is in salient contrast to that of Hf atoms.

In this section, we have studied the electronic contribution to the local dielectric constant of the cubic, tetragonal, and monoclinic hafnia crystals. The local dielectric property is particularly useful for the analysis of impurities and interfaces, such as oxygen vacancies and interface between Si substrate and HfO_2 film. We can separate the local effect by these parts from macroscopic effects in terms of the local dielectric constant. This work is the first step of this analysis. We should clarify the local dielectric property without impurities and interfaces, before we analyze the effects of these parts, since the science of the local dielectric property has not sufficiently been established yet. Hence, we have shown the electronic contribution to the local dielectric constant of the cubic, tetragonal, and monoclinic hafnia crystals in this work. In a future work, we will tackle nuclear contribution to the local dielectric constant, which gives the origin of the difference of the macroscopic dielectric

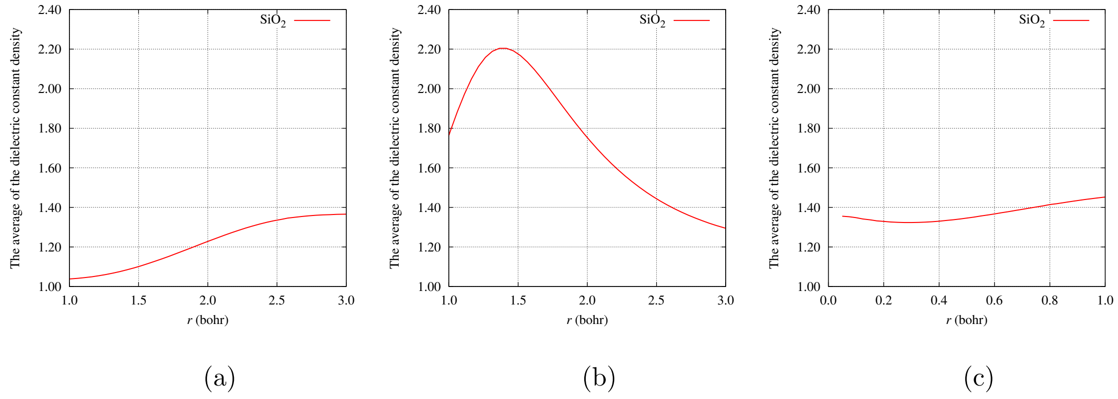

Figure 9.12: The average of dielectric constant density around (a) a Si atom, (b) an O atom, and (c) a Si-O bond as a function of on the integration radius of sphere or cylinder.

constant between the cubic, tetragonal, and monoclinic hafnia crystals. Then, the local analysis will be a good tool to clarify the science of the effects of oxygen vacancies and interface between Si substrate and HfO_2 film.

9.5 Conclusions

In this work, the dielectric property of hafnia has been investigated in terms of the local polarizability density and dielectric constant density using cluster models of the cubic, tetragonal, and monoclinic structures of HfO_2. We have also studied the dielectric property of SiO_2 for a comparison between the electronic contribution to the dielectric constant by ionic property of HfO_2 bond and covalent property of SiO_2 bond.

We have shown that the choice of the termination condition of models is important for the realization of the condensed property of dielectric. In this work, we have compared point charge models and hydrogen termination models in terms of DOS, the distribution of the Mulliken charges, and the macroscopic dielectric constant. As a result, it is shown that the appropriate termination conditions for this analysis are point charge conditions for all structures of HfO_2 and hydrogen termination conditions for SiO_2, respectively. This is because point charges are appropriate for the realization of ionic bond and hydrogen termination is better for that of covalent bond.

We have calculated the local polarizability density tensor and local dielectric constant density tensor of HfO_2. It is shown that local parts of materials have complicated responses

to external fields, in particular, rotational ones. Hence, the nanosize material should be studied in the local and tensor quantity analysis to describe rotational responses correctly. It is shown that three structures of HfO_2 crystals have common properties of the electronic contribution to local polarizability and dielectric constant densities. The response of electrons in SiO_2 to external electric fields is significantly weaker compared to those in HfO_2 due to small shifts of electrons in SiO_2. In addition, we have shown that the average values of dielectric constant around O atoms are larger than those of other regions. Particularly, this tendency is more salient in SiO_2 than HfO_2. Hence, our results show that the electronic contribution to macroscopic dielectric constant is dominated by O atoms in silicon dioxide, while in hafnia there is some contribution from Hf atoms.

As future works, we must take the lattice contribution to the dielectric property as local density quantity in order to reveal the dielectric property of nano-materials, since the lattice contribution to the dielectric constant dominates over the electronic one and depends on the structures of crystals. We must also study the modification of the local polarizability density and dielectric constant density by the existence of vacancies. In addition, the frequency dependence of the dielectric constant is also mandatory for the study of gate dielectric thin films for future electronics devices, since these devices work with high frequency.

Reference

[1] G. D. Wilk, R. M. Wallace, and L. M. Anthony, J. Appl. Phys. **89**, 5243 (2001).

[2] J. Robertson, Eur. Phys. J. Appl. Phys. **28**, 265 (2004).

[3] D. G. Schlom and J. H. Haeni, MRS Bull. **27**, 198 (2002).

[4] X. Zhao and D. Vanderbilt, Phys. Rev. B **65**, 233106 (2002).

[5] E. Cockayne, J. App. Phys. **103**, 084103 (2008).

[6] K. Kita, K. Kyuno, and A. Toriumi, Appl. Phys. Lett. **86**, 102906 (2005).

[7] D. H. Triyoso, R. I. Hegde, K. K. Schaeffer, D. Roan, P. J. Tobin, S. B. Samavedam, and B. E. White, Jr., Appl. Phys. Lett. **88**, 222901 (2006).

[8] Y. Watanabe, Y. Kamimuta, S. Migita, A. Ogawa, K. Iwamoto, H. Ito, T. Nabatame, and A. Toriumi, presented at Silicon Nanoelectronics Workshop, 2007.

[9] Y. Kikuchi, C. Tamura, R. Hasunuma, and K. Yamabe, presented at Gate Stack Technology and Physics, 2011.

[10] A. Tachibana, J. Mol. Model. **11**, 301 (2005).

[11] A. Tachibana, J. Mol. Struct.: THEOCHEM **943**, 138 (2010).

[12] K. Doi, Y. Mikazuki, S. Sugino, T. Doi, P. Szarek, M. Senami, K. Shiraishi, H. Iwai, N. Umezawa, T. Chikyo, K. Yamada, and A. Tachibana, Jpn. J. Appl. Phys. **47**, 205 (2008).

[13] P. Szarek, Dr. thesis, Micro Engineering, Kyoto University, Kyoto, (2008) [http://hdl.handle.net/2433/66212].

[14] A. Fukushima, S. Sugino, Y. Tsuchida, M. Senami, and A. Tachibana, Jpn. J. Appl. Phys. **49**, 121504 (2010).

[15] A. Fukushima, M. Senami, Y. Tsuchida, and A. Tachibana, Jpn. J. Appl. Phys. **49**, 111504 (2010).

[16] M. Senami, Y. Ikeda, A. Fukushiam, and A. Tachibana, Jpn. J. Appl. Phys. **49**, 115002 (2010).

[17] M. Senami, Y. Ikeda, and A. Tachibana, Jpn. J. Appl. Phys. **50**, 010103 (2011).

[18] M. Senami, Y. Ikeda, T. Hara, and A. Tachibana, Key Eng. Mater. **470**, 66 (2011).

[19] M. Senami, J. Nishikawa, T. Hara, and A. Tachibana, J. Phys. Soc. Jpn. **79**, 084302 (2010).

[20] S. Zafar, A. Callegari, E. Gusev, and M. V. Fischetti, J. Appl. Phys. **93**, 9298 (2003).

[21] C. C. Hobbs, L. R. C. Fonseca, A. Knizhnik, V. Dhandapani, S. B. Samavedam, W. J. Taylor, J. M. Grant, L. G. Dip, D. H. Triyoso, R. I. Hegde, D. C. Gilmer, R. Garcia, D. Roan, M. L. Lovejoy, R. S. Rai, E. A. Hebert, H.-H. Tseng, S. G. H. Anderson, B. E. White, and P. J. Tobin, IEEE Trans. Electron Devices **51**, 978 (2004).

[22] K. Shiraishi, K. Yamada, K. Torii, Y. Akasaka, K. Nakajima, M. Konno, T. Chikyow, H. Kitajima, and T. Arikado, Jpn. J. Appl. Phys. **43**, L1413 (2004).

[23] X. P. Wang, M. F. Li, A. Chin, C. X. Zhu, J. Shao, W. Lu, X. C. Shen, X. F. Yu, R. Chi, C. Shen, A. C. H. Huan, J. S. Pan, A. Y. Du, P. Lo, D. S. H. Chan, and D. L. Kwong, Solid-State Electron. **50**, 986 (2006).

[24] N. Umezawa, K. Shiraishi, S. Sugino, A. Tachibana, K. Ohmori, K. Kakushima, H. Iwai, T. Chikyow, T. Ohno, Y. Nara, and K. Yamada, Appl. Phys. Lett. **91**, 132904 (2007).

[25] H. Momida, T. Hamada, T. Yamamoto, T. Uda, N. Umezawa, T. Chikyow, K. Shiraishi, and T. Ohno, Appl. Phys. Lett. **88**, 112903 (2006).

[26] H. Momida, T. Hamada, and T. Ohno, Jpn. J. Appl. Phys. **46**, 3255 (2007).

[27] J. Wang, H. P. Li, and R. Stivens, J. Mater. Sci. **27**, 5397 (1992).

[28] A. A. Demkov, Phys. Status Solidi B **226**, 57 (2001).

[29] J. Wang, H. P. Li, and R. Stivens, J. Mater. Sci. **27**, 5397 (1992).

[30] T. Mizoguchi, M. Saitoh, and Y. Ikuhara, J. Phys.: Condens. Matter **21**, 104212 (2009).

[31] M. Harb, P. Labéguerie, I. Baraille, and M. Rérat, Phys. Rev. B **80**, 235131 (2009).

[32] Gaussian 03, Revision B.05 (Gaussian, Inc., Pittsburgh, PA, 2003).

[33] S. Baroni and R. Resta, Phys. Rev. B **33**, 7017 (1988).

[34] Z. H. Levine and D. C. Allan, Phys. Rev. B **43**, 4187 (1991).

[35] Z. H. Levine and D. C. Allan, Phys. Rev. B **44**, 12781 (1991).

[36] Z. H. Levine and D. C. Allan, Phys. Rev. Lett. **63**, 1719 (1989).

[37] Z. H. Levine and D. C. Allan, Phys. Rev. Lett. **66**, 41 (1991).

[38] P. J. Hay and W. R. Wadt, J. Chem. Phys. **82**, 270 (1985).

[39] W. R. Wadt and P. J. Hay, J. Chem. Phys. **82**, 284 (1985).

[40] P. J. Hay and W. R. Wadt, J. Chem. Phys. **82**, 299 (1985).

[41] W. J. Hehre, R. Ditchfield, and J. A. Pople, J. Chem. Phys. **56**, 2257 (1972).

[42] P. C. Hariharan and J. A. Pople, Theor. Chim. Acta **28**, 213 (1973).

[43] M. Senami, K. Ichikawa, K. Doi, P. Szarek, K. Nakamura, and A. Tachibana, Molecular Regional DFT program package, ver. 3 (Tachibana Lab., Kyoto University, Kyoto, 2008).

[44] M. Balog, M. Schieber, M. Michman, and S. Patai, Thin Solid Films **41**, 247 (1977).

[45] X. Zhao and D. Vanderbilt, cond-mat/0301016.

[46] J. E. Jaffe, R. A. Bachorz, and M. Gutowski, Phys. Rev. B **72**, 144107 (2005).

[47] D. W. McComb, and A. Howie, Nucl. Instrum. Methods Phys. Res., Sect. B **96**, 569 (1995).

[48] T. Tamura, S. Ishibashi, S. Tanaka, M. Kohyama, and M. H. Lee, Phys. Rev. B **77**, 085207 (2008).

[49] E. Cockayne, Phys. Rev. B **75**, 094103 (2007).

General Conclusion

In this thesis, several materials have been investigated in detail by first-principles calculations. Through this thesis, electric conductive properties and bonding nature of the materials are focused on.

PART I is devoted to the electric conductive properties of nanomaterials. First, two methods for calculating electronic structures with electric currents are developed. The one is based on the SCF method and reported in Chapter 1, and the other is based on the perturbation theory and shown in Chapter 2. In both methods, conduction electrons are treated as quantum states, and Coulomb and exchange interactions are included. The SCF method can determine an electronic structure and vector potential consistently, while the preturbation method can obtain linear responses to external electric field in an analytic form. By using these methods, local electric conductivity which is defined in Rigged QED are analyzed for semiconductor nanowire models. The results are shown in Chapters 3 and 4. As a result, some unique properties such as rotational response are found. This is shown in regions with complex eigenvalues and means that electric current density response to electric field with the change of direction. In addition, $\overleftrightarrow{\sigma}_{\rm int}(\vec{r})$ which reveals response of electric current density to actual electric field at each spatial point is investigated. As a result, it is found that $\overleftrightarrow{\sigma}_{\rm int}(\vec{r})$ show different distribution pattern from $\overleftrightarrow{\sigma}_{\rm ext}(\vec{r})$. It is worth noting that these properties can be found only in microscopic viewpoint.

In PART II, chemical reactions, stability of structures, and dielectric properties are investigated for several materials by focusing on their bonding nature. Growth of GaN crystal is studied based on gas phase and surface reactions in Chapter 5. It is found that a Ga-Ga bond between a molecule in gas phase and a Ga surface of the crystal prevents stable growth, and molecules which have a coordinate bond with NH_3 do not meke the Ga-Ga bond. In this analysis, existance of the Ga-Ga bond is confirmed by calculating the surface where

kinetic energy density is equal to zero. In Chapters 6 and 7, electronic stress tensor density is analyzed for alminum clusters, and Al-Al and Al-H bonds in them are found to show different characteristics in the eigenvalues of the stress tensor. Absorption of lithium atoms on a single wall CNT model is studied in Chapter 8. From the analysis of stabilization energies, It is found that single lithium atom perfers the absorption on the inner surface of the CNT to outer one of it. This result is supported by the analysis of charge transfer and chemical potential density. Dielectric properties of HfO_2 are investigated in terms of local polarizability and local dielectric constants in Chapter 9. From the comparison with the results for SiO_2, it is found that the difference of bonding nature between HfO_2 and SiO_2 causes the significant difference of local dielectric properties, especially around Hf and Si atoms.

In the series of the studies, local phisical quantities which are defined in Rigged QED are used. As a result, it is found that they are powerful tools for understanding characteristics of nanomaterials and functional materials.

Acknowledgements

I wish to express my gratitude to many people who helped me here. First, I am thankful to Professor Akitomo Tachibana for his guidance, valuable suggestions, discussions, and encouragement. Moreover, I also am grateful to Dr. Masato Senami, Dr. Kazuhide Ichikawa, and Dr. Kentaro Doi for their valuable suggestions and discussions. I also thanks Dr. Akinori Fukushima for his discussions to overcome difficulties. Parts of my studies are supported by the Sasakawa Scientific Research Grant from the Japan Science Society. Finally, I would like to express my gratitude to my parents for their continuing encouragement.

List of Publications

Chapter 1

[1] Masato Senami, Yuji Ikeda, Akinori Fukushima, and Akitomo Tachibana, "Calculation of the electronic state in electronic current for nanowire models", Jpn. J. Appl. Phys. **49**, 115002(5) (2010).

Chapter 2

[2] Yuji Ikeda, Masato Senami, and Akitomo Tachibana, "Local electric conductive property of si nanowire models", AIP Adv. **2**, 042168(16) (2012).

Chapter 3

[3] Masato Senami, Yuji Ikeda, and Akitomo Tachibana, "Local Transport Property of GaN Cluster as a Model of Nanowire". Jpn. J. Appl. Phys. **50**, 010103(7) (2011).

Chapter 4

[4] Masato Senami, Y. Ikeda, Takaaki Hara, and Akitomo Tachibana, "Nanosize Electronics Material Analysis by Local Quantities Based on the Rigged QED Theory", Key Eng. Mater. **470**, 66–71 (2011).

Chapter 5

[5] Yuji Ikeda, Norifumi Ohmori, Noriaki Maida, Masato Senami, and Akitomo Tachibana, "Theoretical study of gallium nitride crystal growth reaction mechanism", Jpn. J. Appl. Phys. **50**, 125601(7) (2011).

Chapter 6

[6] Kazuhide Ichikawa, Yuji Ikeda, Ayumu Wagatsuma, Kouhei Watanabe, Pawel Szarek, and Akitomo Tachibana, "Theoretical study of hydrogenated tetrahedral aluminum clusters", Int. J. Quantum Chem. **111**, 3548–3555 (2011).

Chapter 7

[7] Kazuhide Ichikawa, Yuji Ikeda, Ryo Terashima, and Akitomo Tachibana, "Aluminum hydride clusters as hydrogen storage materials and their electronic stress tensor analysis", Mater. Science Forum **706–709**, 1539–1544 (2012).

Chapter 8

[8] Masato Senami, Yuji Ikeda, Akinori Fukushima, and Akitomo Tachibana, "Theoretical study of adsorption of lithium atom on carbon nanotube", AIP Adv. **1**, 042106 (2011).

Chapter 9

[9] Masato Senami, Yasushi Tsuchida, Akinori Fukushima, Yuji Ikeda, and Akitomo Tachibana, "Local dielectric property of cubic, tetragonal, and monoclinic hafnium oxides", Jpn. J. Appl. Phys. **51** 031101 (2012).

References

[10] Yuji Ikeda, Masato Senami, and Akitomo Tachibana, "Non-hermitian coupled perturbed hartree-fock method for calculating electronic structures with electric currents",

in *Proceedings of Conference on Computational Physics*, submitted for publication, Kobe, Japan, (2012).

[11] Yuji Ikeda, Hiroo Nozaki, Kazuhide Ichikawa, and Akitomo Tachibana, "Theoretical study of chemical reactions in gas phase of CVD process for $Ge_2Sb_2Te_5$ by first principle calculations and electronic stress tensor analysis", in preparation.

Conference Appearances

- *First-principles calculations for Si nanowire in electric current and electromagnetic field.* (in Japanese)
  Yuji Ikeda, Akinori Fukushima, Kentaro Doi, Masato Senami, Akitomo Tachibana,
  13th Workshop on GateStack Technology and Physics, 13–15 January 2008, Shizuoka, Japan

- *First-Principles Calculations for Si nanowire in electric current and electromagnetic fields.* (in Japanese)
  Yuji Ikeda, Akinori Fukushima, Kentaro Doi, Masato Senami, Akitomo Tachibana,
  JPS the 63rd Annual Meeting, 22–26 March 2008, Osaka, Japan

- *First-principles study on the conduction properties of Si nanowires.* (in Japanese)
  Yuji Ikeda, Akinori Fukushima, Masato Senami, Akitomo Tachibana,
  JPS 2008 Autumn Meeting, 20–23 September 2008, Iwate, Japan

- *First-principles Study on the Conduction Properties of Si Nanowire.*
  Yuji Ikeda, Akinori Fukushima, Masato Senami, Akitomo Tachibana,
  The IUMRS International Conference in Asia 2008, 9–13 December 2008, Nagoya, Japan

- *First principles analysis for the conduction characteristics of Si nanowires.* (in Japanese)
  Yuji Ikeda, Akinori Fukushima, Masato Senami, Akitomo Tachibana,
  14th Workshop on GateStack Technology and Physics, 22–24 January 2009, Shizuoka, Japan

- *First principles calculations of local electrical conduction in a target system.* (in Japanese)

Masato Senami, Yuji Ikeda, Akinori Fukushima, Akitomo Tachibana,
The 70th Autumn Meeting 2009 (The Japan Society of Applied Physics), 8–11 September 2009, Toyama, Japan

- *Study for Effects of Electric Currents on Chemical Bonding.* (in Japanese)
  Masato Senami, Kazuhide Ichikawa, Yuji Ikeda, Akitomo Tachibana, The 3th Annual Meeting of Japan Society for Molecular Science 2009, 21–24 September 2009, Nagoya, Japan

- *Analysis for Electron Transport Properties of Silicon Nanowires Using Local Electrical Conductivity.* (in Japanese)
  Yuji Ikeda, Akinori Fukushima, Masato Senami, Akitomo Tachibana, 15th Workshop on GateStack Technology and Physics, 21–23 January 2010, Shizuoka, Japan

- *Calculation of the Electronic State in Electric Current for Nanowire Models.* (in Japanese)
  Yuji Ikeda, Akinori Fukushima, Masato Senami, Akitomo Tachibana,
  The 57th Spring Meeting JSAP and Related Societies, 17–20 March 2010, Kanagawa, Japan

- *Analysis for Electron Transport Properties of Silicon Nanowires Using Local Electrical Conductivity.* (in Japanese)
  Yuji Ikeda, Akinori Fukushima, Masato Senami, Akitomo Tachibana,
  JPS the 65th Annual Meeting, 20–23 March 2010, Okayama, Japan

- *Calculations of the electronic structures for the conduction states of silicon nanowires* (in Japanese)
  Yuji Ikeda, Akinori Fukushima, Masato Senami, Akitomo Tachibana,
  The 71st Autumn Meeting 2010 (The Japan Society of Applied Physics), 14–17 September 2010, Nagasaki, Japan

- *Analysis of Silicon Nanowires by Local Electrical Conductivity Based on the Rigged QED Theory.*
  Yuji Ikeda, Masato Senami, Akitomo Tachibana,

2011 International Workshop on DIELECTRIC THIN FILMS FOR FUTURE ELECTRON DEVICES: SCIENCE AND TECHNOLOGY, 20–21 January 2011, Tokyo, Japan

- *Effects of Internal Structure of Hafnia on Dielectric Property.* (in Japanese)
  Masato Senami, Yasushi Tsuchida, Fumiya Yoshino, Akinori Fukushima, Yuji Ikeda, Akitomo Tachibana,
  16th Workshop on GateStack Technology and Physics, 21–23 January 2011, Tokyo, Japan

- *Aluminum Hydride Clusters as Hydrogen Storage Materials and their Electronic Stress Tensor Analysis.*
  Kazuhide Ichikawa, Yuji Ikeda, Ryo Terashima, Akitomo Tachibana
  THERMEC'2011, 1–5 August 2011, Quebec City Convention Center, Quebec City, Canada

- *Study For Local Linear Response of Electronic States to Electric Field.* (in Japanese)
  Yuji Ikeda, Fumiya Yoshino, Masato Senami, Akitomo Tachibana,
  The 72nd Autumn Meeting 2011 (The Japan Society of Applied Physics), 29–2 August 2011, Yamagata, Japan

- *Analysis for Local Linear Response of Electric Current Density to External Electric Field.* (in Japanese)
  Yuji Ikeda, Fumiya Yoshino, Masato Senami, Akitomo Tachibana,
  The 5th Annual Meeting of Japan Society for Molecular Science 2011, 20–23 September 2011, Sapporo, Japan

- *Analysis of Electronic Stress Tensor Density for Aluminum Hydride Clusters and Effects of Electric Currents.* (in Japanese)
  Ryo Terashima, Yuji Ikeda, Kazuhide Ichikawa, Akitomo Tachibana,
  The 5th Annual Meeting of Japan Society for Molecular Science 2011, 20–23 September 2011, Sapporo, Japan

- *Local Electrical Conductivity of Silicon Nanowires with Impurities* (in Japanese)
  Yuji Ikeda, Masato Senami, Akitomo Tachibana,

17th Workshop on GateStack Technology and Physics, 19–21 January 2012, Shizuoka, Japan

- *Time Evolution of Quantum Systems and Local Physical Quantities Based on Rigged QED Theory.* (in Japanese)
  Masato Senami, Toshihide Miyazato, Yuji Ikeda, Akitomo Tachibana,
  The 59th Spring Meeting JSAP and Related Societies, 15–18 March 2012, Tokyo, Japan

- *Analysis of Local Electrical Conductivity for Silicon Nanowire.* (in Japanese)
  Yuji Ikeda, Masato Senami, Akitomo Tachibana,
  JPS the 67th Annual Meeting, 24–27 March 2012, Hyogo, Japan

- *Calculation Method of Electronic Structures in Conduction States for Analysis of Local Electric Conductive Properties.* (in Japanese)
  Yuji Ikeda, Masato Senami, Akitomo Tachibana,
  15th Theoretical Chemistry Symposium, 24–26 May 2012, Sendai, Japan

- *Numerical Simulation for Dielectric Response of Atoms and Molecules Based on Rigged QED.* (in Japanese)
  Toshihide Miyazato, Masato Senami, Yuji Ikeda, Akitomo Tachibana,
  15th Theoretical Chemistry Symposium, 24–26 May 2012, Sendai, Japan

- *Theoretical Study on Relations between Dynamics of Nuclear Field and its Statistics Based on Rigged QED.* (in Japanese)
  Sojiro Takada, Toshihide Miyazato, Yuji Ikeda, Masato Senami, Akitomo Tachibana,
  15th Theoretical Chemistry Symposium, 24–26 May 2012, Sendai, Japan

- *Time Evolution Simulation of Nuclei and Electrons Based on Rigged QED.* (in Japanese)
  Masato Senami, Toshihide Miyazato, Sojiro Takada, Yuji Ikeda, Akitomo Tachibana,
  15th Theoretical Chemistry Symposium, 24–26 May 2012, Sendai, Japan

- *Calculation Method for Electronic Structures with Electric Current Based on Perturbation Theory.* (in Japanese)
  Yuji Ikeda, Masato Senami, Akitomo Tachibana,

The 73rd Autumn Meeting, 2012 (The Japan Society of Applied Physics), 11–14 September 2012, Ehime, Japan

- *Study of Perturbative Approach for Calculating Electronic Structures under the Existence of Electric Currents.* (in Japanese)
  Yuji Ikeda, Masato Senami, Akitomo Tachibana,
  The 6th Annual Meeting of Japan Society for Molecular Science 2012, 18–21 September 2012, Tokyo, Japan

- *Rigged QED Simulation of Atomic Systems in an External Field.* (in Japanese)
  Toshihide Miyazato, Masato Senami, Yuji Ikeda, Sojiro Takada, Akitomo Tachibana,
  The 6th Annual Meeting of Japan Society for Molecular Science 2012, 18–21 September 2012, Tokyo, Japan

- *Theoretical study of the relation between the statistics of nucleus fields and their behavior based on Rigged QED.* (in Japanese)
  Sojiro Takada, Toshihide Miyazato, Yuji Ikeda, Masato Senami, Akitomo Tachibana,
  The 6th Annual Meeting of Japan Society for Molecular Science 2012, 18–21 September 2012, Tokyo, Japan

- *Analysis of Local Electric Conductivities for Si Nanowire Models.*, Yuji Ikeda, Masato Senami, Akitomo Tachibana,
  IUMRS-ICEM 2012, 23–28 September 2012, Yokohama, Japan

- *Analysis of Local Electric Conductive Property for Si Nanowire Models.*
  Yuji Ikeda, Masato Senami, Akitomo Tachibana,
  PRiME 2012, 7–12 Octobar 2012, Honolulu, Hawaii

- *Perturbative Approach for Calculating Electronic Structures with Electric Currents.*
  Yuji Ikeda, Masato Senami, Akitomo Tachibana,
  Conference on Computational Physics (CCP2012), 14–18 Octobar 2012, Kobe, Japan

- *Study of CVD process of GeSbTe by first principles calculations.*
  Kazuhide Ichikawa, Masato Senami, Yuji Ikeda, Hiroo Nozaki, Akitomo Tachibana,
  The 24th Symposium on Phase Change Oriented Science PCOS 2012, 29–30 November 2012, Sizuoka, Japan